5-2017

Shaping Metallic Nanoparticles Toward Integrated Plasmonics and Catalysis

Qingfeng Zhang
University of South Carolina

SHAPING METALLIC NANOPARTICLES TOWARD INTEGRATED PLASMONICS AND CATALYSIS

by

Qingfeng Zhang

Bachelor of Science
Fuzhou University, 2009

Master of Science
Xiamen University, 2012

Submitted in Partial Fulfillment of the Requirements

For the Degree of Doctor of Philosophy in

Chemistry

College of Arts and Sciences

University of South Carolina

2017

Accepted by:

Hui Wang, Major Professor

Donna A. Chen, Committee Member

Hans-Conrad zur Loye, Committee Member

Theodore M. Besmann, Committee Member

Cheryl L. Addy, Vice Provost and Dean of the Graduate School

DEDICATION

This dissertation is dedicated to my family and friends, especially to my wife and parents, for their love and support.

ACKNOWLEDGEMENTS

The past five years at Palmetto State is full of challenges, devotion, and happiness that I will never forget in my whole life. I am deeply grateful to many individuals, without whom it would not have been possible for me to finish this dissertation. It is my great pleasure to express my gratitude to all of them at this point.

The most important thanks go to my advisor, Dr. Hui Wang. I have greatly benefited from his creative thinking, scientific attitude, and constructive guidance. It is him who taught me how to do research and how to do it very well, I'm so proud to work under his guidance in physical chemistry and nanoscience. I really enjoy the moments that we shared exciting results and ideas on scientific questions not only in the lab but also during the lunch time. I also greatly appreciated his continuous support on training of skill-sets, especially when I was facing the challenge of language barrier in the beginning of my PhD. He encouraged me to improve the communication and presentation skills by giving oral talks in the physical chemistry divisional seminar every year, as well as presenting my research work at many important conferences. As a remarkable experimental physical chemist, he is always a tremendous role model for me.

Furthermore, I would like to express my heartfelt gratitude to Dr. Donna Chen, Dr. Hans-Conrad zur Loye, Dr. Theodore Besmann, and Dr. Kenneth Reifsnider for their valuable suggestions and continuous support, which have led to the successful accomplishment of my dissertation. I would also like to thank our collaborators, Dr. Peter Nordlander (Rice University), Dr. Nicolas Large (The University of Texas at San

Antonio), Dr. Shengli Zou and Mr. Yadong Zhou (University of Central Florida), Dr. Huolin Xin and Ms. Lili Han (Brookhaven National Lab), Dr. Douglas Blom (NanoCenter at USC), and Dr. Ye Lin (Chemical Engineering at USC), for their great theoretical simulation and nano-characterization work, which have led to many beautiful pieces of work. Moreover, I would like to thank Dr. Michael Myrick, Dr. Mark Berg, Dr. Vitaly Rassolov, Dr. Sophya Garashchuk, Dr. Andrew Greytak for their great courses and helpful suggestions on my work and presentations. Also thanks a lot to Dr. Qian Wang, Dr. Chuanbing Tang, and Dr. Morgan Stefik for the open access to their experimental instruments. I would also like to thank all of my colleagues at Electron Microscopy Center of USC: Ms. Jibin Zhao, Dr. Soumitra Ghoshroy, Dr. Yingchao Yang, John Alam, Valerie Steinmeyer, Habeeb Alsudani, Max Siegrist. I really enjoy the time that I worked with them on electron microscopy. Also I would like to thank Jennifer Merker, Dr. Michael Dukes, Sam Burgess, and Coyet Greene from chemistry department for their selfless help.

More importantly, I would like to thank all of labmates in Dr. Hui Wang's group, both current and previous members: Lichao Sun, Guangfang Li, Esteban Villarreal, Dr. Hao Jing, Dr. Yihong Zhan, Dr. Li Zhang, Dr. Tingting Zheng, Dr. Chunmei Yu, Dr. Xiaoqi Fu, Mengqi Sun, John He, for their selfless help in both science and life. Also I would like to thank all of my friends for sharing the wonderful life in Columbia.

Finally, I would like to express my deepest love and thanks to my wife, Lichao, for her endless love, to my parents and my parents-in-law for their infinite support, and to my little princess, Mina, for everything she brings to me.

ABSTRACT

Noble metal nanoparticles have been of tremendous interest because of their intriguing size- and shape-dependent plasmonic and catalytic properties. The combination of tunable plasmon resonances with superior catalytic activities on the same nanoparticle, however, has long been challenging because plasmonics and catalysis require nanoparticles in two drastically different size regimes. Tunable plasmon resonances is a unique feature of sub-wavelength metallic nanoparticles, whereas heterogeneous catalysis requires the use of sub-5 nm nanoparticles as the catalysts. In this dissertation, I firstly found a unique way to bridge this size gap between nanoplasmonics and nanocatalysis. I demonstrated that desired plasmonic and catalytic properties can be integrated on the same particle by controllably creating high energy facets on individual sub-wavelength metallic nanoparticles, such as, porous Au nanoparticles, Au nanocrystals enclosed by well-defined high-index facets, multi-faceted Au and bimetallic nanorods. The capabilities to both nanoengineer high energy facets and fine-tune the plasmon resonances through deliberate particle geometry control allow us to use these nanoparticles for a dual purpose: as substrates for plasmon-enhanced spectroscopies and efficient surface catalysts. Such dual functionality enables us to gain quantitative insights into the facet-dependent molecular transformations on metallic nanocatalysts using surface-enhanced Raman spectroscopy (SERS) as an ultrasensitive spectroscopic tool with unique time-resolving and molecular finger-printing capabilities.

More recently, I further expanded my research interest into plasmonic hot electron-driven photocatalytic reactions. I focused on the quantitative understanding of the kinetics and underlying pathways of plasmon-driven photocatalysis. I used SERS to precisely monitor, in real time, the plasmon-driven photoreaction kinetics at the molecule-nanoparticle interfaces. The reductive dimerization of 4-nitrothiophenol and oxidative coupling of thiophenol-derivates were chosen as model reactions to explore the effects of plasmon excitations, molecular adsorption states, local field enhancements, and photothermal processes, on the plasmon-driven photocatalytic reactions.

In summary, the goal of this dissertation is to gain new insights on interfacial molecular transformation kinetics and underlying mechanism of heterogeneous catalysis and plasmon-driven photocatalysis using in situ plasmon-enhanced spectroscopic tool for guiding rational design of high performance metallic nanocatalysts and photocatalysts toward environmental and energy application.

Table Of Contents

LIST OF FIGURES

CHAPTER 1

Introduction

1.1 Localized Surface Plasmon Resonance of Metallic Nanoparticles

Localized surface plasmon resonances (LSPRs) is known as the collective oscillations of free electrons on metal surfaces upon light excitation, which contributes to the fascinating optical characteristics of metallic nanoparticles (Figure 1.1A).[1,2] When a metal nanoparticle is excited to generate surface plasmons at its eigenfrequency upon light excitation, the incident light is both absorbed and scattered, giving rise to vivid colors.[3] The beautiful colors of colloidal metal nanoparticles has been an object of fascination back to ancient times. The famous Lycurgus Cup is one of the oldest examples. This glass cup exhibits a striking red color when light is shone into the cup and transmitted through the glass, and it appears green while viewed in reflected light. This particular behavior is essentially due to the small Au-Ag bimetallic nanoparticles embedded in the glass, which show a strong optical absorption of light in the green part of the visible spectrum. Although these optical characteristics of metallic nanoparticles have been known and used for centuries, our scientific understanding on the origin of these optical properties has emerged far more recently, beginning with the development of classical electromagnetic theory. Gustav Mie firstly applied Maxwell's equations to explain the strong absorption of green light by a Au nanosphere under plane wave illumination about a century ago,[4] which established the rigorous scientific foundation for our understanding on the LSPRs-dominated intriguing optical properties of metallic nanoparticles. The past decades have witnessed significant advances in scientific understanding of the origin of the optical tunability of metallic nanoparticle systems, primarily driven by the rapid advances in the geometry-controlled nanoparticle fabrication and assembly and electrodynamics modeling of nanoparticle systems.[1,3,5,6]

The unique optical features of LSPRs can be well displayed by far-field extinction spectral feature and the near-field enhancement.[2,6] The far-field extinction properties are measured by optical extinction spectroscopy to show the maximized excitation of surface plasmons at specific frequencies/wavelengths (Figure 1.1B). On the other hand, the significant enhanced local electric field induced by collective oscillation of free electrons would greatly increase the molecular optical cross-section when molecules are adsorbed onto the surfaces of metallic nanoparticles (Figure 1.1C).[2,7,8] Both the far-field and near-field optical properties of metallic nanoparticles could be simulated based on either analytic methods (Mie scattering theory and the Gans model) or numerical methods (discrete dipole approximation (DDA) and finite-difference time-domain (FDTD)).[2,6] Remarkably, by judiciously tailoring the geometries of the metal nanoparticles, one can fine-tune the optical resonance frequencies and optimize the electric near field enhancements associated with the plasmonic excitations.[2-6] Expanding the plasmonic tunability of nanoparticles over a broad spectral range is of paramount importance because it opens up a whole set of new opportunities for photonic,[2,9] optoelectronic,[9] spectroscopic,[7,10] and biomedical applications.[11-13] This has, in turn, stimulated rapidly growing interests in a variety of metallic nanostructures with geometrically tunable optical properties, such as nanorods,[5,14] nanoprisms,[15] nanoshells,[2,12,16] and nanocages.[11,17]

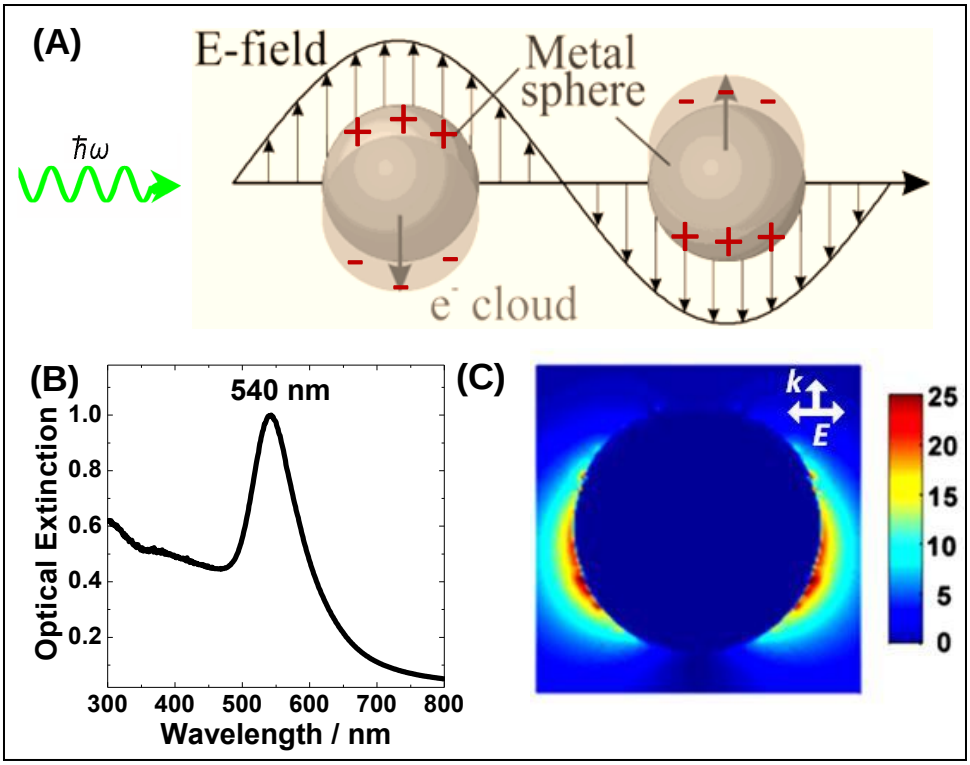

Figure 1.1 (A) Localized surface plasmon resonance (LSPR) of metal nanosphere upon light excitation, showing the displacement of the conduction electron charge cloud relative to the nuclei. (B-C) The far-field optical extinction spectra (B) and the calculated near-field enhancement (C) of the corresponding Au nanospheres with the diameter size of 40 nm.

1.2 Surface-enhanced Raman Scattering (SERS)

The physical phenomenon of Raman spectroscopy is inelastic scattering of photons from a molecule with quantifiable vibrational signals, which was first observed by Raman in 1928.[18] Although Raman spectroscopy could provide rich information of a molecule, it has not become a very common tool for analysis when comparing to Infrared and UV-Vis spectroscopy. It is the weak signal intensity that limited the development of Raman spectroscopy. The weak signal can be attributed to the very low Raman scattering cross section for most of molecules, generally more than 10 orders of magnitude lower than that of infrared absorption.[19]

The Raman signal was significantly enhanced after the discovery of SERS in mid-

1970s.[20-22] In 1974, Fleischmann, Hendra and McQuillan first reported the measurement of a surface Raman spectrum with intense Raman signal from pyridine adsorbed on an electrochemically roughened Ag electrode.[20] Although Fleischmann et al. first discovered the phenomenon, the SERS effect was not really recognized as such at that time. After that, both Van Duyne and Creighton reported the similar results independently in 1977.[21,22] They provided strong evidences to show that the intense Raman signal was caused by a special enhancement of the Raman scattering efficiency itself but not be accounted for simply by the increase in the number of scatterers. Thus, the effect was what we called surface-enhanced Raman scattering (SERS) now. Interestingly, Van Duyne and Creighton proposed different SERS mechanisms in their papers. Van Duyne proposed an electromagnetic (EM) enhancement mechanism,[22] while Creighton speculated that resonance Raman scattering from molecular electronic states was broadened by their interaction with the metal surface, which is called charge-transfer (chemical enhancement) mechanism.[21] Since they are both right in concept, the exact mechanism of SERS is still in debate until now.

SERS is essentially a nanoscale effect directly related to the intense electromagnetic field enhancements generated at nanostructured metallic surfaces upon the excitation of LSPRs, which also represents an ultrasensitive vibrational spectroscopic technique capable of providing detailed structural information of the molecules on or in the vicinity of nanostructured metallic surfaces.[23-25] As a powerful, non-invasive spectroscopic tool for the detection of low-abundance analytes, SERS plays pivotal roles in food safety inspection,[26,27] environmental monitoring,[28] and biomolecular sensing.[29-32] By combining plasmonic metallic nanoparticles with molecular Raman reporters, multifunctional SERS

nanoprobes, or SERS tags, have been developed to target specific biomolecules both *in vitro* and *in vivo*, enabling Raman-based optical bioimaging with high spatial resolution and excellent photostability.[33-37]

One of the most important factors that significantly affect the wide application of SERS is the lack of reliable, reproducible, and high-performance SERS substrates. Due to strong plasmonic coupling effects,[38] aggregated or self-assembled metallic nanoparticles possess "hot spots" for SERS inside the sub-10 nm interparticle gaps with gigantic field enhancements several orders of magnitude higher than those commonly achievable on the individual nanoparticles.[38-42] However, the challenges associated with precise control over the spatial distribution, enhancement magnitude, and structural robustness of the interstitial hot spots limit the utilization of the nanoparticle aggregates as reliable and reproducible SERS substrates for sensing and imaging applications. Therefore, single-particle SERS (spSERS) represents a more promising approach to SERS-based sensing and imaging with optimizable signal amplification and reproducibility in comparison to those strategies relying on the nanoscale interparticle junctions. The plasmonic field enhancements of individual nanoparticles can be optimized through deliberate control over particle geometries.[25,43,44] A widely used strategy of achieving intense field enhancements on the outer surfaces of individual nanoparticle is to controllably introduce nanoscale tipped or spiky features to the particle surfaces.[45-57] Upon plasmonic excitation, the electromagnetic fields are enormously enhanced at the surface vertices and edges, providing SERS hot spots on open surfaces that are easily accessible by molecules. A variety of Au or Ag nanoparticles with tipped surface features, such as surface-textured nanospheres,[45-50] etched nanopolyhedra,[51] multi-branched nanostars,[52-55] and spiky

nanoshells,[56,57] have all been shown to exhibit intense SERS enhancements on individual particles, convincingly demonstrating that the interparticle or intraparticle gap geometries are not always essential for strong SERS enhancements.

1.3 SERS Studies of Surface-Catalytic Reaction

As is well-known, the interaction between molecules and the surface of metallic nanoparticles would greatly affect the SERS pattern. In turn, the variation in the SERS pattern might be used as evidence for studying the change in the local chemical environment, such as, surface coverage of adsorbate, molecular orientations, and the formation of new chemical bonds or new molecules.[58] For example, a change in the orientation of 4-mercaptobenzoic acid was found by studying the SERS spectra during the formation of the hotspot.[59] Another example is that SERS could be used to monitor the conformation of cysteamine molecules on silver because different conformations have different orientation-dependent Raman scattering.[60] Since we could get abundant information of the species on the surface from the SERS, it is undoubted that we can use SERS to analysis the surface catalytic reaction in real time.

SERS provides an unique approach to the *in situ* monitoring of molecular transformations in heterogeneous catalysis with high detection sensitivity, excellent surface selectivity, and rich molecular structural information.[61-67] By measuring the SERS signals from the monolayer molecules pre-adsorbed on the nanocatalyst surfaces, unraveling the intrinsic kinetics and mechanisms of surface-catalyzed reactions becomes possible with minimal complication introduced by the surface-capping ligands as well as the diffusion, adsorption, and desorption of reactants and products. The unique capability of SERS to resolve detailed molecular structures further enables the identification of

transient intermediates along the reaction pathways.[64,65] Using SERS to directly monitor catalytic reactions on Au nanocatalysts, however, has been challenging because SERS and catalysis require Au nanoparticles in two drastically different size regimes. SERS relies on the generation of intense plasmon-field enhancements in close proximity to the particle surfaces,[68-70] which are not achievable on the catalytically active sub-5 nm Au nanoparticles. While Au nanoparticles in the subwavelength size regime exhibit strong plasmon resonances and intense local fields that can be harnessed for SERS, they are no longer catalytically active. Therefore, the combination of strong, tunable plasmon resonances and superior catalytic activities on the same nanoscale entity remains challenging essentially due to the two drastically different size regimes required for nanoplasmonics and nanocatalysis, respectively.

It has been recently demonstrated that the *in situ* monitoring of surface-catalyzed reactions by SERS becomes possible when catalytically active small nanoparticles of Au, Pt, or Pd and plasmonically active large Au nanoparticles are hierarchically assembled into three-dimensional multilayered complex superstructures.[61-64,66] For example, Wong and Halas combined the catalytically responsive and SERS effect into a single substrate by depositing Pd onto Au nanoshells.[61] With Pd islands grow on Au nanoshells, the hybrid SERS substrate can be used to study the catalytic hydrodechlorination of 1,1-dichloroethene (1,1-DCE) in H_2O. Based on the results from SERS, several surface intermediates of 1,1-DCE were proposed and direct evidence of the room-temperature catalytic hydrodechlorination of 1,1-DCE were provided, which greatly helps us to understand the underlying reaction mechanism. Another interesting example is that raspberry-like Au/Pt/Au core/shell nanoparticles with high density of catalytic-active

sites from Pt and strong plasmon resonance from Au were used to study the Pt-catalyzed reaction.[63] Reducing the NO_2 group (R-NO_2) to the corresponding NH_2 group (R-NH_2) through an azo intermediate by $NaBH_4$ was demonstrated by using SERS. Figure 1.2 clearly indicates that the SERS signal of azo initially enhances and then finally decreases with the increase of the amounts of $NaBH_4$. The results from SERS provided us the direct evidence on the existence of the azo intermediate. The structural complexity of these bifunctional hybrid particles, however, makes it challenging to directly correlate the surface structures with the catalytic activities of the nanocatalysts. With the rapid development of nanotechnology, the fabrication of nanomaterials with both SERS activity and catalysis property become possible, which would greatly help us to further study and understand the mechanisms of surface-catalytic reactions.

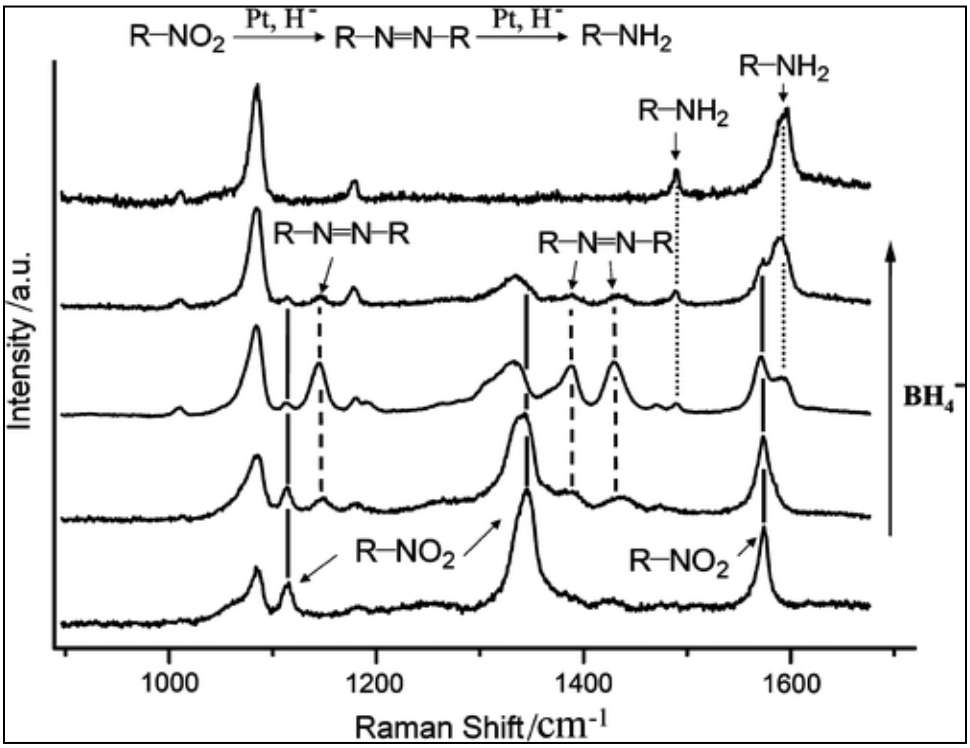

Figure 1.2 SERS spectra recorded during the Pt-catalyzed hydride reduction of an aromatic nitro compound, using different amounts of the reducing reagent $NaBH_4$. Reprinted with permission from reference 63.[63] Copyright 2013 American Chemical Society.

1.4 Plasmon-Driven Photocatalysis

After the excitation of plasmon resonance under light illumination, the energy transferred from light wave to plasmon resonance.[71] The lifetime of the coherent electron oscillation induced by plasmon excitation is extremely fast, typically at ~5-100 fs.[72] There are three main plasmon decay pathways (Figure 1.3):[71-74] (1) Elastic radiative re-emission of photons, also known as scattering; (2) Landau damping: giving rise to the formation of energetic electrons and holes pairs in the metal particle; (3) Chemical interface damping (CID): the interaction of excited surface plasmons with unpopulated adsorbate acceptor states, leading to the direct energetic electron injection into the adsorbate acceptor states. In contrast to CID pathway, if none of proper unpopulated adsorbate acceptor states are presented for energetic electron injection, the energetic electrons generated through Landau damping would undergo thermal dissipation process (electron-phonon coupling), resulting in local heating, also known as photothermal effect. While Landau damping shows much lower quantum yield than that of CID, it is much more sensitively dependent on the local field enhancement in comparison to CID, which would greatly benefit from the rational design of plasmonic nanostructure with high density of hot-spots. Although Landau damping and CID are intrinsically different mechanisms, both of them generate energetic electrons, also known as hot electrons, which can be probably harnessed for energy conversion and catalytic reaction.[75-80] Remarkably, the magnitude of field enhancement, resonant wavelength, and fraction of plasmon excitations decaying through these three mechanisms can be finely modulated by deliberately controlling the size, shape, composition, and local environment of plasmonic nanostructures.[1,2,6]

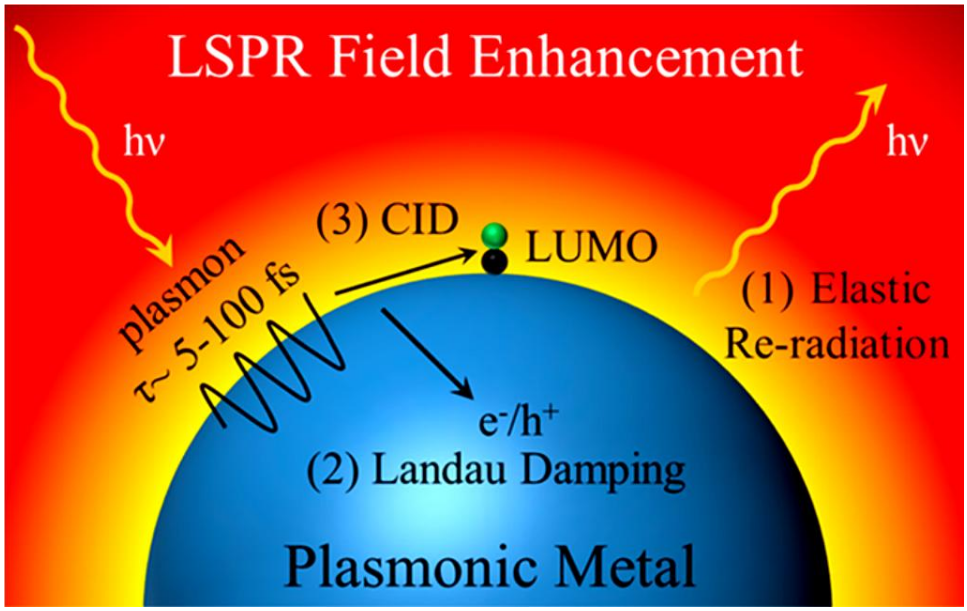

Figure 1.3 Schematically illustration of three typical mechanisms of surface plasmon decay paths. Reprinted with permission from reference 72.[72] Copyright 2014 American Chemical Society.

It has been recently observed that the hot carriers generated through surface plasmon decay play a key role in guiding interesting photo-chemical reactions, such as photochromic reactions,[81] photopolymerization,[82] photo-reductive dimerization of 4-nitrothiophenol (4-NTP),[83,84] and oxidative coupling of 4-aminothiophenol (4-ATP).[85,86] Moreover, some important catalytic reactions, such as, ethylene epoxidation,[75,87,88] dissociation of H_2,[77] styrene hydrogenation,[89] and generation of H_2 via water-splitting,[90] were also found to be either induced or enhanced by the plasmon-driven hot carriers injection into the surface molecular adsorbates upon exposure to light excitation. Particularly, Linic and co-workers[76] demonstrated that plasmonic silver nanostructures with superior visible light absorption and scattering properties, can utilize concurrently photons and thermal energy to drive catalytic oxidation reactions at drastically lower temperatures comparing to those associated with conventional thermal processes. They

also found that energetic hot electrons, formed via the decay of surface plasmon resonance on illuminated silver nanoparticles, are transferred from the silver to adsorbed molecular O_2, allowing for activation of the O-O bond for oxidation of surface molecular adsorbates (Figure 1.4), for example, a commercially important epoxidation of ethylene to form ethylene oxide.[75,88] This work strongly impacted and stimulated the field of plasmonic photocatalysis, allowing one to better understand the reactions mechanisms of plasmonic photocatalysis. The underlying mechanistic understanding of plasmon-mediated photoreactions, however, still remain unclear in this current stage. Therefore, it is imperative to gain quantitative insights into the kinetics and underlying pathways of these plasmon-mediated photoreactions to fully understand the obstacles that might limit the wide applications of plasmonic nanostructures as high-performance photocatalysts.

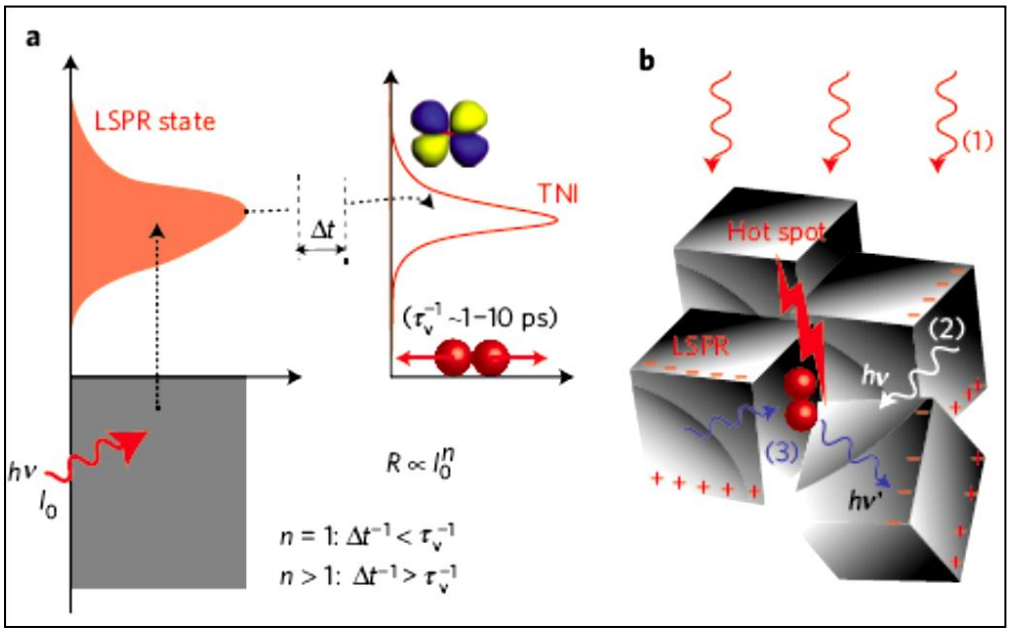

Figure 1.4 Unique features of plasmonic photocatalysts. (a) The schematic shows the plasmon-mediated electron transfer from Ag to the O_2 forming a transient negative ion (TNI). (b) A schematic of the proposed active complex of plasmonic Ag particles that can support a super-linear rate is shown. Reprinted with permission from reference 88.[88] Copyright 2012 Nature Publishing Group.

To more efficiently harness the plasmon resonance for catalytic and photocatalytic reaction, two key factors need to be considered in advance. The first factor is to understanding the interfacial interaction between adsorbate molecules and plasmonic nanostructures.[72,77,80] For instance, the energy of the internal molecular electronic transition of a molecule, compared to the molecule's gas phase gap between the highest occupied molecular orbital (HOMO) and the lowest unoccupied molecular orbital (LUMO), could be modulated through chemical bonding to the plasmonic nanostructure surface, as shown in Figure 1.5.[72] On the other hand, the adsorption states of molecule with varying binding sites and orientations would also play a key role in initiating or affecting the plasmonic hot carriers driven photocatalytic process.

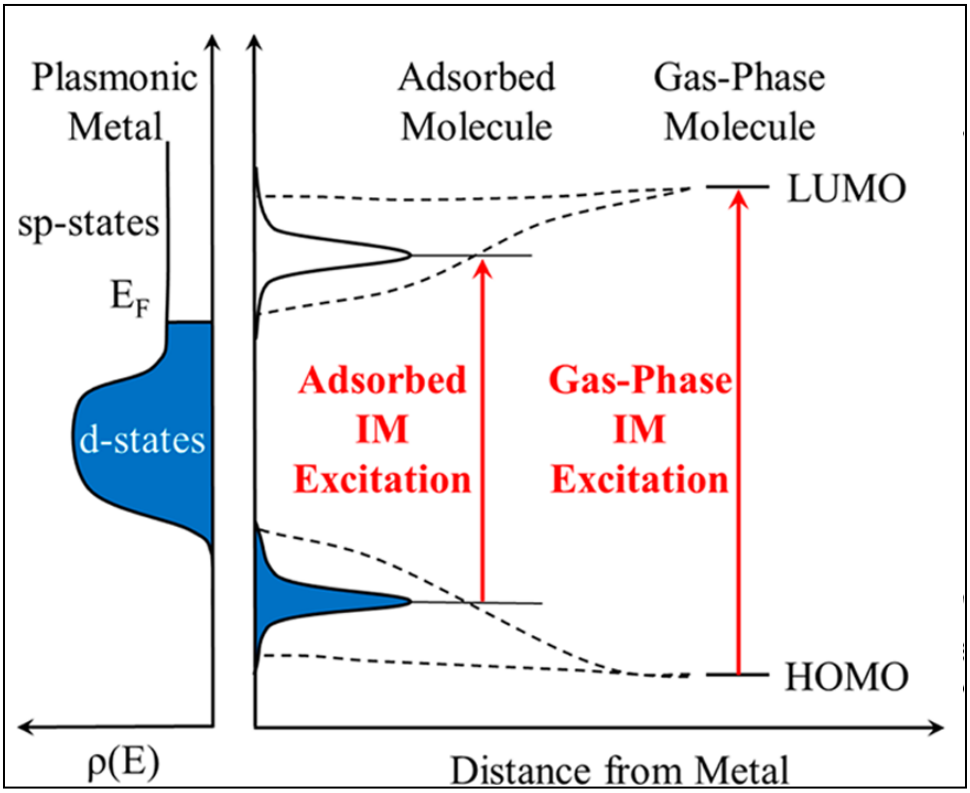

Figure 1.5 The impact of chemisorption on the HOMO-LUMO intermolecular excitation band gap of the adsorbate molecule. Reprinted with permission from reference 72.[72] Copyright 2014 American Chemical Society.

Another key factor that might limit the wide applications of plasmon-driven photocatalysis is the lifetime of plasmonic hot carriers.[71,73] It is very important to investigate not only the total number of carriers generated through plasmon decay, but also their energy distribution.[73] As shown in Figure 1.6, Nordlander and co-workers carried out an interesting simulation on the energy distribution of the hot carriers generated by silver nanoparticles with diameters of 15 nm using four different hot carrier lifetimes.[73] It was demonstrated that the energy distribution of the hot carriers change strikingly as the lifetime of hot carriers is varied within that time range, that is, long lifetimes give rise to the generation of carriers with large energies. The hot carriers with large energies show promising applications for one to harness them to drive or enhance interesting and unexpected catalytic reactions that are extremely difficult to achieve through traditional thermal-induced catalytic reactions or semiconductor-based photocatalytic reactions. While the detailed mechanisms might be much more complicated, the lifetime-dependent hot carriers energy distribution provides significant insights on the basic principle toward rational design of high performance plasmonic photocatalysts. Moreover, the lifetime of plasmonic hot carriers is also one of the most important reasons why we chose to work on nanomaterials instead of bulk materials because the plasmonic nanoparticles show much longer plasmon lifetime than their corresponding bulk materials, which would significantly facilitate the development of plasmon-driven photocatalysis toward renewable solar energy conversion.

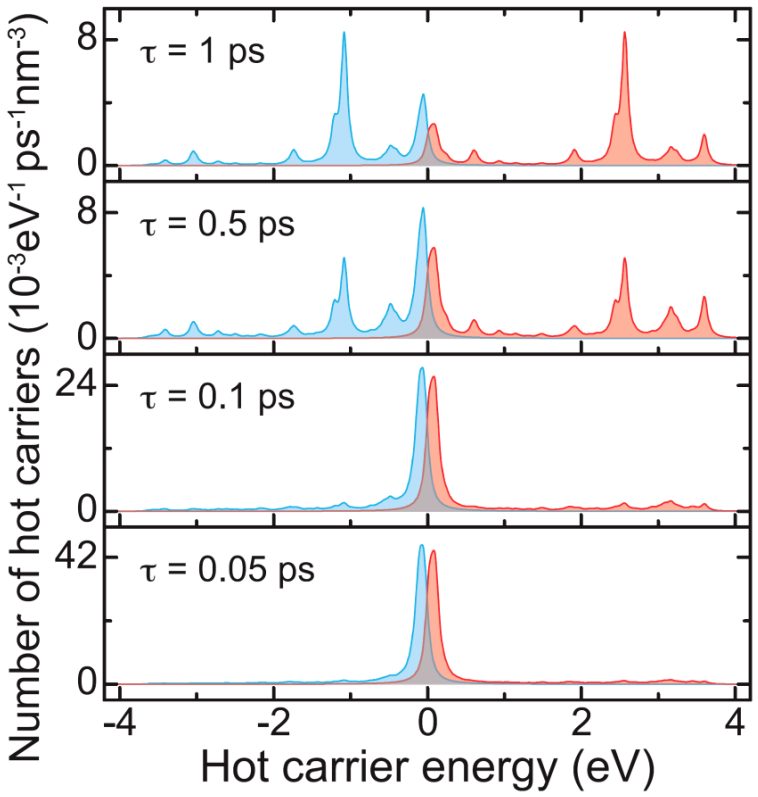

Figure 1.6 Hot carrier distribution from simulation. The number of hot electrons (red lines) and hot holes (blue lines) generated per unit of time and volume as a function of their energy. Four different hot carrier lifetimes were simulated on Ag nanoparticle with the diameter of 15 nm. The frequency of the external illumination is fixed to 3.65 eV, which corresponds to the plasmon frequency. Zero energy refers to the Fermi level. Reprinted with permission from reference 73.[73] Copyright 2014 American Chemical Society.

1.5 Goal and Outline of the Dissertation

The goal of this dissertation is to gain new insights on interfacial molecular transformation kinetics and underlying mechanism of heterogeneous catalysis and plasmon-driven photocatalysis using *in situ* plasmon-enhanced spectroscopic tool for guiding rational design of high performance metallic nanocatalysts and photocatalysts toward environmental and energy application.

Metal nanoparticles have been of tremendous interest because of their intriguing size- and shape-dependent plasmonic and catalytic properties. The combination of tunable

plasmon resonances with superior catalytic activities on the same nanoparticle, however, has long been challenging because plasmonics and catalysis require nanoparticles in two drastically different size regimes. Tunable plasmon resonances is a unique feature of sub-wavelength metallic nanoparticles, whereas heterogeneous catalysis requires the use of sub-5 nm nanoparticles as the catalysts. I found a unique way to bridge this size gap between nanoplasmonics and nanocatalysis by demonstrating that the desired plasmonic and catalytic properties can be integrated on the same particle by controllably creating high-index facets on individual sub-wavelength metallic nanoparticles. The capabilities to both nanoengineer high-index facets and fine-tune the plasmon resonances through deliberate particle geometry control allow us to use these nanoparticles for a dual purpose: as substrates for plasmon-enhanced spectroscopies and efficient surface catalysts. Such dual functionality enables us to gain quantitative insights into the facet-dependent molecular transformations on metallic nanocatalysts using surface-enhanced Raman spectroscopy (SERS) as an ultrasensitive spectroscopic tool with unique time-resolving and molecular finger-printing capabilities.

In Chapter 2, I demonstrated the effects of the nanoscale porosity on the far- and near-field optical properties of the nanoparticles have been investigated both experimentally by optical extinction and single-nanoparticle Raman spectroscopic measurements and theoretically through finite-difference time-domain (FDTD) calculations. Furthermore, I showed that subwavelength Au nanoparticles with nanoscale surface porosity represent a unique bifunctional nanostructure that serves as both high-performance SERS substrates and efficient surface catalysts, allowing one to unravel the kinetics and pathways of

surface-catalyzed reactions with unprecedented sensitivity and detail through time-resolved plasmon-enhanced spectroscopic measurements (Chapter 3).

In Chapter 4, I further demonstrated that Au nanoparticles with tipped surface structures, such as concave nanocubes, nanotrisoctahedra, and nanostars, possess size-dependent tunable plasmon resonances and intense near-field enhancements exploitable for single-particle SERS under near-infrared excitation. In Chapter 5, I studied the intrinsic facet-dependent catalytic activities of colloidal subwavelength Au nanoparticles enclosed by various types of well-defined high-index facets using the catalytic hydrogenation of 4-nitrothiophenol as a model reaction. Our results provide compelling experimental evidence on the crucial roles of undercoordinated surface atoms in Au-based heterogeneous catalysis and shed light on the underlying relationship between the atomic-level surface structures and the intrinsic catalytic activities of Au nanocatalysts.

In Chapter 6 and 7, I focused on the facet control of Au nanorods, which are optically tunable anisotropic nanoparticles with built-in catalytic activities. I demonstrated that cylindrical Au nanorods undergo controlled facet evolution during their overgrowth in the presence of cuprous ions and cationic surfactants, resulting in the formation of anisotropic nanostructures enclosed by specific types of well-defined high-index and low-index facets. Taking full advantage of the combined structural and plasmonic tunability, I have further studied the facet-dependent heterogeneous catalysis on well-faceted Au nanorods using SERS. In Chapter 8, I investigated the foreign ion- and surfactant-coguided overgrowth of single-crystalline Au nanorods as a model system to elucidate the intertwining roles of silver foreign ions, surface-capping surfactants, and reducing agents that underpin the intriguing structural evolution of Au nanocrystals. I

demonstrated that the geometry-controlled nanorod overgrowth involves two distinct underlying pathways, Ag underpotential deposition and Au-Ag electroless codeposition, which are interswitchable upon maneuvering the interplay of the silver ions, surfactants, and reducing agents.

More recently, I further expanded my research interest into plasmonic hot electron-driven photocatalytic reactions (Chapter 9 and 10). It has been recently observed that the localized surface plasmon resonance supported by metallic nanostructures plays a crucial role in either driving or enhancing a series of interesting chemical or photochemical reactions. However, key scientific questions concerning about the detailed mechanisms of plasmon-driven photocatalytic reactions are still poorly understood. Therefore, I focused on the quantitative understanding of the kinetics and underlying pathways of plasmon-driven photocatalysis. I used SERS to precisely monitor, in real time, the plasmon-driven photoreaction kinetics at the molecule-nanoparticle interfaces. The reductive dimerization of 4-nitrothiophenol and oxidative coupling of thiophenol-derivates were chosen as model reactions to explore the effects of plasmon excitations, molecular adsorption states, local field enhancements, and photothermal processes, on the plasmon-driven photocatalytic reactions. In addition, I further discovered the unique capability of plasmon excitation toward decarboxylation of mercaptobenzoic acid, and also acting as plasmonic scissor for aromatic side-chain cleavage.

1.6 References

(1) Burda, C.; Chen, X.; Narayanan, R.; El-Sayed, M. A. *Chem Rev* **2005**, *105*, 1025-1102.

(2) Halas, N. J.; Lal, S.; Chang, W. S.; Link, S.; Nordlander, P. *Chem Rev* **2011**, *111*, 3913-3961.

(3) El-Sayed, M. A. *Accounts Chem Res* **2001**, *34*, 257-264.

(4) Mie, G. *Ann Phys-Berlin* **1908**, *25*, 377-445.

(5) Murphy, C. J.; Sau, T. K.; Gole, A. M.; Orendorff, C. J.; Gao, J.; Gou, L.; Hunyadi, S. E.; Li, T. *J Phys Chem B* **2005**, *109*, 13857-13870.

(6) Rycenga, M.; Cobley, C. M.; Zeng, J.; Li, W. Y.; Moran, C. H.; Zhang, Q.; Qin, D.; Xia, Y. N. *Chem Rev* **2011**, *111*, 3669-3712.

(7) Willets, K. A.; Van Duyne, R. P. *Annu Rev Phys Chem* **2007**, *58*, 267-297.

(8) Jain, P. K.; Huang, X. H.; El-Sayed, I. H.; El-Sayed, M. A. *Accounts Chem Res* **2008**, *41*, 1578-1586.

(9) Knight, M. W.; Sobhani, H.; Nordlander, P.; Halas, N. J. *Science* **2011**, *332*, 702-704.

(10) Camden, J. P.; Dieringer, J. A.; Zhao, J.; Van Duyne, R. P. *Acc Chem Res* **2008**, *41*, 1653-1661.

(11) Chen, J. Y.; Wiley, B.; Li, Z. Y.; Campbell, D.; Saeki, F.; Cang, H.; Au, L.; Lee, J.; Li, X. D.; Xia, Y. N. *Adv Mater* **2005**, *17*, 2255-2261.

(12) Lal, S.; Clare, S. E.; Halas, N. J. *Accounts Chem Res* **2008**, *41*, 1842-1851.

(13) Giljohann, D. A.; Seferos, D. S.; Daniel, W. L.; Massich, M. D.; Patel, P. C.; Mirkin, C. A. *Angew Chem Int Ed Engl* **2010**, *49*, 3280-3294.

(14) Nikoobakht, B.; El-Sayed, M. A. *Chem Mater* **2003**, *15*, 1957-1962.

(15) Jin, R. C.; Cao, Y. W.; Mirkin, C. A.; Kelly, K. L.; Schatz, G. C.; Zheng, J. G. *Science* **2001**, *294*, 1901-1903.

(16) Oldenburg, S. J.; Averitt, R. D.; Westcott, S. L.; Halas, N. J. *Chem Phys Lett* **1998**, *288*, 243-247.

(17) Sun, Y. G.; Xia, Y. N. *Science* **2002**, *298*, 2176-2179.

(18) Raman, C. V.; Krishnan, K. S. *Nature* **1928**, *122*, 169-169.

(19) Kneipp, K.; Kneipp, H.; Itzkan, I.; Dasari, R. R.; Feld, M. S. *Chem Rev* **1999**, *99*, 2957-+.

(20) Fleischmann, M.; Hendra, P. J.; Mcquillan, A. J. *Chem Phys Lett* **1974**, *26*, 163-166.

(21) Albrecht, M. G.; Creighton, J. A. *J Am Chem Soc* **1977**, *99*, 5215-5217.

(22) Jeanmaire, D. L.; Vanduyne, R. P. *J Electroanal Chem* **1977**, *84*, 1-20.

(23) Moskovits, M. *Rev. Mod. Phys.* **1985**, *57*, 783-826.

(24) Campion, A.; Kambhampati, P. *Chem. Soc. Rev.* **1998**, *27*, 241-250.

(25) Camden, J. P.; Dieringer, J. A.; Zhao, J.; Van Duyne, R. P. *Accounts Chem. Res.* **2008**, *41*, 1653-1661.

(26) Craig, A. P.; Franca, A. S.; Irudayaraj, J. *Annual Review of Food Science and Technology, Vol 4* **2013**, *4*, 369-380.

(27) Li, J. F.; Huang, Y. F.; Ding, Y.; Yang, Z. L.; Li, S. B.; Zhou, X. S.; Fan, F. R.; Zhang, W.; Zhou, Z. Y.; Wu, D. Y.; Ren, B.; Wang, Z. L.; Tian, Z. Q. *Nature* **2010**, *464*, 392-395.

(28) Halvorson, R. A.; Vikesland, P. J. *Environ. Sci. Technol.* **2010**, *44*, 7749-7755.

(29) Shafer-Peltier, K. E.; Haynes, C. L.; Glucksberg, M. R.; Van Duyne, R. P. *J. Am. Chem. Soc.* **2003**, *125*, 588-593.

(30) Barhoumi, A.; Halas, N. J. *J. Am. Chem. Soc.* **2010**, *132*, 12792-12793.

(31) Anker, J. N.; Hall, W. P.; Lyandres, O.; Shah, N. C.; Zhao, J.; Van Duyne, R. P. *Nat. Mater.* **2008**, *7*, 442-453.

(32) Alvarez-Puebla, R. A.; Liz-Marzan, L. M. *Small* **2010**, *6*, 604-610.

(33) Qian, X. M.; Peng, X. H.; Ansari, D. O.; Yin-Goen, Q.; Chen, G. Z.; Shin, D. M.; Yang, L.; Young, A. N.; Wang, M. D.; Nie, S. M. *Nat. Biotechnol.* **2008**, *26*, 83-90.

(34) Kim, J. H.; Kim, J. S.; Choi, H.; Lee, S. M.; Jun, B. H.; Yu, K. N.; Kuk, E.; Kim, Y. K.; Jeong, D. H.; Cho, M. H.; Lee, Y. S. *Anal. Chem.* **2006**, *78*, 6967-6973.

(35) Doering, W. E.; Piotti, M. E.; Natan, M. J.; Freeman, R. G. *Adv. Mater.* **2007**, *19*, 3100-3108.

(36) Zavaleta, C. L.; Smith, B. R.; Walton, I.; Doering, W.; Davis, G.; Shojaei, B.; Natan, M. J.; Gambhir, S. S. *Proc. Natl. Acad. Sci. U. S. A.* **2009**, *106*, 13511-13516.

(37) Maiti, K. K.; Dinish, U. S.; Samanta, A.; Vendrell, M.; Soh, K. S.; Park, S. J.; Olivo, M.; Chang, Y. T. *Nano Today* **2012**, *7*, 85-93.

(38) Halas, N. J.; Lal, S.; Chang, W. S.; Link, S.; Nordlander, P. *Chem. Rev.* **2011**, *111*, 3913-3961.

(39) Wang, H.; Levin, C. S.; Halas, N. J. *J. Am. Chem. Soc.* **2005**, *127*, 14992-14993.

(40) Lee, S. J.; Morrill, A. R.; Moskovits, M. *J. Am. Chem. Soc.* **2006**, *128*, 2200-2201.

(41) Wang, H. H.; Liu, C. Y.; Wu, S. B.; Liu, N. W.; Peng, C. Y.; Chan, T. H.; Hsu, C. F.; Wang, J. K.; Wang, Y. L. *Adv. Mater.* **2006**, *18*, 491-495.

(42) Osberg, K. D.; Rycenga, M.; Harris, N.; Schmucker, A. L.; Langille, M. R.; Schatz, G. C.; Mirkin, C. A. *Nano Lett.* **2012**, *12*, 3828-3832.

(43) Lal, S.; Grady, N. K.; Kundu, J.; Levin, C. S.; Lassiter, J. B.; Halas, N. J. *Chem. Soc. Rev.* **2008**, *37*, 898-911.

(44) Xia, Y. N.; Halas, N. J. *MRS Bull.* **2005**, *30*, 338-344.

(45) Wang, H.; Halas, N. J. *Adv. Mater.* **2008**, *20*, 820-825.

(46) Fang, J. X.; Du, S. Y.; Lebedkin, S.; Li, Z. Y.; Kruk, R.; Kappes, M.; Hahn, H. *Nano Lett.* **2010**, *10*, 5006-5013.

(47) Liu, Z.; Zhang, F. L.; Yang, Z. B.; You, H. J.; Tian, C. F.; Li, Z. Y.; Fang, J. X. *J. Mater. Chem. C* **2013**, *1*, 5567-5576.

(48) Lin, H. X.; Li, J. M.; Liu, B. J.; Liu, D. Y.; Liu, J. X.; Terfort, A.; Xie, Z. X.; Tian, Z. Q.; Ren, B. *Phys. Chem. Chem. Phys.* **2013**, *15*, 4130-4135.

(49) Li, S. W.; Xu, P.; Ren, Z. Q.; Zhang, B.; Du, Y. C.; Han, X. J.; Mack, N. H.; Wang, H. L. *ACS Appl. Mater. Interfaces* **2013**, *5*, 49-54.

(50) Liang, H. Y.; Li, Z. P.; Wang, W. Z.; Wu, Y. S.; Xu, H. X. *Adv. Mater.* **2009**, *21*, 4614-4618.

(51) Mulvihill, M. J.; Ling, X. Y.; Henzie, J.; Yang, P. D. *J. Am. Chem. Soc.* **2010**, *132*, 268-274.

(52) Barbosa, S.; Agrawal, A.; Rodriguez-Lorenzo, L.; Pastoriza-Santos, I.; Alvarez-Puebla, R. A.; Kornowski, A.; Weller, H.; Liz-Marzan, L. M. *Langmuir* **2010**, *26*, 14943-14950.

(53) Rodriguez-Lorenzo, L.; Alvarez-Puebla, R. A.; de Abajo, F. J. G.; Liz-Marzan, L. M. *J. Phys. Chem. C* **2010**, *114*, 7336-7340.

(54) Khoury, C. G.; Vo-Dinh, T. *J. Phys. Chem. C* **2008**, *112*, 18849-18859.

(55) Hrelescu, C.; Sau, T. K.; Rogach, A. L.; Jackel, F.; Feldmann, J. *Appl. Phys. Lett.* **2009**, *94*, 3.

(56) Sanchez-Gaytan, B. L.; Swanglap, P.; Lamkin, T. J.; Hickey, R. J.; Fakhraai, Z.; Link, S.; Park, S. J. *J. Phys. Chem. C* **2012**, *116*, 10318-10324.

(57) Wang, H.; Goodrich, G. P.; Tam, F.; Oubre, C.; Nordlander, P.; Halas, N. J. *J. Phys. Chem. B* **2005**, *109*, 11083-11087.

(58) Huang, Y. F.; Wu, D. Y.; Zhu, H. P.; Zhao, L. B.; Liu, G. K.; Ren, B.; Tian, Z. Q. *Phys Chem Chem Phys* **2012**, *14*, 8485-8497.

(59) Chen, T.; Wang, H.; Chen, G.; Wang, Y.; Feng, Y. H.; Teo, W. S.; Wu, T.; Chen, H. Y. *Acs Nano* **2010**, *4*, 3087-3094.

(60) Michota, A.; Kudelski, A.; Bukowska, J. *J Raman Spectrosc* **2001**, *32*, 345-350.

(61) Heck, K. N.; Janesko, B. G.; Scuseria, G. E.; Halas, N. J.; Wong, M. S. *J. Am. Chem. Soc.* **2008**, *130*, 16592-16600.

(62) Joseph, V.; Engelbrekt, C.; Zhang, J. D.; Gernert, U.; Ulstrup, J.; Kneipp, J. *Angew. Chem.-Int. Edit.* **2012**, *51*, 7592-7596.

(63) Xie, W.; Herrmann, C.; Kompe, K.; Haase, M.; Schlucker, S. *J Am Chem Soc* **2011**, *133*, 19302-19305.

(64) Xie, W.; Walkenfort, B.; Schlucker, S. *J. Am. Chem. Soc.* **2013**, *135*, 1657-1660.

(65) Jing, H.; Zhang, Q. F.; Large, N.; Yu, C. M.; Blom, D. A.; Nordlander, P.; Wang, H. *Nano Lett.* **2014**, *14*, 3674−3682.

(66) Liu, R.; Liu, J. F.; Zhang, Z. M.; Zhang, L. Q.; Sun, J. F.; Sun, M. T.; Jiang, G. B. *J. Phys. Chem. Lett.* **2014**, *5*, 969-975.

(67) Huang, J. F.; Zhu, Y. H.; Lin, M.; Wang, Q. X.; Zhao, L.; Yang, Y.; Yao, K. X.; Han, Y. *J. Am. Chem. Soc.* **2013**, *135*, 8552-8561.

(68) Campion, A.; Kambhampati, P. *Chem. Soc. Rev.* **1998**, *27*, 241-250.

(69) Willets, K. A.; Van Duyne, R. P. In *Annual Review of Physical Chemistry*; Annual Reviews: Palo Alto, 2007; Vol. 58, p 267-297.

(70) Kneipp, K.; Kneipp, H.; Itzkan, I.; Dasari, R. R.; Feld, M. S. *Chem. Rev.* **1999**, *99*, 2957–2976.

(71) Brongersma, M. L.; Halas, N. J.; Nordlander, P. *Nat Nanotechnol* **2015**, *10*, 25-34.

(72) Kale, M. J.; Avanesian, T.; Christopher, P. *Acs Catalysis* **2014**, *4*, 116-128.

(73) Manjavacas, A.; Liu, J. G.; Kulkarni, V.; Nordlander, P. *Acs Nano* **2014**, *8*, 7630-7638.

(74) Wu, K.; Chen, J.; McBride, J. R.; Lian, T. *Science* **2015**, *349*, 632-635.

(75) Christopher, P.; Xin, H. L.; Linic, S. *Nature Chemistry* **2011**, *3*, 467-472.

(76) Linic, S.; Christopher, P.; Xin, H. L.; Marimuthu, A. *Accounts Chem Res* **2013**, *46*, 1890-1899.

(77) Mukherjee, S.; Libisch, F.; Large, N.; Neumann, O.; Brown, L. V.; Cheng, J.; Lassiter, J. B.; Carter, E. A.; Nordlander, P.; Halas, N. J. *Nano Lett* **2013**, *13*, 240-247.

(78) Ueno, K.; Misawa, H. *Journal of Photochemistry and Photobiology C-Photochemistry Reviews* **2013**, *15*, 31-52.

(79) Wang, F.; Li, C. H.; Chen, H. J.; Jiang, R. B.; Sun, L. D.; Li, Q.; Wang, J. F.; Yu, J. C.; Yan, C. H. *J Am Chem Soc* **2013**, *135*, 5588-5601.

(80) Govorov, A. O.; Zhang, H.; Demir, H. V.; Gun'ko, Y. K. *Nano Today* **2014**, *9*, 85-101.

(81) Tsuboi, Y.; Shimizu, R.; Shoji, T.; Kitamura, N. *J Am Chem Soc* **2009**, *131*, 12623-12627.

(82) Deeb, C.; Ecoffet, C.; Bachelot, R.; Plain, J.; Bouhelier, A.; Soppera, O. *J Am Chem Soc* **2011**, *133*, 10535-10542.

(83) Dong, B.; Fang, Y. R.; Chen, X. W.; Xu, H. X.; Sun, M. T. *Langmuir* **2011**, *27*, 10677-10682.

(84) van Schrojenstein Lantman, E. M.; Deckert-Gaudig, T.; Mank, A. J. G.; Deckert, V.; Weckhuysen, B. M. *Nat Nanotechnol* **2012**, *7*, 583-586.

(85) Huang, Y. F.; Zhu, H. P.; Liu, G. K.; Wu, D. Y.; Ren, B.; Tian, Z. Q. *J Am Chem Soc* **2010**, *132*, 9244-9246.

(86) Sun, M. T.; Huang, Y. Z.; Xia, L. X.; Chen, X. W.; Xu, H. X. *J Phys Chem C* **2011**, *115*, 9629-9636.

(87) Linic, S.; Christopher, P.; Ingram, D. B. *Nature Materials* **2011**, *10*, 911-921.

(88) Christopher, P.; Xin, H. L.; Marimuthu, A.; Linic, S. *Nature Materials* **2012**, *11*, 1044-1050.

(89) Huang, H.; Zhang, L.; Lv, Z.; Long, R.; Zhang, C.; Lin, Y.; Wei, K.; Wang, C.; Chen, L.; Li, Z. Y.; Zhang, Q.; Luo, Y.; Xiong, Y. *J Am Chem Soc* **2016**, *138*, 6822-6828.

(90) Mubeen, S.; Lee, J.; Singh, N.; Kramer, S.; Stucky, G. D.; Moskovits, M. *Nat Nanotechnol* **2013**, *8*, 247-251.

CHAPTER 2

Porous Au Nanoparticles with Tunable Plasmon Resonances and Intense Field Enhancements for Single-Particle SERS

2.1 Introduction

Noble metal nanoparticles exhibit intriguing plasmon-dominated optical properties.[1-3] By judiciously tailoring the geometries of the metal nanoparticles, one can fine-tune the optical resonance frequencies and optimize the electric near field enhancements associated with the plasmonic excitations.[2-6] Expanding the plasmonic tunability of nanoparticles over a broad spectral range is of paramount importance because it opens up a whole set of new opportunities for photonic,[7,8] optoelectronic,[9,10] spectroscopic,[11,12] and biomedical applications.[13,14] This has, in turn, stimulated rapidly growing interests in a variety of metallic nanostructures with geometrically tunable optical properties, such as nanorods,[2,15] nanoprisms,[16,17] nanoshells,[18] and nanocages.[19] In this chapter, we report a new class of metallic nanostructures, porous Au nanoparticles, which combine highly tunable plasmon resonances and intense local electric field enhancements exploitable for single-particle surface-enhanced Raman spectroscopy (SERS).

Two-dimensional mesoporous or nanoporous Au Two-dimensional mesoporous or nanoporous Au thin films[20] have been of tremendous interest due to their interesting porosity-dependent optical properties[21-23] and superior catalytic activities.[24-26] While a planar Au thin film only supports propagating surface plasmon waves, it has been demonstrated that the excitation of both propagating and localized plasmon resonances can be achieved in nanoporous Au membranes.[23] In this context, the large local field enhancements associated with the localized plasmon modes sustained by the nanoporous films can be harnessed for SERS-based molecular characterization and sensing applications.[27,28] For finite Au nanoparticles whose plasmons are already localized, how the nanoscale porosity influences the optical properties of the particles still remains

unknown. Although smooth spherical nanoparticles (SSNPs) of Au or Ag possess well-defined localized plasmon resonances in the visible region, their plasmonic tuning range is rather limited. In this work, we show that Au porous nanoparticles (PNPs) exhibit greatly enhanced plasmonic tunability over a much broader spectral range with significantly intensified near-field enhancements in comparison to the SSNPs of the same sizes. We demonstrate, both experimentally and theoretically, that introducing nanoscale porosity to a Au nanoparticle has profound influence on both the far- and near-field optical properties of the particle.

2.2 Experimental Section

Chemicals and Materials. Gold(III) chloride trihydrate ($HAuCl_4$ $3H_2O$, ACS grade) was obtained from J.T. Baker. Sodium borohydride ($NaBH_4$, 99%), L-ascorbic acid (AA, 99.5+%), hydrochloric acid (HCl, 37%), and poly(4-vinylpyridine) (PVP, Mw~60,000) were obtained from Sigma-Aldrich. (1-Hexadecyl)trimethylammonium chloride (CTAC, 96%) and 4-aminothiophenol (C_6H_7NS, 4-ATP, 97%) were obtained from Alfa Aesar. Hydrogen peroxide (H_2O_2, 30%), sulfuric acid (H_2SO_4, 96.10%), and ethanol (200 proof) were purchased from Fisher Scientific. All reagents were used as received without further purification. Ultrapure water (18.2 MΩ resistivity, Barnstead EasyPure II 7138) was used for all experiments. Silicon wafers were obtained from University Wafers.

Synthesis of Au Seeds. Colloidal Au seeds were prepared by the reducing $HAuCl_4$ with $NaBH_4$ in the presence of CTAC. In a typical procedure, 0.30 mL of ice-cold, freshly prepared $NaBH_4$ (10 mM) were quickly injected into a solution composed of CTAC (10.00 mL, 0.10 M) and $HAuCl_4$ (0.25 mL, 10 mM) under magnetic stir. The seed solution was stirred for 1 min and then left undisturbed for 2 h. The seed solution was

diluted 1000-fold with CTAC (0.10 M) and the diluted seed solution was used for the subsequent seed-mediated growth.

Synthesis of Au Porous Nanoparticles (PNPs). The Au PNPs were prepared through a seed-mediated growth process. The growth solution was prepared by sequentially adding $HAuCl_4$ (0.50 mL, 10 mM) and AA (0.10 mL, 0.10 M) into a CTAC (10.00 mL, 0.10 M) solution. After gently mixing the growth solution for 30 s, the growth of Au PNPs was initiated by adding certain volumes of the diluted Au seed solution. The reaction solution was gently mixed for 30 s immediately after the addition of Au seeds and then left undisturbed at room temperature for 4 h. The as-obtained Au PNPs were washed with water three times through centrifugation/redispersion cycles, and finally redispersed in 5.0 mL of water. The overall sizes of the resulting Au PNPs were controlled by adjusting the amount of Au seeds added.

Synthesis of Au Quasi-Spherical (QS) Nanoparticles. The Au QS nanoparticles were fabricated following a similar protocol for the Au PNPs except for the addition of HCl. The growth solution was prepared by sequentially adding $HAuCl_4$ (0.50 mL, 10 mM), HCl (0.20 mL, 1.0 M) and AA (0.10 mL, 0.10 M) into a CTAC (10.00 mL, 0.10 M) solution. After gently mixing the reactants for 30 s, the growth of Au QS nanoparticles was initiated by adding certain volumes of the diluted Au seed solution. The reaction solution was gently mixed for 30 s immediately after the addition of Au seeds and then left undisturbed at room temperature for 4 h. The obtained Au QS nanoparticles were washed with water three times through centrifugation/redispersion cycles, and finally redispersed in 5.0 mL of water. The sizes of the Au QS nanoparticles could be controlled by adjusting the amount of Au seeds added.

Synthesis of Au Trisoctahedral (TOH) Nanoparticles. The Au TOH nanoparticles were fabricated following a similar protocol for the Au PNPs except for the increased amount of AA. The growth solution was prepared by sequentially adding $HAuCl_4$ (0.50 mL, 10 mM) and AA (1.0 mL, 0.10 M) into a CTAC (10.00 mL, 0.10 M) solution. After gently mixing the growth solution for 30 s, the growth of Au TOH nanoparticles was initiated by adding 0.01 mL of the diluted Au seed solution. The reaction solution was gently mixed for 30 s immediately after the addition of Au seeds and then left undisturbed at room temperature for 4 h. The obtained Au TOH nanoparticles were washed with water three times through centrifugation/redispersion cycles, and finally redispersed in 5.0 mL of water.

Characterizations. The morphologies and structures of the nanoparticles were characterized by transmission electron microscopy (TEM) and selected area electron diffraction (SAED) using a Hitachi H-8000 transmission electron microscope operated at an accelerating voltage of 200 kV. All samples for TEM measurements were dispersed in water and drop-dried on 200 mesh Formvar/carbon-coated Cu grids. The structures of the nanoparticles were also characterized by SEM using a Zeiss Ultraplus thermal field emission scanning electron microscope. The samples for SEM measurements were dispersed in water and drop-dried on silicon wafers. The optical extinction spectra of the nanoparticles were measured on aqueous colloidal suspensions at room temperature, using a Beckman Coulter Du 640 spectrophotometer. Raman spectra and dark-field optical images were obtained on a Bayspec *Nomadic*TM Raman microscopy built on an Olympus BX51 microscope equipped with a 785 nm CW diode laser.

Single-Particle SERS Measurements. Sub-monolayer films of isolated Au particles were prepared by immobilizing the particles onto PVP (polyvinylpyridine)-functionalized silicon substrates. In a typical procedure, silicon substrates were cleaned in a piranha solution (sulfuric acid : hydrogen peroxide, 7:3) for 15 min, and then immersed in a 1% wt. of PVP ethanolic solution for 24 h. The silicon substrates were thoroughly rinsed with ethanol, dried with N_2 gas, and then immersed in an aqueous solution of Au particles for 1 h. The silicon substrates were thoroughly rinsed with ethanol and dried with N_2 gas after they were removed from the solution of Au particles. The coverage of Au particles on the substrates can be controlled by changing the immersion time. The samples for single-particle SERS experiments were prepared by evaporating 20 μL of a 1.0 mM ethanolic solution of 4-ATP on the surface of the isolated Au particles on PVP-functionalized silicon substrates. The substrates were then thoroughly rinsed with ethanol and dried with N_2 gas. A couple of drops of water were dropped onto the substrates to ensure that the surrounding medium of the Au particles was water, and then a clean glass slide with a 0.17 mm thickness was covered onto the top of the water layer before the Raman spectral collection. The distance between silicon substrate and the glass slide is about 0.5 mm. Figure S4A shows the scheme of the substrate geometry of the single-particle SERS measurements. SERS spectra were obtained on a Bayspec *Nomadic*™ Raman microscopy built on an Olympus BX51 reflected optical system under 785 nm laser excitation in the confocal mode (focal area of 2 μm diameter). A 50× dark field objective (NA=0.5, WD=10.6 mm, Olympus LMPLFLN-BD) was used for both Raman signal collection and dark field scattering imaging. The laser beam was focused on one particle each time for Raman spectrum collection. The laser power focused on the

samples was measured to be 3.6 mW and the spectrum acquisition time was 20 s. Normal Raman spectra of 4-ATP were collected on solid films of neat 4-ATP on the silicon wafers under the same conditions.

Enhancement Factor (EF) Calculations. We estimated the enhancement factors (EFs) of Raman signals using the following equation: $EF = (I_{SERS} \times N_{normal}) / (I_{normal} \times N_{SERS})$, where I_{SERS} is the intensity of a specific band in the SERS spectra of 4-ATP; I_{normal} is the intensity of the same band in the normal Raman spectra of 4-ATP under the same condition; N_{normal} is the number of probe molecules in the excitation volume for the normal Raman measurements; N_{SERS} is the number of adsorbed molecules on an individual particle. Two Raman modes of 4-ATP at 1078 cm^{-1} and 1590 cm^{-1} were chosen for the EF calculations. To estimate the N_{normal}, we calculated the effective excitation volume by using the following equation: $V = \pi \times (d/2)^2 \times H$, where d is the diameter of the beam size (d = 2 μm) and H is the effective depth of focus (H= 10 μm, which was estimated by finely controlling the height of the stage during the Raman measurement of silicon wafers). Thus, we estimated an effective excitation volume of 3.14×10^{-17} m^3 for our Raman microscopy with 785 nm excitation using the 50× objective. Then N_{normal} was calculated by using the following expression: $N_{normal} = (V \times D/M) \times N_A = 1.80 \times 10^{11}$ molecules, where D is the density of 4-ATP (1.17 g/mL), M is the molar mass of 4-ATP (125 g/mol) and N_A is the Avogadro constant (6.02×10^{23} mol^{-1}). To determine N_{SERS}, a self-assembled monolayer of 4-ATP molecules (molecular footprint size of 0.39 nm^2) was assumed to be closely packed on the surface of each Au particle. The surface area of the particle was estimated by assuming that each Au PNP has four times of the surface area than a smooth sphere of the same overall size. For instant, a Au PNP with the

diameter of $2R$=189 nm: S=16×π×R^2 nm^2 = 448656 nm^2, and then N_{SERS} = S/0.39 = 1.15×10^6 molecules. In this way we were able to estimate the N_{SERS} values for particles with different size and then calculate the EFs.

Finite-Difference Time-Domain (FDTD) Calculations. FDTD simulations (FDTD, Lumerical Solutions) were performed to calculate the far-field and near-field properties of the Au nanoparticles. Dielectric permittivity tabulated by Johnson and Christy was used for Au and a refractive index of 1.34 was used for water. The geometric parameters used in the simulations for the Au PNPs, smooth spherical, and TOH nanoparticles were extracted from the experimental TEM and SEM images. The Au PNPs and the smooth spherical particles were 67, 108, 135, 165, 189, and 215 nm in diameter, while the side length of the TOH particle was 94 nm. *N* spherical pores ranging from 10 to 40 nm in diameter were generated and distributed randomly at the surface of the spherical nanoparticles. The number of pores, *N*, increased with the nanoparticle size, in agreement with experimental observations. The random distribution of the pores allowed the formation of larger craters at the nanoparticle surface and craters with random depths, thus showing a good morphological agreement with the actual particle geometry. To account for the small morphological details and ensure a good numerical convergence, a uniform FDTD meshgrid of 2 nm was used. Extinction spectra were calculated by averaging three incident polarizations. This allowed us to reproduce the orientation averaging, the random pore distribution, and unpolarized-light excitation of the experimental configuration. Near-field enhancement distributions ($|\boldsymbol{E}/\boldsymbol{E}_0|^2$) were calculated at 785 nm for a given incident polarization. The near-field ($|\boldsymbol{E}/\boldsymbol{E}_0|^2$ and $|\boldsymbol{E}/\boldsymbol{E}_0|^4$) were spatially integrated over a spherical volume of radius R+1 nm where R was the

radius of the nanoparticle. The mean enhancements, $<|\boldsymbol{E}/\boldsymbol{E}_0|^2>$ and $<|\boldsymbol{E}/\boldsymbol{E}_0|^4>$ with the unit of nm^{-3}, were calculated by normalizing the integrated $<|\boldsymbol{E}/\boldsymbol{E}_0|^2>$ and $<|\boldsymbol{E}/\boldsymbol{E}_0|^4>$ over the integration volumes.

2.3 Results and Discussion

The Au PNPs were fabricated through a seed-mediated growth process in aqueous solution at room temperature. Briefly, colloidal Au seeds were prepared by reducing chloroauric acid ($HAuCl_4$) with sodium borohydride ($NaBH_4$) in the presence of cetyltrimethylammonium chloride (CTAC). The growth of the Au PNPs was initiated by injecting various volumes of diluted Au seeds into the particle growth solution, which contained $HAuCl_4$, *L*-ascorbic acid (AA), and CTAC. The reaction solution was gently mixed immediately after the addition of Au seeds and then left undisturbed at room temperature for 4 h. The as-fabricated particles were separated from the reaction mixtures through centrifugation and redispersion in water. Figure 2.1A shows a representative scanning electron microscopy (SEM) image of the as-fabricated Au PNPs with diameters of 189 ± 8 nm. Each individual particle appeared to be highly porous with nanoscale pores in the range of 10-40 nm randomly distributed over the particle surfaces. The nanoporosity of the particles was more clearly visualized in the high-magnification SEM and transmission electron microscopy (TEM) images taken on individual particles, as shown in Figure 2.1B and C, respectively. Figure 2.1D shows the corresponding selected area electron diffraction (SAED) pattern of the particle shown in Figure 2.1C, which indicated that each PNP was polycrystalline in nature and was composed of crystalline domains that adopted different orientations.

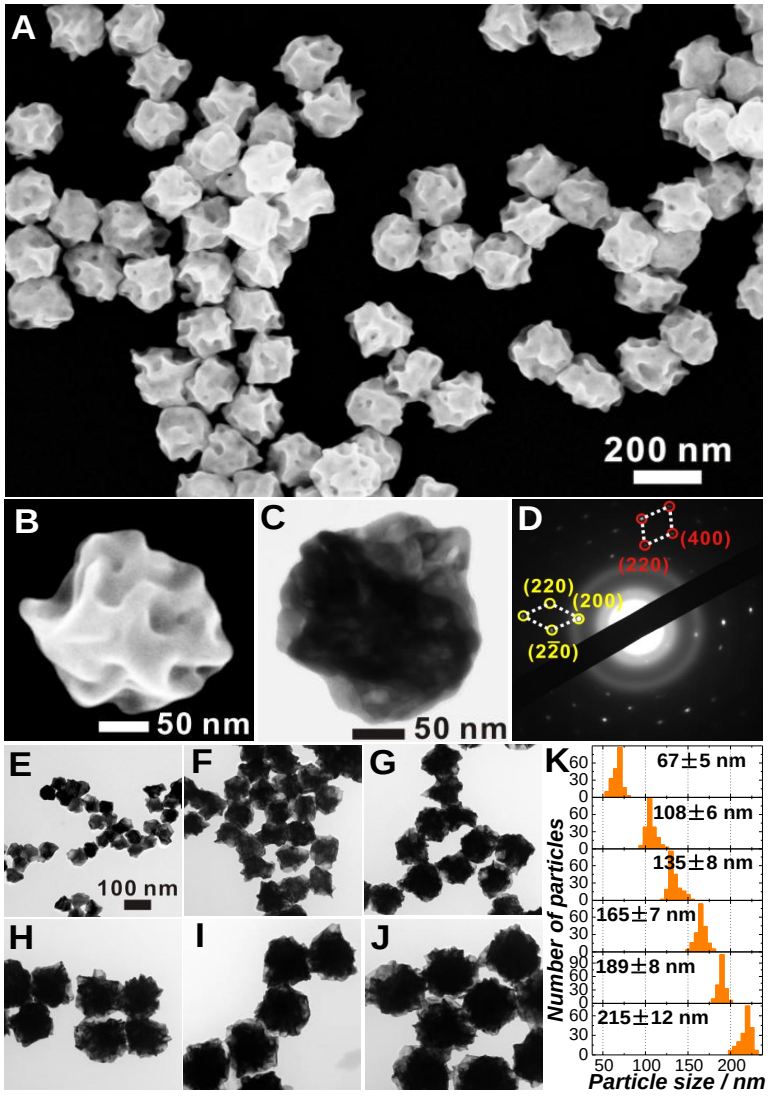

Figure 2.1. (A) SEM image of Au PNPs with an average size of 189 nm. (B) SEM image and (C) TEM image of an individual Au PNP. (D) SAED pattern obtained from the particle in panel C. (E-J) TEM images of Au PNPs of various average sizes fabricated by adding (E) 0.5, (F) 0.1, (G) 0.05, (H) 0.025, (I) 0.015, and (J) 0.01 mL of Au seed solution. Panels E-J share the same scale bar in panel E. (K) Histograms showing the size distribution of the Au PNPs shown in panels E-J.

The average size of the particles can be fine-controlled in the range from ~50 nm to sub-μm by simply adjusting the amount of Au seeds added into the growth solution. As shown in Figure 2.1E-J, the average sizes of the PNPs increased as the volume of the Au seeds decreased. The particles were highly monodisperse with narrow size distribution, as

shown in Figure 2.1K. Unlike some other seed-mediated growth methods through which the nanoparticles evolve into different morphologies as the overall particle size varies,[29,30] the nanoscale porous morphology of the particles fabricated using this protocol was well-preserved throughout the whole particle size tuning range. Although the average size of the pores appeared to be independent on the overall particle size, the average numbers of pores on individual Au PNPs were observed to increase with the overall particle sizes.

The kinetics of the seed-mediated particle growth was found to be a key factor in determining the morphology of the resulting nanoparticles. Figure 2.2A schematically illustrates the correlation between particle morphologies and the reaction kinetics. By adding HCl into the particle growth solution, the growth of nanoparticles could be significantly slowed down due to the decreased reducibility of AA in acidic environment,[31] leading to the formation of Au quasi-spherical (QS) nanoparticles (Figure 2.2B), which are thermodynamically more stable than the PNPs. The TEM image (Figure 2.2C) and SAED pattern (Figure 2.2D) of an individual particle clearly show that each Au QS particle was polycrystalline with several crystalline domains packed together into a multi-twined structure. The nanoparticle growth process could be significantly accelerated by increasing the amount of AA added to the particle growth solution. The faster particle growth facilitated the formation of the kinetically favored, single-crystalline Au trisoctahedral (TOH) nanoparticles enclosed by 24 high-index {221} facets[32] (see Figure 2.2E and 2.F). The SAED pattern of an individual TOH particle (Figure 2.2G) confirmed the single-crystalline nature of the particle. In this context, the Au PNPs can be considered as a unique "metastable" product resulting from the

intermediate particle growth kinetics that fall between the thermodynamically controlled regime and kinetically favored regime.

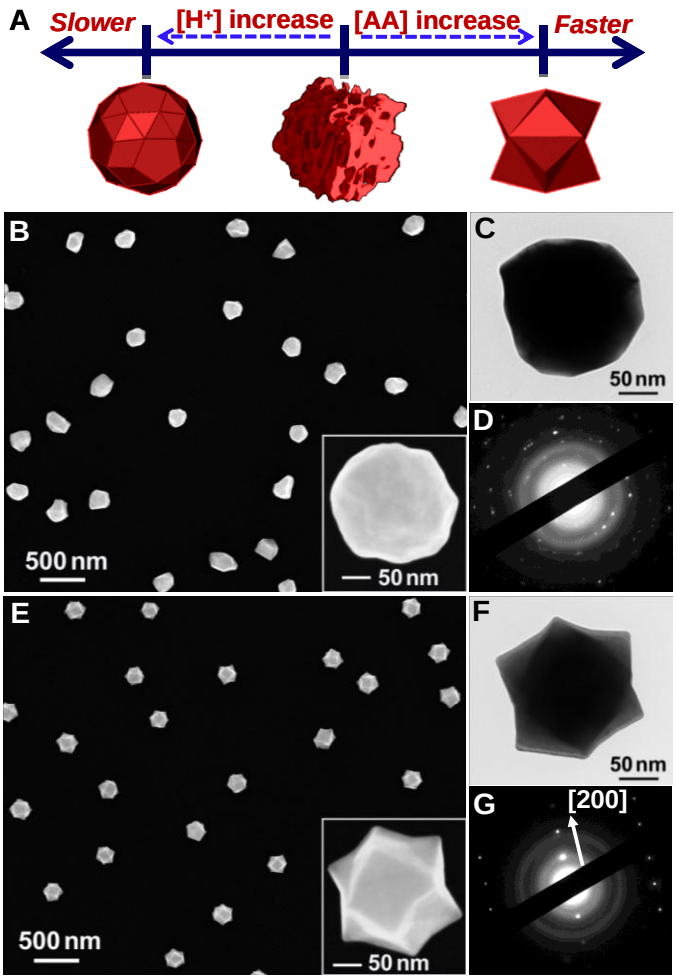

Figure 2.2. (A) Schematics illustrating the morphology control of Au nanocrystals through controlling the particle growth kinetics. (B) SEM image of Au QS nanoparticles. The inset highlights one individual particle. (C) TEM image of one Au QS nanoparticle. (D) SAED pattern obtained from the particle in panel C. (E) SEM image of Au TOH nanoparticles. The inset highlights one individual nanoparticle. (F) TEM image of one Au TOH nanoparticle. (G) SAED pattern obtained from the particle in panel F.

The Au PNPs exhibit size-dependent localized plasmon resonances whose frequencies are highly tunable across the visible and near-IR spectral regions. As shown in Figure 2.3A, the plasmon resonance progressively red-shifted and became increasingly broadened as the overall particle size increased. In comparison to the Au QS particles

with similar sizes, the PNPs exhibited significantly enhanced plasmonic tunability over a much broader spectral range. For SSNPs within the quasi-static limit (diameters smaller than ~60 nm), the plasmon resonance wavelengths lie around 520 nm and are essentially independent of particle size. As the size of a SSNP increases to the size regime beyond the quasi-static limit, the dipole plasmon mode starts to red shift and becomes significantly broadened. In addition, the multipolar plasmon modes, such as quadrupole, octupole, and even higher order multipole modes, become increasingly pronounced and begin to dominate the overall extinction spectral line shapes as a consequence of the phase-retardation effects.[33,34] We have experimentally demonstrated such size dependence of the plasmonic features by measuring the extinction spectra of Au QS particles with various sizes. For the Au TOH particles with a side length of 94 ± 4 nm, a strong quadrupole mode together with a broad, weaker dipole plasmon band was also observed in the extinction spectrum. Remarkably, when nanoscale porosity was introduced into the Au nanoparticles, the higher-order mode (quadrupole) was significantly dampened, whereas the dipole plasmon mode remained robust and shifted to longer wavelengths.

In addition to the greatly enhanced tunability of the far-field optical responses, the nanoscale porosity also creates sharp, nanoscale surface features, giving rise to intense near-field "hot spots" upon plasmonic excitation. The Au PNPs thus combine highly tunable plasmon resonances with intense local field enhancements, allowing for single-particle SERS under near-IR excitation (785 nm). 4-Aminothiophenol (4-ATP) was used as a nonresonant probe molecule to evaluate the overall Raman enhancements on individual Au PNPs. A submonolayer of isolated particles was immobilized on a

polyvinylpyridine-functionalized silicon substrate and was used as the SERS substrates. We used a confocal Raman microscope to collect the SERS spectra one particle at a time. SERS spectra were collected from more than 100 individual particles for each sample. Figure 2.3B shows the representative normal Raman spectrum of 4-ATP and SERS spectra of 4-ATP adsorbed on individual PNPs. The SERS signal was the largest when the plasmon was resonant with the laser and gradually decreased as the plasmon resonances were detuned from the laser. The plasmon-dependent SERS activity was further confirmed by the histograms of the Raman intensities of the 1078 and 1590 cm^{-1} modes obtained from 100 individual particles (Figure 2.3C and D) for each sample. The Raman enhancement factors (EFs) were estimated to be on the order of 10^5, approaching 10^6 when the plasmon resonance was resonant with the excitation laser. These estimated EFs were averaged over the entire particle surfaces. The local enhancements in the near-field hot spots, however, are anticipated to be at least 1 order of magnitude higher. In contrast, the Au QS and TOH particles exhibited much weaker Raman enhancements than the PNPs.

To gain more quantitative insights into the structure-property relationship of the nanoporous particles, finite-difference time-domain (FDTD) simulations were performed to calculate their extinction spectra and near-field enhancements. Figure 2.4A shows the calculated extinction spectra of a Au sphere (189 nm in diameter) with a varying number of pores randomly generated at the particle surface. Both the dipole and quadrupole plasmon bands progressively red-shifted upon an increase of the porosity. As the number of nanoscale pores increased, the intensity of the quadrupole mode gradually decreased while the dipole plasmon mode remained robust (Figure 2.4B). The effects of

nanoporosity on the far-field optical extinction of the particles were also found to be size-dependent. For relatively small Au particles within the quasi-static limit, the nanoscale porosity caused a decrease of the dipolar extinction peak and a broadening and red shift with increasing number of pores. Larger particles exhibit greatly enhanced tunability of the dipole resonance, with higher-order multipolar resonances significantly dampened. In Figure 2.4C and D, we compare the calculated extinction spectra of Au PNPs and SSNPs with various overall sizes. It is apparent that the plasmon resonance frequencies became much more sensitively dependent on the overall size of the PNPs than those of the SSNPs. The FDTD results showed excellent agreement with our experimental observations.

We have further used FDTD to calculate the near-field enhancements of the particles. Figure 2.4E shows the cross-sectional views of the calculated near-field distributions ($|E/E_0|^2$) of PNP and SSNP with various sizes at 785 nm excitation. Each PNP possesses large numbers of hot spots with local field enhancements significantly more intense than those achievable on the SSNP of the same overall size. As shown in Figure 2.4F and G, the average near-field intensity ($|E/E_0|^2$) enhancements of Au PNP were about 10 times higher than those on the SSNP. The Au TOH particle with a side length of 94 nm showed larger near-field enhancements than the SSNPs largely due to the presence of sharp tips at the particle surfaces. This is in agreement with the experimental observations that the Raman enhancements on individual TOH particles were higher than those on the Au QS nanoparticles, though they were not as high as those achieved on individual Au PNPs.

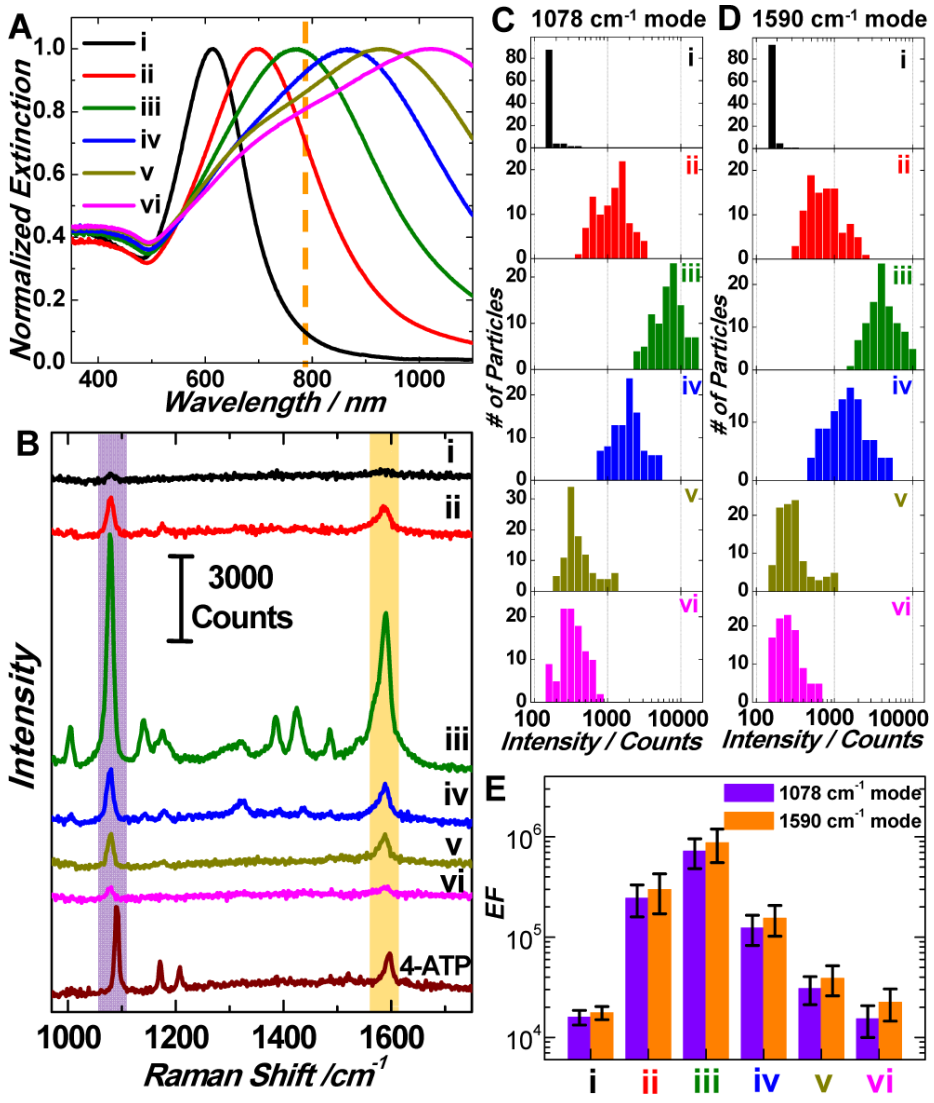

Figure 2.3. (A) Extinction spectra of colloidal Au PNPs of various sizes. The vertical dashed line shows the excitation laser wavelength (785 nm) for Raman measurements. (B) Representative SERS spectra of 4-ATP adsorbed on individual Au PNPs of various sizes. The bottom spectrum is the normal Raman spectrum of the neat 4-ATP film. Histograms of the Raman intensity of the (C) 1078 and (D) 1590 cm^{-1} modes obtained from individual Au PNPs. (E) Average SERS EFs on individual Au PNPs of various sizes. The labels of i, ii, iii, iv, v, and vi in all of the panels correspond to the Au PNP samples shown in Figure 1E–J, respectively.

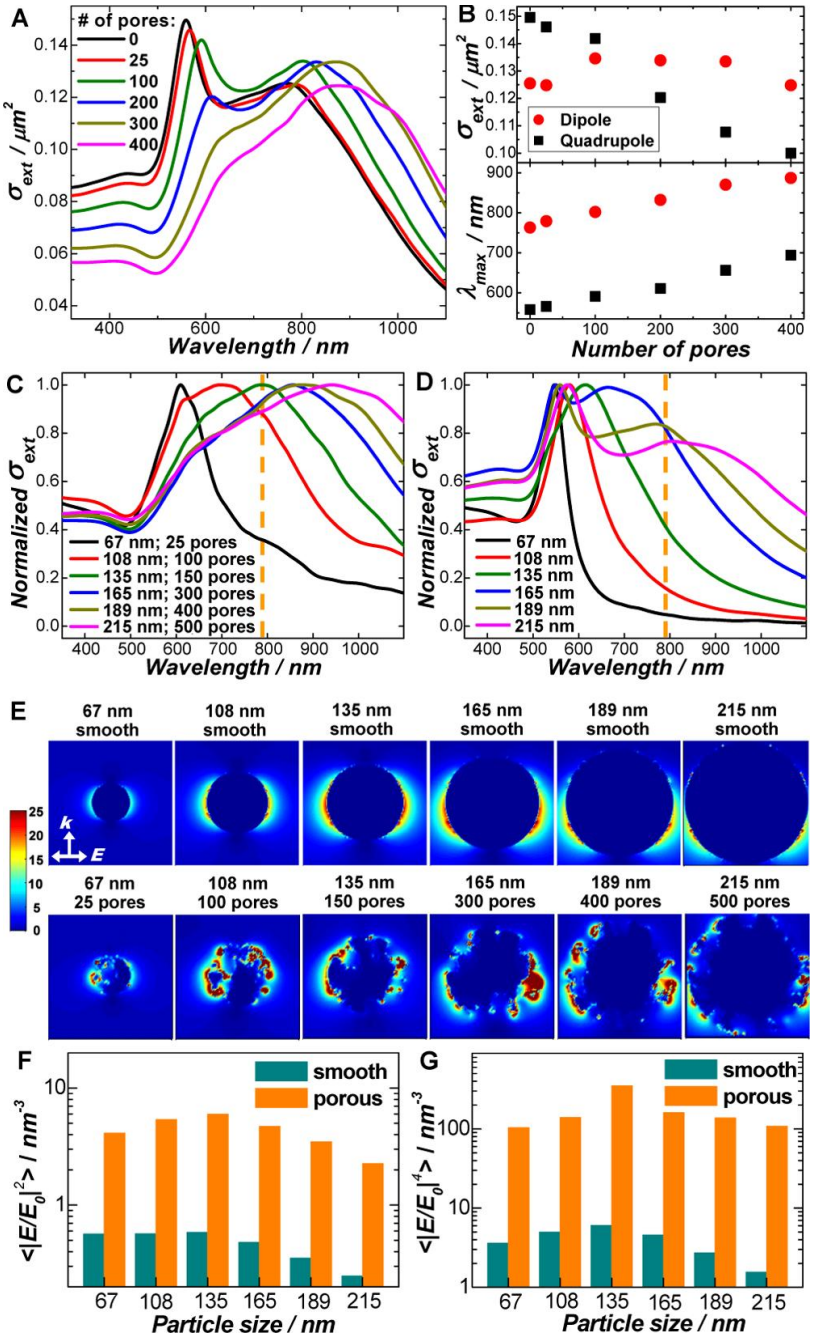

Figure 2.4. (A) Calculated extinction spectra of spherical Au particles (189 nm in diameter) with 0, 25, 100, 200, 300, and 400 pores. (B) Calculated extinction cross sections at the dipole and quadrupole resonance wavelengths (upper panel) and the plasmon resonance wavelengths (lower panel) of the Au particles (189 nm) with a varying number of pores. Calculated extinction spectra of (C) Au PNPs and (D) Au SSNPs of different particle sizes. The particle sizes and the numbers of pores in each particle are labeled in panel C. (E) The cross-sectional views of the calculated near-field enhancements $|E/E_0|^2$ of SSNPs (upper row) and PNPs (lower row) with various sizes at 785 nm excitation. Mean-field enhancements averaged over volume: (F) $\langle|E/E_0|^2\rangle$ and (G) $\langle|E/E_0|^4\rangle$ of PNPs and SSNPs of overall particle sizes of 67, 108, 135, 165, 189, and 215 nm.

2.4 Conclusions

In summary, kinetically controlled seed-mediated growth allows for the fabrication of nanoscale porous Au particles with fine-controlled overall particle sizes. The nanoporous Au particles represent a new class of subwavelength photonic materials that combine tunable localized plasmon resonances with intense near-field enhancements exploitable for single particle SERS. In addition to their attractive optical properties, nanoporous Au may also exhibit superior catalytic activities toward a variety of chemical reactions, as previously demonstrated on nanoporous Au films.[24-26] Therefore, these optically tunable porous nanoparticles may serve a dual purpose, as substrates for plasmon-enhanced spectroscopies and efficient surface catalysts. This dual functionality may allow for quantitative spectroscopic studies of kinetics and reaction pathways of surface-catalyzed reactions with unprecedented sensitivity and detail.

2.5 References

(1) Halas, N. J.; Lal, S.; Chang, W. S.; Link, S.; Nordlander, P. *Chem. Rev.* **2011**, *111*, 3913-3961.

(2) Murphy, C. J.; San, T. K.; Gole, A. M.; Orendorff, C. J.; Gao, J. X.; Gou, L.; Hunyadi, S. E.; Li, T. *J. Phys. Chem. B* **2005**, *109*, 13857-13870.

(3) Jain, P. K.; Huang, X. H.; El-Sayed, I. H.; El-Sayed, M. A. *Acc. Chem. Res.* **2008**, *41*, 1578-1586.

(4) Burda, C.; Chen, X. B.; Narayanan, R.; El-Sayed, M. A. *Chem. Rev.* **2005**, *105*, 1025-1102.

(5) El-Sayed, M. A. *Acc. Chem. Res.* **2001**, *34*, 257-264.

(6) Xia, Y. N.; Halas, N. J. *MRS Bull.* **2005**, *30*, 338-344.

(7) Lal, S.; Link, S.; Halas, N. J. *Nat. Photonics* **2007**, *1*, 641-648.

(8) Oulton, R. F.; Sorger, V. J.; Zentgraf, T.; Ma, R. M.; Gladden, C.; Dai, L.; Bartal, G.; Zhang, X. *Nature* **2009**, *461*, 629-632.

(9) Knight, M. W.; Sobhani, H.; Nordlander, P.; Halas, N. J. *Science* **2011**, *332*, 702-704.

(10) Ferry, V. E.; Munday, J. N.; Atwater, H. A. *Adv. Mater.* **2010**, *22*, 4794-4808.

(11) Willets, K. A.; Van Duyne, R. P. *In Annual Review of Physical Chemistry; Annual Reviews: Palo Alto, CA*, **2007**; *Vol. 58*, pp 267-297.

(12) Camden, J. P.; Dieringer, J. A.; Zhao, J.; Van Duyne, R. P. *Acc. Chem. Res.* **2008**, *41*, 1653-1661.

(13) Giljohann, D. A.; Seferos, D. S.; Daniel, W. L.; Massich, M. D.; Patel, P. C.; Mirkin, C. A. *Angew. Chem., Int. Ed.* **2010**, *49*, 3280-3294.

(14) Lal, S.; Clare, S. E.; Halas, N. J. *Acc. Chem. Res.* **2008**, *41*, 1842-1851.

(15) Nikoobakht, B.; El-Sayed, M. A. *Chem. Mater.* **2003**, *15*, 1957-1962.

(16) Jin, R. C.; Cao, Y. W.; Mirkin, C. A.; Kelly, K. L.; Schatz, G. C.; Zheng, J. G. *Science* **2001**, *294*, 1901-1903.

(17) Pastoriza-Santos, I.; Liz-Marzan, L. M. *Nano Lett.* **2002**, *2*, 903-905.

(18) Halas, N. J. *MRS Bull.* **2005**, *30*, 362-367.

(19) Chen, J. Y.; Wiley, B.; Li, Z. Y.; Campbell, D.; Saeki, F.; Cang, H.; Au, L.; Lee, J.; Li, X. D.; Xia, Y. N. **2005**, *17*, 2255-2261.

(20) Erlebacher, J.; Aziz, M. J.; Karma, A.; Dimitrov, N.; Sieradzki, K. *Nature* **2001**, *410*, 450-453.

(21) Bosman, M.; Anstis, G. R.; Keast, V. J.; Clarke, J. D.; Cortie, M. B. *ACS Nano* **2012**, *6*, 319-326.

(22) Biener, J.; Nyce, G. W.; Hodge, A. M.; Biener, M. M.; Hamza, A. V.; Maier, S. A. *Adv. Mater.* **2008**, *20*, 1211-1217.

(23) Yu, F.; Ahl, S.; Caminade, A. M.; Majoral, J. P.; Knoll, W.; Erlebacher, J. *Anal. Chem.* **2006**, *78*, 7346-7350.

(24) Ding, Y.; Chen, M. W. *MRS Bull.* **2009**, *34*, 569-576.

(25) Fujita, T.; Guan, P. F.; McKenna, K.; Lang, X. Y.; Hirata, A.; Zhang, L.; Tokunaga, T.; Arai, S.; Yamamoto, Y.; Tanaka, N.; Ishikawa, Y.; Asao, N.; Erlebacher, J.; Chen, M. W. *Nat. Mater.* **2012**, *11*, 775-780.

(26) Wittstock, A.; Zielasek, V.; Biener, J.; Friend, C. M.; Baumer, M. *Science* **2010**, *327*, 319-322.

(27) Kelf, T. A.; Sugawara, Y.; Baumberg, J. J.; Abdelsalam, M.; Bartlett, P. N. *Phys. Rev. Lett.* **2005**, *95*, 116802.

(28) Lang, X. Y.; Qian, L. H.; Guan, P. F.; Zi, J.; Chen, M. W. *Appl. Phys. Lett.* **2011**, *98*, 093701.

(29) Sau, T. K.; Murphy, C. J. Room Temperature, *J. Am. Chem. Soc.* **2004**, *126*, 8648-8649.

(30) Huang, Y. J.; Wu, L.; Chen, X. D.; Bai, P.; Kim, D. H. *Chem. Mater.* **2013**, *25*, 2470-2475.

(31) Ming, T.; Feng, W.; Tang, Q.; Wang, F.; Sun, L. D.; Wang, J. F.; Yan, C. H. *J. Am. Chem. Soc.* **2009**, *131*, 16350-16351.

(32) Ma, Y. Y.; Kuang, Q.; Jiang, Z. Y.; Xie, Z. X.; Huang, R. B.; Zheng, L. S. *Angew. Chem., Int. Ed.* **2008**, *47*, 8901-8904.

(33) Rodriguez-Fernandez, J.; Perez-Juste, J.; de Abajo, F. J. G.; Liz-Marzan, L. M. *Langmuir* **2006**, *22*, 7007-7010.

(34) Wang, H.; Halas, N. J. *Adv. Mater.* **2008**, *20*, 820-825.

CHAPTER 3

Nanoporosity-Enhanced Catalysis on Subwavelength Au Nanoparticles: a Plasmon-Enhanced Spectroscopic Study

3.1 Introduction

Au nanoparticles have attracted immense attention owing to their intriguing size- and shape-dependent catalytic and optical properties.[1-4] Distinct from Au bulk materials that are chemically inert, Au nanoparticles with diameters smaller than 5 nm exhibit remarkable catalytic activities towards a variety of oxidation and hydrogenation reactions even under mild conditions such as ambient temperature and pressure,[5-11] whereas Au particles with characteristic dimensions beyond 5 nm are found to be catalytically inactive. When used for heterogeneous catalysis, the catalytically active small Au nanoparticles are typically supported on high-surface-area oxide materials.[5, 6, 12-14] These supports can significantly enhance the synergistic catalytic performance of the hybrid materials through various mechanisms,[15-18] making it extremely challenging to delineate the role of the supports and the intrinsic catalytic activities of Au. Using free-standing, unsupported colloidal Au nanoparticle as catalysts, compelling evidence on the intrinsic, size-dependent catalytic activities of Au nanoparticles has been obtained.[19-21] It has become increasingly unanimous that the undercoordinated surface atoms located at the particle edges and corners provide a key contribution to the catalytic activities of sub-5 nm Au nanoparticles.[5, 22-25] Interestingly, it has been recently shown that dealloyed nanoporous Au films without any support exhibit similar catalytic activities as the oxide-supported sub-5 nm Au nanoparticles toward oxidation reactions even though the feature lengths of their nanopores and ligaments are far beyond 5 nm.[25-30] The origin of such high catalytic activity has been interpreted, based on high-resolution electron microscopic observations, as a result of the high fraction of undercoordinated surface atoms, comparable to that of sub-5 nm nanoparticles, present on the highly curved surfaces of

the dealloyed nanoporous Au films,[31] which serve as the active sites for catalytic reactions.

The development of detailed mechanistic understanding of Au-based heterogeneous catalysis requires the capabilities not only to fine-control the dimensions and surface structures of Au nanocatalysts but also to precisely monitor, in real time, the reaction kinetics and chemical transformations occurring at the reactant-catalyst interfaces. Surface-enhanced Raman spectroscopy (SERS) provides a unique approach to the *in situ* monitoring of molecular transformations in heterogeneous catalysis with high detection sensitivity, excellent surface selectivity, and rich molecular structural information.[32-38] By measuring the SERS signals from the monolayer molecules pre-adsorbed on the nanocatalyst surfaces, unraveling the intrinsic kinetics and mechanisms of surface-catalyzed reactions becomes possible with minimal complication introduced by the surface-capping ligands as well as the diffusion, adsorption, and desorption of reactants and products. The unique capability of SERS to resolve detailed molecular structures further enables the identification of transient intermediates along the reaction pathways.[35, 36] Using SERS to directly monitor catalytic reactions on Au nanocatalysts, however, has been challenging because SERS and catalysis require Au nanoparticles in two drastically different size regimes. SERS relies on the generation of intense plasmon-field enhancements in close proximity to the particle surfaces,[39-41] which are not achievable on the catalytically active sub-5 nm Au nanoparticles. While Au nanoparticles in the subwavelength size regime exhibit strong plasmon resonances and intense local fields that can be harnessed for SERS, they are no longer catalytically active. It has been recently demonstrated that the *in situ* monitoring of surface-catalyzed reactions by SERS

becomes possible only when catalytically active small nanoparticles of Au, Pt, or Pd and plasmonically active large Au nanoparticles are hierarchically assembled into three-dimensional multilayered complex superstructures.[32-35, 37] The structural complexity of these bifunctional hybrid particles, however, makes it challenging to directly correlate the surface structures with the catalytic activities of the nanocatalysts.

In this chapter, we study the nanoporosity-enhanced catalytic activities of subwavelength Au nanoparticles using the hydrogenation of nitrophenol by sodium borohydride as a model reaction. The introduction of nanoscale surface porosity to subwavelength Au nanoparticles dramatically enhances not only the tunability of plasmon resonance frequencies but also the near-field intensities of the particles, making the Au porous nanoparticles (PNPs) ideal substrates for single-particle SERS.[42] In addition, Au PNPs possess highly curved surfaces rich of undercoordinated atoms at the surface steps and kinks, well-mimicking the surfaces of the sub-5 nm nanoparticles and dealloyed nanoporous Au films. Therefore, Au PNPs exhibit drastically enhanced catalytic activities than the Au quasi-spherical nanoparticles (QSNPs) of the same sizes. Furthermore, the monometallic Au PNPs are compositionally simpler than the dealloyed nanoporous Au films containing residual less-noble elements, such as Ag, that cannot be completely removed through the dealloying process.[25-31, 43] The catalytic activity of the dealloyed nanoporous Au films has been found to strongly depend on the amount and spatial distribution of the residual Ag,[12, 31, 44, 45] though the exact roles of the residual Ag still remain unclear. The compositional simplicity of free-standing Au PNPs allows us to build direct correlations between the surface structures and the intrinsic catalytic activities without the complication due to the effects of oxide supports and residual less-

noble elements. As demonstrated in this work, the unique dual functionality of Au PNPs as both substrates for plasmon-enhanced spectroscopy and efficient surface catalysts enables detailed, quantitative spectroscopic study of the intrinsic kinetics and mechanisms of surface reactions on Au nanocatalysts.

3.2 Experimental Section

Materials. Gold(III) chloride trihydrate ($HAuCl_4$ $3H_2O$, ACS grade) were obtained from J.T. Baker. Sodium borohydride ($NaBH_4$, 99%), hydrochloric acid (HCl, 37%), L-ascorbic acid (AA, 99.5%), and 4-nitrophenol ($C_6H_5NO_2$, 4-NP, 99%) were obtained from Sigma-Aldrich. Silver nitrate (AgNO3, 99.9995% metals basis), (1-Hexadecyl)trimethylammonium chloride (CTAC, 96%), 4-aminothiophenol (C_6H_7NS, 4-ATP, 97%), and 4-nitrothiophenol ($C_6H_5NO_2S$, 4-NTP, 80%) were obtained from Alfa Aesar. (1-Hexadecyl)trimethylammonium bromide (CTAB, > 98%) and sodium oleate (NaOL, >97%) were purchased from TCI America. Ethanol (200 proof) was purchased from Fisher Scientific. All reagents were used as received without further purification. Ultrapure water (18.2 MΩ resistivity, Barnstead EasyPure II 7138) was used for all experiments.

Synthesis of Au PNPs and QSNPs. Au PNPs and QSNPs were prepared following a recently published protocol based on seed-mediated growth in aqueous solution.[42] First, colloidal Au seeds about 2 nm in diameter were prepared by the reducing $HAuCl_4$ with $NaBH_4$ in the presence of CTAC. In a typical procedure, 0.30 mL of ice-cold, freshly prepared $NaBH_4$ (10 mM) were quickly injected into a solution containing CTAC (10.00 mL, 0.10 M) and $HAuCl_4$ (0.25 mL, 10 mM) under magnetic stir (1200 rpm). The seed solution was stirred for 1 min, then left undisturbed for 2 h, and finally diluted 1000-fold

with CTAC (0.10 M). The particle growth solution was prepared by sequentially adding $HAuCl_4$ (0.50 mL, 10 mM) and AA (0.10 mL, 0.10 M) into a CTAC (10.00 mL, 0.10 M) solution. To prepare Au PNPs with average diameter of ~ 125 nm, 50 μL of the diluted Au seed solution was added into the growth solution. The reaction solution was gently mixed for 30 s and then left undisturbed at room temperature for 4 h. The as-obtained Au PNPs were washed with water three times through centrifugation/redispersion cycles, and finally redispersed in 4.0 mL of water. The Au QSNPs were fabricated following a similar protocol for the Au PNPs except for the addition of HCl. The growth solution was prepared by sequentially adding $HAuCl_4$ (0.50 mL, 10 mM), HCl (0.20 mL, 1.0 M) and AA (0.10 mL, 0.10 M) into a CTAC (10.00 mL, 0.10 M) solution. After gently mixing the reactants for 30 s, the growth of Au QSNPs was initiated by adding 40 μL of the diluted Au seed solution, and then left undisturbed at room temperature for 4 h. The obtained Au QSNPs were washed with water three times, and finally redispersed in 4.0 mL of water.

Synthesis of Au TOH and ETHH Nanoparticles. Au TOH nanoparticles were fabricated following a similar protocol for the Au PNPs except for the increased amount of AA.[42] The growth solution was prepared by sequentially adding $HAuCl_4$ (0.50 mL, 10 mM) and AA (1.0 mL, 0.10 M) into a CTAC (10.00 mL, 0.10 M) solution. After gently mixing the growth solution for 30 s, the growth of Au TOH nanoparticles was initiated by adding 15 μL of the diluted Au seed solution, and then left undisturbed at room temperature for 4 h. The obtained Au TOH nanoparticles were washed with water three times, and finally redispersed in 4.0 mL of water.

Au ETHH nanoparticles were prepared following a previously protocol.[60] Colloidal Au seeds were prepared by the reducing $HAuCl_4$ with $NaBH_4$ in the presence of CTAB. First, 5.0 mL of 0.5 mM $HAuCl_4$ was mixed with 5 mL of 0.2 M CTAB solution. Then, 1.0 mL of ice-cold, freshly prepared 6 mM $NaBH_4$ was quickly injected into the mixture under magnetic stir (1200 rpm). The seed solution was stirred for 2 min and then left undisturbed for 30 min before use. To prepare the Au ETHH nanoparticle growth solution, 7.0 g of CTAB and 1.234 g of NaOL were dissolved in 250 mL of water at 60 ℃. The solution was cooled to 30 ℃ and then 24 mL of 4 mM $AgNO_3$ was added. The mixture was kept undisturbed at 30 ℃ for 15 min, followed by the addition of 250 mL of 1 mM $HAuCl_4$. The solution became colorless after 90 min of stirring at 700 rpm and 2.1 mL HCl (37 wt % in water, 12.1 M) was then introduced into the mixture. After another 15 min of slow magnetic stir at 400 rpm, 1.25 mL of 64 mM ascorbic acid was added. 0.8 mL of seed solution was injected into the growth solution and the mixture solution was vigorously stirred for another 30 s and then left undisturbed at 30 ℃ for 12 h for particle growth. The resulting Au ETHH nanoparticles were collected by centrifugation and finally redispersed in 30 mL of 0.1 M CTAC.

Characterizations. The morphologies and structures of the nanoparticles were characterized by bright-field TEM using a Hitachi H-8000 transmission electron microscope operated at an accelerating voltage of 200 kV. All samples for TEM measurements were dispersed in water and drop-dried on 300 mesh Formvar/carbon-coated Cu grids. The structures of the nanoparticles were also characterized by SEM using a Zeiss Ultraplus thermal field emission scanning electron microscope. The samples for SEM measurements were dispersed in water and drop-dried on silicon

wafers. The atomic level structures of the nanoparticles were resolved by high-resolution HAADF-STEM using a JEOL 2100F 200 kV FEG-STEM/TEM microscopy equipped with a CEOS CS corrector on the illumination system. The samples for HAADF-STEM measurements were dispersed in water and drop-dried on 400 mesh Cu grids with ultrathin carbon support film (Electron Microscopy Science Inc.). The optical extinction spectra of the nanoparticles were measured on aqueous colloidal suspensions at room temperature, using a Beckman Coulter Du 640 spectrophotometer. Raman spectra were obtained on a Bayspec *Nomadic*^{TM} Raman microscopy built on an Olympus BX51 microscope equipped with a 785 nm CW diode laser.

UV-vis Spectroscopic Measurements of Catalytic Reaction Kinetics. We used the hydrogenation of 4-nitrophenol by $NaBH_4$ at room temperature as a model reaction to evaluate the catalytic activities of Au PNPs, QSNPs, and Au seeds. In a typical procedure, 0.2 mL of 1.0 mM 4-nitrophenol and 0.1 mL of 0.5 M $NaBH_4$ (freshly prepared, ice-cold) were sequentially added to 2.6 mL of ultrapure water in a cuvette and mixed thoroughly. Then, 100 μL of Au PNPs solution were injected into the system. After thoroughly mixed for 5 s, UV-vis extinction spectra were collected in real time to monitor the catalytic reaction process. We compared the catalytic activities of Au PNPs, QSNPs, and Au seeds at the same particle concentration (3.0×10^8 particles mL^{-1}) and nominally the same surface area (the particle concentrations for PNPs, QSNPs, and Au seeds were 3.0×10^8, 3.0×10^9, and 6.0×10^{12} particles mL^{-1}, respectively to keep the total surface areas available for catalysis the same). To recycle the Au PNPs, the particles was centrifuged (2500 rpm, 3min) upon depletion of 4-nitrophenol and the washed with water once and were redispersed in 100 μL of ultrapure water for next catalytic reaction cycle.

The effects of particle concentrations on the reaction kinetics were evaluated by adding different amounts of Au PNP catalysts (particle concentrations: 1.8×10^8, 2.4×10^8, 3.0×10^8, 3.6×10^8, and 4.5×10^8 particles mL^{-1}).

Monitoring Reaction Kinetics by Time-Resolved SERS. To use SERS to monitor the catalytic reactions, we first pre-adsorbed SAMs of 4-NTP onto the surfaces of Au PNPs. In a typical procedure, 500 μL colloidal suspension of Au PNPs with (~10^{10} particles mL^{-1}) were incubated with 500 μL ethanol solution of 50.0 μM 4-NTP overnight to form saturated SAMs of 4-NTP on the nanoparticle surfaces. Then, the 4-NTP-coated Au PNPs were centrifuged (3000 rpm, 3 min) and redispersed in 500 μL ultrapure water. The nanoparticle-catalyzed 4-NTP reduction occurred at room temperature upon the addition of 50 μL of PNPs, 20 μL of ultrapure water, and 30 μL of 100 mM $NaBH_4$ in a 0.5 mL Eppendorf centrifuge tube. The kinetics of the catalyzed reactions were measured in real time using time-resolved SERS. SERS spectra were obtained on a Bayspec *Nomadic*^{TM} confocal Raman microscopy built on an Olympus BX51 reflected optical system with a 785 nm continuous wave excitation laser. The excitation laser was focused on the reaction mixture using a 10× objective [Numerical Aperture (NA) = 0.30, working distance (WD) = 11.0 mm, Olympus MPLFLN]. The laser power was measured to be 10.0 mW at the samples. Successive SERS spectra were collected during the reaction until complete reduction of 4-NTP into 4-ATP. We evaluated the catalytic activities of Au PNPs at various $NaBH_4$ concentrations (10, 15, 20, 30, 50, 80, 120, and 160 mM) and various concentrations of Au PNPs (3.0×10^9, 4.5×10^9, 6.0×10^9, 7.5×10^9, and 9.0×10^9 particles mL^{-1}). The coverage of 4-NTP on surfaces of Au PNPs was controlled by

incubating the Au PNPs with different concentrations of 4-NTP. The total volume of the reaction mixture was already fixed at 100 μL.

$NaBH_4$-Induced Desorption of 4-ATP from Au PNP Surfaces. We pre-adsorbed 4-ATP onto the surfaces of Au PNPs, Au TOH, and Au ETHH nanoparticles by incubating 500 μL of Au nanoparticles (~10^{10} particles mL^{-1}) with 500 μL ethanol solution of 50.0 μM 4-ATP overnight to form saturated SAMs of 4-ATP on the nanoparticle surfaces. Then, the nanoparticles were centrifuged (3000 rpm, 3 min) and redispersed in 500 μL ultrapure water. The desorption occurred at room temperature upon the addition of 50 μL of Au nanoparticles, 30 μL of ultrapure water, and 20 μL of 100 mM $NaBH_4$ in a 0.5 mL Eppendorf centrifuge tube. The desorption kinetics was measured in real time using time-resolved SERS. We compared the desorption rates of 4-ATP from Au PNPs, Au TOH, and Au ETHH nanoparticles under same particle concentration (7.5×10^9 particles mL^{-1}) and same $NaBH_4$ concentration (20 mM). We also investigated the desorption rates of 4-ATP from Au PNPs under various $NaBH_4$ concentrations (10, 20, 30, and 40 mM).

3.3 Results and Discussions

Subwavelength Au PNPs were fabricated using a versatile, room temperature seed-mediated growth method we recently developed.[42] This approach allows for the selective fabrication of various Au nanostructures, such as QSNPs, PNPs, and trisoctahedral (TOH) nanoparticles, through deliberate control over the particle growth kinetics. As demonstrated in detail in our previous publication,[42] fast nanoparticle growth resulted in the selective formation of single-crystalline TOH nanoparticles enclosed by high index {221} facets, while slow nanoparticle growth favored the formation of multi-twinned QSNPs enclosed by thermodynamically stable low index {111} and {100} facets. The

Au PNPs were found to be a unique structure resulting from the intermediate particle growth kinetics that fell between the kinetically favored regime and the thermodynamically controlled regime. As schematically illustrated in Figure 3.1A, we started with colloidal Au seeds prepared by reducing chloroauric acid ($HAuCl_4$) with sodium borohydride ($NaBH_4$) in the presence of cetyltrimethylammonium chloride (CTAC). The as-prepared Au seed particles were 2 ± 0.2 nm in diameter and no plasmon resonance peak was observed in the optical extinction spectrum due to the small particle sizes. The growth of the Au PNPs was initiated by injecting various volumes of diluted Au seeds into the particle growth solution, which contained $HAuCl_4$, CTAC, and appropriate amount of L-ascorbic acid (AA). Addition of HCl into the growth solution significantly slowed down the growth of the nanoparticles, leading to the formation of Au QSNPs. The average sizes of the PNPs and QSNPs can be both fine-controlled in the range from ~ 50 nm to ~ 250 nm by simply adjusting the amount of Au seeds added into the growth solution. Figures 3.2B-2E show the scanning electron microscopy (SEM) and bright-field transmission electron microcopy (TEM) images of the Au PNPs and QSNPs with the same average overall particle size around 125 nm. While the QSNPs exhibited relatively smooth, multifaceted surfaces, the surfaces of the PNPs were porous and highly curved with pore diameters in the range from 5 nm to 30 nm. In this study, we used the PNPs and QSNPs of the same overall size (125 nm) to systematically investigate the effects of the nanoscale surface porosity on the catalytic activities of the subwavelength Au particles.

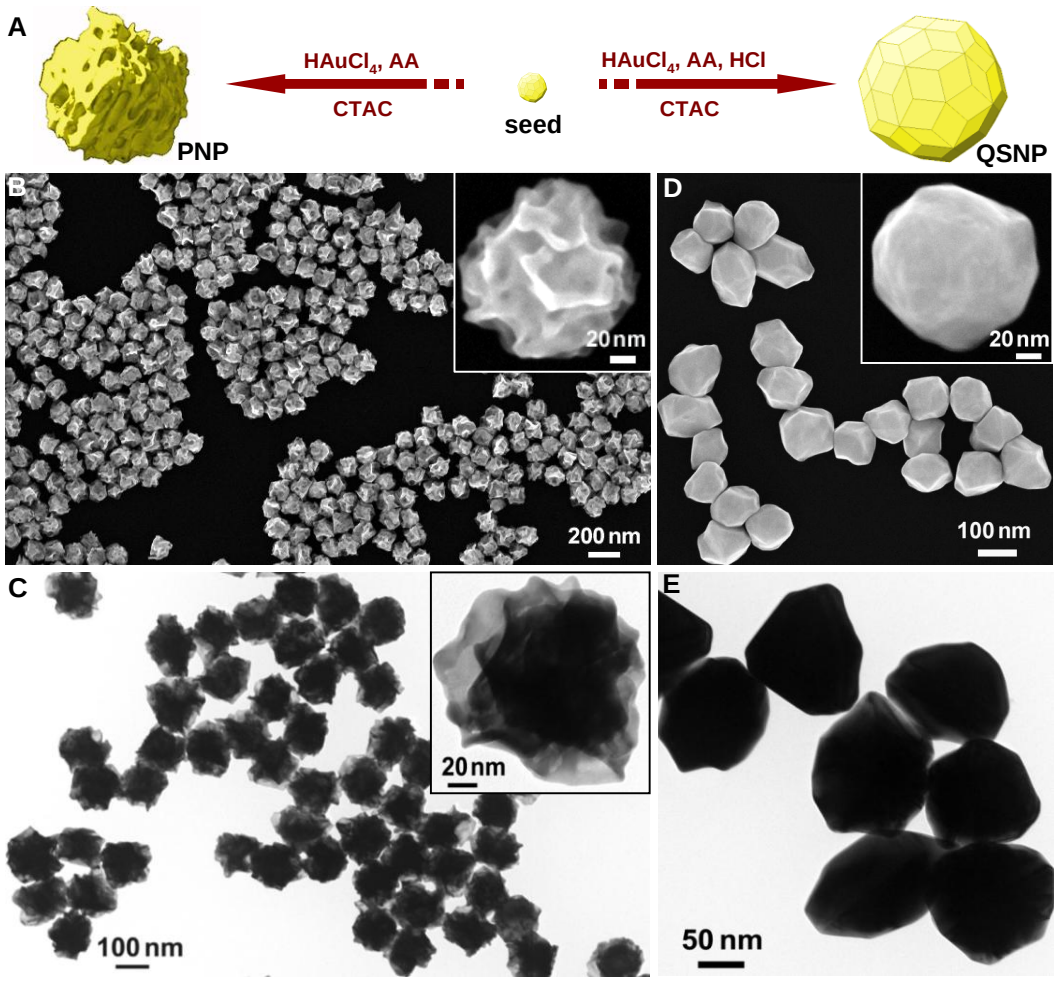

Figure 3.1. Morphologies of Au porous nanoparticles (PNPs) and Au quasi-spherical nanoparticles (QSNPs). (A) Schematics illustrating the fabrication of Au PNPs and Au QSNPs using a kinetically controlled seed-mediated growth method. (B) SEM and (C) bright-field TEM images of Au PNPs with diameters of 125 $\pm$ 8 nm. The insets highlight one individual particle. (D) SEM and (E) bright-field TEM images of Au QSNPs with diameters of 125 $\pm$ 11 nm. The inset of panel D shows the SEM image of one individual Au QSNP.

The catalytic hydrogenation of p-nitrophenol by $NaBH_4$[19] was used as a model reaction to quantitatively evaluate the catalytic activities of subwavelength Au PNPs, QSNPs, and 2 nm Au seeds. In a basic environment, p-nitrophenolate ions showed a strong absorption peak at ~ 400 nm, whose intensity gradually decreased as the catalytic reduction reaction proceeded in the presence of $NaBH_4$ and Au nanocatalysts (Figure 3.2A). Meanwhile, a new absorption band emerged at ~ 315 nm and became progressively more intense,

indicating the formation of the product, p-aminophenol. The intensities of the absorption peak at 400 nm were used to quantify the concentration of p-nitrophenol as a function of reaction time, based on which the reaction kinetics was analyzed. In Figure 3.2B, we directly compare the kinetics of the reactions catalyzed by the Au seeds, PNPs, and QSNPs with the same particle concentration at 3.0×10^{8} particles mL^{-1}. For all these experiments, the initial concentrations of p-nitrophenol and $NaBH_4$ were kept at 66.7 μM and 16.7 mM, respectively. In the absence of Au nanoparticles, no reaction was observed over extended time periods up to a few days. At the same nanocatalyst concentration, the Au PNPs exhibited much higher catalytic activity than the Au QSNPs. The 2 nm Au seeds, which were expected to be highly active as catalysts, also showed much slower reaction kinetics than the Au PNPs because of the much smaller total surface areas available for catalysis. Interestingly, an induction time in which no reduction took place, was observed regardless of the sizes and morphologies of the Au nanocatalysts. This induction time was previously observed in the p-nitrophenol reduction catalyzed by other Au nanostructures as well, which was hypothetically ascribed to the time required for p-nitrophenol to diffuse and adsorb onto the Au surfaces[46, 47] or the molecular adsorption-induced surface restructuring of the Au nanocatalysts[48, 49] before the reaction could be initiated. We also adjusted the particle concentrations to compare the reaction kinetics in the presence of nominally the same total surface areas of the nanocatalysts. As shown in Figure 3.2C, with the same total surface areas, Au seeds exhibited the highest catalytic activity, and the Au PNPs were still catalytically much more active than the Au QSNPs. Therefore, the nanoporosity-enhanced catalysis observed on the subwavelength Au nanoparticles should be interpreted as a result of not only the much larger surface areas

per particle but also, more essentially, the higher reactivity of the highly curved nanoporous surfaces of Au PNPs than the relatively smooth surfaces of Au QSNPs.

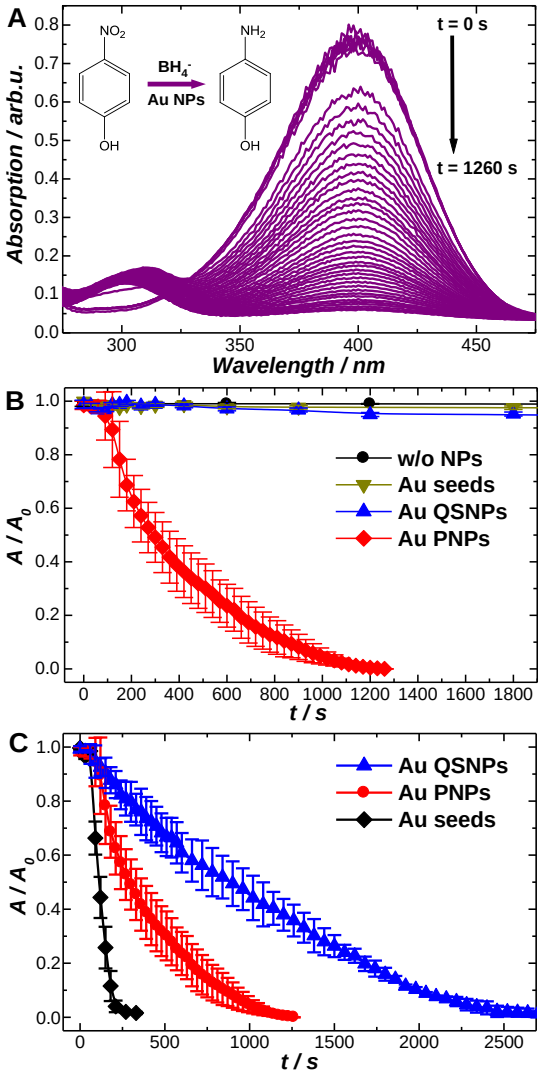

Figure 3.2. Comparison of catalytic activities of Au PNPs, Au QSNPs, and Au seeds (~ 2 nm). (A) Time-resolved extinction spectra of the reaction mixtures during the nanoparticle-catalyzed hydrogenation of 4-nitrophenol (4-NP) by $NaBH_4$. The time interval between two consecutive spectra is 30 s. (B) Absorption (normalized against the initial point) at the peak position for 4-NP (λ = 400 nm) as a function of reaction time in the absence and in the presence of nanoparticle catalysts with the same particle concentrations. In all cases, the concentrations of p-NP and NaBH4 were 66.7 μM and 16.7 mM, respectively. The concentrations of the Au PNPs, QSNPs, and seeds were all 3.0×10^{8} particles mL^{-1}. (C) Absorption (normalized against the initial point) at λ = 400 nm as a function of reaction time in the presence of nanoparticle catalysts with roughly the same the same total surface areas. In all cases, the concentrations of p-NP and NaBH4 were 66.7 μM and 16.7 mM, respectively. The concentrations of the Au PNPs, QSNPs, and seeds were 3.0×10^{8}, 3.0×10^{9}, and 6.0×10^{12} particles mL^{-1}. The error bars in Panels B and C represent the standard deviations obtained from five experimental runs.

To gain further insights into the nanoporosity-enhanced catalytic activity, we used high resolution high-angle annular dark-field scanning transmission electron microscopy (HAADF-STEM) to resolve the atomic-level surface structures of Au PNPs. The central panel of Figure 3.3 shows a HAADF-STEM image of one individual Au PNP, which exhibited porous and highly curved surface structures. Each Au PNP consisted of several monocrystalline domains packed together to form a twinned crystalline structure. HAADF-STEM images from four different monocrystalline regions labeled as i, ii, iii, and iv in the central panel, respectively, are shown with higher magnification in Figure 3.3. The crystalline domains in these four regions were all imaged with the electron beam projected along the [110] zone axis, and the fast Fourier transform (FFT) patterns further confirmed the orientation and single-crystalline nature of each domain. Exposed facets with Miller indices of {100} and {111} were observed on relatively flat local regions, whereas at surfaces with convex or concave curvatures, a series of high-index facets with high densities of atomic steps and kinks were observed. The orientation of the high-index facets appeared to be highly localized and essentially defined by the local surface curvature. Although the overall characteristic dimensions of the nanopores and protrusions on the surfaces of the Au PNPs were much larger than 5 nm, the surface atomic steps and kinks well-mimicked the local surface structures of the catalytically active sub-5 nm Au nanoparticles. The Au PNPs also exhibited similar density of undercoordinated surface atoms on their surfaces in comparison to the dealloyed porous Au films. It has been reported that the residual Ag plays a key role in stabilizing the stepped and kinked surfaces of the dealloyed porous Au films.[31, 44] In contrast, the Au PNPs were monometallic in nature with no residual Ag present on their surfaces.

Therefore, the high stability of the atomic steps and kinks on the surfaces of Au PNPs can be interpreted mostly likely as the consequence of the structural integrity of the particles and the surface stabilization by the capping ligand, CTAC.

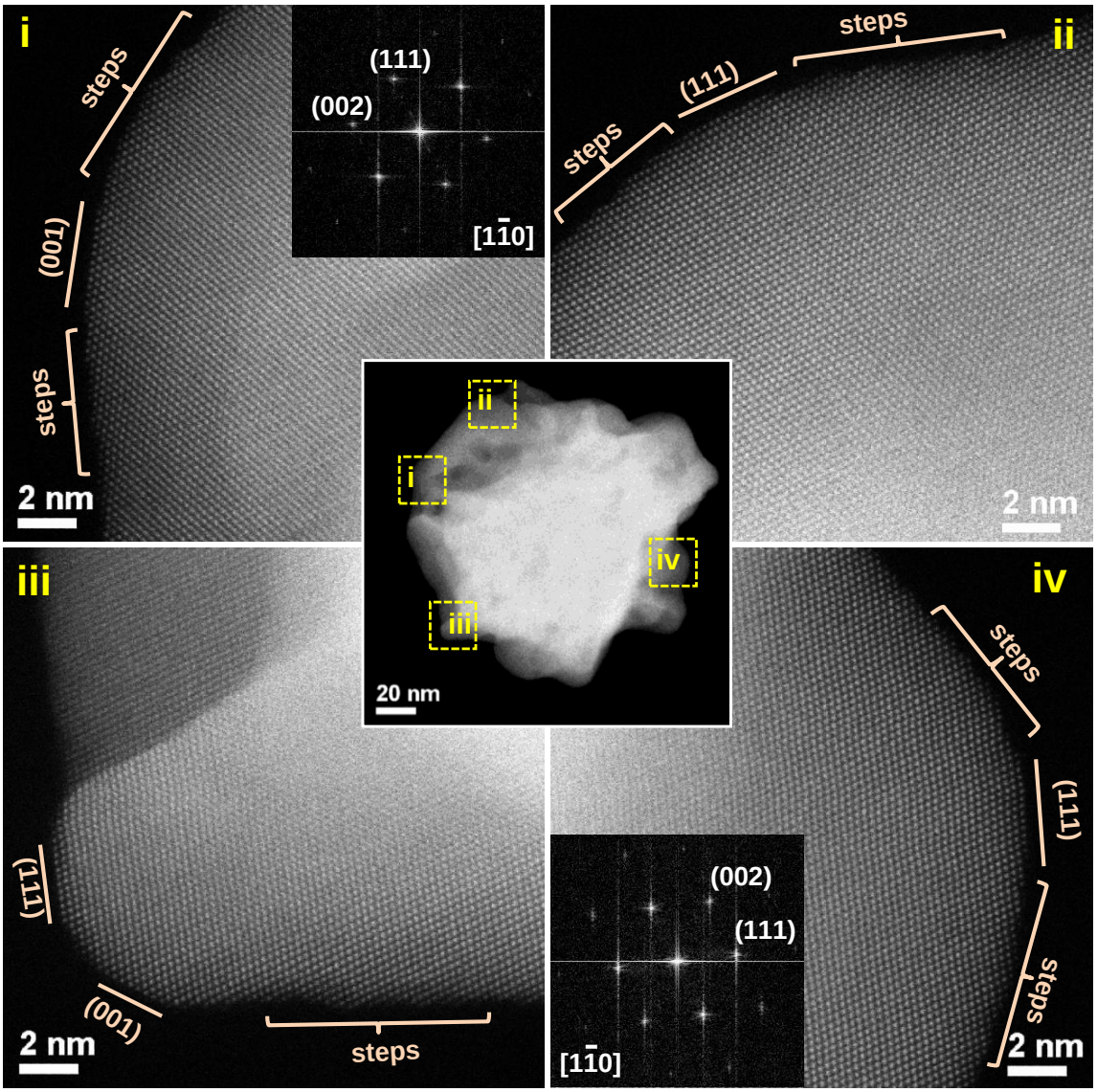

Figure 3.3. Atomic-level surface structures of Au PNPs. The central panel shows the HAADF-STEM image of an individual Au PNP. Panels i, ii, iii and iv show the high-resolution HAADF-STEM images of 4 different regions (i, ii, iii and iv) marked in the central panel. The inset in panel i is the fast Fourier transform (FFT) pattern of the region shown in panel i. The inset in panel iv is the FFT pattern of the region shown in panel iv. The high-resolution HAADF-STEM images were taken with the electron beam projected along the [110] zone axis.

The Au PNPs exhibited extraordinarily robust catalytic activity toward the hydrogenation of 4-nitrophenol by $NaBH_4$. As shown in Figure 3.4A, the Au PNPs could be recycled after the completion of the hydrogenation reaction and their catalytic activity was well-preserved over multiple reaction cycles. The observed robustness of catalytic activity was intimately tied to the structural stability of the Au PNPs. We found that the nanoscale porosity and highly curved surface features of the Au PNPs were both well-preserved after three cycles of hydrogenation reactions (Figure 3.4B and 3.4C). High-resolution HAADF-STEM images showed that after multiple cycles of reactions, the atomic steps and kinks on the surfaces of the Au PNPs were well-preserved and the fraction of the undercoordinated surface atoms was comparable to that of the freshly prepared Au PNPs, indicating the robustness of the surface structures of the Au PNPs during the catalytic reactions. Although surface atomic migration during the reactions cannot be completely ruled out, such dynamic surface restructuring apparently did not result in the loss of the undercoordinated, catalytically active surface atoms. Since the plasmon resonance frequencies and extinction spectral lineshapes were sensitive to both the overall particle size and the surface morphologies of the Au PNPs,[42] optical extinction spectroscopy was also used to track the structural changes of Au PNPs during the catalytic reactions. Extinction spectra of colloidal suspensions of freshly prepared Au PNPs and the Au PNPs collected after one, two, and three cycles of reactions showed almost identical spectral features, further verifying lack of morphological or structural changes of the Au PNPs during the catalytic hydrogenation reactions.

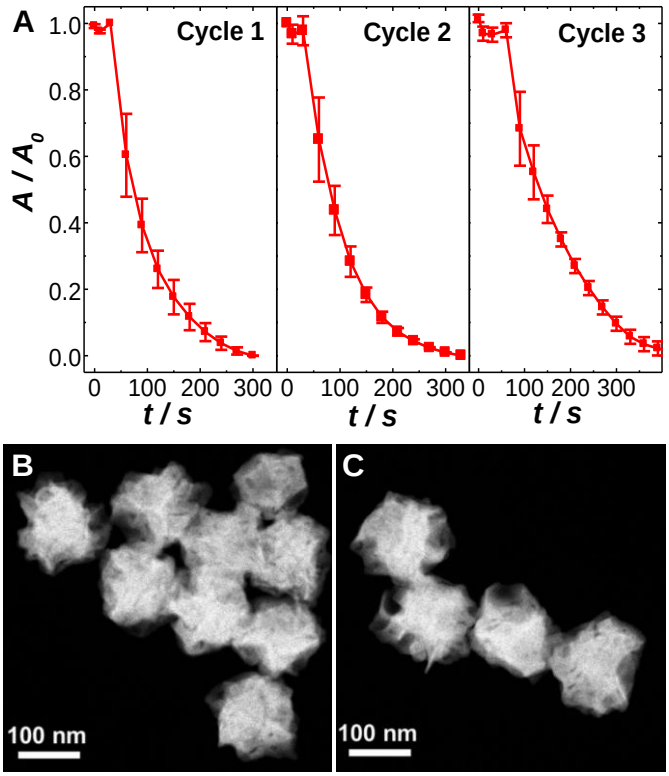

Figure 3.4. Robustness of the catalytic activities of Au PNPs. (A) Absorption (normalized against the initial point) at λ = 400 nm as a function of reaction time over three reaction cycles. In each cycle, the initial concentrations of p-NP and NaBH4 were 66.7 μM and 16.7 mM, respectively. The concentrations of the Au PNPs was 3.0×10^{8} particles mL^{-1}. The error bars represent the standard deviations obtained from five experimental runs. HAADF-STEM images of Au PNPs (B) before reactions and (C) after 3 cycles of catalytic reactions.

The catalytic hydrogenation of p-nitrophenol is a model reaction that has been widely used for the evaluation of catalytic activities of noble metal nanoparticles.[19] It is known that the catalytic hydrogenation of p-nitrophenol by borohydride is a multistep process.[19] Borohydride ions first interact with the metallic nanoparticle surfaces and transfer an active hydrogen species to the particle surface to form metal hydrides. Once p-nitrophenol molecules are adsorbed onto the surface of the nanoparticles, reduction of p-nitrophenol is induced by the surface hydrogen species. The final step of the catalytic cycle is desorption of the product, p-aminophenol, from the nanoparticle surfaces. It is worth mentioning that the overall reaction kinetics measured by solution-phase UV-vis

absorption spectroscopy depends on the structures and surface properties of the nanocatalysts. Esumi et al.[50] investigated the catalytic activity of bulky dendrimer-stabilized metal nanoparticles and concluded that the reaction was diffusion controlled, whereas Ballauff and coworkers showed that the surface reaction became the rate limiting step when polymer-supported small Au nanoparticles were used as the catalysts.[48, 49] Assuming that the diffusion of the reactants to the nanocatalysts and all the adsorption/desorption steps are much faster than the surface catalyzed reaction step, the catalytic hydrogenation reaction is expected to obey pseudo-first order reaction kinetics in the presence of excessive borohydride and the analysis of the kinetic data can be done using the Langmuir-Hinshelwood (LH) model.[19,48,49] As shown in Figure 3.5A, the hydrogenation of p-nitrophenol started after a certain period of induction time and followed a first-order rate law at the early stage of the reaction in the presence of excessive borohydride. An apparent initial rate constant was obtained through least square fitting of the linear part of the curves using the following equation:

$$-\ln(\frac{A}{A_0})=k_0\times(t-t_0) \qquad (1),$$

where A is absorption intensity at 400 nm at particular time spots during the reaction, A_0 is absorption intensity at 400 nm before the reaction started, t is the reaction time, t_0 is the induction time, and k_0 is apparent initial rate constant.

It is interesting that at later stages of the reaction, significant deviation from the first order rate law was observed, and the apparent rate constant became larger as the concentration of p-nitrophenol further went down. We hypothesized that the reaction might follow altered pathways at the later stages of the reaction when the coverage of p-nitrophenol on the surfaces of the Au PNPs became low. The UV-vis spectroscopy results

shown in Figure 3.5A, unfortunately, did not provide further mechanistic insights into the possible reaction pathways.

The reaction kinetics was also found to be sensitively dependent on the concentration of Au PNPs when fixed amounts of p-nitrophenol and borohydride were introduced. As shown in Figure 3.5B and 3.5C, the rate constant increased with a concomitant decrease in the induction time as the concentration of Au PNPs increased. The acceleration of the reaction at high Au PNP concentrations can be interpreted as a result of increased total surface areas available for catalysis. If we assume that the overall kinetics measured by UV-vis spectroscopy truly reflects the intrinsic kinetics of the surface reactions, the rate constant is expected to be proportional to the total surface area, or the concentration of Au PNPs based on the following equation:

$$-\frac{dC(t)}{dt}) = k_0 \times C(t) = k^* \times S \times C(t) \qquad (2),$$

where $C(t)$ is the concentration of p-nitrophenol at time t, k_0 is the initial rate constant, S is the total surface area of Au PNPs, and k^* is the rate constant normalized to S. However, the plots of k_0 *vs.* particle concentration (C_{PNPs}) showed significant deviation from a linear relationship, strongly indicating that the overall kinetics was not only determined by the surface-catalyzed molecular transformation but also further complicated by the molecular diffusion processes and the interactions between the molecules and Au PNPs. UV-vis absorption spectroscopy is only capable of measuring the overall reaction kinetics that involves multiple steps including the diffusion and surface adsorption of the reactants, the surface catalyzed reactions, and the desorption of the final products, and thus does not necessarily provide the information about the intrinsic kinetics and detailed mechanisms of the surface reactions. This inspired us to

gain more detailed, quantitative insights into the intrinsic kinetics and mechanisms of the surface catalyzed reactions through time-resolved SERS measurements.

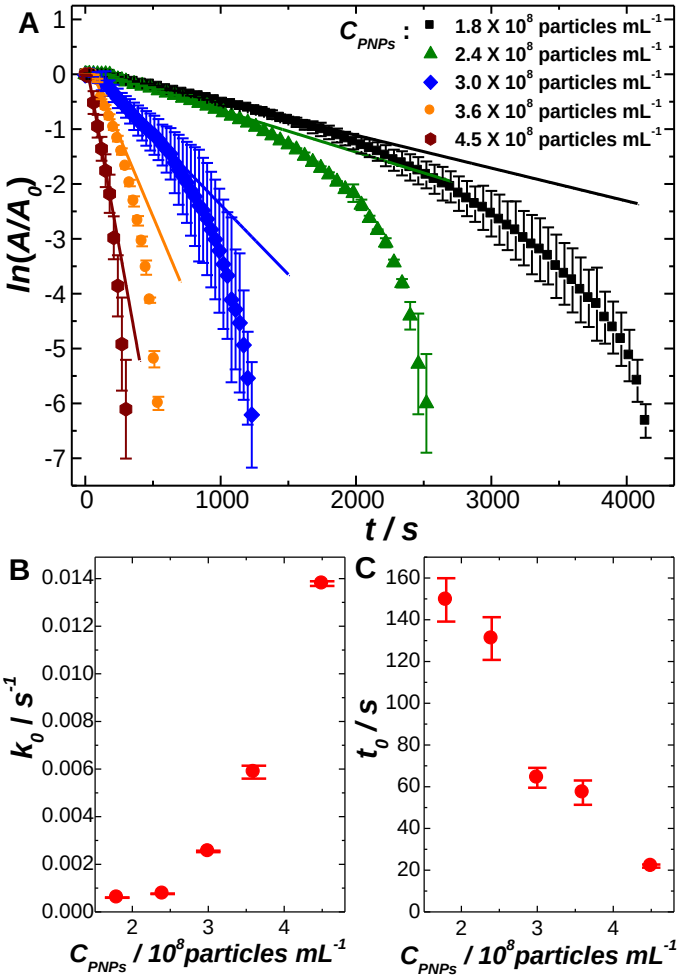

Figure 3.5. Kinetics of hydrogenation of 4-NP by $NaBH_4$ catalyzed by Au PNPs at different particle concentrations. (A) Natural logarithms of absorption (normalized against the initial point) at λ = 400 nm as a function of reaction time at different particle concentrations as labeled in the figures. The solid lines show the least square results to the linear part of the curves at the early stage of the reactions. Plots of (B) the initial rate constant (k_0) and (C) induction time (t_0) as a function of particle concentration (C_{PNPs}).

In addition to their superior catalytic properties, Au PNPs also possess unique plasmonic properties highly desirable for single-particle SERS.[42] Although the overall particle sizes were similar, the localized plasmon resonance of the PNPs exhibited significant spectral red-shift in comparison to that of the QSNPs, and was tuned to be

resonant with the near-infrared excitation laser (λ_{exc} = 785 nm) for SERS measurements. Drastically stronger Raman enhancements were observed from self-assembled monolayers (SMAs) of 4-nitrothiophenol (4-NTP) molecules adsorbed on colloidal Au PNPs than on the Au QSNPs. We have previously demonstrated both experimentally and theoretically that the Raman enhancements of 4-aminothiophenol (4-ATP) adsorbed on individual subwavelength Au PNPs are more than two orders of magnitude higher than those on Au QSNPs of the same overall particle sizes, approaching enhancement factors on the order of 10^6 when the plasmon is on resonance with the excitation laser.[42] Previously published results of finite-difference time-domain (FDTD) calculations[42] showed that the near-field "hot-spots" for SERS were located precisely at the catalytically active, highly curved particle surfaces of the Au PNPs, providing a unique platform for the monitoring of surface-catalyzed molecular transformations by SERS.

To monitor the kinetics of the hydrogenation reaction using SERS, we immobilized a saturated SAM of 4-NTP onto the surfaces of Au PNPs through Au-thiol interactions. A confocal Raman microscope was used for the SERS measurements with the laser beam focused into a small volume (~ 100 pL) of the colloidal suspensions of 4-NTP-coated Au PNPs. In this confocal mode, each freely-diffusing Au PNP was exposed to the excitation laser for a short time period (within the diffusion time), effectively eliminating possible photo-reactions of 4-NTP[51] and photo-induced damage of the samples. As shown in Figure 3.6A, 4-NTP had three characteristic vibrational bands in the SERS spectrum at 1080, 1338, and 1571 cm^{-1}, corresponding to C-S stretching (ν_{CS}), O-N-O stretching (ν_{NO}), and the phenol-ring modes, respectively.[52] Upon exposure to 30 mM $NaBH_4$, there was an induction time of ~ 100 s during which the SERS features of 4-NTP remained

unchanged. Because the 4-NTP molecules were pre-adsorbed on the surfaces of Au PNPs, this induction time was apparently not related to the diffusion and adsorption of the 4-NTP and was thus mostly likely due to the interactions of borohydride ions with the Au surfaces through which active surface hydrogen species were generated. Only when the concentration of the surface hydrogen species was built up to a certain threshold value can the catalytic hydrogenation of the surface-adsorbed 4-NTP be initiated. Once the hydrogenation reaction started, the intensities of both 1338 cm^{-1} and 1571 cm^{-1} Raman bands were observed to decrease progressively with the concomitant emergence of a new band corresponding to the phenol-ring modes (ν_{CC}) of 4-ATP at 1590 cm^{-1}.[53] All the vibrational modes observed in SERS correlate well with the bands in normal Raman spectra of 4-NTP and 4-ATP.[36] Interestingly, at the intermediate stages of the reaction, Raman modes at 1140, 1388, and 1438 cm^{-1}, which could be assigned to the characteristic vibrational modes of 4,4´-dimercaptoazobenzene (DMAB),[54, 55] were clearly resolved, allowing us to identify DMAB as the intermediate along the reaction pathway. We also found that while the SAMs of 4-NTP and DMAB were stable on the surfaces of Au PNPs, the final product, 4-ATP, dissociated from the Au PNP surfaces in the presence of excessive $NaBH_4$, as the characteristic peaks of the ν_{CS} (1080 cm^{-1}) and ν_{CC} (1590 cm^{-1}) modes of 4-ATP both gradually decreased in intensity upon the completion of the hydrogenation reaction. It has been recently reported that $NaBH_4$ induces desorption of small organothiol molecules from Au nanoparticle surfaces predominantly through organothiol displacement by hydride.[56, 57] The SAMs of 4-NTP and DMAB appeared to be more robust against $NaBH_4$-induced desorption than those of 4-ATP mostly likely due to the fact that 4-NTP and DMAB have delocalized electrons distributed over larger

conjugation systems than 4-ATP, which may optimize the charge distribution and thus enhance the stability of the surface-adsorbed molecules.[57] The evolution of the peak intensities of the ν_{NO} mode (1338 cm^{-1}) of 4-NTP, the $\nu_{NN} + \nu_{CC} + \beta_{CH}$ mode (1432 cm^{-1}) mode of DMAB, the ν_{CC} mode (1590 cm^{-1}) of 4-ATP, and the ν_{CS} mode (1080 cm^{-1}) as a function of reaction time was shown in Figure 3.6B. Based on the SERS results, a possible reaction mechanism was proposed and schematically illustrated in Figure 3.6C. The entire catalytic hydrogenation reaction may involve four key steps: (1) generation of surface-hydrogen species through interactions between borohydride ions and metal surfaces, which gave rise to the induction time; (2) reduction of surface-adsorbed 4-NTP by the surface-hydrogen species to form the intermediate, DMAB; (3) further reduction of DMAB into the final product, 4-ATP; and (4) desorption of 4-ATP from the metallic surfaces.

To further confirm the $NaBH_4$-induced desorption of 4-ATP from the surfaces of Au PNPs, we first saturated the surfaces of Au PNPs with 4-ATP SAMs and then exposed the 4-ATP-coated PNPs to 20 mM $NaBH_4$. The $NaBH_4$-induced 4-ATP desorption could be monitored in real time using SERS, as shown in Figure 3.7A. The stability of the 4-ATP was found to be highly dependent on the surface curvature of the Au nanoparticles. 4-ATP SAMs formed on Au trisoctahedral (TOH) and elongated tetrahexahedral (ETHH) nanoparticles were much more stable than those on the Au PNPs with almost no detectable desorption when exposed to 20 mM $NaBH_4$ (Figure 3.7B). Although both Au TOH and ETHH nanoparticles were also enclosed by catalytically active high index facets ({221} for TOH[58] and {730} for ETHH particles[59]), their surfaces were relatively flat in comparison to the highly curved surfaces of Au PNPs. The nanoscale curvature of

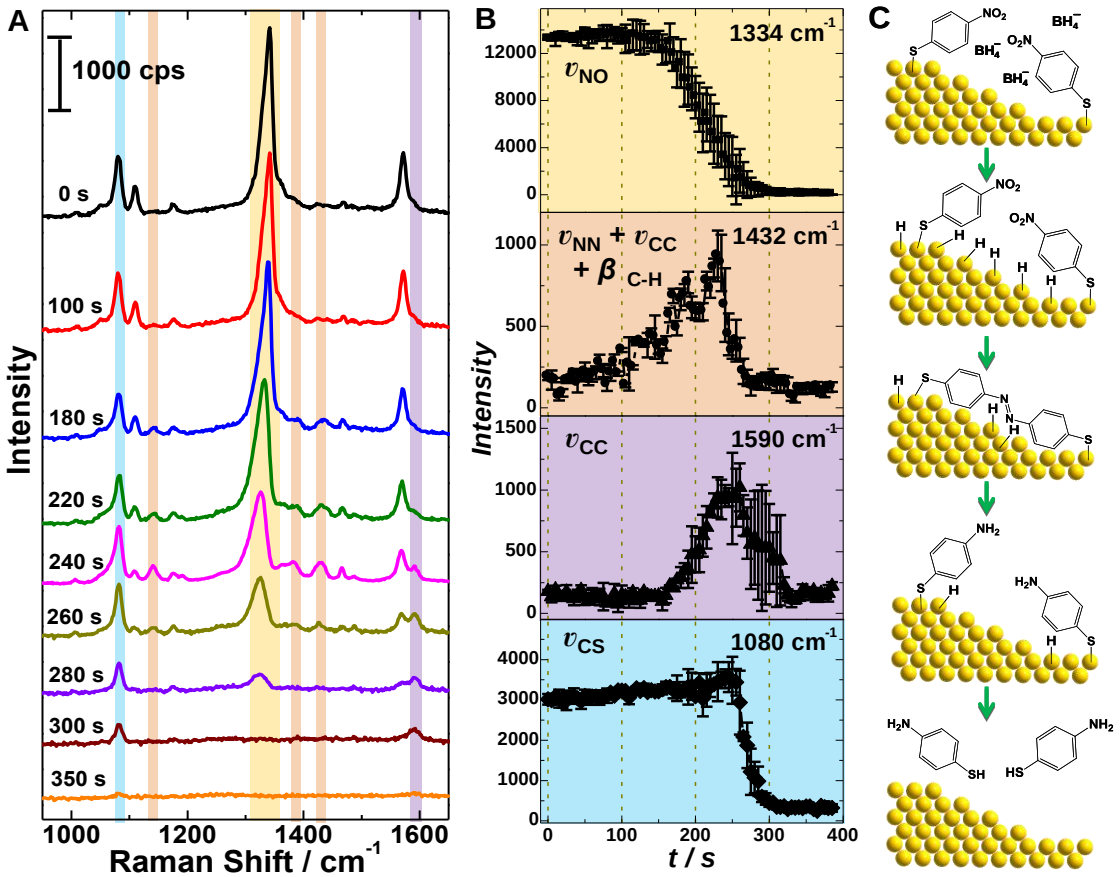

Figure 3.6. Time-resolved SERS measurements of the Au PNP-catalyzed hydrogenation of 4-NTP. (A) SERS spectra collected from SAMs of 4-NTP molecules on the surfaces of Au PNPs at different reaction times of 0, 180, 220, 240, 260, 280, 300, and 350 s after exposure to 30 mM $NaBH_4$. (B) The intensities of Raman peaks at 1334 cm^{-1}, 1080 cm^{-1}, 1432 cm^{-1}, and 1590 cm^{-1} as a function of reaction time. The error bars represent the standard deviations obtained from five experimental runs. (C) Schematic illustration of the surface-adsorption of BH_4^-, the hydrogenation of surface-adsorbed 4-NTP (reactant) to DMAB (intermediate), and finally to 4-ATP (product), and the subsequent $NaBH_4$-induced desorption of 4-ATP from the surfaces of Au PNPs.

the Au PNP surfaces may decrease the stability of the 4-ATP SAMs, which makes the surface-adsorbed 4-ATP more vulnerable to $NaBH_4$. This is in line with previous observation that SAMs of organothiols were more stable on the surfaces of larger Au nanoparticles than on smaller Au nanoparticles.[57] As shown in Figure 3.7C, the kinetics of the 4-ATP desorption was also dependent on the concentration of $NaBH_4$. Higher $NaBH_4$ concentration resulted in faster desorption kinetics. Similar to the catalytic

hydrogenation reaction, an induction time was also observed during the $NaBH_4$-induced 4-ATP desorption, which became shorter as the concentration of $NaBH_4$ increased.

We chose the O-N-O stretching (ν_{NO}) mode of 4-NTP at 1338 cm^{-1} to quantify the fraction of reactant at various reaction times, based on which the kinetics of the reactant consumption was analyzed (Figures 3.8A). In our SERS measurements, $NaBH_4$ was in excess and its concentration remained constant throughout the entire reaction process. Therefore, this surface reaction obeyed pseudo-first-order kinetics and the rate constants could be determined by performing least square curve fitting to the reaction trajectories shown in Figures 3.8A using the following rate equation:

$$-\ln(\frac{I}{I_0})=k_{app}\times(t-t_0) \qquad (3),$$

where I is intensity of ν_{NO} mode at particular time spots during the reaction, I_0 is intensity of ν_{NO} mode before the reaction started, t is the reaction time, t_0 is the induction time, and k_{app} is apparent first order rate constant.

The kinetic curves obtained through SERS measurements (Figure 3.8A) exhibited two remarkable features that were strikingly different from the solution-phase UV-vis spectroscopy results shown in Figure 3.5. First, the reactions obeyed the first order rate law throughout the entire reaction process until the depletion of 4-NTP. Second, both the apparent rate constant and the induction time were independent on the concentration of Au PNPs (Figure 3.8B and 3.8C). These features strongly indicate that performing SERS measurements on pre-adsorbed reactants allows one to resolve the intrinsic kinetics of the surface-catalyzed reactions with minimal interference from the diffusion, adsorption, and desorption of the reactants and products.

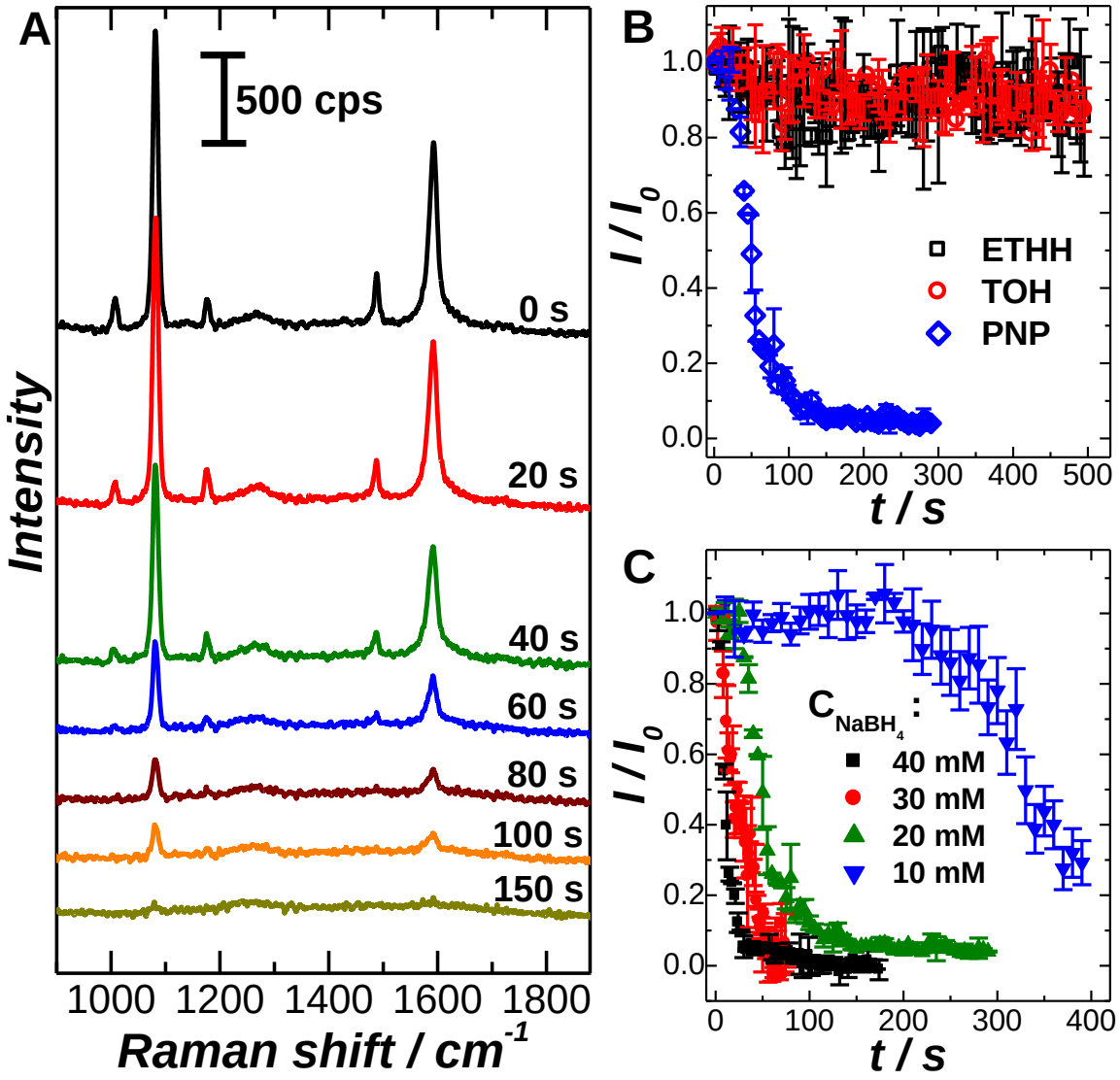

Figure 3.7. $NaBH_4$-induced desorption of 4-ATP from the surfaces of Au PNPs. (A) SERS spectra collected from 4-ATP molecules adsorbed on the surfaces of Au PNPs at different reaction times of 0, 20, 40, 60, 80, 100, and 150 s after exposure to 20 mM $NaBH_4$. (B) Raman intensities at 1080 cm^{-1} (normalized against the initial point) as a function of time for SAMs of 4-ATP adsorbed on the surfaces of Au PNPs, Au elongated tetrahexahedral (ETHH) nanoparticles, and Au trisoctahedral (TOH) nanoparticles exposed to 20 mM $NaBH_4$. (C) Raman intensities at 1080 cm^{-1} (normalized against the initial point) as a function of time for SAMs of 4-ATP adsorbed on the surfaces of Au PNPs upon exposure to 10, 20, 30, and 40 mM $NaBH_4$. The error bars in Panels B and C represent the standard deviations obtained from five experimental runs.

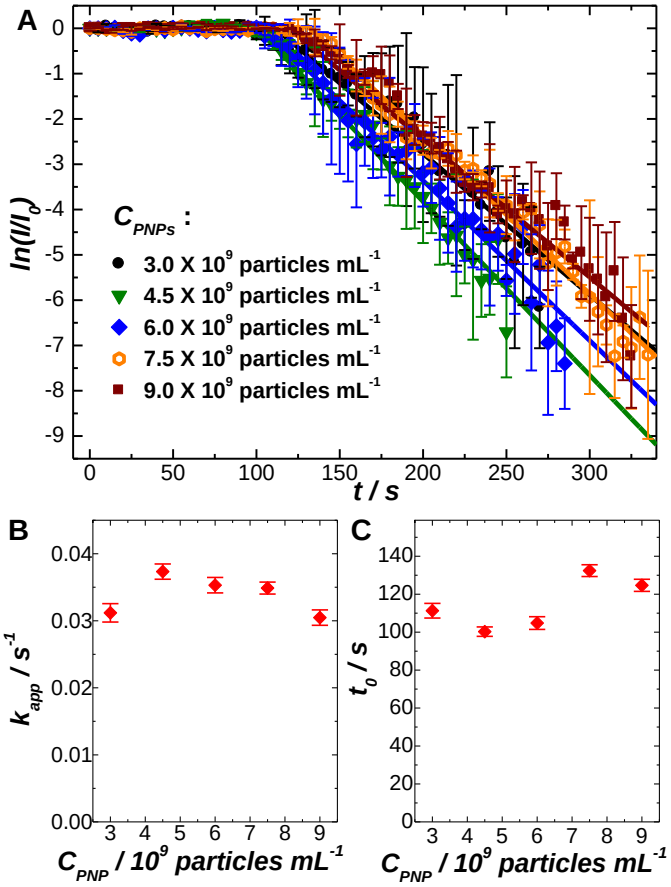

Figure 3.8. Effects of Au PNP concentrations on the kinetics of hydrogenation of surface-adsorbed 4-NTP SAMs. (A) Natural logarithms of Raman intensity at 1334 cm^{-1} (normalized against the initial point) as a function of time upon exposure to 30 mM $NaBH_4$ in the presence of various concentrations of Au PNPs as labeled in the figure. The error bars represent the standard deviations obtained from five experimental runs. (B) The apparent rate constant (k_{app}) and (C) induction time (t_0) as a function of Au PNP concentration (C_{PNP}).

Assuming that the surface-catalyzed hydrogenation is an elementary reaction between the surface-adsorbed BH_4^- and 4-NTP, the apparent rate constant can be described as:

$$k_{app} = k \times S \times \theta_{4-NTP} \times \theta_{BH_4^-} = a \times \theta_{BH_4^-} \qquad (4),$$

where $\theta_{4\text{-}NTP}$ and $\theta_{BH_4^-}$ are the relatively degree of surface coverage by 4-NTP and BH_4^-, respectively, k is the molar rate constant per unit surface area, S is the surface area of the Au PNPs, and a is a fractional constant. Since a saturated SAM of 4-NTP was pre-adsorbed on the surfaces of Au PNPs, $\theta_{4\text{-}NTP}$ was a constant and k_{app} became proportional

to $\theta_{BH_4^-}$. In Figure 3.9A, we show the kinetic curves obtained from time-resolved SERS measurements in the presence of various concentrations of $NaBH_4$. The k_{app} and t_0 values as a function of $NaBH_4$ concentrations (C_{NaBH_4}) were plotted in Figure 3.9B and 3.9C, respectively. The k_{app} progressively increased while t_0 decreased as C_{NaBH_4} increased until reaching a plateau at C_{NaBH_4} above 120 mM. We performed least square curve fitting using the Langmuir adsorption isotherm (Equation 5) and Hill equation (Equation 6), respectively.

$$k_{app} = a \times \theta_{BH_4^-} = a \times \frac{\alpha \times C_{NaBH_4}}{1 + \alpha \times C_{NaBH_4}} \qquad (5),$$

$$k_{app} = a \times \theta_{BH_4^-} = a \times \frac{C_{NaBH_4}^n}{K_a + C_{NaBH_4}^n} \qquad (6),$$

where α and Ka are two constants describing the binding affinities between the molecules and substrates and n is the Hill coefficient rated to the adsorption cooperativity. The major difference between these two models is that Hill equation includes the cooperativity of molecular adsorption whereas the Langmuir monolayer adsorption model does not consider the adsorption cooperativity. The best fitting results obtained using these two models were shown as the solid and dash curves in Figure 3.9B. It is apparent that the Hill equation gave us much better fit to the experimental results than the Langmuir adsorption isotherm. Previous studies showed that the adsorption of $NaBH_4$ onto the polymer-supported ~ 2nm Au nanoparticles followed the Langmuir adsorption isotherm.[48, 49] However, our results strongly indicate that the adsorption of $NaBH_4$ onto the surfaces of Au PNPs was highly cooperative because the least square curve fitting gave a Hill coefficient (n) of 2.35 ± 0.23, which was much larger than 1. The surface structures of the Au PNPs were fundamentally different from the sub-5 nm Au

nanoparticles. While each sub-5 nm Au nanoparticle only has limited surface areas accessible to adsorbate molecules, the total surface area of each subwavelength PNP is much larger and may thus accommodate much larger numbers of molecules. The local curvature of the PNPs surfaces may also facilitate the cooperative binding of adsorbate molecules onto the Au surfaces. Although the origin of such adsorption cooperativity still remains unclear, our results clearly indicate that BH_4^- adsorbs onto the nanoporous Au surfaces in a highly cooperative manner.

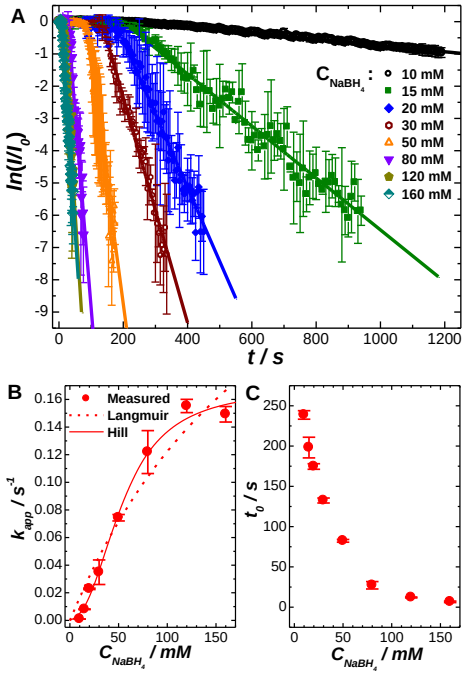

Figure 3.9. Effects of $NaBH_4$ concentrations on the kinetics of hydrogenation of 4-NTP SAMs adsorbed on Au PNPs. (A) Natural logarithms of Raman intensity at 1334 cm^{-1} (normalized against the initial point) as a function of time upon exposure to various concentrations of $NaBH_4$ as labeled in the figure. The error bars represent the standard deviations obtained from five experimental runs. (B) The apparent rate constant (k_{app}) and (C) induction time (t_0) as a function of $NaBH_4$ concentration (C_{NaBH4}).

We have further performed SERS measurements to study the effects of 4-NTP surface coverage on the reaction kinetics. The surface coverage of 4-NTP could be fine-controlled by adjusting the concentration of 4-NTP incubated with Au PNPs (Figure 3.10A). Interestingly, the adsorption of 4-NTP on the surfaces of Au PNPs was also

found to be cooperative and followed the Hill equation very well with a Hill coefficient of 2.31 $\pm$ 0.32, which was extremely similar to that of $NaBH_4$. Although the cooperative adsorption on the Au PNP surfaces appeared to be general for various adsorbate molecules, whether the cooperative adsorption is a unique feature of the nanoporous surface structures still remains an open question at this stage. In Figure 3.10B, we show the spectral evolution of 4-NTP adsorbed on Au PNPs at a nominal $\theta_{4\text{-}NTP}$ of 47% during the catalytic hydrogenation reaction. At this unsaturated 4-NTP coverage, the surface-adsorbed 4-NTP molecules were more separated from each other in comparison to the saturated coverage, and thus the formation of DMAB, which required two 4-NTP molecules in close proximity to each other, was suppressed. No spectroscopic features of DMAB were observed in the SERS spectra during the reaction (Figure 3.10B), indicating that the hydrogenation reaction might have switched to an alternative reaction pathway. At low 4-NTP coverages, the catalytic hydrogenation reaction may undergo a direct transformation from 4-NTP to 4-ATP or an altered pathway involving extremely short-lived transient intermediates that are not resolvable by the time-resolved SERS measurements. As shown in Figure 3.10C-E, as the surface coverage of 4-NTP decreased, the rate constant became significantly larger and the induction time became shorter. This can be interpreted as a consequence of larger surface areas available for $NaBH_4$ adsorption when 4-NTP coverage became lower. The SERS results presented here provide quantitative insights into the 4-NTP coverage-dependent reaction kinetics, which can be used to interpret the deviation from the pseudo-first-order kinetics at late stages of the reactions observed by UV-vis spectroscopic measurements (see Figure 3.5).

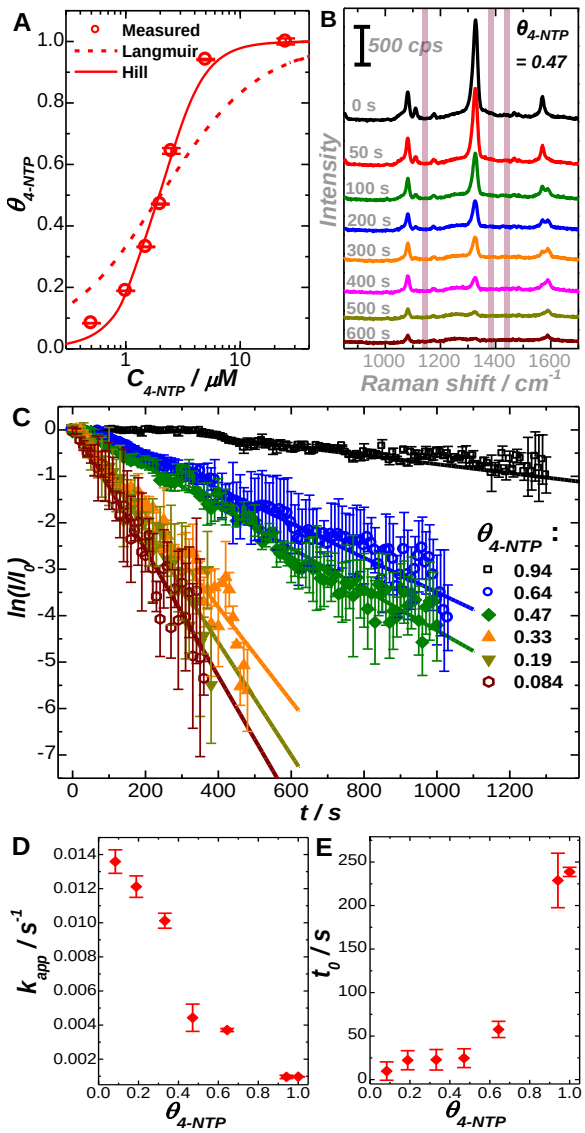

Figure 3.10. Effects of surface-coverage of 4-NTP ($\theta_{4\text{-NTP}}$) on the hydrogenation kinetics. (A) 4-NTP coverages ($\theta_{4\text{-NTP}}$) as a function of 4-NTP concentration ($C_{4\text{-NTP}}$). (B) SERS spectra collected from 4-NTP absorbed on surfaces of Au PNPs (incubated with 4-NTP of 2 μM, $\theta_{4\text{-NTP}}$ = 0.47) at different reaction times of 0, 50, 100, 200, 300, 400, 500, and 600 s upon exposure to 10 mM $NaBH_4$. (C) Natural logarithms of Raman intensity at 1334 cm^{-1} (normalized against the initial point) as a function of time upon exposure to 10 mM $NaBH_4$ in the presence of Au PNPs at a concentration of 7.5×10^9 particles mL^{-1} for different surface-coverages of 4-NTP as labeled in the figure. The error bars represent the standard deviations obtained from five experimental runs. (D) The apparent rate constant (k_{app}) and (E) induction time (t_0) as a function of 4-NTP surface coverage ($\theta_{4\text{-NTP}}$).

3.4 Conclusions

In summary, subwavelength Au PNPs possess highly curved, porous surfaces with high abundance of undercoordinated atoms at the surface steps and kinks, well-mimicking the

catalytically active surfaces of oxide-supported sub-5 nm Au nanoparticles and dealloyed nanoporous Au membranes. The catalytically active surface structures of the Au PNPs were highly robust and the catalytic activity of Au PNPs was well-preserved over multiple cycles of catalytic hydrogenation reactions. The Au PNPs also provide a compositionally simple, free-standing nanocatalyst system that enables direct correlation of catalytic activities with surface structures without complication introduced by the oxide supports and residual less-noble elements. Meanwhile, the nanoscale surface porosity dramatically enhances the tunability of localized plasmon resonances and optimizes the near-field enhancements of the subwavelength particles for single-particle SERS under near-infrared excitations. Using catalytic hydrogenation of 4-NTP as a model reaction, we have demonstrated that the dual functionality of Au PNPs opens up unique opportunities for us to develop detailed, quantitative understanding of the intrinsic kinetics and mechanisms of surface-catalyzed reactions through noninvasive *in situ* SERS measurements. The knowledge gained through this work provides significant new insights on the structure-property relationship of Au nanocatalysts and sheds light on the kinetics and mechanisms of the interfacial molecular transformations catalyzed by nanoarchitectured Au surfaces.

3.5 References

(1) Burda, C.; Chen, X. B.; Narayanan, R.; El-Sayed, M. A., *Chem. Rev.* **2005,** *105*, 1025-1102.

(2) Daniel, M. C.; Astruc, D., *Chem. Rev.* **2004,** *104* , 293-346.

(3) Halas, N. J.; Lal, S.; Chang, W. S.; Link, S.; Nordlander, P., *Chem. Rev.* **2011,** *111*, 3913-3961.

(4) Haruta, M.; Date, M., *Appl. Catal. A-Gen.* **2001,** *222*, 427-437.

(5) Hvolbaek, B.; Janssens, T. V. W.; Clausen, B. S.; Falsig, H.; Christensen, C. H.; Norskov, J. K., *Nano Today* **2007,** *2*, 14-18.

(6) Ishida, T.; Haruta, M., *Angew. Chem.-Int. Edit.* **2007,** *46*, 7154-7156.

(7) Valden, M.; Lai, X.; Goodman, D. W., *Science* **1998,** *281*, 1647-1650.

(8) Hughes, M. D.; Xu, Y. J.; Jenkins, P.; McMorn, P.; Landon, P.; Enache, D. I.; Carley, A. F.; Attard, G. A.; Hutchings, G. J.; King, F.; Stitt, E. H.; Johnston, P.; Griffin, K.; Kiely, C. J., *Nature* **2005,** *437*, 1132-1135.

(9) Schimpf, S.; Lucas, M.; Mohr, C.; Rodemerck, U.; Bruckner, A.; Radnik, J.; Hofmeister, H.; Claus, P., *Catal. Today* **2002,** *72*, 63-78.

(10) Zanella, R.; Louis, C.; Giorgio, S.; Touroude, R., *J. Catal.* **2004,** *223*, 328-339.

(11) Pan, M.; Gong, J. L.; Dong, G. B.; Mullins, C. B., *Accounts Chem. Res.* **2014,** *47*, 750-760.

(12) Chen, M. S.; Goodman, D. W., *Science* **2004,** *306*, 252-255.

(13) Green, I. X.; Tang, W. J.; Neurock, M.; Yates, J. T., *Science* **2011,** *333*, 736-739.

(14) Overbury, S. H.; Schwartz, V.; Mullim, D. R.; Yan, W. F.; Dai, S., *J. Catal.* **2006,** *241*, 56-65.

(15) van Bokhoven, J. A.; Louis, C.; T Miller, J.; Tromp, M.; Safonova, O. V.; Glatzel, P., *Angew. Chem.-Int. Edit.* **2006,** *45*, 4651-4654.

(16) Mavrikakis, M.; Stoltze, P.; Norskov, J. K., *Catal. Lett.* **2000,** *64*, 101-106.

(17) Liu, L. M.; McAllister, B.; Ye, H. Q.; Hu, P., *J. Am. Chem. Soc.* **2006,** *128*, 4017-4022.

(18) Molina, L. M.; Hammer, B., *Phys. Rev. Lett.* **2003,** *90*, 206102.

(19) Herves, P.; Perez-Lorenzo, M.; Liz-Marzan, L. M.; Dzubiella, J.; Lu, Y.; Ballauff, M., *Chem. Soc. Rev.* **2012,** *41*, 5577-5587.

(20) Ma, Z.; Dai, S., *ACS Catal.* **2011,** *1*, 805-818.

(21) Mikami, Y.; Dhakshinamoorthy, A.; Alvaro, M.; Garcia, H., *Catal. Sci. Technol.* **2013,** *3*, 58-69.

(22) Janssens, T. V. W.; Clausen, B. S.; Hvolbaek, B.; Falsig, H.; Christensen, C. H.; Bligaard, T.; Norskov, J. K., *Top. Catal.* **2007,** *44*, 15-26.

(23) Lemire, C.; Meyer, R.; Shaikhutdinov, S.; Freund, H. J., *Angew. Chem.-Int. Edit.* **2004,** *43*, 118-121.

(24) Yim, W. L.; Nowitzki, T.; Necke, M.; Schnars, H.; Nickut, P.; Biener, J.; Biener, M. M.; Zielasek, V.; Al-Shamery, K.; Kluner, T.; Baumer, M., *J. Phys. Chem. C* **2007,** *111*, 445-451.

(25) Wittstock, A.; Baumer, M., *Accounts Chem. Res.* **2014,** *47*, 731-739.

(26) Wittstock, A.; Zielasek, V.; Biener, J.; Friend, C. M.; Baumer, M., *Science* **2010,** *327*, 319-322.

(27) Xu, C. X.; Su, J. X.; Xu, X. H.; Liu, P. P.; Zhao, H. J.; Tian, F.; Ding, Y., Low *J. Am. Chem. Soc.* **2007,** *129*, 42-43.

(28) Asao, N.; Ishikawa, Y.; Hatakeyama, N.; Menggenbateer; Yamamoto, Y.; Chen, M. W.; Zhang, W.; Inoue, A., *Angew. Chem.-Int. Edit.* **2010,** *49*, 10093-10095.

(29) Zielasek, V.; Jurgens, B.; Schulz, C.; Biener, J.; Biener, M. M.; Hamza, A. V.; Baumer, M., *Angew. Chem.-Int. Edit.* **2006,** *45*, 8241-8244.

(30) Ding, Y.; Chen, M. W., *MRS Bull.* **2009,** *34*, 569-576.

(31) Fujita, T.; Guan, P. F.; McKenna, K.; Lang, X. Y.; Hirata, A.; Zhang, L.; Tokunaga, T.; Arai, S.; Yamamoto, Y.; Tanaka, N.; Ishikawa, Y.; Asao, N.; Erlebacher, J.; Chen, M. W., *Nat. Mater.* **2012,** *11*, 775-780.

(32) Heck, K. N.; Janesko, B. G.; Scuseria, G. E.; Halas, N. J.; Wong, M. S., *J. Am. Chem. Soc.* **2008,** *130*, 16592-16600.

(33) Joseph, V.; Engelbrekt, C.; Zhang, J. D.; Gernert, U.; Ulstrup, J.; Kneipp, J., *Angew. Chem.-Int. Edit.* **2012,** *51*, 7592-7596.

(34) Xie, W.; Herrmann, C.; Kompe, K.; Haase, M.; Schlucker, S., *J. Am. Chem. Soc.* **2011,** *133*, 19302-19305.

(35) Xie, W.; Walkenfort, B.; Schlucker, S., *J. Am. Chem. Soc.* **2013,** *135*, 1657-1660.

(36) Jing, H.; Zhang, Q. F.; Large, N.; Yu, C. M.; Blom, D. A.; Nordlander, P.; Wang, H., *Nano Lett.* **2014,** *14*, 3674-3682.

(37) Liu, R.; Liu, J. F.; Zhang, Z. M.; Zhang, L. Q.; Sun, J. F.; Sun, M. T.; Jiang, G. B., *J. Phys. Chem. Lett.* **2014,** *5*, 969-975.

(38) Huang, J. F.; Zhu, Y. H.; Lin, M.; Wang, Q. X.; Zhao, L.; Yang, Y.; Yao, K. X.; Han, Y., Site-Specific. *J. Am. Chem. Soc.* **2013,** *135*, 8552-8561.

(39) Campion, A.; Kambhampati, P., *Chem. Soc. Rev.* **1998,** *27*, 241-250.

(40) Willets, K. A.; Van Duyne, R. P., Annual Reviews: Palo Alto, 2007; Vol. 58, pp 267-297.

(41) Kneipp, K.; Kneipp, H.; Itzkan, I.; Dasari, R. R.; Feld, M. S., *Chem. Rev.* **1999,** *99*, 2957-2976.

(42) Zhang, Q. F.; Large, N.; Nordlander, P.; Wang, H., *J. Phys. Chem. Lett.* **2014,** *5*, 370-374.

(43) Erlebacher, J.; Aziz, M. J.; Karma, A.; Dimitrov, N.; Sieradzki, K., *Nature* **2001,** *410*, 450-453.

(44) Fujita, T.; Tokunaga, T.; Zhang, L.; Li, D. W.; Chen, L. Y.; Arai, S.; Yamamoto, Y.; Hirata, A.; Tanaka, N.; Ding, Y.; Chen, M. W*Nano Letters* **2014,** *14*, 1172-1177.

(45) Zhang, L.; Chen, L. Y.; Liu, H. W.; Hou, Y.; Hirata, A.; Fujita, T.; Chen, M. W., *J. Phys. Chem. C* **2011,** *115*, 19583-19587.

(46) Sarkar, S.; Sinha, A. K.; Pradhan, M.; Basu, M.; Negishi, Y.; Pal, T., *J. Phys. Chem. C* **2011,** *115*, 1659-1673.

(47) Zeng, J.; Zhang, Q.; Chen, J. Y.; Xia, Y. N., *Nano Letters* **2010,** *10*, 30-35.

(48) Wunder, S.; Polzer, F.; Lu, Y.; Mei, Y.; Ballauff, M., *J. Phys. Chem. C* **2010,** *114*, 8814-8820.

(49) Wunder, S.; Lu, Y.; Albrecht, M.; Ballauff, M., *ACS Catal.* **2011,** *1*, 908-916.

(50) Esumi, K.; Isono, R.; Yoshimura, T., *Langmuir* **2004,** *20*, 237-243.

(51) Sun, M. T.; Xu, H. X., *Small* **2012,** *8*, 2777-2786.

(52) Huang, Y. F.; Zhu, H. P.; Liu, G. K.; Wu, D. Y.; Ren, B.; Tian, Z. Q., When the *J. Am. Chem. Soc.* **2010,** *132*, 9244-9246.

(53) Dong, B.; Fang, Y. R.; Chen, X. W.; Xu, H. X.; Sun, M. T., *Langmuir* **2011,** *27*, 10677-10682.

(54) Huang, Y. F.; Wu, D. Y.; Zhu, H. P.; Zhao, L. B.; Liu, G. K.; Ren, B.; Tian, Z. Q., *Physical Chemistry Chemical Physics* **2012,** *14*, 8485-8497.

(55) Ansar, S. M.; Arneer, F. S.; Hu, W. F.; Zou, S. L.; Pittman, C. U.; Zhang, D. M., *Nano Letters* **2013,** *13*, 1226-1229.

(56) Ansar, S. M.; Perera, G. S.; Jiang, D. P.; Holler, R. A.; Zhang, D. M., *J. Phys. Chem. C* **2013,** *117*, 8793-8798.

(57) Ma, Y. Y.; Kuang, Q.; Jiang, Z. Y.; Xie, Z. X.; Huang, R. B.; Zheng, L. S., *Angew. Chem.-Int. Edit.* **2008,** *47*, 8901-8904.

(58) Ming, T.; Feng, W.; Tang, Q.; Wang, F.; Sun, L. D.; Wang, J. F.; Yan, C. H., *J. Am. Chem. Soc.* **2009,** *131*, 16350-16351.

(59) Ye, X. C.; Zheng, C.; Chen, J.; Gao, Y. Z.; Murray, C. B., *Nano Lett.* **2013,** *13*, 765-771.

CHAPTER 4

Gold Nanoparticles with Tipped Surface Structures as Substrates for Single-Particle Surface-Enhanced Raman Spectroscopy: Concave Nanocubes, Nanotrisoctahedra, and Nanostars

---

4.1 Introduction

Surface-enhanced Raman scattering (SERS) is an ultrasensitive vibrational spectroscopic technique capable of providing detailed structural information of the molecules on or in the vicinity of nanostructured metallic surfaces.[1-4] As a powerful, noninvasive spectroscopic tool for the detection of low-abundance analytes, SERS plays pivotal roles in food safety inspection,[5, 6] environmental monitoring,[7] and biomolecular sensing.[8-11] By combining plasmonic metallic nanoparticles with molecular Raman reporters, multifunctional SERS nanoprobes, or SERS tags, have been developed to target specific biomolecules both *in vitro* and *in vivo*, enabling Raman-based optical bioimaging with high spatial resolution and excellent photostability.[12-16] SERS is essentially a nanoscale effect directly related to the intense electromagnetic field enhancements generated at nanostructured metallic surfaces upon the excitation of localized surface plasmon resonances (LSPRs).[1, 2, 17] Due to strong plasmonic coupling effects,[18] aggregated or self-assembled metallic nanoparticles possess "hot spots" for SERS inside the sub-10 nm interparticle gaps with gigantic field enhancements several orders of magnitude higher than those commonly achievable on the individual nanoparticles.[18-22] Although it is possible to detect the Raman signals of just a few or even single molecules inside the tiny interparticle junctions,[23-26] these hot spots only account for a small portion of the total surface areas accessible by the analyte molecules, resulting in huge heterogeneity and poor reproducibility of Raman signals across the entire substrates.[27] The challenges associated with precise control over the spatial distribution, enhancement magnitude, and structural robustness of the interstitial hot spots limit the utilization of the nanoparticle aggregates as reliable and reproducible SERS substrates for sensing and imaging

applications. For *in vivo* bioimaging, it is also highly desirable to use individual plasmonic nanoparticles uniformly appended with Raman reporters as the SERS tags rather than using the nanoparticle aggregates.[28-30] Therefore, single-particle SERS (spSERS) represents a more promising approach to SERS-based sensing and imaging with optimizable signal amplification and reproducibility in comparison to those strategies relying on the nanoscale interparticle junctions.

The plasmonic field enhancements of individual nanoparticles can be optimized through deliberate control over particle geometries.[17, 31, 32] While individual Au or Ag solid nanospheres exhibit modest field enhancements upon plasmonic excitation, multilayered metallic nanoparticles, also known as nanomatryoshkas, possess intraparticle SERS hot spots confined inside the narrow interior gaps.[28, 33, 34] Although individual multilayered nanoparticles may serve as excellent SERS probes for bioimaging, the interior intraparticle gaps are not readily accessible by the analyte molecules when used for SERS sensing. Individual nanoparticles with hot spots exposed on their outer surfaces are thus, more appealing for molecular sensing applications. A widely used strategy of achieving intense field enhancements on the outer surfaces of individual nanoparticle is to controllably introduce nanoscale tipped or spiky features to the particle surfaces.[35-47] Upon plasmonic excitation, the electromagnetic fields are enormously enhanced at the surface vertices and edges, providing SERS hot spots on open surfaces that are easily accessible by molecules. A variety of Au or Ag nanoparticles with tipped surface features, such as surface-textured nanospheres,[35-40] etched nanopolyhedra,[41] multi-branched nanostars,[42-45] and spiky nanoshells,[46, 47] have all been shown to exhibit intense SERS enhancements on individual particles, convincingly demonstrating that the

interparticle or intraparticle gap geometries are not always essential for strong SERS enhancements.

Another key design objective in spSERS optimization is to tailor the LSPRs of individual nanoparticles relative to the excitation laser wavelength[48, 49] because the on-resonance excitations typically generate much higher Raman enhancements than the off-resonance excitations. However, the far-field extinction maximum does not overlap exactly with the wavelength at which the largest near-field enhancements are achieved. Van Duyne and coworkers observed that on Ag nanoparticle arrays, the maximum SERS enhancement was achieved when the far-field plasmon band position was red-shifted compared to the excitation laser wavelength.[49] In contrast to this result, more recent experimental observations and electrodynamic calculations on various metallic nanostructures showed that the maximum near-field enhancements occurred at lower energies than the corresponding far-field LSPRs.[50-55] Such red shift of the near-field peak energies with respect to the far-field resonance energies has been predicted to be a universal phenomenon for metallic nanostructures and can be theoretically interpreted using a driven and damped harmonic oscillator model.[51] The relative spectral shift between near- and far-field resonances of plasmonic nanoantennas, however, depends strongly upon the size and shape of the nanoparticles[50-55] and thus, needs to be further investigated more systematically and quantitatively on a wider variety of metallic nanostructures.

In this chapter, we study the far-field and near-field plasmonic properties of individual Au nanoparticles of three geometries, concave nanocubes, nanotrisoctahedra, and nanostars, with a particular focus on their performances as substrates for spSERS under

near-infrared excitation. These three Au nanostructures all possess tipped surface features and size-dependent LSPRs, allowing us to fine-tune their LSPRs with respect to the excitation laser wavelength and to quantitatively evaluate the size-dependent SERS enhancements on individual nanoparticles. The experimentally observed geometry dependence of the far- and near-field plasmonic properties is further corroborated by finite-difference time-domain (FDTD) calculations. These Au nanoparticles with tunable LSPRs in the near-infrared "water window" and nanoengineered hot spots on their tipped surfaces hold great promise as single-particle nanosensors and nanoprobes for SERS-based biosensing and bioimaging applications.

4.2 Experimental Section

Materials. Gold(III) chloride trihydrate ($HAuCl_4$ $3H_2O$, ACS grade) was purchased from J.T. Baker. Sodium borohydride ($NaBH_4$, 99%), L-ascorbic acid (AA, 99.5+%), hydrochloric acid (HCl, 37%), and poly(4-vinylpyridine) (PVP, Mw~60,000) were obtained from Sigma-Aldrich. Silver nitrate ($AgNO_3$, 99.9995% metals basis), (1-Hexadecyl)trimethylammonium chloride (CTAC, 96%), and 4-aminothiophenol (C_6H_7NS, 4-ATP, 97%) were obtained from Alfa Aesar. Hydrogen peroxide (H_2O_2, 30%), sulfuric acid (H_2SO_4, 96.10%), and ethanol (200 proof) were purchased from Fisher Scientific. All reagents were used as received without further purification. Glass microscope slides were obtained from Gold Seal Products (Portsmouth, NH). Ultrapure water (18.2 MΩ resistivity, Barnstead EasyPure II 7138) was used for all experiments.

Synthesis of Au Seeds. Colloidal Au seeds were prepared by the reducing $HAuCl_4$ with appropriate amounts of $NaBH_4$ in the presence of CTAC. In a typical procedure for single-crystalline Au seed (~ 2 nm in diameter) preparation, 0.30 mL of ice-cold, freshly

prepared 10 mM $NaBH_4$ were quickly injected into a solution composed of CTAC (10.00 mL, 0.10 M) and HAuCl4 (0.25 mL, 10 mM) under magnetic stir (1200 rpm). The seed solution was stirred for 1 min and then left undisturbed for 2 h. The seed solution was diluted 1000-fold with CTAC (0.10 M) and the diluted seed solution was used for the subsequent seed-mediated growth. For the preparation of multi-twinned Au seeds (~ 3.5 nm in diameter), the volume of 10 mM $NaBH_4$ added into the $HAuCl_4$-CTAC solution was increased to 0.60 mL while all the other experimental conditions remained unchanged.

Synthesis of Au Concave Nanocubes. Au concave nanocubes were prepared following a previous protocol based on seed-mediated growth[63] with minor modifications. The growth solution was prepared by sequentially adding $HAuCl_4$ (0.50 mL, 10 mM), $AgNO_3$ (0.1 mL, 10 mM), HCl (0.20 mL, 1.0 M), and AA (0.10 mL, 0.10 M) into a CTAC (10.00 mL, 0.10 M) solution. After gently mixing the growth solution for 30 s, the growth of Au concave nanocubes was initiated by adding the diluted single-crystalline Au seed solution. The reaction solution was gently mixed for 30 s and then left undisturbed at room temperature for 4 h. The obtained Au concave nanocubes were washed with water twice through centrifugation/redispersion cycles, and finally redispersed in 5.0 mL of water. The overall sizes of the resulting Au concave nanocube were controlled by adjusting the amount of Au seeds added.

Synthesis of Au Nanotrisoctahedra. Au nanotrisoctahedra were prepared following seed-mediated growth method we recently published.[65] The growth solution was prepared by sequentially adding $HAuCl_4$ (0.50 mL, 10 mM) and AA (1.0 mL, 0.10 M) into a CTAC (10.00 mL, 0.10 M) solution. After gently mixing the growth solution for 30 s, the

growth of Au nanotrisoctahedra was initiated by adding the diluted single-crystalline Au seed solution. The reaction solution was gently mixed for 30 s and then left undisturbed at room temperature for 4 h. The obtained Au nanotrisoctahedra were washed with water twice through centrifugation/redispersion cycles, and finally redispersed in 5.0 mL of water. The overall sizes of the resulting Au nanotrisoctahedra were controlled by adjusting the amount of Au seeds added.

Synthesis of Au Nanostars. Au nanostars were prepared under the same conditions as the concave nanocubes except that multi-twinned Au seeds were used instead of single-crystalline Au seeds. Briefly, the growth solution was prepared by sequentially adding $HAuCl_4$ (0.50 mL, 10 mM), $AgNO_3$ (0.1 mL, 10 mM), HCl (0.20 mL, 1.0 M), and AA (0.10 mL, 0.10 M) into a CTAC (10.00 mL, 0.10 M) solution. After gently mixing the growth solution for 30 s, the growth of Au nanostars was initiated by adding the diluted multi-twinned Au seed solution. The reaction solution was gently mixed and then left undisturbed at room temperature for 4 h. The obtained Au nanostars were washed with water twice through centrifugation/redispersion cycles, and finally redispersed in 5.0 mL of water. The overall sizes of the resulting Au nanostars were controlled by adjusting the amount of Au seeds added.

Characterizations. TEM and SAED measurements were performed using a Hitachi H-8000 transmission electron microscope operated at an accelerating voltage of 200 kV. SEM images were obtained using a Zeiss Ultraplus thermal field emission scanning electron microscope. The optical extinction spectra of the nanoparticles were measured on aqueous colloidal suspensions at room temperature, using a Beckman Coulter Du 640 spectrophotometer. Raman spectra and dark-field optical microscopy images were

obtained on a Bayspec *Nomadic*^{TM} Raman microscopy built on an Olympus BX51 microscope equipped with a 785 nm CW diode laser.

spSERS Measurements. Sub-monolayer films of isolated Au nanoparticles were prepared by immobilizing the particles onto poly(4-vinylpyridine)-functionalized glass substrates. In a typical procedure, glass slides were cleaned in a piranha solution (sulfuric acid:H_2O_2 = 7:3) for 15 min, and then immersed in a 1% wt. of poly(4-vinylpyridine) ethanolic solution for 24 h. The glass slides were thoroughly rinsed with ethanol, dried with N_2 gas, and then immersed in colloidal suspensions of Au nanoparticles (1.0 X 10^9 particles mL^{-1}) for 1 h. The glass slides were thoroughly rinsed with ethanol and dried with N_2 gas after they were removed from the colloidal suspensions of Au nanoparticles. The coverage of Au nanoparticles on the substrates can be controlled by changing the immersion time.

The samples for spSERS experiments were prepared by evaporating 20 μL of a 1.0 mM ethanolic solution of 4-ATP on the surfaces of the isolated Au nanoparticles on poly(4-vinylpyridine)-functionalized silicon substrates. The substrates were then thoroughly rinsed with ethanol and dried with N_2 gas. Water was dropped onto the substrates to ensure that the surrounding medium of the Au nanoparticles was water, and then a clean glass coverslip with a 0.17 mm thickness was covered onto the top of the water layer before the Raman spectral collection. The distance between the two glass slides was about 0.5 mm. SERS spectra were obtained on a Bayspec *Nomadic*^{TM} Raman microscopy built on an Olympus BX51 reflected optical system equipped with a 785 nm CW diode excitation laser using the confocal mode (focal area of 2 μm in diameter). A 50× dark field objective (NA=0.5, WD=10.6 mm, Olympus LMPLFLN-BD) was used

for both Raman signal collection and dark field scattering imaging. The laser beam was focused on one particle each time for Raman spectrum collection. The laser power focused on the samples was measured to be 3.6 mW and the spectrum acquisition time was 20 s. Normal Raman spectra of 4-ATP were collected on solid films of neat 4-ATP on the silicon wafers under the same conditions.

Enhancement Factor (EF) Calculations. We estimated the enhancement factors (EFs) of Raman signals using the following equation: $EF = (I_{SERS} \times N_{normal}) / (I_{normal} \times N_{SERS})$, where I_{SERS} is the intensity of a specific band in the SERS spectra of 4-ATP; I_{normal} is the intensity of the same band in the normal Raman spectra of 4-ATP under the same condition; N_{normal} is the number of probe molecules in the excitation volume for the normal Raman measurements; N_{SERS} is the number of adsorbed molecules on an individual particle. Two Raman modes of 4-ATP at 1078 cm^{-1} and 1590 cm^{-1} were chosen for the EF calculations. To estimate the N_{normal}, we calculated the effective excitation volume by using the following equation: $V = \pi \times (d/2)^2 \times H$, where d is the diameter of the beam size (d = 2 μm) and H is the effective depth of focus (H= 10 μm, which was estimated by finely controlling the height of the stage during the Raman measurements). We estimated an effective excitation volume of 3.14×10^{-17} m^3 for our Raman microscopy with 785 nm excitation using the 50× objective. Then N_{normal} was calculated by using the following expression: $N_{normal} = (V \times D/M) \times N_A = 1.80 \times 10^{11}$ molecules, where D is the density of 4-ATP (1.17 g/mL), M is the molar mass of 4-ATP (125 g/mol) and NA is the Avogadro constant (6.02×10^{23} mol^{-1}). To determine N_{SERS}, a self-assembled monolayer of 4-ATP molecules (molecular footprint size of 0.39 nm^2)[70] was assumed to be closely packed on the surface of each Au particle. The surface area of

the particle was estimated as follows: (1) Au concave nanocubes: when the indentation angle is 140 °, the surface area were calculated as $S= 6\times D^2\times(1/\sin(70°))$; (2) Au nanotrisoctahedra: the surface area was calculated as $S= 7.09\times D^2$; (3) Au nanostars: the surface area was roughly calculated as $S= 1.52\times D^2$. In this way we were able to estimate the N_{SERS} values on nanoparticles with different size and then calculate the EFs.

FDTD Calculations. FDTD calculations were performed using a commercial FDTD software package (Lumerical Solutions). Dielectric permittivity tabulated by Johnson and Christy[80] was used for Au. The geometric parameters used in the simulations for the Au concave nanocubes, nanotrisoctahedra, and nanostars were extracted from the experimental TEM and SEM images. FDTD calculations were performed on single nanoparticles in water (refractive index of 1.34). The near-field enhancements were calculated for an excitation at 785 nm in all the cases. To account for the small morphological details and ensure a good numerical convergence, a uniform FDTD meshgrid of 1 nm was used.

4.3 Results and Discussions

4.3.1. Shape-Controlled Synthesis of Au Concave Nanocubes, Nanotrisoctahedra, and Nanostars.

Control over particle geometries allows one to fine-tune the LSPRs and surface properties of Au nanoparticles to match specific applications. For face-centered cubic (fcc) Au nanoparticles, the low-index {111} and {100} facets have the lowest surface energies and are thus, thermodynamically much more stable than {110} and other high-index facets.[56] As a consequence, Au nanoparticles enclosed by the low energy facets, such as nanocubes enclosed by 6 {100} facets, nanooctahedra enclosed by 8 {111} facets, and

multi-twined quasi-spherical nanoparticles with multi-faceted surfaces enclosed by {111} and {100} facets, represent the most common nanoparticle geometries that are experimentally realizable. It has been recently demonstrated that Au nanoparticles of more complex geometries enclosed by various high-index facets can be fabricated through deliberate control over the nanoparticle growth kinetics and/or selective surface passivation.[57-64] Here we focus on three nanoparticle geometries with tipped surface structures: concave nanocubes, nanotrisoctahedra, and nanostars. As illustrated in Figure 4.1, the concave nanocube is considered to be derived from a nanocube upon introduction of tetragonal indentation to each {100} facet. A nanotrisoctahedron can be obtained by adding convex trigonal pyramids to each {111} facet of a nanooctahedron. By growing nanoscale tips perpendicular to each exposed facet of a multi-twinned quasi-spherical core, a multi-branched star-shaped nanoparticle can be obtained. As demonstrated in greater detail later in this paper, the Au concave nanocubes, nanotrisoctahedra, and nanostars exhibit significantly enhanced plasmonic tunability and improved performances as substrates for spSERS in comparison to the geometrically simpler nanocubes, nanooctahedra, and quasi-spherical nanoparticles.

As illustrated in Figure 4.2, we adopted a seed-mediated growth method for the shape-selective fabrication of monodisperse Au concave nanocubes, nanotrisoctahedra, and nanostars. Starting with single-crystalline quasi-spherical Au seeds, Au nanotrisoctahedra were obtained through kinetically controlled seeded nanocrystal growth. As demonstrated in previous publications,[58, 59, 62, 65] the Au nanotrisoctahedron is a kinetically favored geometry resulting from fast nanoparticle growth processes, while slower growth kinetics

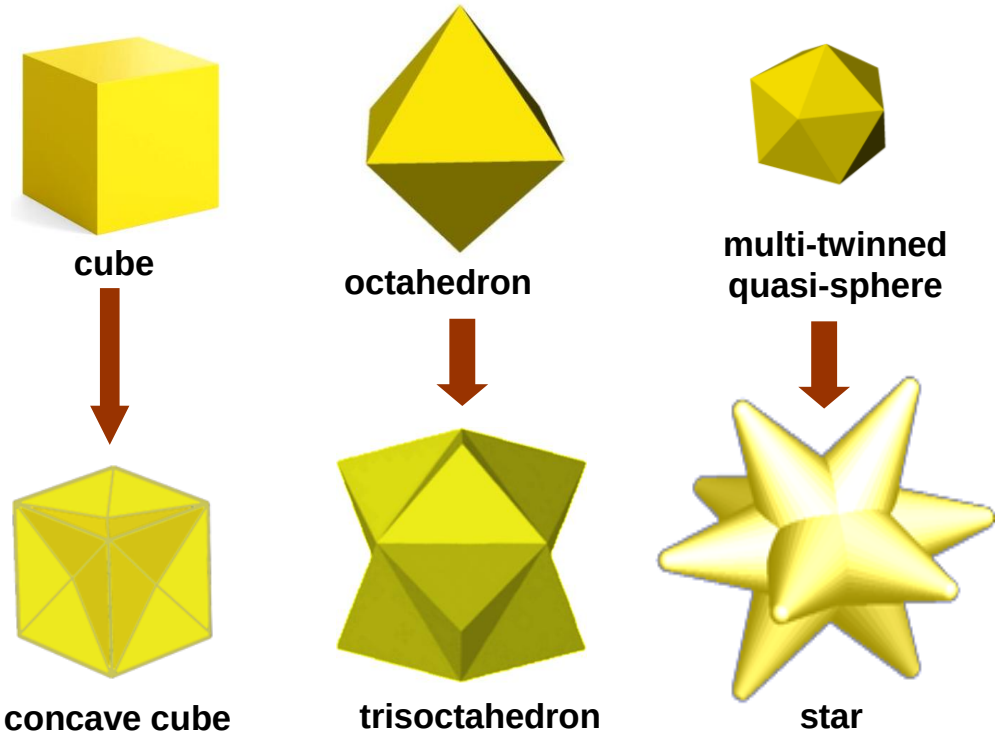

Figure 4.1. Schematics illustrating the geometries of Au concave nanocube, nanotrisoctahedron, nanostar, nanocube, nanooctahedron, and multi-twinned quasi-spherical nanoparticle.

favors the formation of thermodynamically more stable geometries, such as nanocubes, nanooctahedra, and quasi-spherical nanoparticles. Interestingly, by introducing appropriate amount of Ag^{+} into the reaction mixtures, Au concave nanocubes were obtained as a result of the selective passivation of Au surfaces by Ag^{+}.[63] Changing the single-crystalline seeds to multi-twinned seeds allowed for the fabrication of multi-branched Au nanostars. As a consequence, the Au nanostars had multi-twinned crystalline structures while the nanotrisoctahedra and concave nanocubes were both single-crystalline in nature. The capability to fine-control the particle size in each geometry allowed us to gain quantitative insights into the size-dependent plasmonic properties and spSERS performances of the nanoparticles.

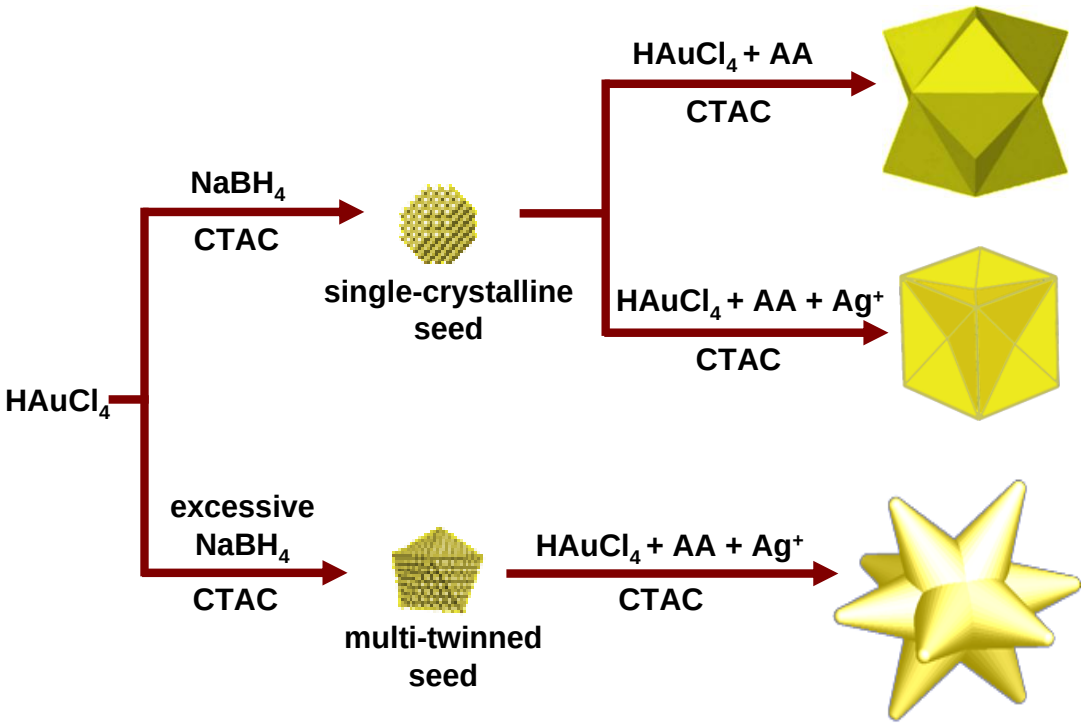

Figure 4.2. Schematics illustrating the shape-controlled synthesis of Au nanotrisoctahedra, concave nanocubes, and nanostars through seed-mediated nanoparticle growth.

4.3.2. Au Concave Nanocubes.

The concave nanocube is an interesting geometry with 24 equivalent indented facets whose miller indices are determined by the degree of indentation. Figure 4.3A shows a transmission electron microscopy (TEM) image of Au concave nanocubes with average edge-length of ~ 130 nm. Each concave nanocube appeared to exhibit darker contrast in the interior regions compared to the edge regions. Concave nanocubes with different orientations with respect to the TEM grid exhibited different overall projection profile and contrast evolution across the particle cross-sections in the TEM images. The morphology of concave nanocubes was also characterized by scanning electron microscopy (SEM). The tetragonal indentation and the boundaries between adjacent indented facets can be both clearly visualized in the SEM image taken on one individual

concave nanocube (inset image of Figure 4.3A). Low-magnification SEM image further reveals that the as-fabricated Au concave nanocubes were highly monodisperse in terms of both particle size and morphology. Figure 4.3B shows the TEM image of one concave nanocube imaged with the electron beam projected along the [001] zone axis. The particle orientation and single-crystalline fcc structures of the concave nanocube were further verified by selected area electron diffraction (Figure 4.3C). While the Au concave nanocube appeared to have a cubic morphological outline, the degree of indentation could be characterized by measuring the indentation angles (the dihedral angel between indented facets) based on the different contrast in the TEM image. As marked in Figure 4.3B, the average indentation angle was measured to be ~ 139 °, indicating that each Au concave nanocube was enclosed by 24 high-index {830} facets. The as-fabricated particles exhibited a higher degree of indentation in comparison to the Au concave nanocubes enclosed by {720} facets (indentation angle of 148 °) fabricated by Mirkin and coworkers.[63] As shown in Figures 4.3D-3J, we were able to fine-control the edge-lengths of the concave nanocubes in the range from ~ 50 nm to over 150 nm by simply adjusting the amount of Au seeds added into the growth solutions. Unlike some other seeded growth methods through which the nanoparticles evolve into different morphologies as the particle size increases,[66, 67] the concave cubic morphology of the particles fabricated using this protocol was well preserved throughout the entire particle size tuning range.

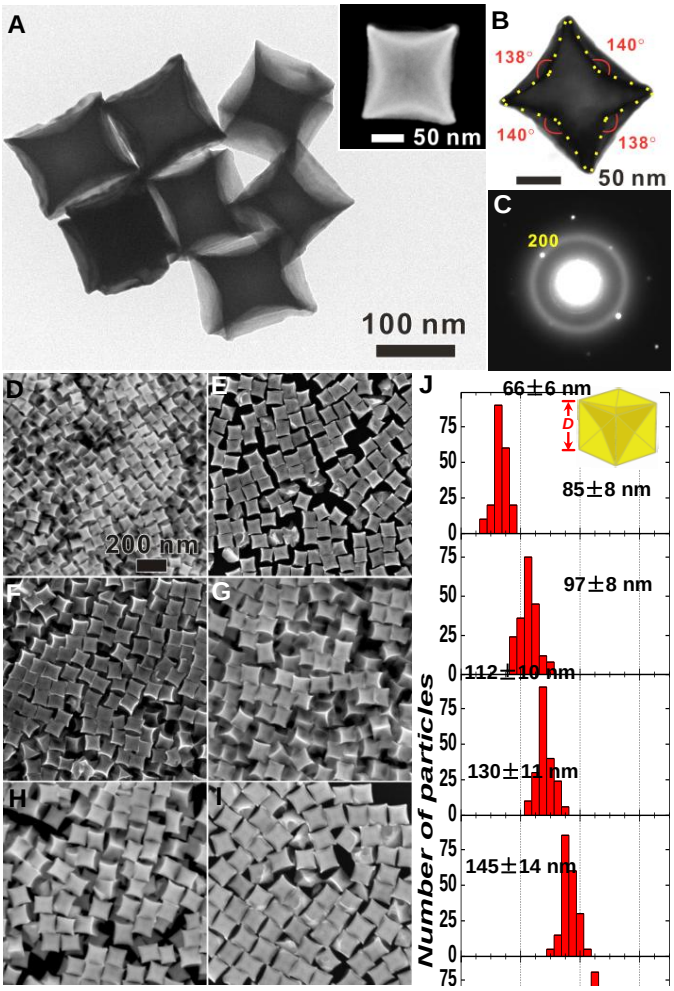

Figure 4.3. (A) TEM image of Au concave nanocubes with average edge length, D, of 130 nm. The inset is an SEM image of one individual concave nanocube. (B) TEM image of one individual concave nanocube with the electron beam projected along the [001] direction. The measured dihedral angles between the concave facets were marked. (C) SAED pattern obtained from the particle in panel B. (D-I) SEM images of Au concave nanocubes with different average edge lengths obtained by adding (D) 0.5 mL, (E) 0.1 mL, (F) 0.05 mL, (G) 0.025 mL, (H) 0.015 mL, and (I) 0.01 mL of Au seed solution. (J) Histograms showing the size distributions of Au concave nanocubes shown in panels D-I.

Au concave nanocubes displayed size-dependent tunable LSPRs. Figure 4.4A shows extinction spectra of colloidal Au concave nanocubes of various average edge-lengths at particle concentration of ~ 1.0 X 10^9 particle mL^{-1}. As the particle size increased, the LSPRs progressively red-shifted and the extinction intensities at the resonance wavelengths increased. For concave nanocubes in the sub-100 nm size regime, the

extinction spectra were dominated by a single-peaked dipole plasmon band, while multiple LSPR peaks were observed when the edge-lengths were beyond 100 nm. In comparison to Au nanocubes of the same edge-lengths, Au concave nanocubes displayed significantly red-shifted LSPRs and more complex spectral line-shapes in the optical extinction spectra. It has been reported that Au concave nanocubes exhibit greatly improved SERS performance in comparison to Au nanocubes and nanospheres of same size due to the intense field enhancements at sharp tips.[68] In addition to the particle geometries, the coupling between LSPRs and the excitation laser is also a key factor that determines SERS enhancements. The size-dependent LSPRs of concave nanocubes allowed us to fine-tune their LSPRs with respect to the excitation laser wavelength (785 nm) and quantify the spSERS enhancements as a function of particle sizes.

To measure spSERS, a sub-monolayer of isolated Au concave nanocubes was immobilized on a poly(4-vinylpyridine)-functionalized glass substrate[47, 69] and was used as substrate for spSERS measurements. The individual nanoparticles were well separated from each other with interparticle distances much larger than the size of each particle. Therefore, interparticle plasmonic coupling was negligible and should have no contribution to the Raman enhancement. The large interparticle distances also allowed us to focus the laser beam on one particle each time using a confocal Raman microscope to collect spSERS signals. 4-aminothiophenol (4-ATP) was chosen as a Raman reporter for the quantification of SERS enhancements because it is a nonresonant molecule with minimal chemical enhancements under near-infrared excitation and forms uniform self-assembled monolayers (SAMs) on Au surfaces with known packing density.[70] Figure 4.4B shows the representative SERS spectra of 4-ATP adsorbed on individual Au

concave nanocubes of various sizes. Two intense Raman bands at 1078 cm^{-1} and 1590 cm^{-1} were observed in the SERS spectra, corresponding to the C-S stretching mode and phenol ring C-C stretching mode, respectively.[19] We collected SERS spectra of 4-ATP SAMs on Au concave nanocubes from more than 100 individual particles for each sample one particle at a time and the intensity histograms of the 1078 cm^{-1} and 1590 cm^{-1} bands are shown in Figures 4C. Maximum SERS signals were obtained on the sample whose far-field plasmon band position was blue-shifted by ~ 30 nm in wavelength with respect to the excitation laser. Murphy and coworkers[55] have recently observed a similar trend on colloidal suspensions of plasmonically tunable Au nanorods and they interpreted their results as a consequence of competition between plasmon-enhanced Raman scattering and light re-absorption along propagation pathway through the colloidal samples. Interestingly, we observed the same trend on surface-immobilized submonolayer of concave nanocubes where re-absorption effects were negligible, strongly indicating that the blue-shift of LSPRs relative to the optimal excitation wavelengths should be a universal feature for metallic nanoparticles regardless of whether they are immobilized on a surface or suspended as colloids. We further estimated the enhancement factors (EFs) by comparing the SERS signals to the normal Raman intensities obtained from neat 4-ATP films (Figure 4.4D). The EFs were estimated to be the orders of 10^4-10^5, approaching 10^6 when the LSPR was tuned to the optimal spectral region with respect to the excitation laser. These estimated EFs were averaged over the entire particle surfaces. The local enhancements in the hot spots at the tips, however, are anticipated to be at least one or two orders of magnitude higher.

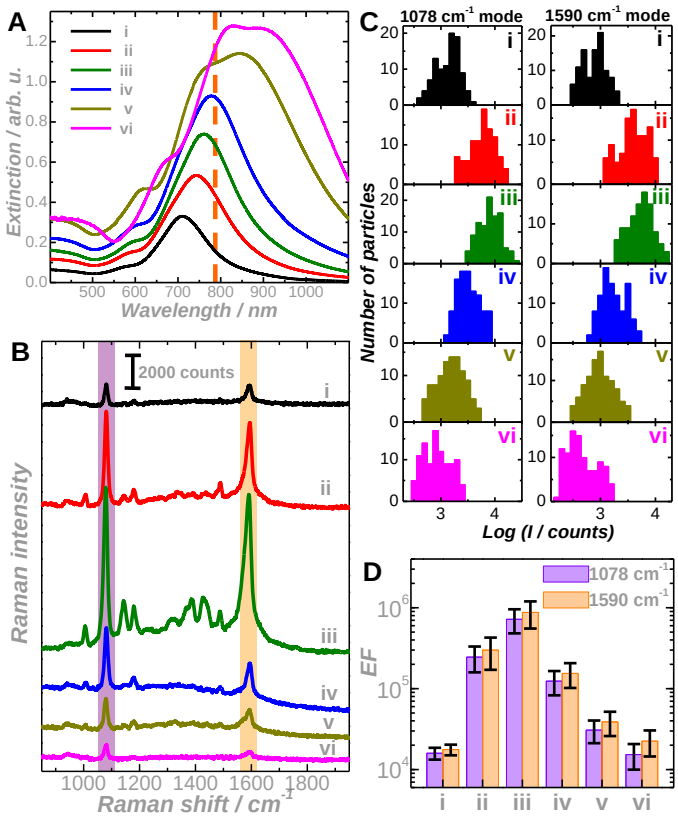

Figure 4.4. (A) Experimental extinction spectra of colloidal Au concave nanocubes of various sizes at particle concentration of ~1.0 × 10^9 particles mL^{-1}. The vertical dashed line shows the excitation laser wavelength (785 nm) for Raman measurements. (B) Representative SERS spectra of 4-ATP adsorbed on individual concave nanocubes of various sizes. Histograms of the Raman intensity of (C) 1078 cm^{-1} mode and (D) 1590 cm^{-1} mode obtained from individual concave nanocubes. (E) SERS enhancement factors (EF) on individual concave nanocubes at 785 nm excitation. The labels of i to vi in all the panels correspond to the concave nanocube samples shown in Figure 1D to 1I, respectively.

To more quantitatively understand how the variation in edge-length and side-facet indentation affect the plasmonic properties of Au concave nanocubes, we used finite-difference time-domain (FDTD) method to calculate the far-field extinction and near-field enhancements of individual concave nanocubes. To more precisely match the experimental particle geometry, corner curvatures of 5 nm in radius were introduced to the nanocubes and concave nanocubes. Each face of the concave nanocubes exhibited a sharp tetragonal indentation angle, θ. Figure 4.5A shows the calculated extinction

spectral evolution of a Au concave nanocube (edge-length of 112 nm) as the indentation angle changes from 180 ° for a nanocube gradually to 125 ° for a highly indented concave nanocube. The far-field extinction spectra were calculated with the incident plane-wave polarized along the edge, the face diagonal, and the body diagonal of the nanocube, respectively. For all three polarizations, the LSPRs progressively red-shifted and the spectral line-shapes became increasingly more complex with multi-peaked features gradually developed as the degree of indentation increased. This is in line with previous observations that Au concave nanocubes display significantly red-shifted LSPRs in comparison to Au nanocubes of the same sizes.[68] As shown in Figure 4.5B, the concave nanocubes exhibited highest field enhancements in the vicinities of the tips and electric fields were significantly enhanced at the particle edges as well. Larger field enhancements were achieved on the surfaces of concave nanocubes with higher degrees of indentation. To assess the SERS enhancements from individual concave nanocubes based on the FDTD results, we calculated the integrated fourth power of the field enhancements, $|E/E_0|^4$, over the entire volume up to 1.5 nm above the cube faces. As shown in Figures 5C and 5D, the integrated field-enhancements increased with the increase in the degree of indentation for both the edge and face diagonal polarizations.

In Figure 4.6A, we compare the calculated extinction spectra of Au concave nanocubes with fixed indentation angle of 140 ° and various edge-lengths. To take into account the ensemble effects of randomly orientated nanoparticles in colloidal suspensions, FDTD-calculated extinction spectra were averaged over three polarizations, that is, the edge, face diagonal, and body diagonal polarizations. The calculated extinction spectra were also averaged for three different indentations $\theta = 140^o \pm 5^o$ to

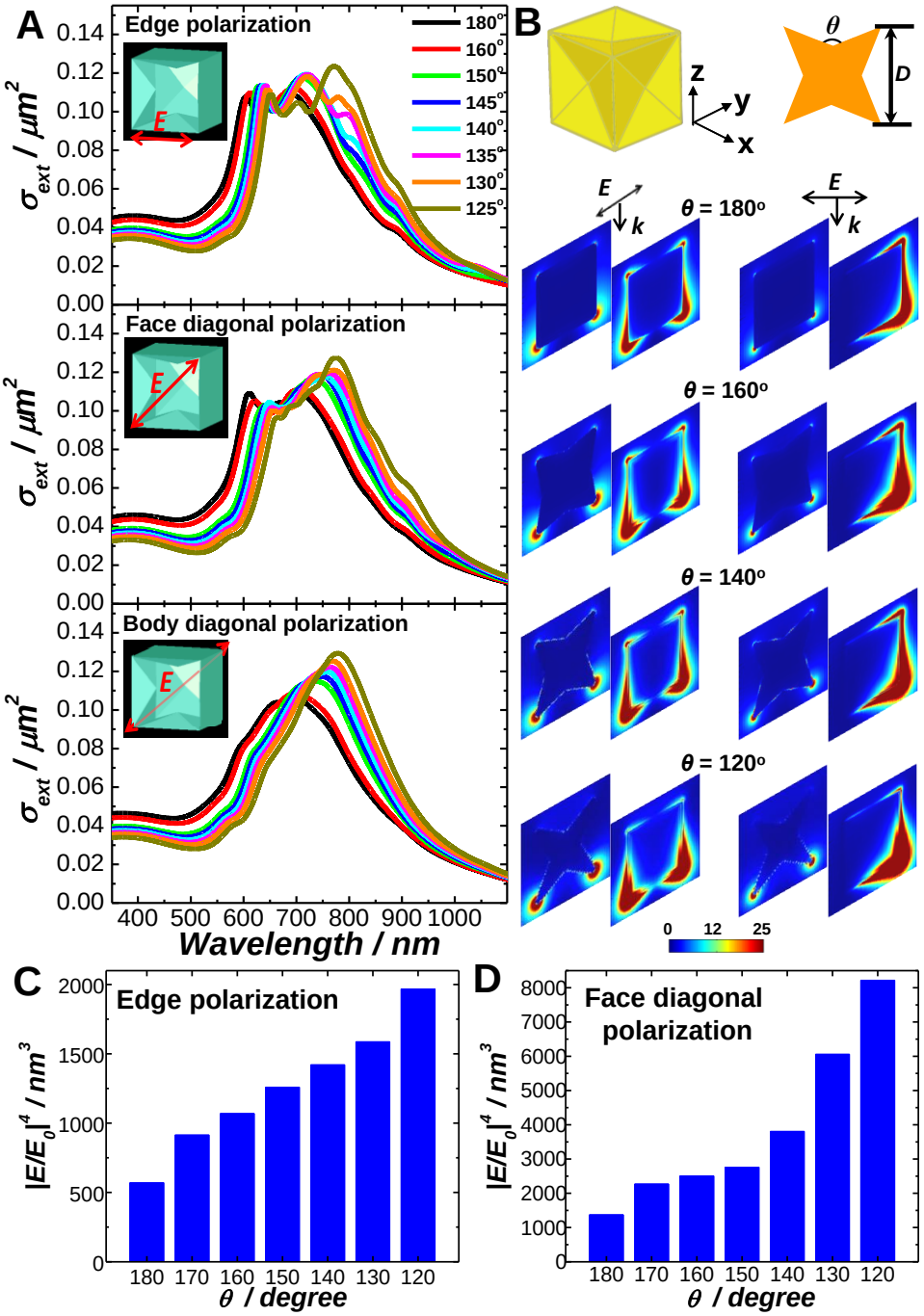

Figure 4.5. (A) Calculated extinction spectra of a Au concave nanocube (D = 112 nm) with varying indentation angles (θ) for three polarizations (edge, face diagonal, and body diagonal polarizations). (B) The cross-sectional views of the calculated near-field enhancements ($|E/E_0|^2$) of Au concave nanocubes with edge length of 112 nm and various indentation angles of 180 °, 160 °, 140 °, and 120 ° at 785 nm excitation. The geometry of a concave nanocube in three-dimensional Cartesian coordinates and the cross-section of the concave nanocube in the yz plane are illustrated. The left column is edge polarization, and the right column is face diagonal polarization. The incident plane wave propagates along z axis and the body center of the concave nanocube is at x = y = z = 0. Two planes parallel to the yz plane at x= 0 and 56 nm are shown for

each polarization and indentation angle. (C-D) Fourth power of the field enhancements integrated over volume ($|E/E_0|^4$) of concave nanocube (D = 112 nm) with various indentation angles for (C) edge and (D) face diagonal polarizations.

account for the inhomogeneous indentations of the experimentally fabricated samples. Both the LSPR wavelengths and the spectral line-shapes of the calculated extinction spectra were in very good agreement with the experimental results shown in Figure 4.4A. We also calculated the integrated $|E/E_0|^4$ on Au concave nanocubes with indentation angle of 140 ° and various edge-lengths at 785 nm excitation. As shown in Figures 4.6B and 4.6C, better coupling between the LSPRs and excitation laser, in general, gave rise to stronger field enhancements; however, the largest integrated field enhancements were obtained on the 112 nm concave nanocube whose LSPR extinction peak was blue-shifted in comparison to the excitation laser wavelength. This trend was in excellent agreement with our size-dependent spSERS results shown in Figure 4.4. Since the FDTD calculations only considered individual particles, the off-set between the far-field extinction and near-field peak wavelengths should not be interpreted as the consequence of light extinction in colloidal samples as previously claimed by Murphy and coworkers.[55] Our spSERS results on plasmonically tunable Au concave nanocubes, together with the FDTD results, provide strong evidence that the red-shift of the near-field resonance wavelengths with respect to the far-field extinction peaks is an intrinsic characteristic of individual metallic nanostructures.

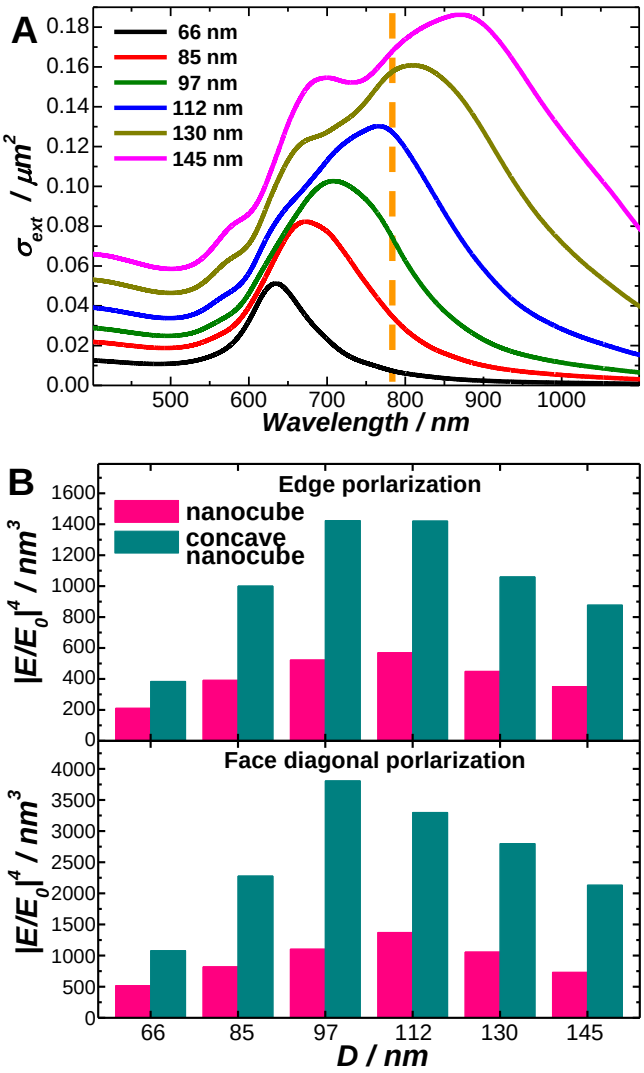

Figure 4.6. (A) Calculated extinction spectra of a concave nanocube with indentation angles of 140 ° and varying edge lengths as labeled in the figure. The vertical dashed line shows the excitation laser wavelength (785 nm) for Raman measurements. (B) Fourth power of the field enhancements integrated over volume ($|E/E_0|^4$) of concave nanocubes with θ of 140° and D of 66, 85, 97, 112, 130, and 145 nm. The upper panel is for edge polarization and the lower panel is for face diagonal polarization.

4.2.3. Au Nanotrisoctahedra.

A trisoctahedral nanoparticle comprises eight trigonal pyramids generated by "pulling out" the centers of the eight triangular {111} facets of a nanooctahedron. This interesting particle geometry could be visualized in the SEM images shown in Figures 4.7A and 4.7B. Although some of the nanoparticles did not appear trisoctahedral at first glance due

to different orientations, a careful survey of particle shapes over a large sample area in low-magnification SEM image showed that around 90 % of the nanoparticles had the trisoctahedral morphology, around 4 % of the particles exhibited slightly elongated bipyramidal morphology, and the rest ~ 6 % of the particles were multifaceted polyhedra with ill-defined facets and overall shapes. Figure 4.7C shows a TEM image of one individual Au nanotrisoctahedron projected from the [011] zone axis. At this orientation, 4 out of the 24 facets of the nanooctahedron were projected edge-on and the Miller indices of the exposed facets of the nanooctahedron were determined to be {221} through an analysis of the three projection angles marked in Figure 4.7C.[58, 59, 62, 65] The Au nanotrisoctahedra fabricated using this seed-mediated growth method have essentially the same facets as those obtained from previously reported one-step seedless approach.[62] The seeded growth method allowed us to fine-tune the size of the nanotrisoctahedra by adjusting the amount of Au seeds added into the growth solutions. As shown in Figures 4.7D-4.7J, the average sizes of the Au nanotrisoctahedra progressively increased as the amount of Au seeds decreased and could be tightly controlled in the range from ~ 50 nm to over 200 nm. Similar to the Au concave nanocubes, the as-fabricated nanotrisoctahedra could also be immobilized onto poly(4-vinylpyridine)-functionalized glass substrates as a sub-monolayer of isolated particles for the spSERS measurements.

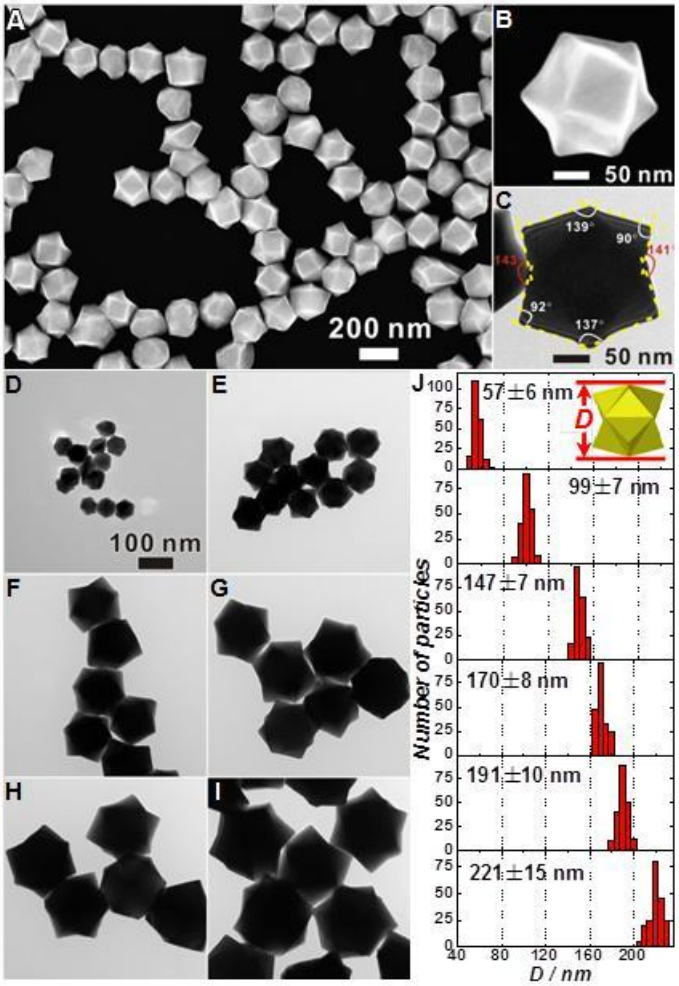

Figure 4.7. (A) SEM image of Au nano-trisoctahedra with average size of 191 nm. (B) SEM image of one nano-trisoctahedron. (C) TEM image of one individual nano-trisoctahedron with the electron beam projected along the [011] direction. The measured angles between the various edges of the nano-trisoctahedron were marked. (D-I) TEM images of Au nano-trisoctahedra with various average sizes fabricated by adding (D) 0.5 mL, (E) 0.1 mL, (F) 0.05 mL, (G) 0.025 mL, (H) 0.015 mL, and (I) 0.01 mL of Au seed solution. (J) Histograms showing the size distributions of Au nano-trisoctahedra shown in panels D-I.

Figure 4.8A shows the extinction spectra of colloidal Au nanotrisoctahedra with various average sizes at particle concentration of ~ 1.0 X 10^9 particle mL^{-1}. As the particle size increased, the dipole LSPRs progressively red-shifted and became increasingly broadened. For nanotrisoctahedra within the sub-100 nm size regime, only one dipole LSPR band was observed in the extinction spectra. A narrower quadrupole LSPR band

emerged at shorter wavelength to the dipole LSPR band and became increasingly pronounced as the size of the nanotrisoctahedra further increased to beyond 100 nm due to the phase retardation effects.[35, 71, 72] While the quadrupole LSPR was less sensitively dependent on the particle size, the broad dipole LSPR band could be systematically shifted with respect to the excitation laser by changing the particle sizes. Figure 4.8B shows the representative SERS spectra of 4-ATP SAMs formed on individual Au nanotrisoctahedra of various sizes. Similar to the results obtained on Au concave nanocubes, maximum SERS signals were obtained on the sample whose far-field plasmon band position was blue-shifted by ~ 70 nm in wavelength with respect to the excitation laser, further verifying that the red-shift of optimal excitation wavelength with respect to LSPR extinction peak is a universal phenomenon for metallic nanoparticles of different geometries. We repeated the spSERS measurements on 100 individual nanotrisoctahedra for each sample and the histograms of intensities of the 1078 cm^{-1} and 1590 cm^{-1} modes are shown in Figure 4.8C. The nanotrisoctahedra exhibited average SERS EFs of ~10^5 when their LSPRs were optimized under 785 nm excitation and the off-resonance enhancements were generally below 10^4. Although the Au nanotrisoctahedra showed SERS enhancements one order of magnitude weaker than those achieved on Au concave nanocubes, they were significantly more efficient as substrates for spSERS than quasi-spherical nanoparticles of the same sizes[65] primarily due to their tipped surface features. The surface tips of the nanotrisoctahedra were less sharp than those of the concave nanocubes, which may be one of the main reasons why Au concave nanocubes showed higher SERS enhancements than the nanotrisoctahedra.

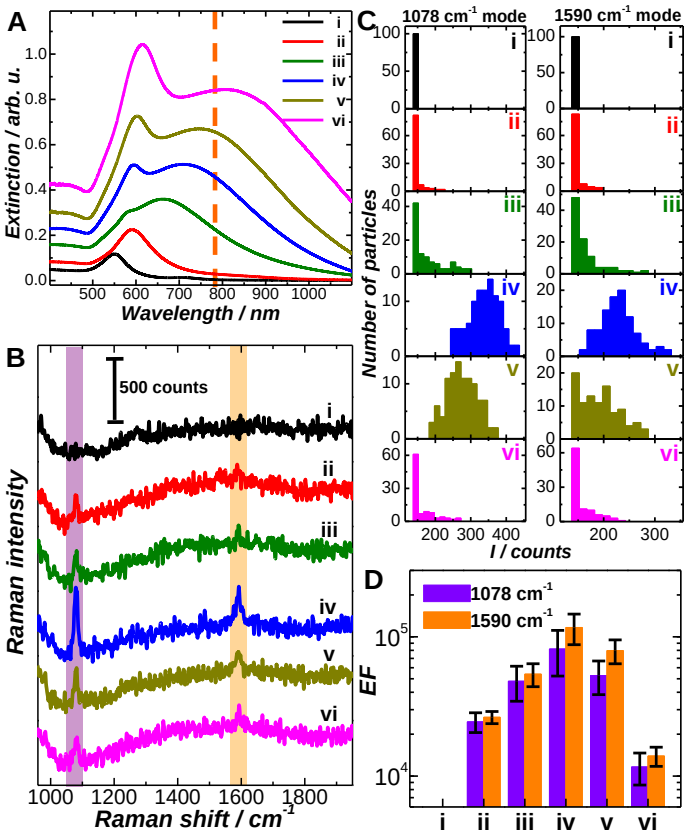

Figure 4.8. (A) Experimental extinction spectra of colloidal Au nano-trisoctahedra of various sizes at particle concentration of ~ 1.0 X 10^9 particles mL^{-1}. The vertical dashed line shows the excitation laser wavelength (785 nm) for Raman measurements. (B) Representative SERS spectra of 4-ATP adsorbed on individual nano-trisoctahedra of various sizes. Histograms of the Raman intensity of (C) 1078 cm^{-1} mode and (D) 1590 cm^{-1} mode obtained from individual nano-trisoctahedra. (E) SERS enhancement factors (EF) on individual nano-trisoctahedra at 785 nm excitation. The labels of i to vi in all the panels correspond to the nano-trisoctahedron samples shown in Figure 5D to 1I, respectively.

We also used FDTD to calculate the size-dependent far-field extinction spectra and near-field enhancements of individual Au nanotrisoctahedra. The extinction spectra were calculated and averaged over two polarizations, X- and Y-polarizations, as illustrate in the inset of Figure 4.9A. Integrated near-field enhancements were obtained by integrating the electric field intensities in a sphere of radius $D/2+1.5$ nm, where D is the particle size of the nanotrisoctahedra. As shown in Figure 4.9A, the calculated extinction spectra of the nanotrisoctahedra were in excellent agreement with the experimental results shown in

Figure 4.8A. The calculated results on the near-field enhancements (Figures 4.9B-4.9C) clearly showed that the largest integrated field-enhancements were achieved on the 170 nm nanotrisoctahedron whose dipole LSPR was on the blue side of the excitation laser though the dipole LSPR band of the 191 nm nanotrisoctahedron better matched the laser wavelength. We have further studied the effects of facet convexity on the far-field and near-field properties of a nanooctahedron (D = 170 nm). The convex nanotrisoctahedron exhibited red-shifted and broadened LSPR line-shapes in comparison to the nanooctahedron. The integrated near-field enhancements on the nanotrisoctahedron were several times higher than on the nanooctahedron at 785 nm excitation, indicating that introducing convexity to the nanooctahedron surfaces would give rise to improved SERS enhancements.

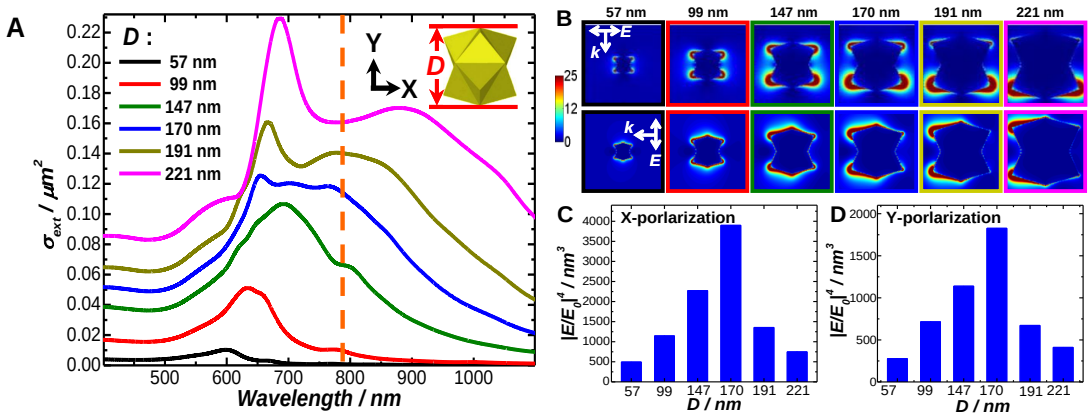

Figure 4.9. (A) Calculated extinction spectra of Au nano-trisoctahedra of various particle sizes as labeled in the figure. The vertical dashed line shows the excitation laser wavelength (785 nm) for Raman measurements. (B) The cross-sectional views of the calculated near-field enhancements ($|E/E_0|^2$) of TOH Au nanoparticles with various sizes at 785 nm excitation. The upper panel is for X-polarization and the lower panel is for Y-polarization. Fourth power of the field enhancements integrated over volume ($|E/E_0|^4$) of Au nano-trisoctahedra with various sizes for (C) X-polarization and (D) Y-polarization.

4.2.4. Au Nanostars.

Au nanostars are multibranched nanoparticles with geometrically tunable LSPRs and strong electromagnetic field enhancements exploitable for SERS.[42-45] Au nanostars with different sizes, tip sharpness, and number of tips have been chemically synthesized through seedless reduction of Au(III) chlorate with 4-(2-hydroxyethyl)-1-piperazineethanesulfonic acid (HEPES)[73, 74] or seed-mediated growth in the presence of surface stabilizers, such as poly(vinylpyrrolidone) (PVP) and cetyltrimethylammonium bromide (CTAB).[42-45, 75, 76] Our protocol of size-controlled synthesis of Au nanostars was essentially the same as that for the concave nanocubes except that multi-twinned Au seeds were used instead of single-crystalline seeds. As shown in Figure 4.10A, the as-fabricated Au nanostars were highly monodisperse in terms of overall particle sizes and the multibranched morphology while the tip sharpness and the relative orientations of the branches on each nanostar varied form particle to particle. Our method allowed for the fabrication of Au nanostars with nearly 100 % yield as revealed by SEM images taken over large sample areas. The number of branches on each nanostar varied in the range from 6 to 10, which was determined by the number of facets exposed on the multi-twinned Au seeds. In contrast to the single-crystalline Au concave nanocubes and nanotrisoctahedra, the Au nanostars had multi-twinned crystalline structures, as revealed by TEM image and SAED pattern shown in Figures 4.10B and 4.10C, respectively. The overall size of the Au nanostars could be controlled by adjusting the amount of multi-twinned Au seeds added into the growth solutions (Figures 4.10D-4.10I). Both the average tip sharpness and average number of branches on each nanostar remained unchanged for the nanostars with different overall sizes.

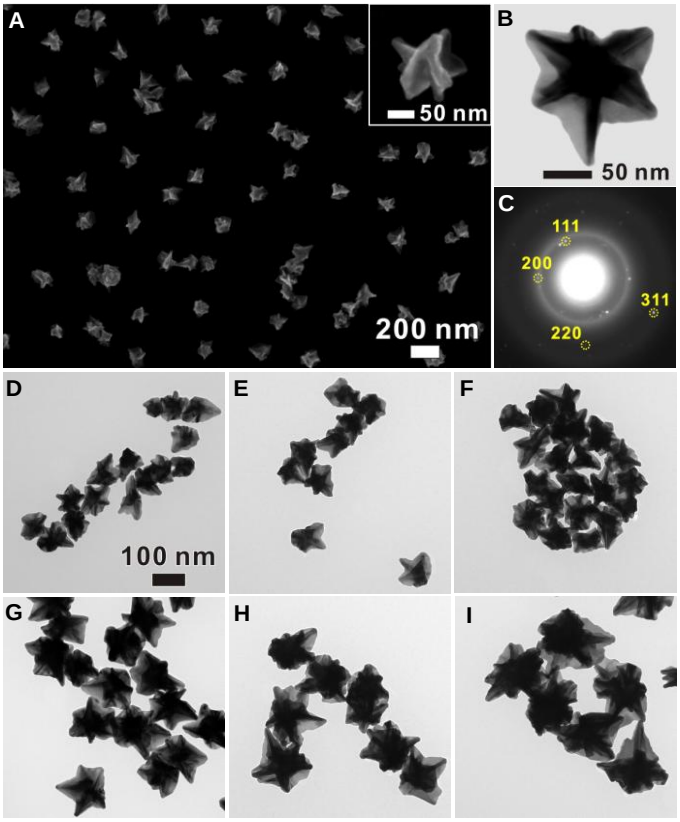

Figure 4.10. (A) SEM image of Au nanostars fabricated by adding 0.025 mL of Au seed solution. The inset highlights one individual Au nanostar. (B) TEM image of one Au nanostar. (C) SAED pattern obtained from the particle shown in panel B. (D-I) TEM images of Au nanostars with different average sizes fabricated by adding (D) 0.5 mL, (E) 0.1 mL, (F) 0.05 mL, (G) 0.025 mL, (H) 0.015 mL, and (I) 0.01 mL of Au seed solution.

The control over the size of Au nanostars allowed us to fine-tune the LSPRs over a broad spectral region across the visible and near-infrared (Figure 4.11A). As the nanostars became larger in size, their LSPR band progressively red-shifted and became more intense due to the increase in the particles' extinction cross-sections. The plasmonic tunability of nanostars results from the hybridization of plasmons focalized at the core and the tips of the nanoparticles.[77] The red-shift in LSPRs can be interpreted as the results of increase in the aspect ratios of the branches. Similar to the Au concave nanocubes and nanotrisoctahedra, spSERS measurements were performed on sub-monolayers of isolated nanostars immobilized on polyvinylpyridine-functionalized glass substrates. Red-shift of

optimal excitation wavelength with respect to LSPR extinction peak was also observed on the Au nanostars. As shown in Figures 4.11B and 4.11C, the nanostar sample with far-field extinction peak at ~ 740 nm exhibited the largest SERS enhancements. The surface-averaged Raman EFs on individual nanostars were on the order of 10^6 for off-resonance excitations and well exceeded 10^7 when the LSPR was optimized with respect to the excitation laser. The tips of nanostars were sharper than those of the concave nanocubes, giving rise to stronger field enhancements on each tip of the nanostars. In addition, the cores of the nanostars also displayed strong plasmonic antenna effects, dramatically increasing the excitation cross section and the electromagnetic field enhancements of the tip plasmons.[77] Therefore, the SERS enhancements observed on individual nanostars were approximately one order of magnitude higher than those on individual concave nanocubes.

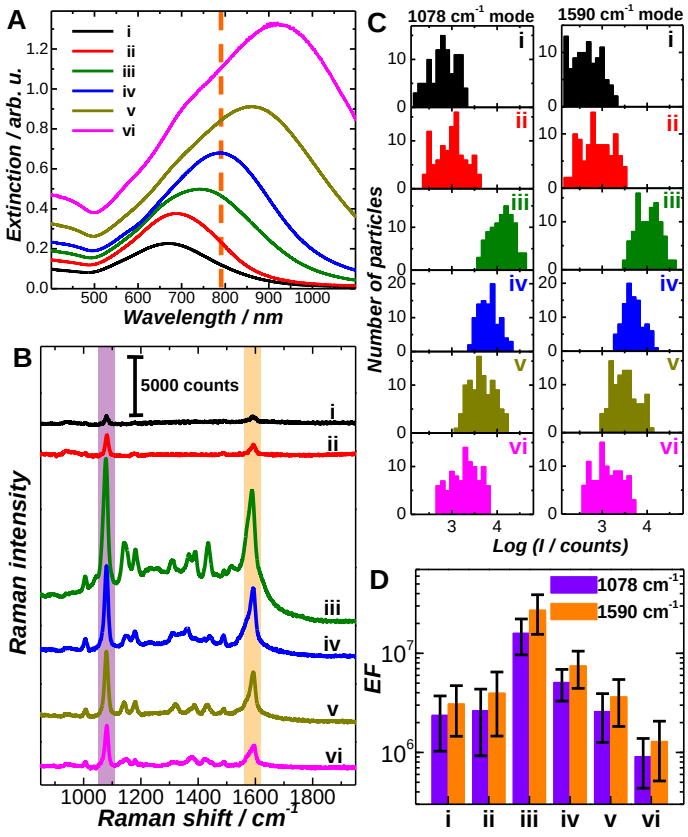

Figure 4.11. (A) Experimental extinction spectra of colloidal Au nanostars of various sizes at particle concentration of ~ 1.0 X 10^9 particles mL^{-1}. The vertical dashed line shows the excitation laser wavelength (785 nm) for Raman measurements. (B) Representative SERS spectra of 4-ATP adsorbed on individual Au nanostars of various sizes. Histograms of the Raman intensity of (C) 1078 cm^{-1} mode and (D) 1590 cm^{-1} mode obtained from individual Au nanostars. (E) SERS enhancement factors (EF) on individual nano-stars at 785 nm excitation. The labels of i to vi in all the panels correspond to the Au nanostars samples shown in Figure 8D to 1I, respectively.

To quantitatively understand the geometry dependence of LSPRs and SERS performance of Au nanostars, we performed FDTD calculations on Au nanostars with various numbers and sizes of tipped branches. The nanostar geometries used for FDTD calculations were taken with conical branches with a tip radius of 5 nm and a tip angle of 30 º. Extinction spectra were calculated and averaged for 6, 8, and 10 branches and over two different orthogonal polarizations (X- and Y-polarizations). Figure 4.12A shows the calculated extinction spectra of Au nanostars with various sizes, which are in very good agreement with the experimental results shown in Figure 4.11A. It was found the length of the branches had a major effect on the LSPR frequencies of the nanostars with longer branches resulting in more red-shifted LSPRs. The LSPR wavelengths of nanostars were also dependent on the thickness of the tipped branches. It is found that decrease in the thickness of the branches led to red-shift of the LSPRs. The dependence of nanostar LSPRs on the length and thickness of the branches can be interpreted in the context of the well-understood longitudinal nanorod plasmon whose resonance wavelength red-shifts as the particle aspect ratio increases.[78, 79] Interesting, the number of branches per nanostar had minimal effects on the LSPRs. Increasing the number of branches from 6 to 10 only resulted in slight broadening of the LSPR band while the LSPR peak positions were essentially unchanged. Figures 4.12B-4.12D show the calculated near-field distributions and integrated field enhancements of Au nanostars of various sizes at 785 nm excitation.

Integrated near-field enhancements were obtained by integrating the electric field in a sphere of radius *D*/2+1.5 nm, where *D* is the particle size of nanostar (twice of the length of each branch). Once again, largest integrated field-enhancement was obtained on the nanostar with LSPR band blue-shifted from excitation laser wavelength (Figures 4.12C and 4.12D), which matched the experimental results on spSERS shown in Figure 11D. The calculated integrated field-enhancements on Au nanostars were about one order of magnitude higher than those on Au concave nanocubes, also in excellent agreement with the experimental observations.

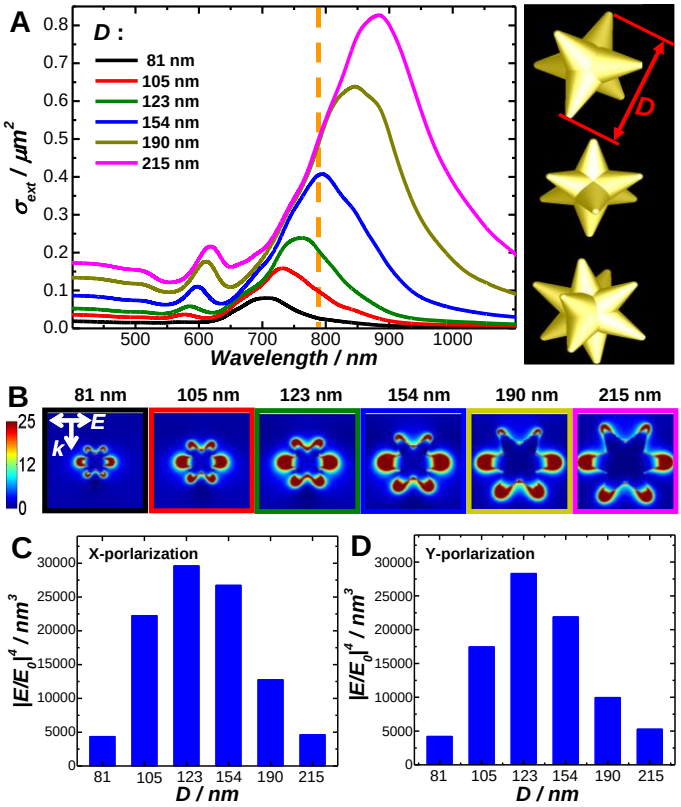

Figure 4.12. (A) Calculated extinction spectra of individual Au nanostars with varying tip-to-tip distance, D, as labeled in the figure. The right panel shows the geometries of Au nanostar with 6, 8, and 10 arms. The calculated extinction spectra were averaged over different arm numbers and various polarizations. The vertical dashed line shows the excitation laser wavelength (785 nm) for Raman measurements. (B) The cross-sectional views of the calculated near-field enhancements ($|E/E_0|^2$) of Au nanostars with various sizes at 785 nm excitation. Fourth power of the field enhancements integrated over volume ($|E/E_0|^4$) of Au nanostars with various sizes for (C) X-polarization, and (D) Y-polarization.

4.4 Conclusions

In summary, we have demonstrated that Au concave nanocubes, nanotrisoctahedra, and nanostars with fine-controlled particle sizes and narrow size distributions can be fabricated using a robust solution phase, seed-mediated growth method through deliberate control over the nanoparticle growth kinetics, surface passivation by Ag^{+}, or the crystalline structures (single-crystalline vs. multi-twinned) of the Au seeds. The capability to precisely control the particle size in each geometry allows us to fine-tune the particle LSPRs with respect to the excitation laser wavelength and quantitatively evaluate the performance of individual nanoparticles as SERS substrates. Our spSERS results, further corroborated by FDTD calculations, provide strong evidence that the red-shift of the near-field enhancement peak wavelengths from the far-field LSPR extinction peaks is a universal intrinsic feature of individual metallic nanoparticles in different geometries. Au nanostars, concave nanocubes, and nanotrisoctahedra exhibit SERS enhancements on the orders of 10^7, 10^6, and 10^5, respectively, on individual particles at 785 nm excitation when their LSPRs are tuned to the optimal spectral regions with respect to the excitation laser. Our experimental and FDTD results show that individual Au nanoparticles with nanoengineered surface tips may provide plasmonic field enhancements that are sufficiently high for spSERS without involving the strongly coupling plasmons confined in nanoscale interparticle or intraparticle junctions. The knowledge gained through this work provides important information that may guide the design and fabrication of metallic nanoparticles with increasing geometric complexity and further optimized plasmonic properties for SERS-based biosensing and bioimaging applications.

4.5 References

(1) Moskovits, M., *Rev. Mod. Phys.* **1985,** *57*, 783-826.

(2) Campion, A.; Kambhampati, P., *Chem. Soc. Rev.* **1998,** *27*, 241-250.

(3) Kneipp, K.; Kneipp, H.; Itzkan, I.; Dasari, R. R.; Feld, M. S., *Chem. Rev.* **1999,** *99*, 2957-2976.

(4) Stiles, P. L.; Dieringer, J. A.; Shah, N. C.; Van Duyne, R. R., In *Annual Review of Analytical Chemistry*, Annual Reviews: Palo Alto, 2008; Vol. 1, pp 601-626.

(5) Craig, A. P.; Franca, A. S.; Irudayaraj, J., *Annual Review of Food Science and Technology*, *Vol 4* **2013,** *4*, 369-380.

(6) Li, J. F.; Huang, Y. F.; Ding, Y.; Yang, Z. L.; Li, S. B.; Zhou, X. S.; Fan, F. R.; Zhang, W.; Zhou, Z. Y.; Wu, D. Y.; Ren, B.; Wang, Z. L.; Tian, Z. Q., *Nature* **2010,** *464*, 392-395.

(7) Halvorson, R. A.; Vikesland, P. J., *Environ. Sci. Technol.* **2010,** *44* , 7749-7755.

(8) Shafer-Peltier, K. E.; Haynes, C. L.; Glucksberg, M. R.; Van Duyne, R. P., *J. Am. Chem. Soc.* **2003,** *125*, 588-593.

(9) Barhoumi, A.; Halas, N. J., *J. Am. Chem. Soc.* **2010,** *132*, 12792-12793.

(10) Anker, J. N.; Hall, W. P.; Lyandres, O.; Shah, N. C.; Zhao, J.; Van Duyne, R. P., *Nat. Mater.* **2008,** *7*, 442-453.

(11) Alvarez-Puebla, R. A.; Liz-Marzan, L. M., *Small* **2010,** *6*, 604-610.

(12) Qian, X. M.; Peng, X. H.; Ansari, D. O.; Yin-Goen, Q.; Chen, G. Z.; Shin, D. M.; Yang, L.; Young, A. N.; Wang, M. D.; Nie, S. M., *Nat. Biotechnol.* **2008,** *26*, 83-90.

(13) Kim, J. H.; Kim, J. S.; Choi, H.; Lee, S. M.; Jun, B. H.; Yu, K. N.; Kuk, E.; Kim, Y. K.; Jeong, D. H.; Cho, M. H.; Lee, Y. S., *Anal. Chem.* **2006,** *78*, 6967-6973.

(14) Doering, W. E.; Piotti, M. E.; Natan, M. J.; Freeman, R. G., *Adv. Mater.* **2007,** *19*, 3100-3108.

(15) Zavaleta, C. L.; Smith, B. R.; Walton, I.; Doering, W.; Davis, G.; Shojaei, B.; Natan, M. J.; Gambhir, S. S., *Proc. Natl. Acad. Sci. U. S. A.* **2009,** *106*, 13511-13516.

(16) Maiti, K. K.; Dinish, U. S.; Samanta, A.; Vendrell, M.; Soh, K. S.; Park, S. J.; Olivo, M.; Chang, Y. T., *Nano Today* **2012,** *7*, 85-93.

(17) Camden, J. P.; Dieringer, J. A.; Zhao, J.; Van Duyne, R. P., *Accounts Chem. Res.* **2008,** *41*, 1653-1661.

(18) Halas, N. J.; Lal, S.; Chang, W. S.; Link, S.; Nordlander, P., *Chem. Rev.* **2011,** *111*, 3913-3961.

(19) Wang, H.; Levin, C. S.; Halas, N. J., *J. Am. Chem. Soc.* **2005,** *127*, 14992-14993.

(20) Lee, S. J.; Morrill, A. R.; Moskovits, M., *J. Am. Chem. Soc.* **2006,** *128*, 2200-2201.

(21) Wang, H. H.; Liu, C. Y.; Wu, S. B.; Liu, N. W.; Peng, C. Y.; Chan, T. H.; Hsu, C. F.; Wang, J. K.; Wang, Y. L., *Adv. Mater.* **2006,** *18*, 491-495.

(22) Osberg, K. D.; Rycenga, M.; Harris, N.; Schmucker, A. L.; Langille, M. R.; Schatz, G. C.; Mirkin, C. A., *Nano Lett.* **2012,** *12*, 3828-3832.

(23) Kneipp, K.; Wang, Y.; Kneipp, H.; Perelman, L. T.; Itzkan, I.; Dasari, R.; Feld, M. S., *Physical Review Letters* **1997,** *78*, 1667-1670.

(24) Michaels, A. M.; Nirmal, M.; Brus, L. E., *J. Am. Chem. Soc.* **1999,** *121*, 9932-9939.

(25) Xu, H. X.; Bjerneld, E. J.; Kall, M.; Borjesson, L., *Physical Review Letters* **1999,** *83*, 4357-4360.

(26) Camden, J. P.; Dieringer, J. A.; Wang, Y. M.; Masiello, D. J.; Marks, L. D.; Schatz, G. C.; Van Duyne, R. P., *J. Am. Chem. Soc.* **2008,** *130*, 12616-12617.

(27) Fang, Y.; Seong, N. H.; Dlott, D. D., *Science* **2008,** *321*, 388-392.

(28) Lim, D. K.; Jeon, K. S.; Hwang, J. H.; Kim, H.; Kwon, S.; Suh, Y. D.; Nam, J. M.,. *Nat. Nanotechnol.* **2011,** *6*, 452-460.

(29) Qian, X. M.; Nie, S. M., *Chem. Soc. Rev.* **2008,** *37*, 912-920.

(30) Sha, M. Y.; Xu, H. X.; Natan, M. J.; Cromer, R., *J. Am. Chem. Soc.* **2008,** *130*, 17214-17215.

(31) Lal, S.; Grady, N. K.; Kundu, J.; Levin, C. S.; Lassiter, J. B.; Halas, N. J., *Chem. Soc. Rev.* **2008,** *37*, 898-911.

(32) Xia, Y. N.; Halas, N. J., *MRS Bull.* **2005,** *30*, 338-344.

(33) Gandra, N.; Singamaneni, S., *Adv. Mater.* **2013,** *25*, 1022-1027.

(34) Song, J. B.; Duan, B.; Wang, C. X.; Zhou, J. J.; Pu, L.; Fang, Z.; Wang, P.; Lim, T. T.; Duan, H. W., *J. Am. Chem. Soc.* **2014,** *136*, 6838-6841.

(35) Wang, H.; Halas, N. J., *Adv. Mater.* **2008,** *20*, 820-825.

(36) Fang, J. X.; Du, S. Y.; Lebedkin, S.; Li, Z. Y.; Kruk, R.; Kappes, M.; Hahn, H., *Nano Lett.* **2010,** *10*, 5006-5013.

(37) Liu, Z.; Zhang, F. L.; Yang, Z. B.; You, H. J.; Tian, C. F.; Li, Z. Y.; Fang, J. X., *J. Mater. Chem. C* **2013,** *1*, 5567-5576.

(38) Lin, H. X.; Li, J. M.; Liu, B. J.; Liu, D. Y.; Liu, J. X.; Terfort, A.; Xie, Z. X.; Tian, Z. Q.; Ren, B., *Phys. Chem. Chem. Phys.* **2013,** *15*, 4130-4135.

(39) Li, S. W.; Xu, P.; Ren, Z. Q.; Zhang, B.; Du, Y. C.; Han, X. J.; Mack, N. H.; Wang, H. L., *ACS Appl. Mater. Interfaces* **2013,** *5*, 49-54.

(40) Liang, H. Y.; Li, Z. P.; Wang, W. Z.; Wu, Y. S.; Xu, H. X., *Adv. Mater.* **2009,** *21*, 4614-4618.

(41) Mulvihill, M. J.; Ling, X. Y.; Henzie, J.; Yang, P. D., *J. Am. Chem. Soc.* **2010,** *132*, 268-274.

(42) Barbosa, S.; Agrawal, A.; Rodriguez-Lorenzo, L.; Pastoriza-Santos, I.; Alvarez-Puebla, R. A.; Kornowski, A.; Weller, H.; Liz-Marzan, L. M., *Langmuir* **2010,** *26*, 14943-14950.

(43) Rodriguez-Lorenzo, L.; Alvarez-Puebla, R. A.; de Abajo, F. J. G.; Liz-Marzan, L. M., *J. Phys. Chem. C* **2010,** *114*, 7336-7340.

(44) Khoury, C. G.; Vo-Dinh, T., *J. Phys. Chem. C* **2008,** *112*, 18849-18859.

(45) Hrelescu, C.; Sau, T. K.; Rogach, A. L.; Jackel, F.; Feldmann, J., *Appl. Phys. Lett.* **2009,** *94*, 3.

(46) Sanchez-Gaytan, B. L.; Swanglap, P.; Lamkin, T. J.; Hickey, R. J.; Fakhraai, Z.; Link, S.; Park, S. J., *J. Phys. Chem. C* **2012,** *116*, 10318-10324.

(47) Wang, H.; Goodrich, G. P.; Tam, F.; Oubre, C.; Nordlander, P.; Halas, N. J., *J. Phys. Chem. B* **2005,** *109*, 11083-11087.

(48) Jackson, J. B.; Halas, N. J., *Proc. Natl. Acad. Sci. U. S. A.* **2004,** *101*, 17930-17935.

(49) McFarland, A. D.; Young, M. A.; Dieringer, J. A.; Van Duyne, R. P., *J. Phys. Chem. B* **2005,** *109*, 11279-11285.

(50) Ross, B. M.; Lee, L. P., *Opt. Lett.* **2009,** *34*, 896-898.

(51) Zuloaga, J.; Nordlander, P., *Nano Lett.* **2011,** *11*, 1280-1283.

(52) Menzel, C.; Hebestreit, E.; Muhlig, S.; Rockstuhl, C.; Burger, S.; Lederer, F.; Pertsch, T., *Optics Express* **2014,** *22*, 9971-9982.

(53) Moreno, F.; Albella, P.; Nieto-Vesperinas, M., *Langmuir* **2013,** *29*, 6715-6721.

(54) Alonso-Gonzalez, P.; Albella, P.; Neubrech, F.; Huck, C.; Chen, J.; Golmar, F.; Casanova, F.; Hueso, L. E.; Pucci, A.; Aizpurua, J.; Hillenbrand, R., *Physical Review Letters* **2013,** *110* (20).

(55) Sivapalan, S. T.; DeVetter, B. M.; Yang, T. K.; van Dijk, T.; Schulmerich, M. V.; Carney, P. S.; Bhargava, R.; Murphy, C. J., *ACS Nano* **2013,** *7*, 2099-2105.

(56) Chiu, C. Y.; Chung, P. J.; Lao, K. U.; Liao, C. W.; Huang, M. H., *J. Phys. Chem. C* **2012,** *116*, 23757-23763.

(57) Personick, M. L.; Mirkin, C. A., *J. Am. Chem. Soc.* **2013,** *135*, 18238-18247.

(58) Yu, Y.; Zhang, Q. B.; Lu, X. M.; Lee, J. Y., *J. Phys. Chem. C* **2010,** *114*, 11119-11126.

(59) Eguchi, M.; Mitsui, D.; Wu, H. L.; Sato, R.; Teranishi, T., *Langmuir* **2012,** *28*, 9021-9026.

(60) Ming, T.; Feng, W.; Tang, Q.; Wang, F.; Sun, L. D.; Wang, J. F.; Yan, C. H., *J. Am. Chem. Soc.* **2009,** *131*, 16350-16351.

(61) Yin, P. G.; You, T. T.; Tan, E. Z.; Li, J.; Lang, X. F.; Jiang, L.; Guo, L., *J. Phys. Chem. C* **2011,** *115*, 18061-18069.

(62) Ma, Y. Y.; Kuang, Q.; Jiang, Z. Y.; Xie, Z. X.; Huang, R. B.; Zheng, L. S., *Angew. Chem.-Int. Edit.* **2008,** *47*, 8901-8904.

(63) Zhang, J.; Langille, M. R.; Personick, M. L.; Zhang, K.; Li, S. Y.; Mirkin, C. A., *J. Am. Chem. Soc.* **2010,** *132*, 14012-14014.

(64) Hong, J. W.; Lee, S. U.; Lee, Y. W.; Han, S. W., *J. Am. Chem. Soc.* **2012,** *134*, 4565-4568.

(65) Zhang, Q. F.; Large, N.; Nordlander, P.; Wang, H., *J. Phys. Chem. Lett.* **2014,** *5*, 370-374.

(66) Huang, Y. J.; Wu, L.; Chen, X. D.; Bai, P.; Kim, D. H., *Chem. Mat.* **2013,** *25*, 2470-2475.

(67) Sau, T. K.; Murphy, C. J., *J. Am. Chem. Soc.* **2004,** *126*, 8648-8649.

(68) Rycenga, M.; Langille, M. R.; Personick, M. L.; Ozel, T.; Mirkin, C. A., *Nano Lett.* **2012,** *12*, 6218-6222.

(69) Malynych, S.; Luzinov, I.; Chumanov, G., *J. Phys. Chem. B* **2002,** *106*, 1280-1285.

(70) Mohri, N.; Matsushita, S.; Inoue, M.; Yoshikawa, K., *Langmuir* **1998,** *14*, 2343-2347.

(71) Kumbhar, A. S.; Kinnan, M. K.; Chumanov, G., *J. Am. Chem. Soc.* **2005,** *127*, 12444-12445.

(72) Rodriguez-Fernandez, J.; Perez-Juste, J.; de Abajo, F. J. G.; Liz-Marzan, L. M., *Langmuir* **2006,** *22*, 7007-7010.

(73) Xie, J.; Lee, J. Y.; Wang, D. I. C., *Chem. Mat.* **2007,** *19*, 2823-2830.

(74) Dam, D. H. M.; Lee, J. H.; Sisco, P. N.; Co, D. T.; Zhang, M.; Wasielewski, M. R.; Odom, T. W., *ACS Nano* **2012,** *6*, 3318-3326.

(75) Nehl, C. L.; Liao, H. W.; Hafner, J. H., *Nano Lett.* **2006,** *6*, 683-688.

(76) Yamamoto, M.; Kashiwagi, Y.; Sakata, T.; Mori, H.; Nakamoto, M., *Chem. Mater.* **2005,** *17*, 5391-5393.

(77) Hao, F.; Nehl, C. L.; Hafner, J. H.; Nordlander, P., *Nano Lett.* **2007,** *7*, 729-732.

(78) Link, S.; El-Sayed, M. A., *J. Phys. Chem. B* **1999,** *103*, 8410-8426.

(79) Murphy, C. J.; San, T. K.; Gole, A. M.; Orendorff, C. J.; Gao, J. X.; Gou, L.; Hunyadi, S. E.; Li, T., *J. Phys. Chem. B* **2005,** *109*, 13857-13870.

(80) Johnson, P. B.; Christy, R. W., *Physical Review B* **1972,** *6*, 4370-4379.

CHAPTER 5

Facet-Dependent Catalytic Activities of Au Nanoparticles Enclosed by High-Index Facets

5.1 Introduction

Intriguing nanoscale effects are broadly involved in heterogeneous catalysis, which can probably be best manifested by the size-dependent catalytic activities observed on Au nanoparticles (NPs).[1-6] In striking contrast to their mesoscopic and bulk counterparts that are chemically inert, sub-5 nm Au NPs supported on high-surface-area oxide materials exhibit exceptionally high catalytic activities toward a series of oxidation and hydrogenation reactions under mild conditions.[1-10] It is ubiquitously believed that the undercoordinated surface atoms located at the particle corners and edges, whose abundance increases significantly as the particle size shrinks down to the sub-5 nm size regime, provide a key contribution to the remarkable catalytic activities of small Au NPs.[6,11-13] Interestingly, free-standing dealloyed nanoporous Au membranes also possess highly curved local surface structures with high fraction of undercoordinated surface atoms and thus exhibit similar catalytic activities as the oxide-supported sub-5 nm Au NPs even though their nanopores and ligaments are far beyond 5 nm in size.[14-17] Building detailed, quantitative correlation between the surface structures and the intrinsic catalytic activities of Au, however, has been extremely challenging due to the structural and compositional complexity of these nanocatalyst systems. Both the oxide supports in contact with the Au NPs[18,19] and the residual Ag present in the dealloyed Au nanoporous membranes[17,20] have been found to have strong synergistic effects on the overall catalytic competence of the materials. In addition, the lack of precise control over the atomic-level surface structures of these Au nanocatalysts remains a substantial obstacle to the elucidation of detailed structure-property relationship that underpins the Au-based heterogeneous catalysis.

In this chapter, we endeavor to gain quantitative insights into the intrinsic facet-dependent catalytic activities of Au NPs using the room temperature catalytic hydrogenation of 4-nitrothiophenol (4-NTP) as a model reaction. We are particularly interested in the catalytic activities of high-index facets of Au because high-index facets are open surface structures with high densities of coordinatively unsaturated atoms at the surface steps and kinks and thereby exhibit dramatically enhanced catalytic activities toward a variety of chemical and electrochemical reactions in comparison to the close-packed low-index facets.[21-23] In this work, Au elongated tetrahexahedral (ETHH), concave cubic (CC), and trisoctahedral (TOH) NPs are selected as three representative model nanostructures each of which is exclusively enclosed by one specific type of high-index facets. The Au ETHH, CC, and TOH NPs are all in the subwavelength size regime with well-defined facets significantly larger than 5 nm in size, ensuring that the catalytic activities are essentially determined by the characteristic distribution of undercoordinated surface atoms on each type of facets rather than those at the particle corners and edges. Distinct from the sub-5 nm Au NPs whose plasmon resonances are vanishingly weak, subwavelength Au ETHH, CC, and TOH NPs exhibit appealing plasmonic properties that enable the use of surface-enhanced Raman scattering (SERS) as a unique noninvasive ultrasensitive spectroscopic tool to precisely monitor, in real time, the molecular transformations occurring at the molecule catalyst interfaces.[24-28]

5.2 Experimental Section

Chemicals and Materials. All reagents were used as received without further purification. Ultrapure water (18.2 MΩ resistivity, Barnstead EasyPure II 7138) was used for all experiments. Silicon wafers were obtained from University Wafers.

Synthesis of Au Elongated Tetrahexahedral (ETHH) Nanoparticles. Au ETHH nanoparticles were prepared following a recently reported protocol[31] with some minor modifications. Colloidal Au seeds were prepared by the reducing $HAuCl_4$ with $NaBH_4$ in the presence of CTAB. In a typical procedure, 0.60 mL of ice-cold, freshly prepared $NaBH_4$ (10 mM) were quickly injected into a solution composed of CTAB (9.75 mL, 0.10 M) and $HAuCl_4$ (0.25 mL, 10 mM) under magnetic stir (1000 rpm). The seed solution was stirred for 1 min and then left undisturbed for 2 h. The seed solution was diluted by 50-fold with CTAB (0.10 M) and the diluted seed solution was used for the subsequent seed-mediated growth. The growth solution was prepared by sequentially adding $HAuCl_4$ (2.0 mL, 10 mM), $AgNO_3$ (0.40 mL, 10 mM), HCl (0.80 mL, 1.0 M), and AA (0.32 mL, 0.10 M) into a CTAB (40.00 mL, 0.10 M) solution. After gently mixing the growth solution for 30 s, the growth of Au ETHH nanoparticles was initiated by adding 0.1 mL of the diluted Au seed solution. The reaction solution was gently mixed for 30 s immediately after the addition of Au seeds and then left undisturbed at 30 ^{o}C for overnight. The obtained Au ETHH nanoparticles were washed with water twice through centrifugation-redispersion cycles, and finally redispersed in 5.0 mL of water.

Synthesis of Au Concave Cubic (CC) Nanoparticles. Au CC nanoparticles were prepared following a previously reported seed-mediated growth protocol[33] with minor modifications. Colloidal Au seeds were first prepared by the reducing $HAuCl_4$ with $NaBH_4$ in the presence of CTAC. In a typical procedure, 0.30 mL of ice-cold, freshly prepared $NaBH_4$ (10 mM) were quickly injected into a solution composed of CTAC (10.00 mL, 0.10 M) and $HAuCl_4$ (0.25 mL, 10 mM) under magnetic stir (1000 rpm). The seed solution was stirred for 1 min and then left undisturbed for 2 h. The seed solution

was diluted by 1000-fold with CTAC (0.10 M) and the diluted seed solution was used for the subsequent seed-mediated growth. Then the growth solution was prepared by sequentially adding $HAuCl_4$ (0.50 mL, 10 mM), $AgNO_3$ (0.1 mL, 10 mM), HCl (0.20 mL, 1.0 M), and AA (0.10 mL, 0.10 M) into a CTAC (10.00 mL, 0.10 M) solution. After gently mixing the growth solution for 30 s, the growth of Au CC nanoparticles was initiated by adding 0.1 mL of the diluted Au seed solution. The reaction solution was gently mixed for 30 s immediately after the addition of Au seeds and then left undisturbed at room temperature for 4 h. The obtained Au CC nanoparticles were washed with water twice through centrifugation-redispersion cycles, and finally redispersed in 5.0 mL of water.

Synthesis of Au Trisoctahedral (TOH) Nanoparticles. Au TOH nanoparticles were prepared following our previous protocol based on seed-mediated growth. Colloidal Au seeds were prepared by the reducing $HAuCl_4$ with $NaBH_4$ in the presence of CTAC. In a typical procedure, 0.30 mL of ice-cold, freshly prepared $NaBH_4$ (10 mM) were quickly injected into a solution composed of CTAC (10.00 mL, 0.10 M) and $HAuCl_4$ (0.25 mL, 10 mM) under magnetic stir (1000 rpm). The seed solution was stirred for 1 min and then left undisturbed for 2 h. The seed solution was diluted by 1000-fold with CTAC (0.10 M) and the diluted seed solution was used for the subsequent seed-mediated growth. The growth solution was prepared by sequentially adding $HAuCl_4$ (0.50 mL, 10 mM) and AA (1.0 mL, 0.10 M) into a CTAC (10.00 mL, 0.10 M) solution. After gently mixing the growth solution for 30 s, the growth of Au TOH nanoparticles was initiated by adding 0.015 mL of the diluted Au seed solution. The reaction solution was gently mixed for 30 s immediately after the addition of Au seeds and then left undisturbed at room

temperature for 4 h. The obtained Au TOH nanoparticles were washed with water twice through centrifugation redispersion cycles, and finally redispersed in 5.0 mL of water.

Synthesis of Au Quasi-Spherical (QS) Nanoparticles. Au QS nanoparticles were prepared following a previously published protocol with minor modification. Reducing chloroauric acid with formaldehyde at room temperature led to the formation of Au QS nanoparticles. In a typical procedure, 25.0 mg of K_2CO_3 was dissolved in 100 mL of water, followed by the addition of $HAuCl_4$ (1.5 mL, 25.0 mM). The mixture solution was aged in the dark for 18 h. Then 0.167 mL of formaldehyde solution (37 wt %) was added into the mixture under magnetic stir (300 rpm). A brick-red colloidal suspension began to form after ~15 min. The colloidal suspension was kept stirring for 30 min. The obtained Au QS nanoparticles were washed with water twice through centrifugation-redispersion cycles, and finally redispersed in 5.0 mL of water.

Characterizations. The morphologies and structures of the nanoparticles were characterized by transmission electron microscopy (TEM) and selected area electron diffraction (SAED) using a Hitachi H-8000 transmission electron microscope operated at an accelerating voltage of 200 kV. All samples for TEM measurements were dispersed in water and drop-dried on 200 mesh Formvar/carbon-coated Cu grids. The structures of the nanoparticles were also characterized by SEM using a Zeiss Ultraplus thermal field emission scanning electron microscope. The samples for SEM measurements were dispersed in water and drop-dried on silicon wafers. The optical extinction spectra of the nanoparticles were measured on aqueous colloidal suspensions at room temperature, using a Beckman Coulter Du 640 spectrophotometer.

Time-Resolved SERS Measurements. The facet-dependent catalytic reaction kinetics was measured by time-resolved SERS. 100 μL colloidal suspensions of Au ETHH, CC, TOH, and QS nanoparticles with the same particle concentrations (~ 10^{10} particles mL^{-1}) were each incubated with 500 μL ethanol solution of 1.0 mM 4-NTP overnight to form self-assembled monolayers of 4-NTP on the nanoparticle surfaces. Then the nanoparticles were centrifuged (3500 rpm, 3 min) and redispersed in 50 μL ultrapure H_2O. The catalytic 4-NTP hydrogenation occurred at room temperature upon the addition of 50 μL of 200 mM $NaBH_4$ in a 0.5 mL Eppendorf centrifuge tube. SERS spectra were obtained on a Bayspec *Nomadic*^{TM} confocal Raman microscopy built on an Olympus BX51 reflected optical system with a 785 nm continuous wave excitation laser. The excitation laser was focused on the reaction mixture using a 10× objective [Numerical Aperture (NA) = 0.30, working distance (WD) = 11.0 mm, Olympus MPLFLN]. The laser power was measured to be 10.0 mW at the samples and the signal acquisition times were 1 s for ETHH and CC, 5 s for TOH, and 10 s for QS nanoparticles, respectively. Successive SERS spectra were collected in real time during the reactions until complete reduction of 4-NTP into 4-ATP.

5.3 Results and Discussions

For Au NPs with face-centered cubic (fcc) crystalline structures, the surface energies of the low-index {111} and {100} facets are significantly lower than the {110} and other high-index facets.[22,29] As a consequence, Au nanoparticles enclosed by the low energy facets, such as nanocubes ({100} facets), nano-octahedra ({111} facets), and multi-twined quasi-spherical NPs ({111} and {100} facets), represent the most stable

nanoparticle geometries that are experimentally realizable. Although synthetically more challenging, polyhedral Au NPs enclosed by various types of high-index facets have been fabricated through facet-controlled nanocrystal growth processes.[30-34] Here we adopted a versatile seed-mediated growth method to fabricate Au ETHH, CC, and TOH NPs in a shape-selective and size-controlled manner. As shown by the scanning electron microscopy (SEM) and transmission electron microscopy (TEM) images in Figure 5.1, the as-fabricated Au ETHH, CC, and TOH NPs all exhibited high monodispersity in terms of both particle sizes and morphologies. An ETHH NP is derived geometrically from a nanocuboid enclosed by 6 {100} facets upon introduction of surface convexity (Figures 5.1A-C). The Au ETHH NPs displayed different projected contours in the TEM images when they were orientated differently on the TEM grid and the orientation-dependent projection contours fit the geometric model very well. The insets of Figure 5.1C show the TEM image and selected area electron diffraction (SAED) pattern of one ETHH NP imaged with the electron beam projected along the [001] zone axis. Under this orientation, 8 out of the 24 facets became parallel to the projection direction, allowing us to measure the characteristic dihedral angles as labeled in the figure. This result indicates that each ETHH NP is enclosed by 24 high-index {730} facets.[31] A CC NP is geometrically derived by introducing tetragonal indentation to each {100} facet of a nanocube (Figures 5.1D and 5.1E). Each CC NP appeared darker in the interior regions than in the edge regions and displayed orientation-dependent projection profiles and contrast in the TEM images. The insets of Figure 5.1E show the TEM image and SAED pattern of one CC NP imaged with the electron beam projected along the [001] zone axis. While the Au CC NP appeared to have a cubic morphological outline under this

projection, the degree of indentation could be characterized by measuring the indentation angles (the dihedral angle between indented facets) based on the different contrast in the TEM image. As marked in the figure, the indentation angles were measured to be 136 ± 1 °, indicating that each Au CC NP is enclosed by 24 high-index {520} facets. The as-fabricated Au CC NPs exhibited a higher degree of indentation in comparison to the Au CC NPs with {720} facets (indentation angle of 148 °) previously reported by Mirkin and co-workers.[33] A TOH NP is obtained by creating a trigonal pyramid on each triangular {111} facet of a nanooctahedron (Figures 5.1F and 5.1G). The insets of Figure 5.1G show the TEM image and the SAED pattern of one Au TOH NP projected from the [011] zone axis. Under this orientation, 4 out of the 24 facets of the TOH NP were projected edge-on, and the exposed facets were determined to be {221}[32] through analysis of the characteristic projection angles marked in the figure. The TEM projection outlines of individual TOH NPs with various orientations are clearly observed, which is a great agreement with the geometric model. The single-crystalline Au ETHH, CC, and TOH NPs provided unique NP systems for us to quantitatively compare the catalytic activities of three types of high-index facets, {730}, {520}, and {221} facets. We also fabricated multi-twinned Au quasi-spherical (QS) NPs enclosed by {100} and {111} facets (Figures 5.1H and 5.1I) to further compare the catalytic activities of the high-index facets with those of the low-index facets.

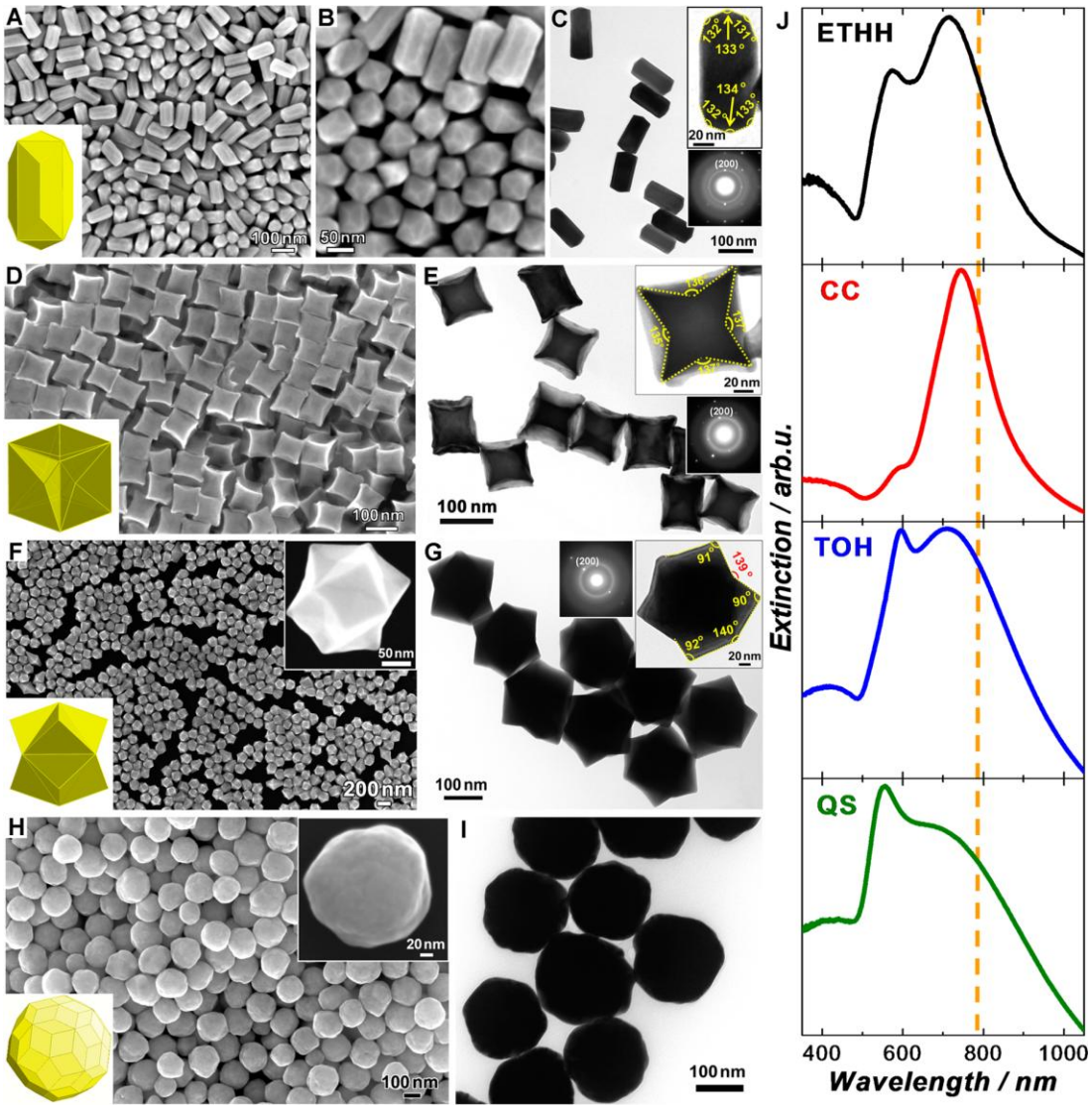

Figure 5.1. Structures of Au ETHH, CC, TOH, and QS NPs. (A, B) SEM images of Au ETHH NPs. The inset of panel A shows the geometric model of an ETHH NP. (C) TEM images of Au ETHH NPs (insets: high-magnification TEM image and SAED pattern of an individual Au ETHH NP viewed along the [001] projection). (D) SEM image of Au CC NPs (inset: geometric model of a CC NP). (E) TEM image of Au CC NPs (insets: high-magnification TEM image and SAED pattern of an individual Au CC NP viewed along the [001] projection). (F) SEM image of Au TOH NPs (upright inset: high-magnification SEM image of an individual Au TOH NP; bottom left inset: geometric model of a TOH NP). (G) TEM image of Au TOH NPs (insets: high-magnification TEM image and SAED pattern of an individual Au TOH NP viewed along the [011] projection). (H) SEM image of Au QS NPs (upright inset: high-magnification SEM image of an individual Au QS NP; bottom left inset: geometry model of a QS NP). (I) TEM image of Au QS NPs. (J) Optical extinction spectra of colloidal suspensions of Au ETHH, CC, TOH, and QS NPs. The vertical dashed line indicates the wavelength (785 nm) of the excitation laser for SERS measurements.

Using the seed-mediated growth method, the size of the NPs can be precisely controlled for each geometry by adjusting the amount of Au seeds added into the reaction mixtures. The Au ETHH, CC, and TOH NPs all exhibited size-dependent plasmonic tunability, allowing us to fine-tune, through deliberate size control, their plasmon resonances with respect to the excitation laser wavelength to achieve optimal SERS enhancements on individual NPs. While on-resonance excitations typically generate higher Raman enhancements than the off-resonance excitations,[35] the far-field plasmon resonance bands do not overlap exactly with the wavelengths at which the largest near-field enhancements are achieved. It has been demonstrated both theoretically and experimentally on various metallic nanostructures that the maximum near-field enhancements occurred at longer wavelengths relative to the far-field extinction peaks.[36-40] With this key design principle in mind, the characteristic plasmon resonances of the Au ETHH, CC, TOH, and QS NPs were all tuned to be within the same spectral region that was blue-shifted by 35 to 70 nm in wavelength with respect to the excitation laser (785 nm). As shown in Figure 5.1J, subwavelength Au ETHH, CC, TOH, and QS NPs exhibited their own geometry-dependent plasmonic characteristics. Due to the rod-like anisotropic structures, colloidal Au ETHH NPs exhibited a longitudinal and a transverse plasmon bands at ~720 nm and ~570 nm, respectively. Au CC NPs displayed a well-define dipole plasmon resonance band at ~750 nm and a quadrupole shoulder at ~590 nm. Due to the phase retardation effects,[41] the dipole plasmon bands of TOH and QS NPs were both significantly broadened, and sharper quadrupole bands emerged at shorter wavelengths relative to the dipole bands.

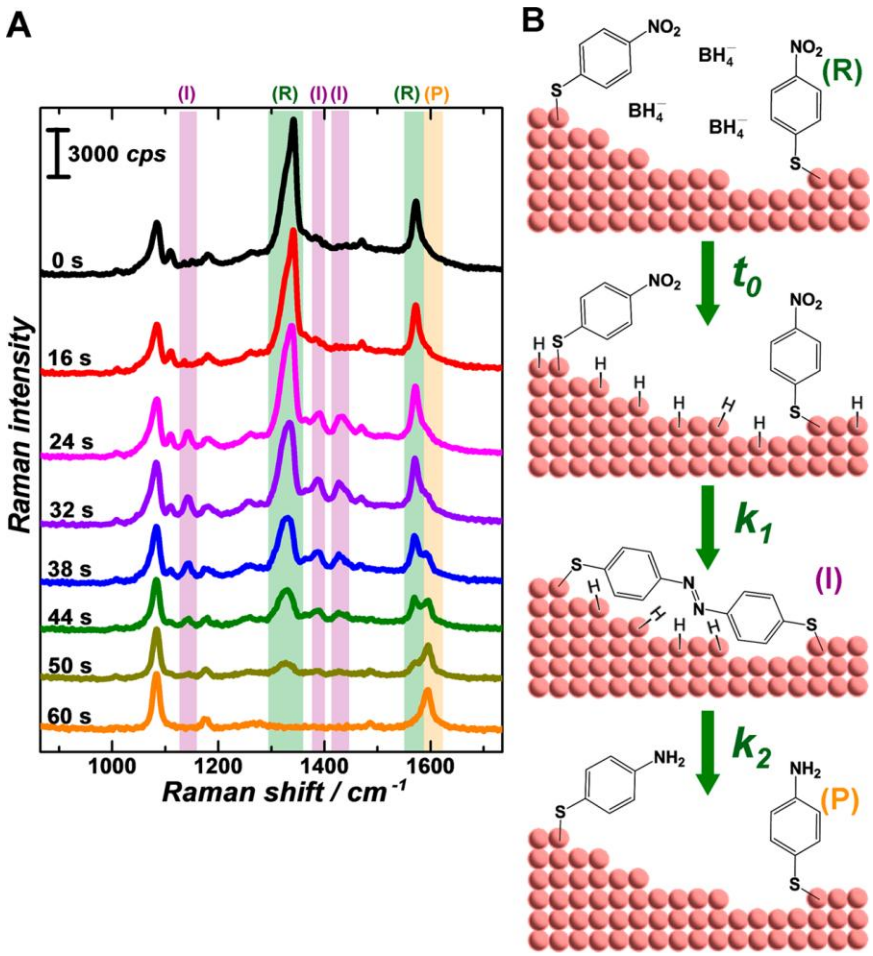

Figure 5.2. Monitoring surface-catalyzed reactions on Au CC NPs by time-resolved SERS. (A) Representative SERS spectra collected from 4-NTP adsorbed on the surfaces of Au CC NPs at different reaction times of 0, 16, 24, 32, 38, 44, 50, and 60 s after introducing $NaBH_4$. The spectra were offset for clarity. (B) Schematic illustration of the reduction of surface-adsorbed 4-NTP (reactant, R) to DMAB (intermediate, I) and finally to 4-ATP (product, P).

We used SERS to monitor, in real time, the catalytic hydrogenation of 4-NTP adsorbed on the surfaces of the Au ETHH, CC, TOH, and QS NPs. Colloidal suspensions of the NPs were first incubated with ethanolic solution of 4-NTP overnight to undergo a ligand exchange process through which saturated self-assembled monolayers (SAMs) of 4-NTP were immobilized on the NP surfaces. The 4-NTP-coated NPs were redispersed as colloidal suspensions in water, and the catalytic reactions were initiated upon introduction of $NaBH_4$ at room temperature (298 K). Figure 5.2A shows the evolution of

SERS spectra upon exposure of 4-NTP-coated Au CC NPs to 100 mM $NaBH_4$. 4-NTP showed three characteristic SERS bands at 1076, 1338, and 1571 cm^{-1}, respectively.[26-28] Upon exposure to $NaBH_4$, there was an induction time (t_0) of ~20 s during which the SERS features of 4-NTP remained unchanged. This induction time is most likely due to the formation of active surface hydrogen species upon adsorption of borohydride ions onto the Au surfaces.[42] Only when the concentration of the surface hydrogen species was built up to a certain threshold value was the hydrogenation of 4-NTP initiated. As the reaction proceeded, the peak intensities at both 1338 and 1571 cm^{-1} decreased progressively with the concomitant emergence of a new Raman peak at 1590 cm^{-1}, which was assigned to 4-aminothiophenol (4-ATP).[28] The time-resolved SERS measurements also allowed us to identify 4,4′-dimercaptoazobenzene (DMAB), whose characteristic Raman modes are at 1140, 1388, and 1438 cm^{-1},[43-45] as an intermediate species formed during the reaction. Based on the spectroscopic evolution observed in the SERS measurements, a possible reaction mechanism is proposed, which is schematically illustrated in Figure 5.2B. The Au NP-catalyzed hydrogenation of 4-NTP by $NaBH_4$ involves three major steps: (1) generation of surface-hydrogen species upon adsorption of borohydride ions to Au surfaces; (2) reduction of surface-adsorbed 4-NTP by the surface-hydrogen species to form the intermediate, DMAB; and (3) further hydrogenation of DMAB into the final product, 4-ATP. Although similar spectral evolutions were observed on Au ETHH, TOH, and QS NPs, the reaction rates varied significantly among the Au NPs of different geometries.

The time-resolved SERS results clearly showed that the catalytic reaction rates decreased in the order of ETHH > CC ≫ TOH > QS NPs. The facet-dependent catalytic

activities observed here were intimately tied to the distribution of coordinatively unsaturated surface atoms on various facets. The atomic-level structures of {730} (ETHH NPs), {520} (CC NPs), {221} (TOH NPs), and {111} + {100} (QS NPs) facets are schematically illustrated in Figures 5.3A-5.3D, respectively, based on which the fractions of surface atoms with different coordination numbers can be calculated. We used the Raman modes at 1338 and 1590 cm^{-1} to quantify the fraction of 4-NTP and 4-ATP molecules, respectively, at various reaction times. Under our experimental conditions, $NaBH_4$ (100 mM) was in excess, and its concentration maintained constant throughout the entire reaction processes. Therefore, this catalytic reaction obeyed pseudo-first-order kinetics, and the induction times and rate constants were obtained by performing least-squares curve fitting to the reactant and product trajectories shown in Figures 3E-3H. The rate equations for this two-step consecutive reaction are listed as follows:

$$\theta_R = e^{-k_1 \times (t - t_0)} \quad (1),$$

$$\theta_P = 1 - \frac{(k_1 \times e^{-k_2 \times (t - t_0)} - k_2 \times e^{-k_1 \times (t - t_0)})}{k_2 - k_1} \quad (2),$$

$$\theta_I = 1 - \theta_R - \theta_P \quad (3),$$

where θ_R, θ_P, and θ_I are the fractions of 4-NTP, 4-ATP, and the intermediate (DMAB), respectively. k_1 and k_2 are the rate constants for the first and second hydrogenation steps, respectively, and t_0 is the induction time. During the catalytic reactions, successive SERS spectra were collected in real time until complete hydrogenation of 4-NTP into 4-ATP. The time resolutions of the kinetic measurements were limited by the integration times for SERS spectral collection, which were 1 s for ETHH and CC, 5 s for TOH, and 10 s for QS NPs, respectively, under the current experimental conditions. Although the

excitation of plasmon resonances may enhance the rates of some catalytic surface reactions,[46,47] the catalytic 4-NTP hydrogenation was found to be neither driven by plasmons nor affected by the coupling of plasmon excitations to the reaction coordinates. The reaction rates were observed to remain essentially unchanged when various time intervals (the excitation laser was blocked by a laser beam shutter) were introduced between SERS spectral collections.

In Figures 5.3I and 5.3J, we compare the rate constants and induction times on various Au NPs. The increase in rate constants was accompanied by decrease in induction times. Interestingly, the k_2 was significantly larger than k_1 on all four nanostructures, and, as a consequence, the fraction of the intermediate remained low during the reactions (see the blue dash curves in Figures 5.3E-5.3H). However, the high detection sensitivity of SERS and the large Raman cross-section of DMAB[43-45] allowed us to indentify DMAB as the intermediate and further resolve the complex kinetics of the two-step reaction. It is apparent that all the high-index facets were catalytically more active than the low-index {111} and {100} facets. The observed facet-dependent catalytic activities correlated well with the characteristic distributions of undercoordinated surface atoms on various facets as shown in Figure 5.3K. The {730} facets of ETHH NPs and {520} facets of CC NPs showed significantly higher catalytic activities than the {221} facets of TOH NPs because both the {730} and {520} facets have significant fraction of surface atoms with a coordination number of 6, while the lowest surface atomic coordination number on the {221} facets is 7. The {730} facets were observed to be more active than the {520} facets largely due to the higher fraction of surface atoms with coordination number of 6. In contrast, the low-index {100} and {111} facets only have surface atomic coordination

numbers of 8 and 9, respectively, and thus showed much lower catalytic activities than the high-index facets.

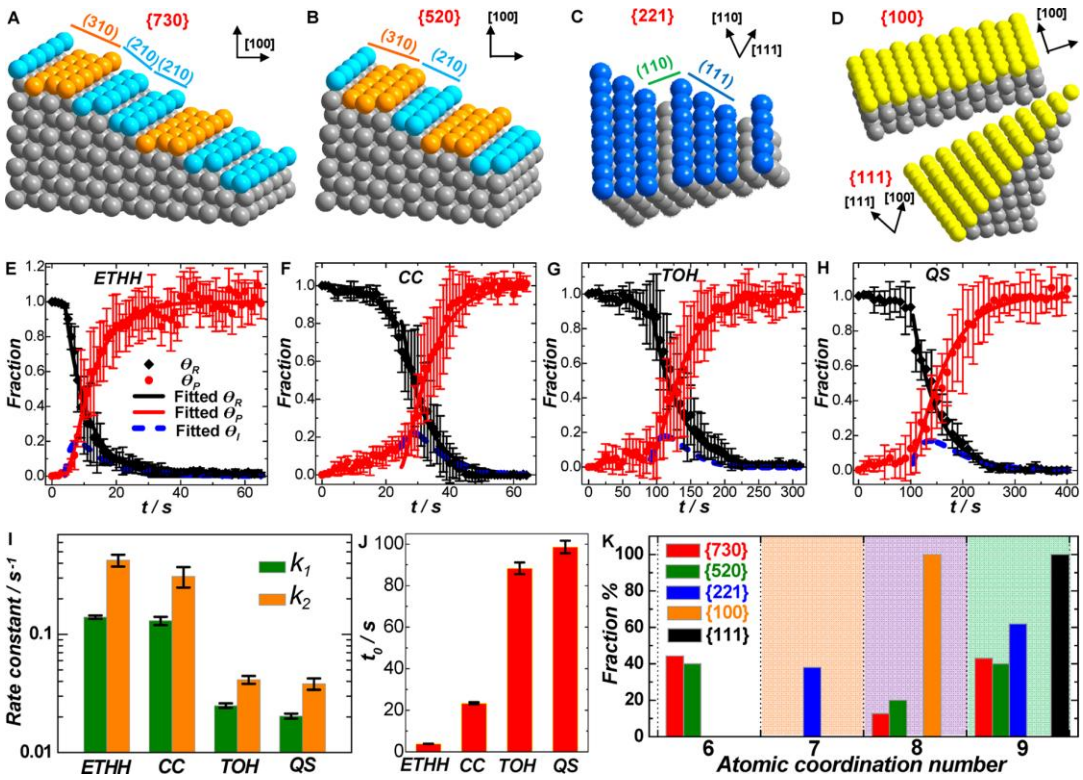

Figure 5.3. Facet-dependent catalytic activities of Au NPs. Schemes of the atomic level surface structures of (A) the {730} facet of Au ETHH NPs, (B) the {520} facet of Au CC NPs, (C) the {221} facet of Au TOH NPs, and (D) the {111} and {100} facets of Au QS NPs. (E-H) Fraction of reactant (θ_R), intermediate (θ_I), and product (θ_P) as a function of reaction time during the reactions catalyzed by Au (E) ETHH, (F) CC, (G) TOH, and (H) QS NPs. The error bars show the standard deviations obtained from five experimental runs. The results of the least-squares fitting are shown as solid curves for the reactants and products. The fitted results for the intermediate trajectories are shown as dash blue curves. Panels E-H share the same legends in Panel E. (I) The comparison of rate constants, k_1 and k_2, of the two-step surface reactions on Au ETHH, CC, TOH, and QS nanoparticles. (J) The comparison of induction time, t_0, of the reactions on Au ETHH, CC, TOH, and QS NPs. (K) Fraction of the coordination numbers of the surface atoms for the {730} (ETHH), {520} (CC), {221} (TOH), and {111}/{100} (QS) facets.

Using this SERS-based approach to monitor the surface-catalyzed reactions has several unique advantages. Because both the reactant and product molecules were immobilized as SAMs on the nanocatalyst surfaces, it became possible to unravel the intrinsic surface reaction kinetics with minimal complication introduced by the surface-capping ligands as

well as the diffusion, adsorption, and desorption of reactants and products. In addition, the catalytic reaction kinetics probed by SERS of surface-immobilized SAMs was independent of the total nanocatalyst surface areas, i.e. the concentrations of the colloidal Au NPs, in the presence of excessive $NaBH_4$, which was quantitatively demonstrated on porous Au NPs in a recent publication[48] and was further verified on the Au ETHH, CC, and TOH NPs in this work. This allowed us to compare the catalytic activities of various Au facets without the necessity to normalize the particle surface areas for different geometries. Furthermore, the high sensitivity and unique fingerprinting capability of SERS enabled the identification of transient intermediates along the reaction pathways. In our SERS measurements, we used a confocal Raman microscope with the laser beam focused into a small volume of the colloidal NP suspensions, and the SERS signals were collected from an observation volume of ~100 pL. Therefore, each freely diffusing NP was exposed to the excitation laser for a short time period (within the diffusion time), effectively eliminating the plasmon-driven photoconversion of 4-NTP to DMAB[43,45] and photo-induced sample damage. The relatively low excitation power (10.0 mW CW laser) and limited exposure time of each diffusing NP to the confocal laser beam also effectively minimized photothermal effects and suppressed other possible plasmon-enhanced surface reactions, allowing one to precisely measure the intrinsic kinetics of the catalytic chemical transformations occurring at the NP-molecule interfaces.

Our results provide clear experimental evidence on the critical contribution of undercoordinated surface atoms to the catalytic activities of Au NPs. The quantitative insights on the intrinsic facet-dependent catalytic activities of Au NPs gained through this

work provide important information that guides the rational design and construction of nanoarchitectured Au surfaces for the optimization of heterogeneous catalysis.

5.4 Conclusions

In summary, we employed surface-enhanced Raman scattering as a noninvasive in situ spectroscopic tool to quantitatively study the intrinsic facet-dependent catalytic activities of colloidal subwavelength Au nanoparticles enclosed by various types of well-defined high-index facets using the catalytic hydrogenation of 4-nitrothiophenol as a model reaction. Our results provide compelling experimental evidence on the crucial roles of undercoordinated surface atoms in Au-based heterogeneous catalysis and shed light on the underlying relationship between the atomic-level surface structures and the intrinsic catalytic activities of Au nanocatalysts.

5.5 References

(1) Haruta, M.; Date, M. *Appl. Catal., A* **2001**, *222*, 427-437.

(2) Ishida, T.; Haruta, M. *Angew. Chem., Int. Ed.* **2007**, *46*, 7154-7156.

(3) Valden, M.; Lai, X.; Goodman, D. W. *Science* **1998**, *281*, 1647-1650.

(4) Schimpf, S.; Lucas, M.; Mohr, C.; Rodemerck, U.; Bruckner, A.; Radnik, J.; Hofmeister, H.; Claus, P. *Catal. Today* **2002**, *72*, 63-78.

(5) Overbury, S. H.; Schwartz, V.; Mullim, D. R.; Yan, W. F.; Dai, S. *J. Catal.* **2006**, *241*, 56-65.

(6) Hvolbaek, B.; Janssens, T. V. W.; Clausen, B. S.; Falsig, H.; Christensen, C. H.; Norskov, J. K. *Nano Today* **2007**, *2*, 14-18.

(7) Hughes, M. D.; Xu, Y. J.; Jenkins, P.; McMorn, P.; Landon, P.; Enache, D. I.; Carley, A. F.; Attard, G. A.; Hutchings, G. J.; King, F.; Stitt, E. H.; Johnston, P.; Griffin, K.; Kiely, C. J. *Nature* **2005**, *437*, 1132-1135.

(8) Zanella, R.; Louis, C.; Giorgio, S.; Touroude, R. *J. Catal.* **2004**, *223*, 328-339.

(9) Chen, M. S.; Goodman, D. W. *Science* **2004**, *306*, 252-255.

(10) Green, I. X.; Tang, W. J.; Neurock, M.; Yates, J. T. *Science* **2011**, *333*, 736-739.

(11) Janssens, T. V. W.; Clausen, B. S.; Hvolbaek, B.; Falsig, H.; Christensen, C. H.; Bligaard, T.; Norskov, J. K. *Top. Catal.* **2007**, *44*, 15-26.

(12) Lemire, C.; Meyer, R.; Shaikhutdinov, S.; Freund, H. J. *Angew. Chem., Int. Ed.* **2004**, *43*, 118-121.

(13) Yim, W. L.; Nowitzki, T.; Necke, M.; Schnars, H.; Nickut, P.; Biener, J.; Biener, M. M.; Zielasek, V.; Al-Shamery, K.; Kluner, T.; Baumer, M. *J. Phys. Chem. C* **2007**, *111*, 445-451.

(14) Wittstock, A.; Zielasek, V.; Biener, J.; Friend, C. M.; Baumer, M. *Science* **2010**, *327*, 319-322.

(15) Wittstock, A.; Baumer, M. *Acc. Chem. Res.* **2014**, *47*, 731-739.

(16) Zielasek, V.; Jurgens, B.; Schulz, C.; Biener, J.; Biener, M. M.; Hamza, A. V.; Baumer, M. *Angew. Chem., Int. Ed.* **2006**, *45*, 8241-8244.

(17) Fujita, T.; Guan, P. F.; McKenna, K.; Lang, X. Y.; Hirata, A.; Zhang, L.; Tokunaga, T.; Arai, S.; Yamamoto, Y.; Tanaka, N.; Ishikawa, Y.; Asao, N.; Erlebacher, J.; Chen, M. W. *Nat. Mater.* **2012**, *11*, 775-780.

(18) van Bokhoven, J. A.; Louis, C.; T Miller, J.; Tromp, M.; Safonova, O. V.; Glatzel, P. *Angew. Chem., Int. Ed.* **2006**, *45*, 4651-4654.

(19) Molina, L. M.; Hammer, B. *Phys. Rev. Lett.* **2003**, *90*, 206102.

(20) Moskaleva, L. V.; Rohe, S.; Wittstock, A.; Zielasek, V.; Kluner, T.; Neyman, K. M.; Baumer, M. *Phys. Chem. Chem. Phys.* **2011**, *13*, 4529-4539.

(21) Tian, N.; Zhou, Z. Y.; Sun, S. G.; Ding, Y.; Wang, Z. L. *Science* **2007**, *316*, 732-735.

(22) Quan, Z. W.; Wang, Y. X.; Fang, J. Y. *Acc. Chem. Res.* **2013**, *46*, 191-202.

(23) Zhang, H.; Jin, M. S.; Xia, Y. N. *Angew. Chem., Int. Ed.* **2012**, *51*, 7656-7673.

(24) Heck, K. N.; Janesko, B. G.; Scuseria, G. E.; Halas, N. J.; Wong, M. S. *J. Am. Chem. Soc.* **2008**, *130*, 16592-16600.

(25) Joseph, V.; Engelbrekt, C.; Zhang, J. D.; Gernert, U.; Ulstrup, J.; Kneipp, J. *Angew. Chem., Int. Ed.* **2012**, *51*, 7592-7596.

(26) Xie, W.; Herrmann, C.; Kompe, K.; Haase, M.; Schlucker, S. *J. Am. Chem. Soc.* **2011**, *133*, 19302-19305.

(27) Jing, H.; Zhang, Q. F.; Large, N.; Yu, C. M.; Blom, D. A.; Nordlander, P.; Wang, H. *Nano Lett.* **2014**, *14*, 3674-3682.

(28) Huang, J. F.; Zhu, Y. H.; Lin, M.; Wang, Q. X.; Zhao, L.; Yang, Y.; Yao, K. X.; Han, Y. *J. Am. Chem. Soc.* **2013**, *135*, 8552-8561.

(29) Chiu, C. Y.; Chung, P. J.; Lao, K. U.; Liao, C. W.; Huang, M. H. *J. Phys. Chem. C* **2012**, *116*, 23757-23763.

(30) Yu, Y.; Zhang, Q. B.; Lu, X. M.; Lee, J. Y. *J. Phys. Chem. C* **2010**, *114*, 11119-11126.

(31) Ming, T.; Feng, W.; Tang, Q.; Wang, F.; Sun, L. D.; Wang, J. F.; Yan, C. H. *J. Am. Chem. Soc.* **2009**, *131*, 16350-16351.

(32) Ma, Y. Y.; Kuang, Q.; Jiang, Z. Y.; Xie, Z. X.; Huang, R. B.; Zheng, L. S. *Angew. Chem., Int. Ed.* **2008**, *47*, 8901-8904.

(33) Zhang, J.; Langille, M. R.; Personick, M. L.; Zhang, K.; Li, S. Y.; Mirkin, C. A. *J. Am. Chem. Soc.* **2010**, *132*, 14012-14014.

(34) Hong, J. W.; Lee, S. U.; Lee, Y. W.; Han, S. W. *J. Am. Chem. Soc.* **2012**, *134*, 4565-4568.

(35) McFarland, A. D.; Young, M. A.; Dieringer, J. A.; Van Duyne, R. P. *J. Phys. Chem. B* **2005**, *109*, 11279-11285.

(36) Zuloaga, J.; Nordlander, P. *Nano Lett.* **2011**, *11*, 1280-1283.

(37) Menzel, C.; Hebestreit, E.; Muhlig, S.; Rockstuhl, C.; Burger, S.; Lederer, F.; Pertsch, T. *Opt. Express* **2014**, *22*, 9971-9982.

(38) Moreno, F.; Albella, P.; Nieto-Vesperinas, M. *Langmuir* **2013**, *29*, 6715-6721.

(39) Alonso-Gonzalez, P.; Albella, P.; Neubrech, F.; Huck, C.; Chen, J.; Golmar, F.; Casanova, F.; Hueso, L. E.; Pucci, A.; Aizpurua, J.; Hillenbrand, R. *Phys. Rev. Lett.* **2013**, *110*, 203902.

(40) Sivapalan, S. T.; DeVetter, B. M.; Yang, T. K.; van Dijk, T.; Schulmerich, M. V.; Carney, P. S.; Bhargava, R.; Murphy, C. J. *ACS Nano* **2013**, *7*, 2099-2105.

(41) Wang, H.; Halas, N. J. *Adv. Mater.* **2008**, *20*, 820-825.

(42) Herves, P.; Perez-Lorenzo, M.; Liz-Marzan, L. M.; Dzubiella, J.; Lu, Y.; Ballauff, M. *Chem. Soc. Rev.* **2012**, *41*, 5577-5587.

(43) Dong, B.; Fang, Y. R.; Chen, X. W.; Xu, H. X.; Sun, M. T. *Langmuir* **2011**, *27*, 10677-10682.

(44) Huang, Y. F.; Zhu, H. P.; Liu, G. K.; Wu, D. Y.; Ren, B.; Tian, Z. Q. *J. Am. Chem. Soc.* **2010**, *132*, 9244-9246.

(45) Sun, M. T.; Xu, H. X. *Small* **2012**, *8*, 2777-2786.

(46) Christopher, P.; Xin, H. L.; Linic, S. *Nat. Chem.* **2011**, *3*, 467-472.

(47) Kale, M. J.; Avanesian, T.; Christopher, P. *ACS Catal.* **2014**, *4*, 116-128.

(48) Zhang, Q.; Blom, D. A.; Wang, H. *Chem. Mater.* **2014**, *26*, 5131-5142.

CHAPTER 6

Faceted Gold Nanorods: Nanocuboids, Convex Nanocuboids, and Concave Nanocuboids

6.1 Introduction

Development of detailed, quantitative understanding of the intriguing geometry-dependent optical, electronic, and catalytic characteristics of metallic nanoparticles requires precise control over the particle shapes and facets.[1-4] One of the most impactful breakthroughs in shape-controlled nanoparticle synthesis has been the seed-mediated anisotropic growth of single-crystalline Au nanorods (NRs) guided by a structure-directing ion, Ag^{+}, and halide-containing cationic surfactants, most commonly cetyltrimethylammonium bromide (CTAB).[5-11] Au NRs have become a model system for understanding the shape evolution of highly anisotropic nanocrystals with thermodynamically unexpected shapes.[7,12,13] The protocols for NR synthesis, however, have been initially developed and gradually optimized in a largely empirical fashion.[14] The detailed mechanisms regarding the symmetry-breaking of isotropic seeds at the embryonic stage of NR formation and the driving forces of the subsequent anisotropic shape evolution are still elusive and controversial.[15-18] It still remains a significant challenge to pinpoint the effects of multiple interplaying thermodynamic, kinetic, and geometric factors that underpin the anisotropic growth of single-crystalline Au NRs.

Our enthusiasm on Au NRs stems from the unique combination of their tunable plasmon resonances with exceptional catalytic activities. The state-of-the-art NR synthesis allows one to fine-tune the plasmon resonances of Au NRs over a broad spectral range spanning the entire visible and near-infrared regions through tight control over the NR aspect ratios.[7,12-14] However, it remains significantly more challenging to fine-tailor, at the atomic level, the crystallographic facets exposed on NR surfaces,[19-26] which determine the site-specific catalytic properties of Au NRs. While Au NRs typically

exhibit a cylindrical morphology with two rounded, quasi-semispherical tips, they should be more accurately described as reconstructed anisotropic nanocrystals enclosed by various types of facets.[19-22,27,28] The quantitative assignments of the crystallographic facets on Au NRs, nevertheless, are still under intense debate,[19-21,27] and subtle modification of the NR synthesis protocols may drastically change the local curvatures and exposed facets on the NR surfaces. Recent high-resolution electron microscopic studies elucidate that each single-crystalline Au NR is essentially enclosed by coexisting high-index and low-index facets with comparable dimensions and thermodynamic stabilities.[29] The structural complexity of the NR surfaces, however, remains a substantial obstacle to the quantitative assessment of the facet-dependent intrinsic catalytic activities of Au NRs.

In this chapter, we demonstrate that controlled overgrowth of Au NRs guided by Cu^{2+} and cationic surfactants leads to the formation of various anisotropic Au nanostructures each of which is enclosed exclusively by one specific type of low-index or high-index facet. This NR overgrowth approach allows us to precisely tailor the facets of anisotropic Au nanoparticles while still retaining the capability to fine-tune the particle aspect ratios, advancing the NR synthesis toward an unprecedented level of geometry control. As demonstrated in this work, creation of well-defined facets on plasmonically tunable Au NRs provides unique opportunities for us to gain quantitative insights into the facet-dependent molecular transformations on Au nanocatalysts using surface-enhanced Raman scattering (SERS) as an ultrasensitive *in situ* spectroscopic tool.

6.2 Experimental Section

Chemicals and Materials. Gold(III) chloride trihydrate ($HAuCl_4$ $3H_2O$, ACS grade) and potassium carbonate (anhydrous) were purchased from J.T. Baker. Sodium borohydride ($NaBH_4$, 99 %), hydrochloric acid (HCl, 37 %), L-ascorbic acid (AA, 99.5 %), ammonia borane (H_6BN, AB, 97%), and 4-nitrophenol ($C_6H_5NO_3$, 4-NP, 99%) were purchased from Sigma-Aldrich. Sodium oleate (NaOL, > 97 %) and (1-hexadecyl)-trimethylammonium bromide (CTAB, > 98.0%) were purchased from TCI America. (1-hexadecyl)- trimethylammonium chloride (CTAC, 96 %), silver nitrate ($AgNO_3$, 99.9995 % metals basis), copper (II) nitrate hydrate ($Cu(NO_3)_2$ xH_2O, 99.999 % metal basis), benzyldimethylhexadecylammonium chloride (BDAC, 95 %), and 4-nitrothiophenol ($C_6H_5NO_2S$, 4-NTP, 80 %) were obtained from Alfa Aesar. Glycerol ($C_3H_8O_3$, 99.5 %) and ethanol (200 proof) were purchased from Fisher Scientific. All reagents were used as received without further purification. Ultrapure water (18.2 MΩ resistivity, Barnstead EasyPure II 7138) was used for all experiments.

Synthesis of Cylindrical Au Nanorods (NRs). Single-crystalline cylindrical Au nanorods were prepared following a previously published protocol[11] with minor modifications. Colloidal Au seeds were prepared by the reducing $HAuCl_4$ with $NaBH_4$ in the presence of CTAB. First, 5.0 mL of 0.5 mM $HAuCl_4$ was mixed with 5 mL of 0.2 M CTAB solution. Then, 1.0 mL of ice-cold, freshly prepared 6 mM $NaBH_4$ was quickly injected into the mixture under magnetic stirring (1200 rpm). The seed solution was stirred for 2 min and then left undisturbed for 30 min before use. To prepare the Au nanorods growth solution, 7.0 g of CTAB and 1.234 g of NaOL were dissolved in 250 mL of water at 60 ℃. The solution was cooled to 30 ℃ and then 18 mL of 4 mM $AgNO_3$

was added. The mixture was kept undisturbed at 30 ℃ for 15 min, followed by the addition of 250 mL of 1 mM $HAuCl_4$. The solution became colorless after 90 min of stirring at 700 rpm and 1.5 mL HCl (37 wt % in water, 12.1 M) was then introduced into the mixture. After another 15 min of slow magnetic stir at 400 rpm, 1.25 mL of 64 mM ascorbic acid was added. Finally, 0.8 mL of seed solution was injected into the growth solution and the mixture solution was vigorously stirred for another 30 s and then left undisturbed at 30 ℃ for 12 h. The resulting Au nanorods were collected by centrifugation at 7000 rpm for 20 min followed by removal of the supernatant and finally redispersed in 30 mL of 20 mM CTAB.

Synthesis of Au Nanocuboids (NCBs). Au NCBs were prepared via overgrowth of Au nanorods in the presence of Cu^{2+}, $HAuCl_4$, CTAC, and AA. In a typical procedure, 200 μL of Au nanorods were firstly redispersed in 100 L 0.10 M CTAC after being washed once with water. The growth solution was prepared by sequentially adding H_2O (3.53 mL), $HAuCl_4$ (0.15 mL, 10 mM), $Cu(NO_3)_2$ (20 μL, 10 mM), and AA (1.0 mL, 0.10 M) into a CTAC (5.20 mL, 0.10 M) solution. After gently mixing the growth solution for 30 s, the growth of Au NCBs was initiated by adding 100 μL of the Au nanorods (in 0.1 M CTAC). The reaction solution was gently mixed for 30 s immediately after the addition of Au nanorods and then left undisturbed at 30 ℃ for 1 h. The obtained Au NCBs were washed with water twice through centrifugation/redispersion cycles, and finally redispersed in 200 μL of 20 mM CTAC. The total volume of the growth solutions was always fixed at 10.0 mL.

Synthesis of Au Convex Nanocuboids (CVNCBs). Au CVNCBs were prepared via overgrowth of Au nanorods in the presence of Cu^{2+}, $HAuCl_4$, CTAC, BDAC, and AA. In a typical procedure, 200 μL of Au nanorods were first redispersed in 100 μL 0.10 M CTAC after being washed once with water. The growth solution was prepared by sequentially adding BDAC (2.65 mL, 0.10 M), H_2O (3.38 mL), $HAuCl_4$ (0.30 mL, 10 mM), $Cu(NO_3)_2$ (20 μL, 10 mM), and AA (1.0 mL, 0.10 M) into a CTAC (2.55 mL, 0.10 M) solution. After gently mixing the growth solution for 30 s, the growth of Au CVNCBs was initiated by adding 100 μL of the Au nanorods (in 0.1 M CTAC). The reaction solution was gently mixed for 30 s immediately after the addition of Au nanorods and then left undisturbed at 30 ℃ for 1 h. The obtained Au CVNCBs were washed with water twice through centrifugation/redispersion cycles, and finally redispersed in 200 μL of binary surfactant solution containing 10 mM CTAC and 10 mM BDAC. The total volume of the growth solutions was always fixed at 10.0 mL.

Synthesis of Au Concave Nanocuboids (CCNCBs). Au CCNCBs were prepared via controllable overgrowth of Au nanorods in the presence of Cu^{2+}, $HAuCl_4$, CTAC, CTAB, and AA. In a typical procedure, 200 μL of Au nanorods were firstly redispersed in 100 μL 0.10 M CTAB after washed one time with water. The growth solution was prepared by sequentially adding CTAB (0.2 mL, 0.10 M), H_2O (3.45 mL), $HAuCl_4$ (0.20 mL, 10 mM), $Cu(NO_3)_2$ (50 μL, 1 mM), and AA (1.0 mL, 0.10 M) into a CTAC (5.00 mL, 0.10 M) solution. After gently mixing the growth solution for 30 s, the growth of Au CCNCBs was initiated by adding 100 μL of the Au nanorods (0.1 M CTAB). The reaction solution was gently mixed for 30 s immediately after the addition of Au nanorods and then left undisturbed at 30 ℃ for 1 h. The obtained Au CCNCB were washed with water twice

through centrifugation/redispersion cycles, and finally redispersed in 200 μL of binary surfactant solution containing 1.6 mM CTAB and 20 mM CTAC. The total volume of the growth solutions was always fixed at 10.0 mL.

Characterizations. The morphologies and structures of the nanoparticles were characterized by transmission electron microscopy (TEM) using a Hitachi H-8000 transmission electron microscope operated at an accelerating voltage of 200 kV. All samples for TEM measurements were dispersed in water and drop-dried on 300 mesh Formvar/carbon-coated Cu grids. The structure and composition of the nanoparticles were also characterized by SEM and EDS measurements using a Zeiss Ultraplus thermal field emission scanning electron microscope. The samples for SEM measurements were dispersed in water and drop-dried on silicon wafers. The optical extinction spectra of the nanoparticles were measured on aqueous colloidal suspensions at room temperature, using a Beckman Coulter Du 640 spectrophotometer. Raman spectra were obtained on a Bayspec *Nomadic*^{TM} Raman microscopy built on an Olympus BX51 microscope equipped with a 785 nm CW diode laser. ζ–potentials of Au NRs, NCBs, CVNCBs, and CCNCBs were measured using ZETASIZER nanoseries (Nano-ZS, Malvern). The samples for ζ–potential measurements were all freshly prepared, centrifuged, and redispersed in water. XPS measurements were carried out using a Krato AXIS Ultra DLD XPS system equipped with a monochromatic Al Kα source. The samples for XPS measurements were all freshly prepared, dried, and kept in vacuum before being loaded into the XPS chambers.

Refractometric Sensitivity of Plasmon Resonances. Glycerol-water mixtures of varying volume ratios were used to alter the refractive index of the surrounding medium

of Au nanoparticles. The volume percentage of glycerol in the mixtures was varied from 0% to 60% at a step of 10%. The as-prepared Au NRs, NCBs, CVNCBs, and CCNCBs were first washed with water, centrifuged, then redispersed in the glycerol-water mixtures. Extinction spectra were measured to track the shifts of plasmon resonance wavelengths. The plasmon shift was plotted as a function of the refractive index, and the refractometric sensitivities of the longitudinal and transverse plasmon resonances were determined through least squares curve fitting using a linear function. The refractive index of the glycerol-water mixtures were calculated using the Lorentz-Lorenz equation:

$$\frac{n_{12}^2-1}{n_{12}^2+2}=\varphi_1\frac{n_1^2-1}{n_1^2+2}+\varphi_2\frac{n_2^2-1}{n_2^2+2}$$

Where n_{12} is the refractive index of the glycerol-water mixture, n_1 and n_2 are the refractive indices of the glycerol (n_1 = 1.4746) and water (n_2 = 1.3334) respectively, and φ_1 and φ_2 are the volume percentage of glycerol and water in the mixture respectively. The figure of merit (FOM) for plasmon sensing was calculated by dividing the refractometric sensitivity by the full width at half-maximum (FWHM) of the corresponding extinction peak.

UV-Vis Spectroscopic Measurements of Catalytic Reaction Kinetics. We used the hydrogenation of 4-nitrophenol (4-NP) by ammonia borane (AB) at room temperature as a model reaction to evaluate the catalytic activities of Au NRs, NCBs, CVNCBs, and CCNCBs. In a typical procedure, 0.1 mL of 1.0 mM 4-NP, 0.1 mL of 0.1 M AB (freshly prepared), and 0.1 mL of 10 mM K_2CO_3 were sequentially added to 1.0 mL of ultrapure water in a cuvette and mixed thoroughly. Then, 20 μL of Au NRs, NCBs, CVNCBs, or

CCNCBs were injected into the system. After thoroughly mixed for 5 s, UV−vis extinction spectra were collected in real time to monitor the catalytic reaction process. We compared the catalytic activities of Au NRs, NCBs, CVNCBs, and CCNCBs at the same particle concentration (9.0×10^{10} particle/mL).

Monitoring Reaction Kinetics by Time-Resolved SERS Measurements. To use SERS to monitor the catalytic reactions, we first pre-adsorbed SAMs of 4-NTP onto the surfaces of Au NCBs, CVNCBs, and CCNCBs. In a typical procedure, 200 μL colloidal suspensions of Au NCBs, CVNCBs, or CCNCBs (~1.0×10^{11} particles mL^{-1}) were incubated with 400 μL ethanol solution of 50.0 μM 4-NTP overnight to form saturated SAMs of 4-NTP on the nanoparticle surfaces. Then, the 4-NTP-coated NCBs, CVNCBs, and CCNCBs were centrifuged (3500 rpm, 3 min) and redispersed in 160 μL ultrapure water. The nanoparticle-catalyzed 4-NTP reduction occurred at room temperature upon the addition of 20 μL of Au NCBs, CVNCBs, or CCNCBs, 50 μL of ultrapure water, 10 μL of 10 mM K_2CO_3 and 20 μL of 10 mM AB in a 0.5 mL Eppendorf centrifuge tube. The kinetics of the catalyzed reactions were measured in real time using time-resolved SERS. SERS spectra were obtained on a Bayspec NomadicTM confocal Raman microscopy built on an Olympus BX51 reflected optical system with a 785 nm continuous wave excitation laser. The excitation laser was focused on the reaction mixture using a 10× objective [Numerical Aperture (NA) = 0.30, working distance (WD) = 11.0 mm, Olympus MPLFLN]. The laser power was measured to be 10.0 mW at the samples and the signal acquisition time was 2 s for all samples. Successive SERS spectra were collected during the reaction until completion of the reduction of 4-NTP into 4-ATP. We also assessed the catalytic activities of Au NCBs, CVNCBs, and CCNCBs at

various AB concentrations (0.1, 0.2, 0.4, 1, 2, 4, 10, and 20 mM). The total volume of the reaction mixtures was always fixed at 100 μL.

6.3 Results and Discussions

Our success in facet control of anisotropic nanostructures essentially relies on selective modification of the surface energies of various Au facets by Cu^{2+} ions and surface capping surfactants, which has profound impacts on the facet evolution during NR overgrowth. As schematically illustrated in Figure 6.1A, we used the conventional cylindrical Au NRs with rounded ends as the starting materials, which evolved into Au nanocuboids (NCBs) upon overgrowth in the presence of Cu^{2+} and cetyltrimethylammonium chloride (CTAC). Strikingly different shape evolution was observed in the presence of Cu^{2+} and binary surfactant systems. Overgrowth of Au NRs in the benzyldimethylhexadecylammonium Chloride (BDAC)/CTAC binary surfactant system resulted in the formation of Au convex nanocuboids (CVNCBs), while Au concave nanocuboids (CCNCBs) were obtained in the presence of CTAB/CTAC binary surfactants.

We used a combination of scanning electron microscopy (SEM), transmission electron microscopy (TEM), selected area electron diffraction (SAED), and energy dispersive spectroscopy (EDS) to fully characterize the crystalline structures and bulk compositions of the Au NCBs, CVNBCs, and CCNCBs. As shown in Figures 6.1B-D, each Au NCB exhibited well-defined cuboidal morphology enclosed by 6 low-index {100} facets. The SAED pattern of an individual Au NCB projected along the [001] zone axis (Figure 6.1E) further verified the single-crystalline face-centered cubic (fcc) structure of the particle. A CVNCB can be geometrically derived from a NCB upon creation of 4 equivalent convex

facets on each {100} facet. Each CVNCB exhibited 24 well-defined convex facets and displayed orientation-dependent contours in the TEM images (Figures 6.1F-K). Figure 6.1I shows the TEM image and SAED pattern of one single-crystalline CVNCB particle imaged with the electron beam projected along the [001] zone axis. Under this orientation, 8 out of the 24 facets became parallel to the projection direction and the characteristic dihedral angles were measured to be 23.2 ° on average, indicating that each CVNCB was enclosed by 24 high-index {730} facets.[30,31] In striking contrast to CVNCBs, a CCNCB is geometrically derived from a NCB upon introduction of surface indentation to the {100} facet, which can be clearly visualized in SEM (Figures 6.1L and 6.1M) and TEM images (Figures 6.1N-6.1Q). When a single-crystalline CCNCB particle was projected along the [001] zone axis, 8 out of the 24 facets became parallel to the projection direction and the average dihedral angles were measured to be 20.6 ° (Figure 6.1O), allowing us to assign the CCNCB facets as high-index {830} facets. The bulk compositions of the NCBs, CVNCBs, and CCNCBs were all verified to be Au based on the EDS results.

For fcc noble metals, such as Au, Ag and Pd, the high-index facets have significantly higher surface energies than those of the thermodynamically stable low-index {111} and {100} facets and thus are typically eliminated during nanocrystal growth.[32,33] However, interactions of foreign ions and surfactants with the nanocrystal surfaces may shift the relative energies of various facets and consequently guide the nanocrystals to evolve into thermodynamically unexpected morphologies.[34-39] While none of the Cu, N, Cl, or Br elements from the surface-adsorbed ions and surfactants were detectable using EDS, X-ray photoelectron spectroscopy (XPS) results clearly showed the presence of both Cu

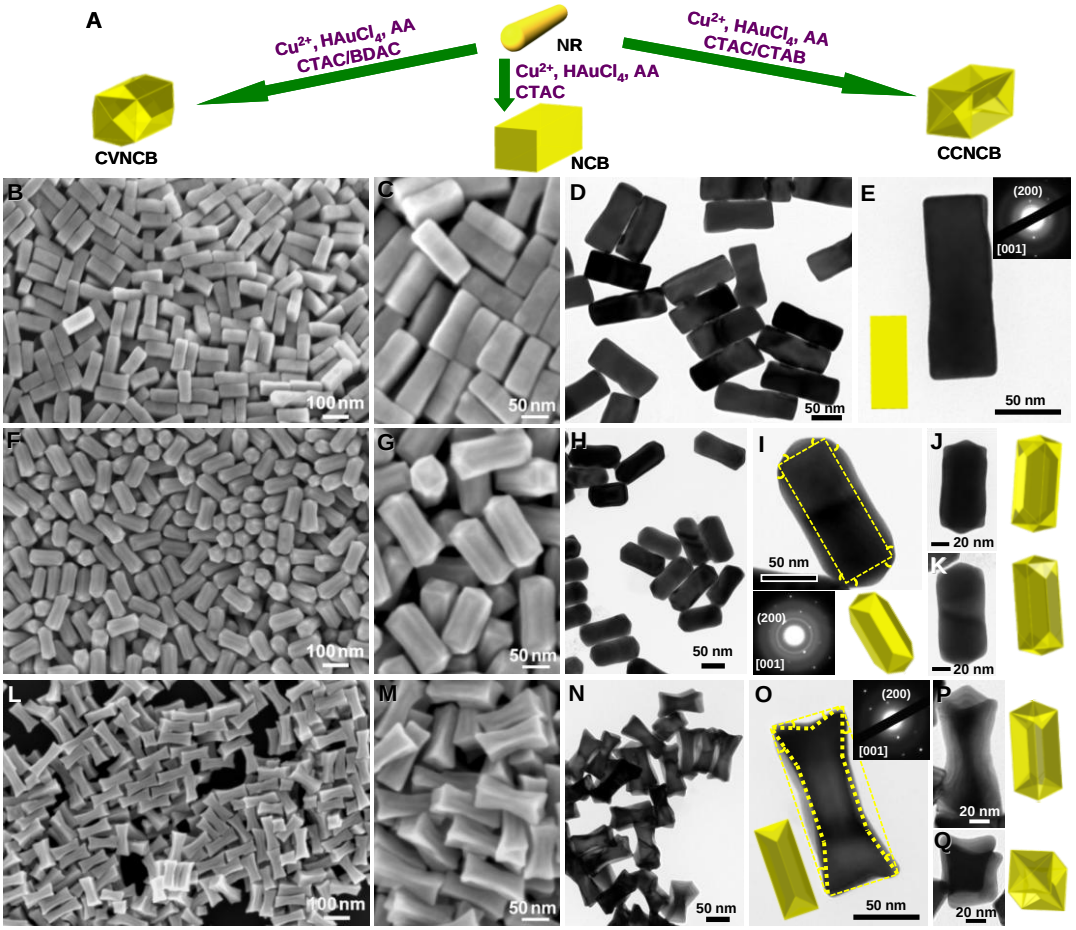

Figure 6.1. Synthesis and structural characterizations of Au NCBs, CVNCBs, and CCNCBs. (A) Schematic illustration of the selective formation of Au NCBs, CVNCBs, and CCNCBs under appropriate conditions. (B,C) SEM and (D) TEM images of Au NCBs. (E) TEM image of one individual Au NCB viewed along the [001] projection. The insets of panel E show the geometric model and SAED pattern of the Au NCB particle. (F,G) SEM and (H) TEM images of Au CVNCBs. (I) TEM image of one individual Au CVNCB viewed along the [001] projection. The bottom insets of panel I show the geometric model and SAED pattern of the Au CVNCB particle. (J,K) TEM images and the corresponding geometric models of individual Au CVNCBs with various orientations on the TEM grid. (L,M) SEM and (N) TEM images of Au CCNCBs. (O) TEM image of one individual Au CCNCB viewed along the [001] projection. The insets of panel O show the geometric model and SAED pattern of the Au CCNCB particle. (P,Q) TEM images and the corresponding geometric models of individual Au CCNCBs with various orientations on the TEM grid.

species and surfactants on the surfaces of NCBs, CVNCBs, and CCNCBs. XPS measurements also verified the presence of Ag and CTAB on the surfaces of the cylindrical Au NRs. While the atomic ratios of Cu:Au on the surfaces of NCBs,

CVNCBs, and CCNCBs were almost the same, the packing densities of the surfactants on the high-index faceting CVNCBs and CCNCBs were significantly higher than on the low-index faceting NCBs as reflected by the atomic ratios of Cl:Au and Br:Au (Figure 6.2A), suggesting that stabilization of high-index facets requires relatively high surfactants packing densities. Au NRs exhibited an intermediate surfactant packing density most likely due to the coexistence of high-index and low-index facets on their surfaces. It has been reported that halide-containing cationic surfactants, such as CTAB, CTAC, and BDAC, form positively charged, self-assembled bilayers on Au nanoparticle surfaces.[6,7,10,14,15,19] As shown in Figure 6.2B, the surfaces of freshly prepared Au NCBs, CVNCBs, CCNCBs, and NRs were all positively charged, and the ζ-potential values correlated very well with the relative surface packing densities of the surfactants. High-resolution XPS spectra of the Cu 2p region (Figure 6.2C) revealed that Cu^{2+} was mostly reduced to Cu(I) species on the surfaces of Au NCBs, CVNCBs, and CCNCBs. Interestingly, we also identified trace amount of Cu (II) species on the surfaces of CVNCBs and CCNCBs, while only Cu(I) signals were detectable on the NCB surfaces. The XPS results indicate that the coexistence of Cu(I) and Cu(II) species may play a crucial role in stabilizing the high-index {hk0} facets, though the detailed mechanisms still remains unclear at this stage. The surface adsorption of Cu (I) and surfactants did not modify the lattices or the electronic band structures of Au surface atoms to any detectable extent because no peak shift or split was observed in the high-resolution XPS spectra of Au 4f region (Figure 6.2D) in comparison to the spectrum of bulk Au.

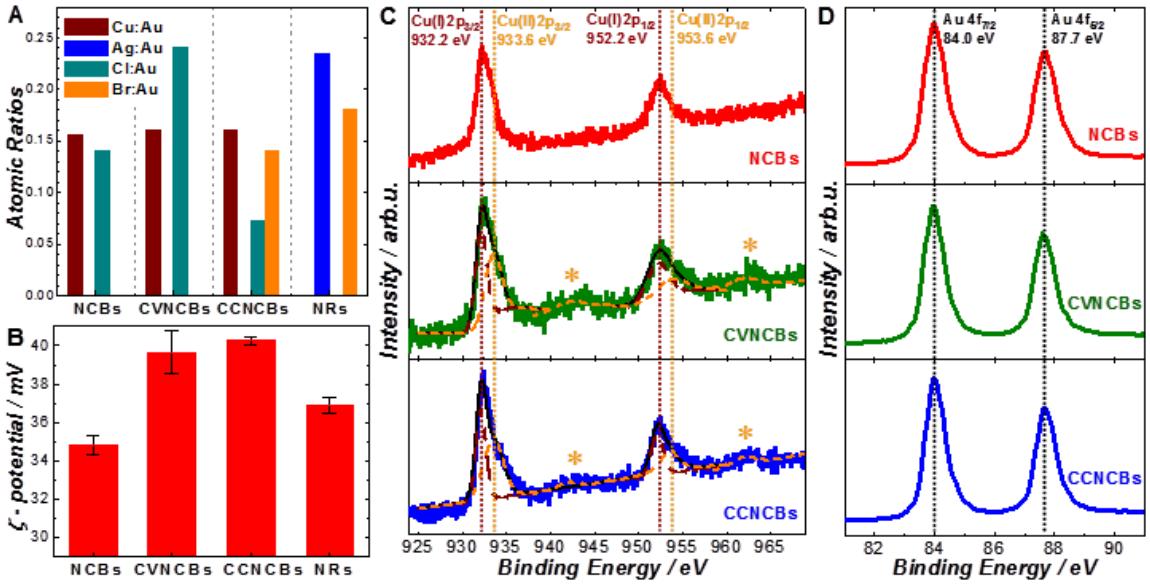

Figure 6.2. Surface compositions of Au NCBs, CVNCBs, and CCNCBs. (A) Atomic ratios of Cu/Au, Ag/Au, Cl/Au, and Br/Au on the surfaces of Au NCBs, CVNCBs, CCNCBs, and NRs obtained from XPS measurements. (B) ζ-Potentials of Au NCBs, CVNCBs, CCNCBs, and NRs. (C) High-resolution XPS spectra of the Cu 2p region of Au NCBs, CVNCBs, and CCNCBs. The Cu $2p_{3/2}$ and Cu $2p_{1/2}$ peaks of the CVNCBs and CCNCBs are further separated into Cu(I) and Cu(II) peaks. The asterisks indicate the satellite peaks of Cu(II) $2p_{3/2}$ and Cu(II) $2p_{1/2}$. (D) High-resolution XPS spectra of the Au 4f region of NCBs, CVNCBs, and CCNCBs.

The formation of well-defined {100} facets on Au NCBs upon NR overgrowth was mostly likely to be a consequence of selective stabilization of the {100} facets by CTAC.[40-42] When BDAC was used as the surfactant, faceted Au NRs with irregular surface convexity were obtained while the use of CTAB as the surfactant led to the formation of faceted NRs with concave surfaces and truncated corners. In BDAC/CTAB binary surfactants, irregularly shaped Au NRs were obtained as the development of surface convexity and concavity canceled out. These interesting observations implicate that BDAC facilitated the formation of convex surfaces while CTAB favored surface concavity. Therefore, the combination of CTAC with BDAC and CATB provided a unique pathway to generate well-defined high-index {hk0} facets upon selective creation of surface convexity and concavity, respectively.

To further investigate the effects of Cu^{2+} on the facet evolution, control experiments were conducted in the presence of varying amount of Cu^{2+} while all the other experimental parameters were kept at the optimal conditions for NCB, CVNCB, and CCNCB growth. We found that only within narrow Cu^{2+} concentration windows could Au NCBs, CVNCBs, and CCNCBs with well-defined facets be obtained through NR overgrowth. Outside the optimal Cu^{2+} concentration windows, Au nanostructures with ill-defined rod-like shapes enclosed by multiple types of facets were obtained. Therefore, it is the unique combination of appropriate surfactants with Cu^{2+} in the optimal concentration range that enabled us to fine-modulate the shape evolution and thus fine-tailor the facets of the anisotropic Au nanoparticles.

The faceted anisotropic Au nanoparticles exhibited greatly enriched extinction spectral features and enhanced plasmonic tunability in comparison to the conventional cylindrical Au NRs. The aspect ratios of the Au NCBs, CVNCBs, and CCNCBs could be fine-tuned either by changing the aspect ratio of the starting Au NR seeds or by adjusting the amount of $HAuCl_4$ added. The Au CVNCBs and CCNCBs shown in Figure 6.1 were both derived from NCBs with the same dimensions, allowing us to quantitatively evaluate the effects of surface convexity and concavity on the plasmonic features of the particles. Figure 6.3A shows the optical extinction spectra of aqueous colloidal suspensions of Au NRs, NCBs, CVNCBs, and CCNCBs at the same particle concentration (5×10^8 particle mL^{-1}), which allowed us to directly compare both the plasmon resonance wavelengths and the relative optical cross-sections of the nanoparticles. The cylindrical Au NRs (length: 98 ± 4.2 nm; transverse width: 32 ± 2.1 nm; aspect ratio: ~ 3) exhibited a strong longitudinal plasmon peak at 769 nm and a weak transverse plasmon peak at 516 nm,

respectively. Although Au NCBs (length: 115 ± 3.8 nm; transverse width: 46 ± 1.8 nm; aspect ratio: ~ 2.5) had a lower aspect ratio than the Au NRs, their transverse and longitudinal plasmon resonances both red-shifted due to their cuboidal morphology. Similar plasmon red-shifts were also observed when Au or Ag nanospheres were converted into nanocubes of similar sizes.[43,44] Interestingly, introduction of surface convexity to the NCBs caused spectral blue-shifts of the plasmon resonances, whereas surface concavity significantly red-shifted both the transverse and longitudinal plasmon resonances. All the faceted anisotropic nanostructures, especially the CVNCBs and CCNCBS, exhibited significantly enhanced transverse plasmon peak intensities in comparison to the cylindrical NRs. To more quantitatively understand the geometry-dependent plasmonic characteristics of the particles, we used discrete dipole approximation (DDA) to calculate the extinction spectra of a Au NR, NCB, CVNCB, and CCNCB whose geometric parameters were extracted from the TEM and SEM images. Both the plasmon resonance frequencies and spectral line-shapes calculated by DDA were in excellent agreement with the experimental results. The calculated extinction spectrum of CCNCB exhibited multiple transverse plasmon peaks, which correlated well with the asymmetrically broadened transverse plasmon band observed in the experimental extinction spectrum of Au CCNCBs.

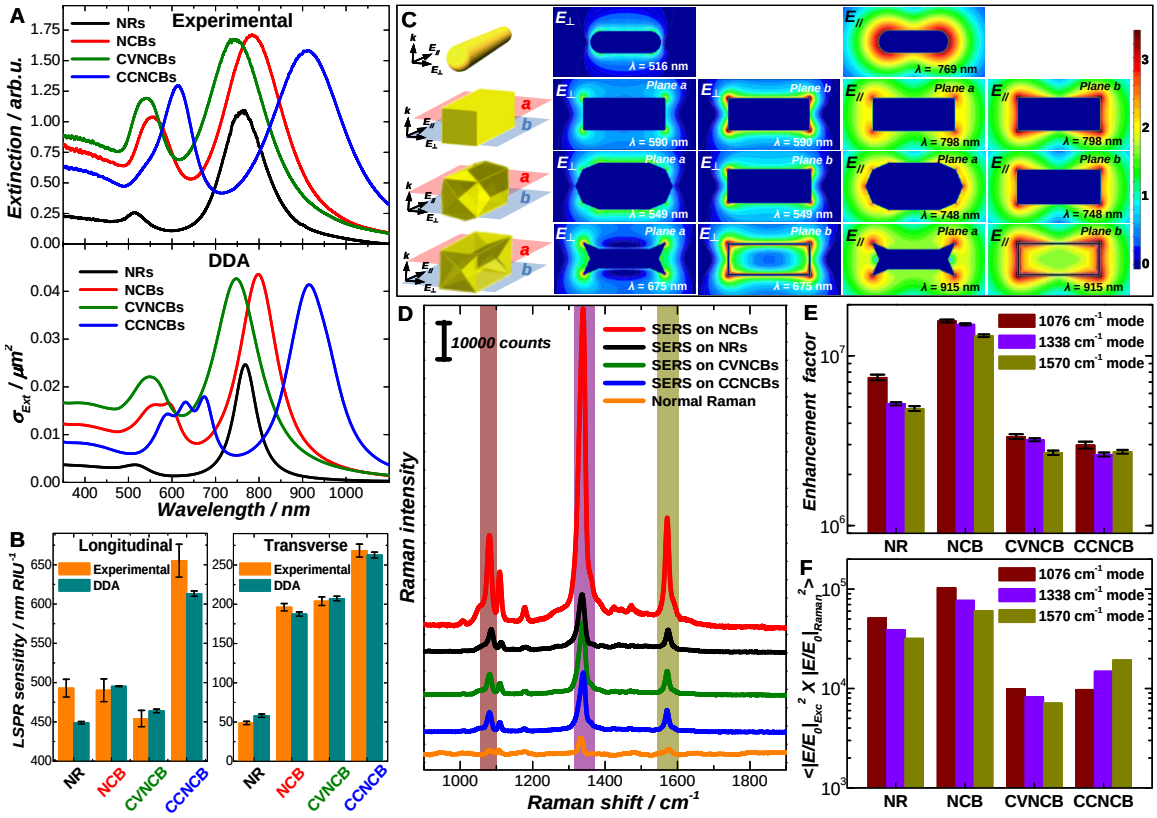

Figure 6.3. Optical properties of Au NRs, NCBs, CVNCBs, and CCNCBs. (A) Experimental (top panel) and calculated (bottom panel) extinction spectra of Au NRs, NCBs, CVNCBs, and CCNCBs. (B) Experimentally measured and calculated localized surface plasmon resonance (LSPR) sensitivities of the longitudinal and transverse plasmon modes of Au NRs, NCBs, CVNCBs, and CCNCBs. The error bars represent the standard deviations of least-squares curve fitting using linear functions. (C) Cross-sectional views of calculated near-field enhancements of Au NR, NCB, CVNCB, and CCNCB at resonant excitations for the longitudinal and transverse plasmon modes. The field enhancements are plotted on a logarithm scale ($\log|E/E_0|^2$). The geometries of NR, NCB, CVNCB, and CCNCB in three-dimensional Cartesian coordinates are illustrated. Two planes (a and b) perpendicular to the incident plane wave k are shown for the transverse and longitudinal modes. (D) Representative SERS spectra of 4-NTP self-assembled monolayers on Au NRs, NCBs, CVNCBs, and CCNCBs. The bottom spectrum is the normal Raman spectrum of 4-NTP. (E) Experimentally determined SERS enhancement factors on Au NRs, NCBs, CVNCBs, and CCNCBs at 785 nm excitation. Three Raman modes of 4-NTP at 1076, 1338, and 1570 cm^{-1} are used for the calculation of enhancement factors. (F) Calculated enhancements averaged over particle surfaces ($\langle |E/E_0|_{Exc}^2 \times |E/E_0|_{Raman}^2 \rangle$) of Au NRs, NCBs, CVNCBs, and CCNCBs at 785 nm excitation. $|E/E_0|_{Exc}$ and $|E/E_0|_{Raman}$ refer to the field enhancements at excitation wavelength (785 nm) and Raman scattering wavelengths, respectively.

Because the plasmonic features were sensitively dependent on both the aspect ratios and surface convexity/concavity of the particles, we were able to use extinction spectroscopy in combination with electron microscopies to gain detailed insights into the

nanoparticle structural evolution as the amount of $HAuCl_4$ varied. In the presence of Cu^{2+} and CTAC, the NR overgrowth resulted in the formation of Au NCBs whose aspect ratios progressively decreased as the amount of $HAuCl_4$ increased until reaching a threshold point where the NCBs evolved into irregularly shaped nanoparticles. Both the longitudinal and transverse plasmon resonances slightly blue-shifted and became progressively more intense as the aspect ratios of NCBs decreased. Au CVNCBs underwent a unique geometric evolution as the amount of $HAuCl_4$ varied. The surface convexity was initiated at discrete locations, then gradually propagated along the longitudinal axis of the particles, and eventually merged into continuous {730} facets as increasing amount of Au was grown on the nanoparticle surfaces. The surface convexity caused blue-shift of the longitudinal plasmon resonances. The double-peaked spectral feature for the transverse plasmon resonances was characteristic of discontinuity of surface convexity and the extinction peak at ~ 570 nm completely disappeared upon the formation of fully developed CVNCBs with well-defined {730} facets. For Au CCNCBs, both the degree of surface indentation and transverse widths increased with the amount of $HAuCl_4$. Both the longitudinal and transverse plasmon peaks of Au CCNCBs progressively red-shifted and became more intense as the amount of $HAuCl_4$ increased. The peak-split and asymmetric broadening of the transverse plasmon band are a unique feature of surface concavity on anisotropic Au nanoparticles.[24]

The faceted Au NRs exhibited enhanced plasmonic refractometric sensitivities in comparison to the conventional cylindrical Au NRs. Both the longitudinal and transverse plasmon resonances progressively red-shifted as the refractive index of the surrounding medium (glycerol-water mixtures with varying volume percentages) increased. The

plasmon resonance shifts exhibited a linear dependence on the refractive indices. For all the anisotropic nanostructures, their longitudinal plasmon resonances displayed higher refractometric sensitivities than transverse plasmon resonances. The longitudinal plasmon resonance of CCNCBs exhibited a refractometric sensitivity of 650 nm RIU^{-1}, significantly higher than those of NRs, NCBs, and CVNCBs (Figure 6.3B). While the transverse plasmon resonance of Au NRs was essentially insensitive to the refractive index of surrounding medium, the transverse plasmon resonances of Au NCBs, CVNCBs, and CCNCBs all exhibited greatly enhanced refractometric sensitivities. The calculated refractometric sensitivities of various plasmon modes were in excellent agreement with the experimental results (Figure 6.3B). The faceted Au NRs, especially CCNCBs, hold great promise for multiplex refractometric molecular sensing using both the longitudinal and transverse plasmon resonances of the same anisotropic nanostructure.

The surface convexity and concavity also introduced interesting modifications to the near-field plasmonic properties of the nanoparticles. Figure 6.4C shows the cross-sectional views of calculated near-field enhancements ($|E/E_0|^2$ plotted in a logarithm scale) of a Au NR, NCB, CVNCB, and CCNCB at resonance excitations. Much higher local-field enhancements were generated upon excitation of the longitudinal plasmons than the transverse plasmons due to the stronger coupling of light with the plasmons along the longitudinal direction. The NCB, CVNCB, and CCNCB all exhibited significantly more intense local-field enhancements than the cylindrical NR upon excitation of their transverse plasmon resonances. The maximum plasmonic field enhancements were located in close proximity to the particle corners and edges,

providing hot spots for SERS on individual nanoparticles. To experimentally assess the near-field enhancements, we measured SERS of 4-nitrothiophenol (4-NTP) self-assembled monolayers (SAMs) on the surfaces of Au NRs, NCBs, CVNCBs, and CCNCBs. After displacements of CTAC, CTAB, or BDAC with 4-NTP on the nanoparticle surfaces, both the facets and particle geometries were well-preserved. The SERS spectra shown in Figure 6.3D were collected on colloidal suspensions (~1.0×10^{11} particles mL^{-1}) of nanoparticles coated with 4-NTP SAMs at 785 nm excitation. We estimated the enhancement factors (EFs) by comparing SERS signals to normal Raman signals from pure 4-NTP based on three Raman modes at 1076 cm^{-1}, 1338 cm^{-1}, and 1570 cm^{-1}, respectively. Among the four nanostructures, Au NCBs exhibited the highest EFs on the order of 10^7 because of the presence of hot spots at the particle corners and the resonance excitation of their longitudinal plasmon. Although the plasmons of Au CVNCBs and CCNCBs were off resonance with the excitation laser, EFs on the order of 10^6 were still achieved on individual colloidal nanoparticles. These empirical EFs represented the averaged enhancements over entire nanoparticle surfaces. The localized EFs in the hot spots at the particle corners were estimated to be at least one order of magnitude higher than the average EFs. We also used DDA to calculate the surface-averaged field enhancements at both the excitation wavelength (785 nm) and the Raman scattering wavelengths. The calculated field enhancements (Figure 6.3F) correlated extremely well with the experimental SERS results. The experimentally estimated EFs were ~100 times higher than the calculated $\langle |E/E_0|_{Exc}^2 \times |E/E_0|_{Raman}^2 \rangle$ values because DDA only calculated the electromagnetic enhancements without considering the chemical enhancements in SERS.

The well-defined facets of Au NCBs, CVNCBs, and CCNCBs enabled us to quantitatively correlate the atomic-level surface structures with the catalytic activities of the nanoparticles. We used the room temperature catalytic hydrogenation of 4-nitrophenol (4-NP) by ammonia borane (AB) as a model reaction to assess the catalytic activities of various facets. AB is a stable hydrogen storage material in aqueous environments with hydrogen storage capacity as high as 19.5 wt %.[45] When AB and 4-NP were mixed in aqueous K_2CO_3 solution (pH ~ 10), no hydrogenation reaction was observed at room temperature over extended time periods up to a few days. Hydrogen release from AB can be catalyzed by metallic nanoparticles and the released hydrogen may be further used to drive hydrogenation of organic molecules.[46] Rapid hydrogenation of 4-NP was observed when AB and 4-NP were mixed in aqueous K_2CO_3 solution in the presence of colloidal Au nanoparticles and the reaction kinetics could be monitored, in real time, using UV-vis spectroscopy. The high-index faceting CVNCBs and CCNCBs exhibited much higher catalytic activities than the low-index faceting NCBs. Au NRs showed intermediate catalytic activities due to the coexistence of high-index and low-index facets on their curved surfaces. However, the UV-vis spectroscopic results only allowed us to qualitatively compare the relative activities of various types of Au facets because they did not necessarily reflect the intrinsic facet-dependent catalytic activities. The UV-vis spectroscopy measured the overall kinetics of multi-step processes including adsorption of the reactants, surface-catalyzed molecular transformations, and desorption of reactants, and the surface-capping ligands might further complicate the overall reaction kinetics. Remarkable deviation from pseudo-first order reaction kinetics was observed even though AB was in great excess with respect to 4-NP. In addition, an induction time

during which no hydrogenation occurred was observed at the initial stage of the reactions, which was most likely due to the complication from diffusion and surface adsorption of 4-NP and AB.

The strong plasmonic field enhancements on Au NCBs, CVNCBs, and CCNCBs provided unique opportunities for us to spectroscopically monitor the catalytic hydrogenation of surface-adsorbed 4-nitrothiophenol (4-NTP) by AB using time-resolved SERS. We used a confocal Raman microscope with an effective excitation volume of ~100 fL such that each freely-diffusing colloidal nanoparticle was exposed to the excitation laser for a short time period (within the diffusion time), effectively eliminating possible plasmon-driven photoreactions. Because both the reactant and product molecules were immobilized as SAMs on the nanocatalyst surfaces, it became possible to unravel the intrinsic surface reaction kinetics with minimal complication introduced by the surface-capping ligands as well as the diffusion, adsorption, and desorption of reactants and products. The high sensitivity and unique fingerprinting capability of SERS further enabled us to identify transient intermediates along the reaction pathways. As schematically illustrated in Figure 6.4A, this catalytic hydrogenation reaction was essentially a two-step consecutive reaction. 4-NTP and 4-aminothiolphenol (4-ATP) were the reactant and final product, respectively, and 4,4'-dimercaptoazobenzene (DMAB) was identified as the intermediate.

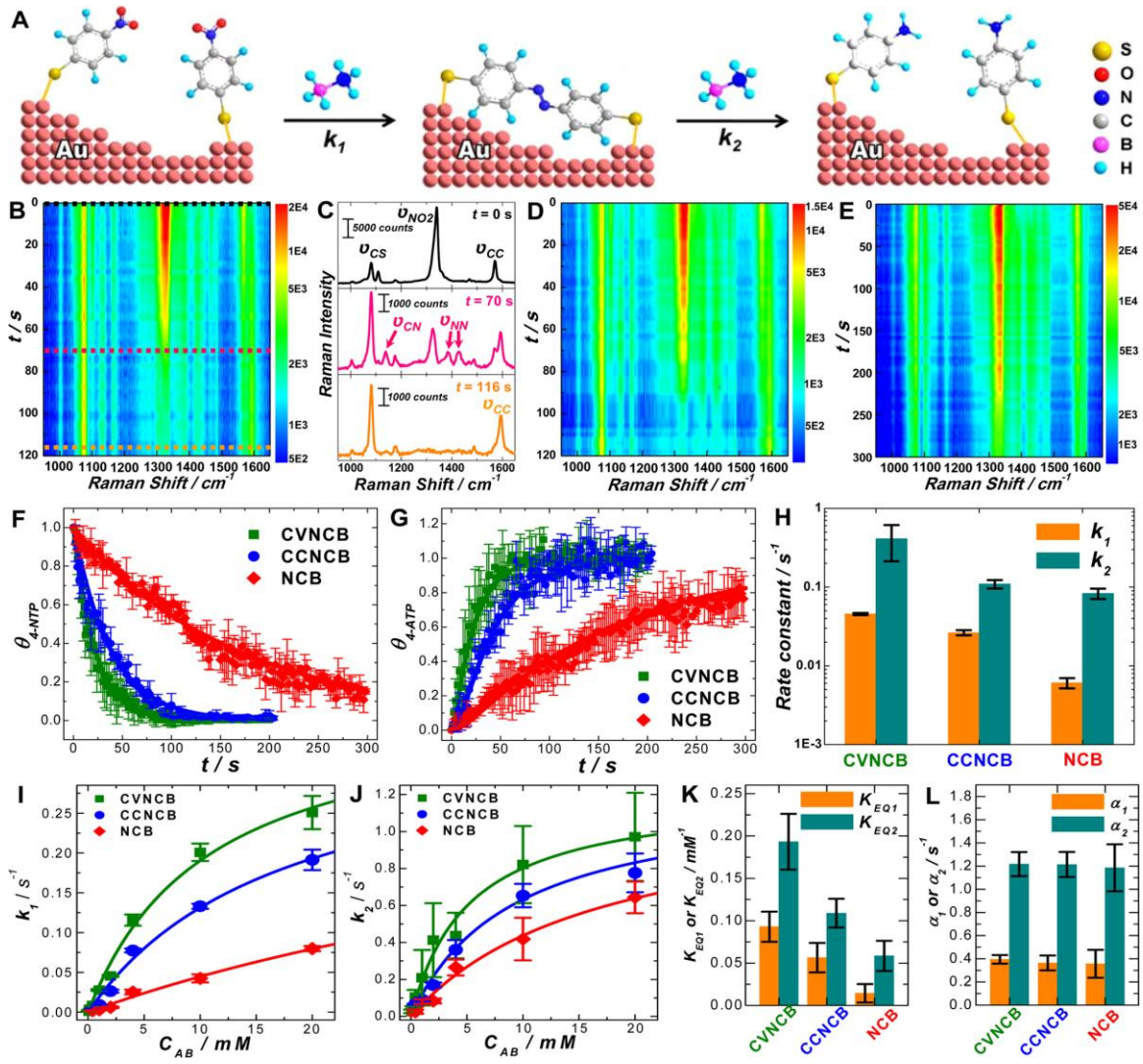

Figure 6.4. Facet-dependent catalytic activities of Au NCBs, CVNCBs, and CCNCBs. (A) Schematic illustration of the catalytic hydrogenation of surface-adsorbed 4-NTP by AB. The reaction is illustrated as a two-step consecutive process (4-NTP is the reactant, DMAB is the intermediate, and 4-ATP is the final product). Two-dimensional color-coded intensity maps of time-resolved SERS spectra collected from 4-NTP molecules adsorbed on the surfaces of Au (B) CVNCB, (D) CCNCB, and (E) NCB at different reaction times after exposure to 2 mM AB. (C) Representative SERS spectra collected from 4-NTP molecules adsorbed on the surfaces of Au CVNCBs at reaction times of 0, 70, and 116 s. (F) $\theta_{4\text{-NTP}}$ and (G) $\theta_{4\text{-ATP}}$ as a function of reaction time (t) during the reactions catalyzed by Au CVNCBs, CCNCBs, and NCBs. The error bars show the standard deviations obtained from five experimental runs under identical reaction conditions. The results of the least-squares curve fitting are shown as solid curves for the reactants and products. (H) Comparison of k_1 and k_2 on Au CVNCBs, CCNCBs, and NCBs. (I) k_1 and (J) k_2 as a function of AB concentrations (C_{AB}) on Au CVNCBs, CCNCBs, and NCBs. The results of the least-squares fitting using the Langmuir adsorption isotherms are shown as solid curves. Comparison of (K) K_{EQ1} and K_{EQ2} and (L) α_1 and α_2 of the two-step surface reactions on Au CVNCBs, CCNCBs, and NCBs.

As shown in Figures 6.4B-E, 4-NTP exhibited three characteristic Raman modes at 1076, 1338, and 1570 cm^{-1}, which were assigned to the C-S stretching, O-N-O stretching, and the phenol-ring modes, respectively.[47,48] Upon exposure of the 4-NTP-coated nanoparticles to 2 mM AB, the intensities of both 1338 and 1570 cm^{-1} peaks gradually decreased with the concomitant emergence of a new peak at 1590 cm^{-1} corresponding to the phenol-ring modes of 4-ATP.[48,49] The Raman peaks at 1140, 1388, and 1438 cm^{-1} were the characteristic C-N and N-N stretching modes of DMAB.[49,50] Time-resolved SERS results clearly showed that high-index faceting Au CVNCBs and CCNCBs exhibited much higher catalytic activities than the low-index faceting NCBs, which was in line with the UV-vis results. Interestingly, because 4-NTP molecules were pre-adsorbed on the nanocatalyst surfaces, no induction time was observed in time-resolved SERS. We chose the Raman modes at 1338 and 1590 cm^{-1} to quantify the fractions of reactant ($\theta_{4\text{-}NTP}$) and product ($\theta_{4\text{-}ATP}$), respectively, at a function of reaction time (t). Because AB was in great excess, this catalytic reaction obeyed pseudo-first-order kinetics. The two rate constants, k_1 and k_2, were obtained by performing least-squares curve fitting to the reactant and product trajectories shown in Figures 6.4F and 6.4G using the following rate equations:

$$\theta_{4-NTP} = e^{-k_1 \times t} \quad (1)$$

$$\theta_{4-ATP} = 1 + \frac{(k_1 \times e^{-k_2 \times t} - k_2 \times e^{-k_1 \times t})}{k_2 - k_1} \quad (2)$$

As shown in Figure 6.4H, k_1 was significantly smaller than k_2 regardless of the nanoparticle geometries, indicating that the formation of DMAB was the rate-limiting step. Both Au CVNCBs and CCNCBs exhibited significantly higher catalytic activities

with k_1 approximately 10 times larger than that of Au NCBs. The enhanced catalysis on high-index facets can be interpreted in the context of undercoordinated surface atoms at the surface atomic steps, which serve as the active sites for heterogeneous catalysis. The atomic coordination number of the surface atoms on the {100} facet is 8 while significant fractions of surface atoms have a lower coordination numbers of 6 on the high-index {730} and {830} facets. The {730} facet exhibited even higher catalytic activity than that of the {830} facet because of the higher fraction of surface atoms with coordination of 6.

To gain further mechanistic insights into the enhanced catalysis on high-index facets, we studied the kinetics of the catalytic hydrogenation reaction at different AB concentrations. As shown in Figures 6.4I and 6.4J, the pseudo-first order rate constants, k_1 and k_2, both increased with the AB concentration, C_{AB}. The rate constants on high-index facets were more sensitively dependent on C_{AB} than those on the low-index {100} facet. Under our experimental conditions, the pseudo-first order rate constants appeared to be proportional to the surface coverage of AB (θ_{AB}) and the adsorption of AB was further found to follow the Langmuir isothermal adsorption. The reaction kinetics could be well described using the apparent rate laws for an elementary reaction between the pre-immobilized 4-NTP and surface-adsorbed AB, though the detailed mechanisms might be even more complicated. The equilibrium constants for adsorption/desorption of AB on various Au facets were obtained by fitting the experimental data with the following equations:

$$k_1 = \alpha_1 \theta_{AB1} = \alpha_1 \frac{K_{EQ1} C_{AB}}{1 + K_{EQ1} C_{AB}} \quad (3)$$

$$k_2 = \alpha_2 \theta_{AB2} = \alpha_2 \frac{K_{EQ2} C_{AB}}{1 + K_{EQ2} C_{AB}} \quad (4)$$

where α_1 and α_2 are two fractional factors linking the pseudo-first-order rate constants and surface-coverages of AB. K_{EQ1} and K_{EQ2} represent two equilibrium constants of adsorption/desorption of AB molecules on Au surfaces pre-adsorbed with 4-NTP and DMAB, respectively. K_{EQ1} was significantly smaller than K_{EQ2} on all three nanostructures (Figures 6.4K and 6.4L), suggesting that the conversion of 4-NTP to DMAB facilitated the adsorption of AB onto the Au surfaces. Therefore, the conversion of 4-NTP into DMAB was the rate limiting step while the conversion of DMAB into 4-ATP was a faster reaction step. While the both α_1 and α_2 appeared facet-independent, both the K_{EQ1} and K_{EQ2} values correlated well with the relative catalytic activities of various facets. The K_{EQ1} and K_{EQ2} values on the high-index facets were significantly higher than those on the {100} facet, strongly indicating that the undercoordinated surface atoms on high-index facets exhibited higher affinity for adsorption of AB molecules, and thus served as catalytically more active sites for this hydrogenation reaction.

The fraction of the intermediate, DMAB, was determined by the ratios between k_1 and k_2, which were both facet- and C_{AB}-dependent. The k_1/k_2 values on the high-index facets were higher than on the {100} facet at the same AB concentrations. Therefore, higher fraction of DMAB could be obtained on Au CVNCBs and CCNCBs than on NCBs (Figures 6.4B-E). Regardless of the nanoparticle facets, the k_1/k_2 values increased with C_{AB} till reaching a plateau at C_{AB} above 4 mM. Maximum faction of DMAB formed during the CVNCB-catalyzed 4-NTP hydrogenation at C_{AB} of 4 mM was much higher than at C_{AB} of 0.1 mM. Therefore, the fraction of the intermediate could be effectively modulated by either tuning the facets of Au nanocatalysts or by changing the concentration of AB.

6.4 Conclusions

In summary, we have demonstrated that well-defined low-index and high-index facets can be controllably created on the surfaces of cylindrical Au NRs through overgrowth processes that are synergistically guided by Cu^{2+} and cationic surfactants. CTAC plays a crucial role in selectively stabilizing the Au {100} facets and thus facilitates the formation of Au NCBs. More interestingly, when binary surfactants, such as CTAC/BDAC and CTAC/CTAB, are used, surface convexity and concavity can be controllably created through which high-index faceting Au CVNCBs and CCNCBs are obtained. This Cu^{2+}- and surfactant-coguided NR overgrowth approach allows us to fine-control both the aspect ratios and the facets of anisotropic Au nanostructures, advancing geometry control of nanoparticles to an unprecedented level of precision and detail far beyond the state-of-the-art seed-mediated Au NR synthesis. The surface convexity and concavity of faceted Au nanostructures provide additional geometric parameters that one can tailor to further fine-tune the far-field and near-field plasmonic properties of nanoparticles. Creation of well-defined facets on optically tunable Au NRs provides unique opportunities of using SERS as a noninvasive *in situ* spectroscopic tool to fully characterize catalytic molecular transformations at nanoparticle-molecule interfaces in real time, further enabling us to gain quantitative insights into the underlying relationship between the atomic-level surface structures and intrinsic activities of Au nanocatalysts.

6.5 References

(1) Xia, Y. N.; Halas, N. J. *MRS Bull.* **2005**, *30*, 338-344.

(2) Jain, P. K.; Huang, X. H.; El-Sayed, I. H.; El-Sayed, M. A. *Accounts Chem. Res.* **2008**, *41*, 1578-1586.

(3) Tao, A. R.; Habas, S.; Yang, P. D. *Small* **2008**, *4*, 310-325.

(4) Xia, Y. N.; Xiong, Y. J.; Lim, B.; Skrabalak, S. E. *Angew. Chem.-Int. Edit.* **2009**, *48*, 60-103.

(5) Jana, N. R.; Gearheart, L.; Murphy, C. J. *J. Phys. Chem. B* **2001**, *105*, 4065-4067.

(6) Nikoobakht, B.; El-Sayed, M. A. *Chem. Mater.* **2003**, *15*, 1957-1962.

(7) Murphy, C. J.; San, T. K.; Gole, A. M.; Orendorff, C. J.; Gao, J. X.; Gou, L.; Hunyadi, S. E.; Li, T. *J. Phys. Chem. B* **2005**, *109*, 13857-13870.

(8) Sau, T. K.; Murphy, C. J. *Langmuir* **2004**, *20*, 6414-6420.

(9) Vigderman, L.; Zubarev, E. R. *Chem. Mater.* **2013**, *25*, 1450-1457.

(10) Ye, X. C.; Jin, L. H.; Caglayan, H.; Chen, J.; Xing, G. Z.; Zheng, C.; Doan-Nguyen, V.; Kang, Y. J.; Engheta, N.; Kagan, C. R.; Murray, C. B. *ACS Nano* **2012**, *6*, 2804-2817.

(11) Ye, X. C.; Zheng, C.; Chen, J.; Gao, Y. Z.; Murray, C. B. *Nano Lett.* **2013**, *13*, 765-771.

(12) Chen, H. J.; Shao, L.; Li, Q.; Wang, J. F. *Chem. Soc. Rev.* **2013**, *42*, 2679-2724.

(13) Perez-Juste, J.; Pastoriza-Santos, I.; Liz-Marzan, L. M.; Mulvaney, P. *Coord. Chem. Rev.* **2005**, *249*, 1870-1901.

(14) Lohse, S. E.; Murphy, C. J. *Chem. Mater.* **2013**, *25*, 1250-1261.

(15) Liu, M. Z.; Guyot-Sionnest, P. *J. Phys. Chem. B* **2005**, *109*, 22192-22200.

(16) Edgar, J. A.; McDonagh, A. M.; Cortie, M. B. *ACS Nano* **2012**, *6*, 1116-1125.

(17) Walsh, M. J.; Barrow, S. J.; Tong, W. M.; Funston, A. M.; Etheridge, J. *ACS Nano* **2015**, *9*, 715-724.

(18) Jackson, S. R.; McBride, J. R.; Rosenthal, S. J.; Wright, D. W. *J. Am. Chem. Soc.* **2014**, *136*, 5261-5263.

(19) Murphy, C. J.; Thompson, L. B.; Alkilany, A. M.; Sisco, P. N.; Boulos, S. P.; Sivapalan, S. T.; Yang, J. A.; Chernak, D. J.; Huang, J. Y. *J. Phys. Chem. Lett.* **2010**, *1*, 2867-2875.

(20) Katz-Boon, H.; Rossouw, C. J.; Weyland, M.; Funston, A. M.; Mulvaney, P.; Etheridge, J. *Nano Lett.* **2011**, *11*, 273-278.

(21) Carbo-Argibay, E.; Rodriguez-Gonzalez, B.; Gomez-Grana, S.; Guerrero-Martinez, A.; Pastoriza-Santos, I.; Perez-Juste, J.; Liz-Marzan, L. M. *Angew. Chem.-Int. Edit.* **2010**, *49*, 9397-9400.

(22) Gai, P. L.; Harmer, M. A. *Nano Lett.* **2002**, *2*, 771-774.

(23) Sohn, K.; Kim, F.; Pradel, K. C.; Wu, J. S.; Peng, Y.; Zhou, F. M.; Huang, J. X. *ACS Nano* **2009**, *3*, 2191-2198.

(24) Huang, Y. J.; Wu, L.; Chen, X. D.; Bai, P.; Kim, D. H. *Chem. Mater.* **2013**, *25*, 2470-2475.

(25) Zhang, L. F.; Zhang, C. Y. *Nanoscale* **2013**, *5*, 5794-5800.

(26) Liu, W. Q.; Zhang, H.; Wen, T.; Yan, J.; Hou, S.; Shi, X. W.; Hu, Z. J.; Ji, Y. L.; Wu, X. C. *Langmuir* **2014**, *30*, 12376-12383.

(27) Goris, B.; Bals, S.; Van den Broek, W.; Carbo-Argibay, E.; Gomez-Grana, S.; Liz-Marzan, L. M.; Van Tendeloo, G. *Nat. Mater.* **2012**, *11*, 930-935.

(28) Wang, Z. L.; Gao, R. P.; Nikoobakht, B.; El-Sayed, M. A. *J. Phys. Chem. B* **2000**, *104*, 5417-5420.

(29) Katz-Boon, H.; Walsh, M.; Dwyer, C.; Mulvaney, P.; Funston, A. M.; Etheridge, J. *Nano Lett.* **2015**, *15*, 1635-41.

(30) Ming, T.; Feng, W.; Tang, Q.; Wang, F.; Sun, L. D.; Wang, J. F.; Yan, C. H. *J. Am. Chem. Soc.* **2009**, *131*, 16350-16351.

(31) Zhang, Q. F.; Wang, H. *ACS Catal.* **2014**, *4*, 4027-4033.

(32) Tian, N.; Zhou, Z. Y.; Sun, S. G.; Ding, Y.; Wang, Z. L. *Science* **2007**, *316*, 732-735.

(33) Quan, Z. W.; Wang, Y. X.; Fang, J. Y. *Accounts Chem. Res.* **2013**, *46*, 191-202.

(34) Xia, X. H.; Zeng, J.; McDearmon, B.; Zheng, Y. Q.; Li, Q. G.; Xia, Y. N. *Angew. Chem.-Int. Edit.* **2011**, *50*, 12542-12546.

(35) Zhang, J. A.; Langille, M. R.; Personick, M. L.; Zhang, K.; Li, S. Y.; Mirkin, C. A. *J. Am. Chem. Soc.* **2010**, *132*, 14012-14014.

(36) Tran, T. T.; Lu, X. M. *J. Phys. Chem. C* **2011**, *115*, 3638-3645.

(37) Ma, Y. Y.; Kuang, Q.; Jiang, Z. Y.; Xie, Z. X.; Huang, R. B.; Zheng, L. S. *Angew. Chem.-Int. Edit.* **2008**, *47*, 8901-8904.

(38) Niu, W. X.; Zhang, W. Q.; Firdoz, S.; Lu, X. M. *Chem. Mater.* **2014**, *26*, 2180-2186.

(39) O'Brien, M. N.; Jones, M. R.; Brown, K. A.; Mirkin, C. A. *J. Am. Chem. Soc.* **2014**, *136*, 7603-7606.

(40) Jing, H.; Zhang, Q. F.; Large, N.; Yu, C. M.; Blom, D. A.; Nordlander, P.; Wang, H. *Nano Lett.* **2014**, *14*, 3674-3682.

(41) Jiang, R. B.; Chen, H. J.; Shao, L.; Li, Q.; Wang, J. F. *Adv. Mater.* **2012**, *24*, OP200-OP207.

(42) Chiu, C. Y.; Chung, P. J.; Lao, K. U.; Liao, C. W.; Huang, M. H. *J. Phys. Chem. C* **2012**, *116*, 23757-23763.

(43) Chen, H. J.; Kou, X. S.; Yang, Z.; Ni, W. H.; Wang, J. F. *Langmuir* **2008**, *24*, 5233-5237.

(44) Ringe, E.; McMahon, J. M.; Sohn, K.; Cobley, C.; Xia, Y. N.; Huang, J. X.; Schatz, G. C.; Marks, L. D.; Van Duyne, R. P. *J. Phys. Chem. C* **2010**, *114*, 12511-12516.

(45) Peng, B.; Chen, J. *Energy Environ. Sci.* **2008**, *1*, 479-483.

(46) Goksu, H.; Ho, S. F.; Metin, O.; Korkmaz, K.; Garcia, A. M.; Gultekin, M. S.; Sun, S. H. *ACS Catal.* **2014**, *4*, 1777-1782.

(47) Xie, W.; Herrmann, C.; Kompe, K.; Haase, M.; Schlucker, S. *J. Am. Chem. Soc.* **2011**, *133*, 19302-19305.

(48) Huang, J. F.; Zhu, Y. H.; Lin, M.; Wang, Q. X.; Zhao, L.; Yang, Y.; Yao, K. X.; Han, Y. *J. Am. Chem. Soc.* **2013**, *135*, 8552-8561.

(49) Huang, Y. F.; Zhu, H. P.; Liu, G. K.; Wu, D. Y.; Ren, B.; Tian, Z. Q. *J. Am. Chem. Soc.* **2010**, *132*, 9244-9246.

(50) Sun, M. T.; Xu, H. X. *Small* **2012**, *8*, 2777-2786.

CHAPTER 7

Facet Control of Gold Nanorods

7.1 Introduction

Ever since its discovery in 1990s,[1] Au nanorod has been a model system for exploring the anisotropic shape evolution of nanocrystals with thermodynamically unexpected geometries.[2-12] The state-of-the-art colloidal synthesis of single-crystalline Au nanorods involves seed-mediated anisotropic nanocrystal growth coguided by a foreign metal ion, Ag+, and halide-containing cationic surfactants, typically cetyltrimethylammonium bromide (CTAB).[2-4,9-14] While detailed mechanistic understanding of the synergy between Ag^+ ions and the surfactants still remains elusive,[15-19] this seed-mediated growth method has become the most popular approach to the realization of precise control over both the longitudinal and transverse dimensions of cylindrical Au nanorods. Tight control over nanorod aspect ratios allows one to fine-tune the plasmon resonances over a broad spectral range that spans the entire visible and near-infrared regions.[3,4,7,8,11] Such exceptional tunability of plasmon-dominated light absorption and scattering properties, when combined with the rich chemistry for surface functionalization of Au, endows Au nanorods with great promise for applications in diverse areas, such as plasmon-enhanced spectroscopies,[20-25] molecular sensing,[26-28] bioimaging,[8,29-33] drug delivery,[30,34,35] and photothermal cancer therapy.[8,29,30,32,36]

Equally important to the control over nanorod aspect ratios is the capability of fine-tailoring the surface structures of Au nanorods with atomic-level precision. For many biomedical and biosensing applications, the nature of the surface ligands around Au nanorods may be even more important than the Au core itself in terms of interfacial chemistry and biocompatibility.[8,9,30] The crystallographic facets exposed on Au nanorod surfaces play pivotal roles in determining the affinity, specificity, and dynamics of the

interactions between ligand molecules and Au surfaces.[9] In addition, deliberate facet control opens up unique opportunities to functionalize the nanorod surfaces with desired molecular moieties in a site-selective manner, enabling the molecularly guided assembly of Au nanorods into mesoscopic hierarchical superstructures with desired architectures and functionalities.[37-41] Furthermore, precise facet control is vital to the optimization of the catalytic performance of Au nanorods. Inhomogeneous site-specific catalytic activities were recently observed on individual single-crystalline Au nanorods, which are intimately tied to the geometric distribution of various local facets and defects on the nanorod surfaces.[42] In striking contrast to the great success achieved in fine-tuning the aspect ratios, the seed-mediated nanorod synthesis unfortunately offers limited capability of facet control.[7,9-11,43-48] Although typically exhibiting a cylindrical morphology with two rounded ends, experimentally fabricated Au nanorods are essentially enclosed by multifaceted surfaces composed of a mixture of various types of high-index and low-index facets that are capped with surfactants and other adsorbates.[9,43-45,49-51] Quantitative assignment of the crystallographic facets exposed on the surfaces of Au nanorods, however, has long been a subject under intense debate.[9,43-45,49-51] While catalytically active sites are abundant on the highly curved nanorod surfaces, it remains a significant challenge to quantitatively correlate the catalytic activities with the atomic-level surface structures due to the intrinsic structural complexity and poor control over the nanorod facets.

Conventional single-crystalline Au nanorods with a cylindrical morphology are typically prepared by seed-mediated growth in the presence of Ag^+ and CTAB.[4,9-11] The nanorod growth is initiated by adding colloidal Au seeds (~2-4 nm in diameter) into a

growth solution containing $HAuCl_4$ (Au precursor), Ag^+ (structure-directing foreign ion), CTAB (surface capping surfactant), and ascorbic acid (mild reducing agent). The most convenient way to tune the nanorod aspect ratios is to vary the concentration of Ag^+ in the growth solution, while the aspect ratios and surface curvature of Au nanorods can be further fine-tuned through post-fabrication overgrowth[46,47,52-56] or anisotropic oxidative etching processes.[57,58] Recently, Murray and co-workers demonstrated that Au nanorods enclosed exclusively by one specific type of high-index {hk0} facets could be fabricated using binary surfactant mixtures instead of CTAB to guide the seed-mediated growth.[59,60] These {hk0}-faceting Au nanorods are geometrically defined as elongated tetrahexahedral (ETHH) nanoparticles (NPs).[61,62] The {hk0} facets, composed of alternating {100}/{110} terraces and steps, possess high fraction of coordinatively unsaturated surface atoms that are catalytically much more active than the close-packed surface atoms on the low-index {100} and {111} facets.[63,64] More recently, we found that the {hk0}-faceting Au ETHH NPs, also known as convex nanocuboids, could be fabricated through overgrowth of preformed cylindrical Au nanorods in the presence of cupric (Cu^{2+}) ions and appropriate binary surfactant mixtures.[65] In this chapter, we use the Au ETHH NPs as the starting materials to demonstrate that an entire family of high-index and low-index facets can be controllably created on the surfaces of single-crystalline nanorods using cuprous (Cu^+) ions and CTAB as a unique pair of surface capping competitors to judiciously maneuver the thermodynamic and kinetic factors that govern the facet evolution during nanorod overgrowth. The unique combination of desired plasmonic properties and fine-tailored surface structures on Au nanorods enables us to gain detailed, quantitative insights into the facet-dependent catalytic molecular

transformations on Au nanoparticle (NP) surfaces using surface-enhanced Raman scattering (SERS) as an *in situ* plasmon-enhanced spectroscopic tool.

7.2 Experimental Section

Chemicals and Materials. All reagents were used as received without further purification. Ultrapure water (18.2 MΩ resistivity, Barnstead EasyPure II 7138) was used for all experiments.

Synthesis of Au ETHH NPs. Au ETHH NPs were prepared following a previously published protocol[59] with minor modifications. Briefly, colloidal Au seeds were prepared by the reducing $HAuCl_4$ with $NaBH_4$ in the presence of CTAB. First, 5.0 mL of 0.5 mM $HAuCl_4$ was mixed with 5 mL of 0.2 M CTAB solution. Then, 1.0 mL of ice-cold, freshly prepared 6 mM $NaBH_4$ was quickly injected into the mixture under magnetic stirring (1200 rpm). The seed solution was stirred for 2 min and then left undisturbed for 30 min before use. To prepare the Au ETHH NP growth solution, 7.0 g of CTAB and 1.234 g of NaOL were dissolved in 250 mL of water at 60 ℃. The solution was cooled to 30 ℃ and then 24 mL of 4 mM $AgNO_3$ was added. The mixture was kept undisturbed at 30 ℃ for 15 min, followed by the addition of 250 mL of 1 mM $HAuCl_4$. The solution became colorless after 90 min of stirring at 700 rpm and 1.8 mL HCl (37 wt % in water, 12.1 M) was then introduced into the mixture. After another 15 min of slow magnetic stir at 400 rpm, 1.30 mL of 64 mM ascorbic acid was added. Finally, 0.4 mL of seed solution was injected into the growth solution and the mixture solution was vigorously stirred for another 30 s and then left undisturbed at 30 ℃ for 12 h. The resulting Au ETHH NPs were collected by centrifugation at 7000 rpm for 20 min followed by removal of the supernatant and finally redispersed in 30 mL of 20 mM CTAB.

Synthesis of Au ETOH NPs. Au ETOH NPs were prepared via overgrowth of Au ETHH NPs in the presence of $HAuCl_4$, CTAB, and AA. In a typical procedure, 200 μL of colloidal Au ETHH NPs were first redispersed in 100 μL 0.10 M CTAB after being washed once with water. The growth solution was prepared by sequentially adding H_2O (7.40 mL), $HAuCl_4$ (0.2 mL, 10 mM), and AA (1.0 mL, 0.10 M) into a CTAB (1.30 mL, 0.10 M) solution. After gently mixing the growth solution for 30 s, the growth of Au ETOH was initiated by adding 100 μL of the Au ETHH NPs (in 0.1 M CTAB). The reaction solution was gently mixed for 30 s immediately after the addition of Au ETHH NPs and then left undisturbed at 30 ℃ for 1 h. The obtained Au ETOH NPs were washed with water twice through centrifugation/redispersion cycles, and finally redispersed in 200 μL of 20 mM CTAB. The size and aspect-ratio of ETOH can be controlled by simply adjusting amount of $HAuCl_4$ added. The total volume of the growth solutions was always fixed at 10.0 mL.

Synthesis of Au CCB, QCB, TCB, and EOH NPs. Au CCB, QCB, TCB, and EOH NPs were synthesized via overgrowth of Au ETHH NPs in the presence of Cu^{2+}, $HAuCl_4$, CTAB, and AA. In a typical procedure of CCB NP synthesis, 200 μL of Au ETHH NPs were first redispersed in 100 μL 0.10 M CTAB after being washed once with water. The growth solution was prepared by sequentially adding H_2O (7.395 mL), $HAuCl_4$ (0.2 mL, 10 mM), $Cu(NO_3)_2$ (5 μL, 10 mM), and AA (1.0 mL, 0.10 M) into a CTAB (1.30 mL, 0.10 M) solution. After gently mixing the growth solution for 30 s, the growth of Au CCB NPs was initiated by adding 100 μL of the Au ETHH NPs (in 0.1 M CTAB). The reaction solution was gently mixed for 30 s immediately after the addition of Au ETHH NPs and then left undisturbed at 30 ℃ for 1 h. The obtained Au CCB NPs were washed

with water twice through centrifugation/redispersion cycles, and finally redispersed in 200 μL of 20 mM CTAB. The morphologies of Au CCB NPs evolved into QCB, TCB, and EOH when increasing amount of Cu^{2+} was added into the growth solution. The morphologies of the NPs could be controlled by adjusting the molar ratios between Cu^{2+} and CTAB. In the presence of 14 mM CTAB, the optimal concentrations of Cu^{2+} were 5 μM for CCB, 70 μM for QCB, 100 μM for TCB, and 300 μM for EOH NPs, respectively. The total volume of the growth solutions was always fixed at 10.0 mL.

Overgrowth of Au ETHH NPs in CTAB/NaOL Binary Surfactants. The ETHH morphology was well-preserved while the particle aspect ratios decreased during overgrowth of Au ETHH NPs in the presence of Ag^{+}, $HAuCl_4$, CTAB, NaOL, HCl, and AA.

Ag^{+}-Guided Overgrowth of Au ETHH NPs. The ETHH NPs evolved into CCB, TCB, and EOH NPs composed of Au nanorod core and Au-Ag alloy shell upon overgrowth of Au ETHH NPs in the presence of Ag^{+}, $HAuCl_4$, CTAB, and AA.

Characterizations. The morphologies, structures, compositions, and surface properties of the NPs were characterized by TEM, SEM, EDS, HAADF-STEM, XPS, and ζ-potential measurements. The optical extinction spectra of the NPs were measured using a Beckman Coulter Du 640 spectrophotometer. Raman spectra were obtained on a Bayspec Nomadic Raman microscopy built on an Olympus BX51 microscope equipped with a 785 nm CW diode laser. SERS spectra were collected on colloidal suspensions of Au ETHH, ETOH, CCB, QCB, and EOH NPs coated with 4-NTP SAMs.

Catalytic Reaction Kinetics Studied by Time-Resolved SERS. To use SERS to study the catalytic reactions, we first pre-adsorbed SAMs of 4-NTP onto the surfaces of

Au ETHH, ETOH, CCB, QCB, and EOH NPs. The nanoparticle-catalyzed 4-NTP hydrogenation occurred at room temperature upon the addition of 20 μL of Au NPs (~1.0 $\times 10^{11}$ particles mL^{-1}), 50 μL of ultrapure water, 10 μL of 10 mM K_2CO_3, and 20 μL of 10 mM AB in a 0.5 mL Eppendorf centrifuge tube. The kinetics of the catalyzed reactions was measured in real time using time-resolved SERS. The excitation laser was focused on the reaction mixture using a 10× objective [Numerical Aperture (NA) = 0.30, working distance (WD) = 11.0 mm, Olympus MPLFLN]. The laser power was measured to be 10.0 mW at the samples and the signal acquisition time was 1 s for Au ETHH NPs, and 2s for all other samples, respectively. Successive SERS spectra were collected during the reaction until completion of the reduction of 4-NTP into 4-ATP. The total volume of the reaction mixtures was fixed at 100 μL.

7.3 Results and Discussions

For noble metals with face centered cubic (fcc) structures, such as Au, Pt, and Pd, the low-index {111} and {100} facets are thermodynamically more stable than the high-index facets and are thus highly favored during nanocrystal growth.[63,64] However, the surface energies of various facets can be significantly altered when the facets interact with surfactants and/or foreign ions, allowing the nanocrystals to evolve into exotic polyhedral geometries that are enclosed by high-index facets.[66-72] On the other hand, the nanocrystal facet evolution can also be kinetically controlled using appropriate combinations of structure-directing ions and surface capping surfactants to modulate the degree of supersaturation of the crystal growth units.[73] Starting from the Au ETHH NPs, we found that a series of interesting nanorod-derived geometries enclosed by well-defined characteristic high-index and low-index facets, such as elongated trisoctahedral

(ETOH) NPs, concave cuboidal (CCB) NPs, quasi-cuboidal (QCB) NPs, truncated cuboidal (TCB) NPs, and elongated octahedral (EOH) NPs, could be obtained in a highly selective and controllable manner by systematically varying the molar ratio between Cu^{2+} and CTAB in the ETHH NP overgrowth solution.

We first used scanning electron microscopy (SEM) and transmission electron microscopy (TEM) to characterize the structural evolution of Au ETHH NPs upon their overgrowth in the presence of 14 mM CTAB and varying concentrations of Cu^{2+}. We synthesized Au ETHH NPs with aspect ratio of ~3 (Figure 7.1A) following a previously reported seed-mediated growth method in a CTAB/oleate binary surfactant system[59] with some minor modifications. Upon exposure to an overgrowth solution containing $HAuCl_4$, ascorbic acid (AA), and CTAB, the Au ETHH NPs evolved into ETOH NPs with significantly increased lateral dimensions (Figure 7.1B). The ETOH NPs represent an interesting geometry derived from elongation of a trisoctahedron enclosed by 24 high-index {hhk} facets (composed of alternating {110}/{111} terraces and steps). When Cu^{2+} ions were introduced into the nanorod overgrowth solution, the ETHH NPs underwent drastically different structural evolution processes and the Cu^{2+}/CTAB molar ratio was found to be a key knob that one could adjust to fine-control the facets of the resulting Au nanorods. At relatively low Cu^{2+} concentrations (e.g., $[Cu^{2+}]$ = 5 μM), Au CCB NPs with well-defined concave facets were obtained (Figure 7.1C). As discussed in greater detail later on, each CCB NP is exclusively enclosed by 24 high-index {hkk} facets, which are geometrically derived through combination of alternating {100}/{111} terraces and steps. As the Cu^{2+} concentration increased, the degree of surface indentation of the CCB NPs gradually decreased until Au QCB NPs (Figure 7.1D) whose surfaces were dominated by

{100} facets formed when the concentration of Cu^{2+} reached 70 μM. Further increase in Cu^{2+} concentration resulted in corner truncation of the QCB NPs, giving rise to the formation of TCB NPs (Figure 7.1E). Each TCB NP is enclosed by 4 {100} facets on the lateral sides, 2 {100} facets at the ends, and 8 {111} facets at the truncated corners. The corner truncation became progressively more significant as the Cu^{2+} concentration increased. The TCB NPs eventually evolved into EOH NPs with two sharp tips each of which was enclosed by 4 {111} facets (Figure 7.1F) when the {100} end facets completely disappeared at Cu^{2+} concentrations higher than 200 μM. The as-fabricated Au ETHH, ETOH, CCB, QCB, TCB, and EOH NPs all exhibited narrow size distributions and high geometric uniformity with yields typically higher than 95%.

Each faceted nanorod geometry exhibited its own characteristic plasmonic features in the optical extinction spectra (Figure 7.1G). The ETHH NPs displayed a longitudinal and a transverse plasmon resonance at ~770 nm and ~514 nm, respectively. The longitudinal plasmon peak was much stronger than the transverse plasmon peak because of stronger coupling of the incident light with the plasmons along the longitudinal axis of the NPs. Upon formation of ETOH NPs, both the longitudinal and transverse plasmon resonances red-shifted and the transverse plasmon peak became significantly stronger largely due to the increased lateral dimensions of the NPs. The development of surface concavity during the transition of ETOH to CCB NPs caused significant red-shifts of both the longitudinal and transverse plasmon resonances accompanied by increase in peak intensities. Interestingly, the transverse plasmon band split into two peaks, which was a unique spectral signature of nanorods with surface indentations on their lateral sides.[47,65] Decrease in surface indentation led to progressive blue-shift and weakening of both the

longitudinal and transverse plasmon peaks until the formation of QCB NPs. The longitudinal plasmon peak was observed to gradually blue-shift and become weaker while the transverse plasmon peak remained very robust at essentially fixed wavelengths as the degree of corner truncation of TCB NPs increased. The transverse plasmon peak became even stronger than the longitudinal plasmon peak when the TCB NPs eventually evolved into EOH NPs. Because both the plasmon resonance wavelengths and the optical extinction spectral line-shapes were sensitively dependent on the geometric details of the faceted Au nanorods, we were able to use optical extinction spectroscopy in combination with TEM to track detailed structural evolution as the Cu^{2+}/CTAB ratio systematically varied.

We further used high-angle annular dark-field scanning transmission electron microscopy (HAADF-STEM) to resolve the atomic-level surface structures of the faceted Au nanorods. The high-resolution HAADF-STEM images shown in Figure 7.2 were all taken with the electron beam projected along specific zone axes of individual NPs, which allowed us to resolve the atomic structures of specific facets exposed on the nanorod surfaces. The relative orientation of each NP with respect to the electron beam was further verified by the crystalline lattices in the high-resolution HAADF-STEM images and the fast-Fourier transform patterns of the images. In Figure 7.2, the geometric models and atomic-level structures of various facets were also illustrated. As shown in Figure 7.2A-C, each Au ETHH NPs was exclusively enclosed by 24 {730} facets, which were identified by both the atomic steps shown in high resolution STEM images (Figure 7.2C-i, 7.2C-ii, and 7.2C-iii) and the characteristic dihedral angles when the particle was projected along the [001] zone axis. The {730} facet consists of repeating high-index

{210} and {310} local facets as illustrated in Figure 7.2A. The two ends of each ETOH NP were enclosed exclusively by high-index {221} facets while the lateral side facets were indexed as {110} (Figure 7.2D-F). Four of the 24 {221} facets and 2 of the 4 {110} facets became parallel to the electron beam when an ETOH NP was projected along the $[1\bar{1}0]$ zone axis (Figure 7.2F, 2F-i, 2F-ii, and 2F-iii). The CCB NPs, each of which was enclosed by 24 concave facets with equivalent Miller indices, exhibited orientation-dependent geometrical contours in the HAADF-STEM images (Figure 7.2G-J). When a CCB NP was projected along $[1\bar{1}0]$ zone axis (Figure 7.2J and 2J-i), 4 of the 24 facets were aligned parallel to the electron beam, allowing us to assign the facets to high-index {511} facet based on the arrangement of surface atoms. In comparison to the high-index faceting NPs, Au QCB NPs had a simpler geometry enclosed predominantly by 6 low-index {100} facets with minor structural nonideality, such as slight corner truncations and defects on side facets, with respect to a perfect cuboid (Figure 7.2K,L). The exposed facets on Au TCB NPs were resolved as {111} at the truncated corners and {100} on side and end faces. When a TCB NP further evolved into an EOH NP, the {100} facets disappeared as the 4 {111} facets merged at each end of the NP (Figure 7.2M-O). The arrangement of surface atoms on {111} facets were resolved by high-resolution HAADF STEM images when an EOH NP was imaged under the project along the $[1\bar{1}0]$ zone axis (Figure 7.2O, 2O-i, and 2O-ii). We analyzed the characteristic angles of the high-index faceting NPs and the image intensity profiles along various lines across the NP cross sections, which further qualitatively confirmed the three-dimensional (3D) geometric profiles of the NPs observed in the SEM and TEM images. In all the high-resolution HAADF-STEM images shown in Figure 7.2, only the crystalline lattices of fcc Au were

resolved. Neither surface deposition of metallic Cu nor the formation of Au-Cu bimetallic alloy domains was observed, indicating the absence of metallic Cu(0) in these faceted nanorods.

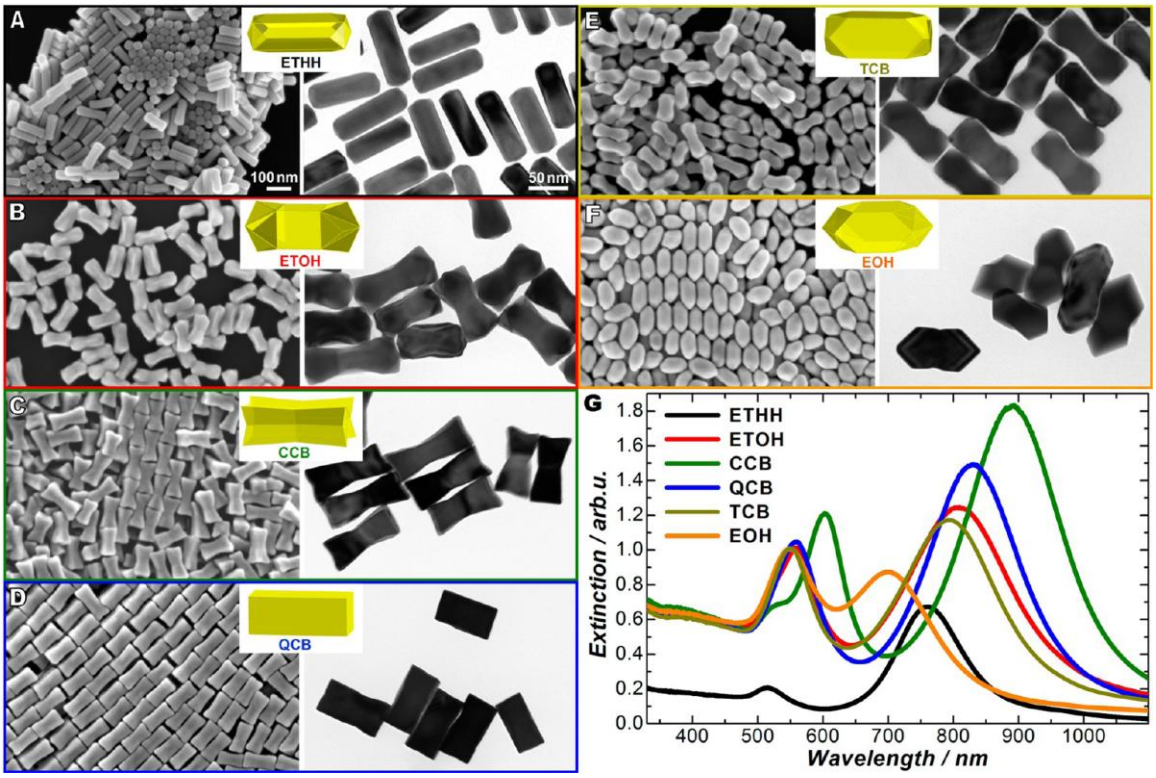

Figure 7.1. SEM and TEM images of Au (A) ETHH, (B) ETOH, (C) CCB, (D) QCB, (E) TCB, and (F) EOH NPs. The SEM images and TEM images are shown in the left and right columns, respectively. The insets show the geometric models of individual NPs. All the SEM and TEM images share the same scale bars in panel A. (G) Extinction spectra of colloidal Au ETHH, ETOH, CCB, QCB, TCB, and EOH NPs. The particle concentration was ~1.0×10^{11} particles mL^{-1} for all the samples.

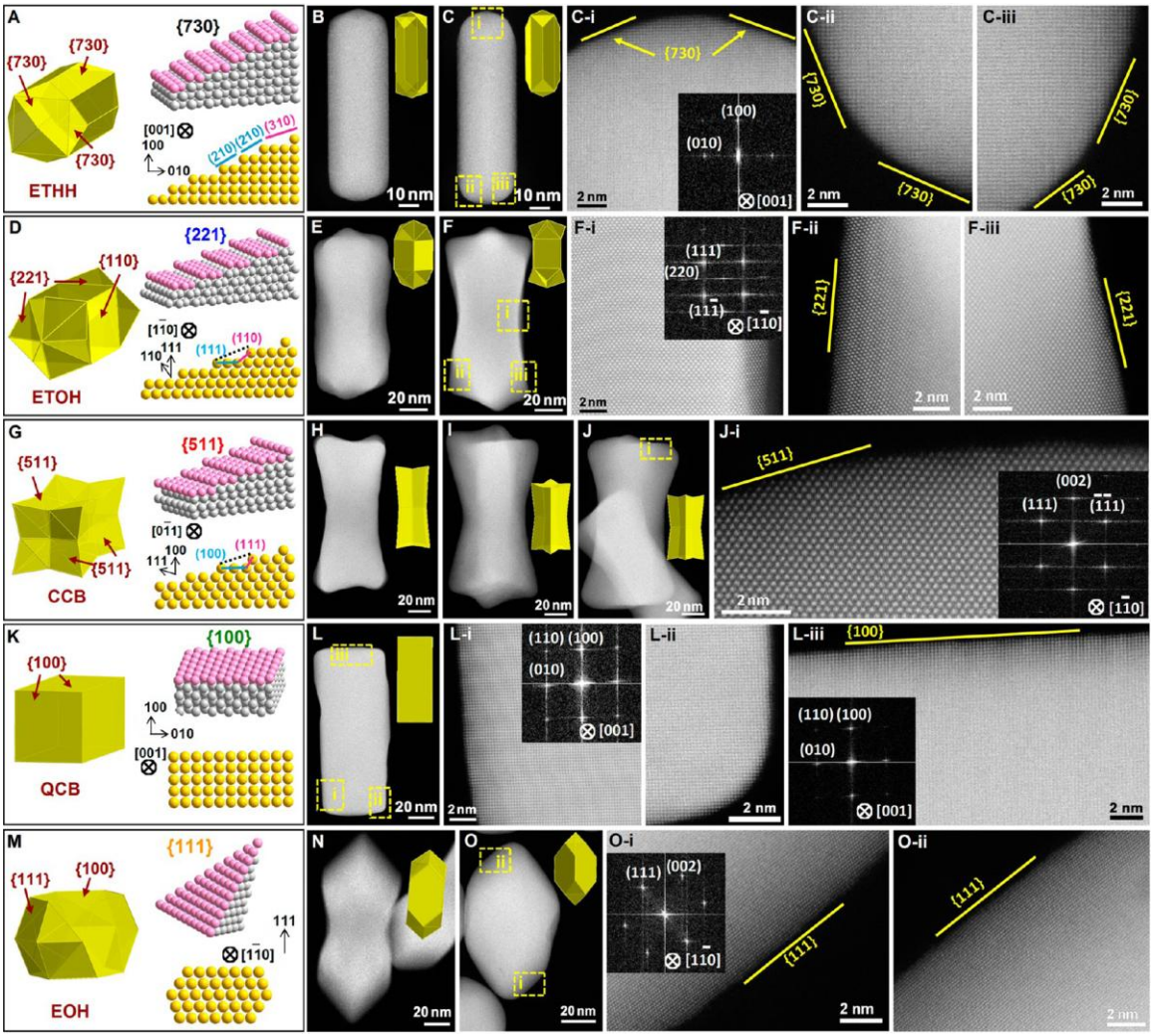

Figure 7.2. Atomic level surface structures of Au ETHH, ETOH, CCB, QCB, and EOH NPs. (A) Geometric models of an ETHH NP and {730} facet. (B,C) HAADF-STEM images of individual ETHH NPs. (D) Geometric models of an ETOH NP and {221} facet. (E,F) HADDF-STEM images of individual ETOH NPs. (G) Geometric models of a CCB NP and {511} facet. (H-J) HADDF-STEM images of individual CCB NPs. (K) Geometric models of a QCB NP and {100} facet. (L) HADDF-STEM image of an individual QCB NP. (M) Geometric models of EOH and {111} facet. (N,O) HADDF-STEM images of individual EOH NPs. The insets show the geometric models of the NPs viewed at the corresponding orientation. (x-i, x-ii, x-iii, x = C, F, J, L, O) High-resolution HAADF-STEM images of various regions (i, ii, and iii) for each NP shown in panels C, F, J, L, and O, respectively. These NPs were imaged with projection along the [001] zone axis for ETHH and QCB NPs, and $[1\bar{1}0]$ zone axis for ETOH, CCB and EOH NPs. The insets in panels C-i, F-i, J-i, L-i, L-iii, and O-i are the fast Fourier transform (FFT) patterns of the region shown in each panel, respectively.

Complementary to the two-dimensional (2D) microscopic imaging characterizations, electron tomography measurements allowed us to more accurately visualize the unique

3D structures and more quantitatively index the facets of the high-index faceting NPs. For the 3D electron tomography, a series of Z-contrast STEM images were acquired by tilting the specimen over a wide range of angles from -70 ° to +70 ° at every 2 ° intervals using a field-emission instrument operated at 200 kV. The 3D tomograms were reconstructed using a multiplicative simultaneous iterative reconstruction technique (SIRT). The 3D reconstructions were visualized using isovalue surfaces in the Amira software. As shown in Figure 7.3, the reconstructed 3D geometries matched very well with the structural information obtained from the 2D TEM and HAADF-STEM images. The 3D tomography results further verified that the ETHH NPs and CCB NPs were predominantly enclosed by {730} and {511} facets, respectively. The two ends along the longitudinal axis of each ETOH NP were enclosed by {221} facets while the lateral sides were dominated by {110} facets. The experimentally fabricated NPs exhibited only slight deviations from the ideal geometric models. The corners and edges of the ETOH and CCB NPs appeared to be less sharp in the reconstructed 3D geometries in comparison to those observed in the TEM and SEM images possibly due to the fact that the exposure of NPs to electron beam over extended time periods during tilt-series tomography measurements may introduce slight geometric modifications to the sharp corners and edges of the NPs. In spite of their structural nonideality, all the nanorod-derived structures exhibited well-defined multifaceted geometries and their surfaces were dominated by their characteristic facets. The structural information obtained from SEM, TEM, HAADF-STEM, and 3D tomography measurements all agree with each other.

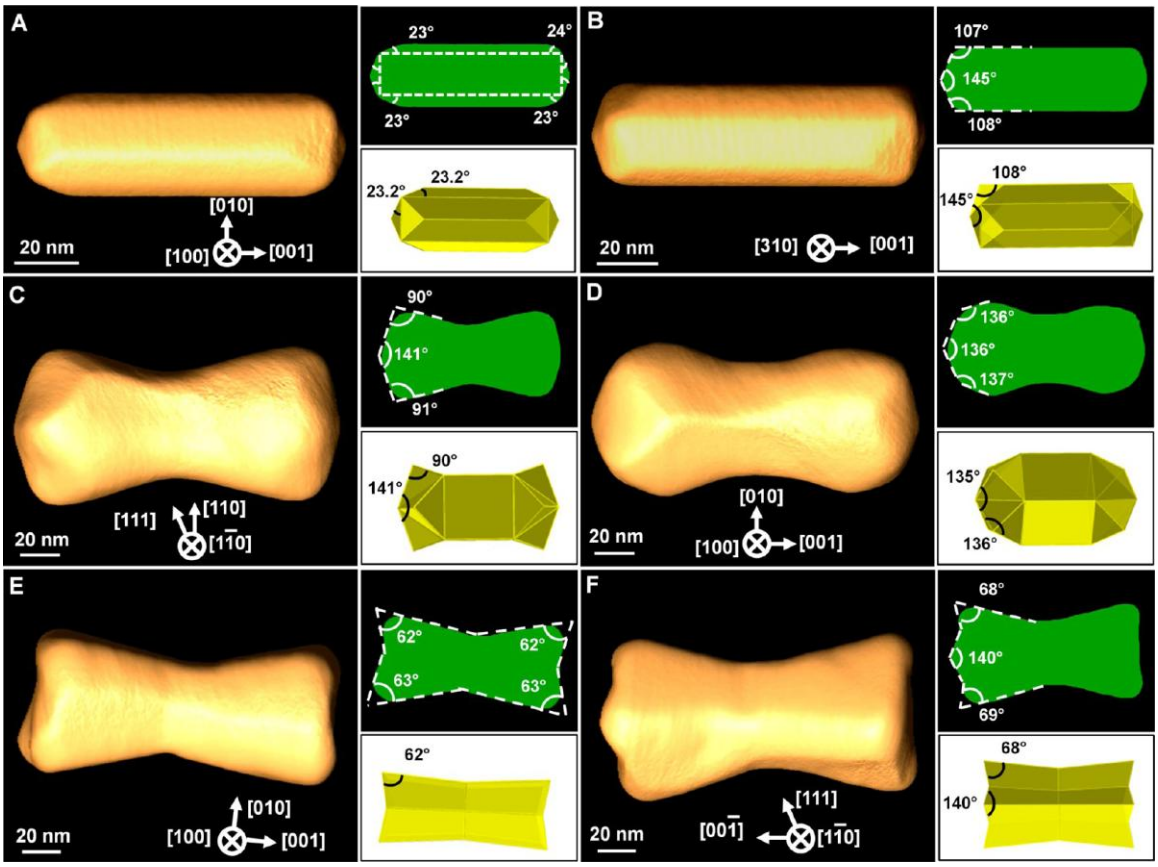

Figure 7.3. 3D electron tomographic reconstructions (left panels), cross-sectional views of the 2D projection of tomographic reconstructions (right upper panels), and the corresponding ideal geometric models (right bottom panels) of the high-index faceting nanorods: an ETHH NP viewed along (A) [100] zone axis and (B) [310] zone axis, an ETOH NP viewed along (C) [1$\bar{1}$0] zone axis and (D) [100] zone axis, and a CCB NP viewed along (E) [100] zone axis and (F) [1$\bar{1}$0] zone axis. The characteristic geometric angles on the 2D projections are labeled for each geometry.

To gain further insights into the synergistic effects of Cu^{2+} and CTAB on the facet evolution of Au nanorods, we used X-ray photoelectron spectroscopy (XPS) and ζ-potential measurements to fully characterize the surface compositions and charges of the faceted nanorods. Energy dispersive spectroscopy (EDS) results verified that the bulk composition of the faceted nanorods was monometallic Au and none of the Cu, Br, or N elements possibly existing in the surface adsorbates were detectable in EDS. However, Br signals were clearly resolved in XPS spectra collected on the Au ETHH, ETOH, CCB,

QCB, TCB, and EOH NPs, indicating the capping of the Au surfaces with CTAB. XPS results also verified the presence of Ag on the surfaces of Au ETHH NPs as a consequence of Ag^{+}-guided seed-mediated growth. However, Ag became undetectable by XPS when the ETHH NPs overgrew into various faceted nanorods because XPS was a surface characterization technique with a penetration depth of only ~1 nm under our experimental conditions. While no XPS signal of Cu was detectable on the surfaces of Au ETOH NPs, the XPS spectral features of Cu species were clearly resolvable on the CCB, QCB, TCB, and EOH NPs. High-resolution XPS spectra of the Cu 2p region (Figure 7.4A) further revealed that Cu^{2+} was mostly reduced to Cu (I) species on the surfaces of Au CCB, QCB, and EOH NPs while the XPS signals of Cu (II) species were almost undetectable. The relative intensities of the Cu (I) 2p XPS peaks increased in the order of CCB < QCB < EOH NPs whereas the intensities of Br 3d peaks showed an opposite trend (Figure 7.4B), decreasing in the order of ETHH > ETOH > CCB > QCB > EOH NPs. As shown in Figure 7.4C, no peak shift or split was observed in the high-resolution XPS spectra of Au 4f region in comparison to the spectrum of bulk Au, indicating that the surface capping of Au facets by Cu (I) and CTAB did not modify the lattices or the electronic band structures of Au surface atoms to any detectable extent. This result provided additional evidence to the absence of metallic Cu on the overgrown faceted Au nanorods, which was in line with previous observations that Cu(II) ions could only be reduced to Cu(I), not metallic Cu(0), by ascorbic acid (AA) or sodium ascorbate in the presence of CTAB.[70,74] To further verify the reduction of Cu^{2+} by AA into Cu(I) species during the nanorod overgrowth, bicinchoninic acid (BCA), a Cu^{+}-specific chelating agent, was added into the nanorod overgrowth solution. The absorption peak centered at

560 nm in the extinction spectrum was characteristic of the water-soluble, purple-colored Cu(I)-BCA complex.[75] Therefore, it was cuprous ions (Cu^{+}) rather than cupric ions (Cu^{2+}) that played a key role in controlling the facet evolution of Au nanorods.

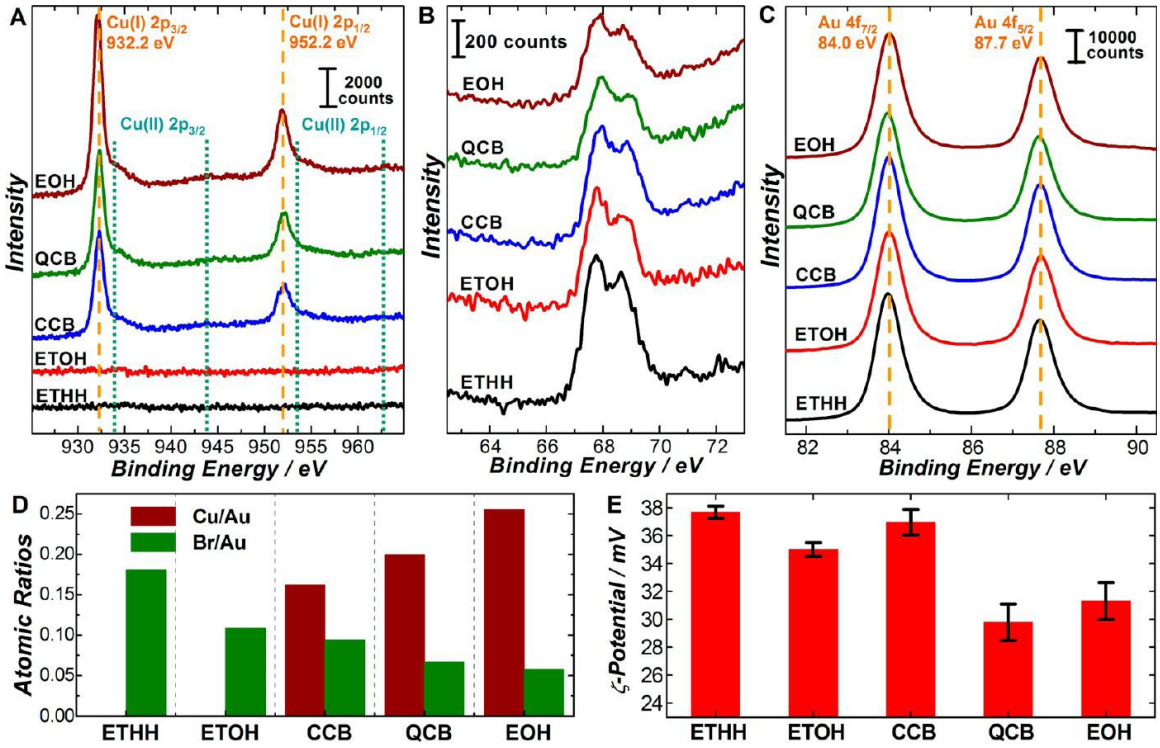

Figure 7.4. High-resolution XPS spectra of the (A) Cu 2p, (B) Br 3d, and (C) Au 4f regions of Au ETHH, ETOH, CCB, QCB, and EOH NPs. The spectra are offset for clarity. (D) Atomic ratios of Cu/Au and Br/Au on the surfaces of Au ETHH, ETOH, CCB, QCB, and EOH NPs probed by XPS. (E) ζ-potentials of colloidal Au ETHH, ETOH, CCB, QCB, and EOH NPs. The samples for ζ-potential measurements were all freshly prepared, centrifuged, and redispersed in 1 mM CTAB. The concentration of the colloids for ζ-potential measurements were kept at 2.0×10^{11} particles mL^{-1} for all the samples. The pH of the colloidal suspension was 7.4.

We used the XPS results to quantify the relative packing densities of Cu (I) and CTAB on the NP surfaces based on the atomic ratios of Cu/Au and Br/Au. As shown in Figure 7.4D, the packing densities of CTAB on the high-index faceting nanorods were significantly higher than those on the low-index faceting nanorods, decreasing in the order of ETHH > ETOH > CCB > QCB > EOH NPs. This trend correlated well with the

relative thermodynamic stability of the naked facets, suggesting that high surface packing density of CTAB might lower the surface energies and hence stabilize the high-index facets. In contrast, Cu(I) ions, when adsorbed on the Au surfaces, appeared to favor the formation of thermodynamically stable low-index facets. As a consequence, the high-index {hkk} facets on CCB NPs gradually evolved into {100} facets on QCB NPs and eventually into the thermodynamically most stable {111} facets on EOH NPs as the surface coverage of Cu(I) increased. Cu(I) ions and CTAB appeared to be a pair of surface-capping competitors because the increase in surface packing density of Cu(I) was accompanied by a decrease in packing density of CTAB (Figure 7.4D). The relative surface packing densities of Cu(I) and CTAB on the surfaces of various faceted Au nanorods were further correlated to the ζ-potentials of the NPs (Figure 7.4E). All the nanostructures had positively charged surfaces due to the formation of CTAB self-assembled bilayers on Au nanorod surfaces.[9] The surface adsorbed Cu(I) ions provided additional contribution to the positive surface charges of the NPs. Despite their lower surface packing density of CTAB, the CCB NPs exhibited higher surface charges than the ETOH NPs owing to the presence of surface-adsorbed Cu(I). Although CTAB was more sparsely packed on the surfaces of EOH NPs than QCB NPs, the EOH NPs displayed a more positive ζ-potential value than the QCB NPs due to the higher surface packing density of Cu(I) ions. It is noteworthy that the ζ-potential values reported here represented the apparent effective ζ-potentials, which allowed us to qualitatively compare the relative surface charge densities of various NP samples. In our ζ-potential measurements, a commercial zeta potentiometer was used to measure the free mobility and effective hydrodynamic sizes of NPs, which were then converted into ζ-potentials

using simple theoretical formulas approximating the NP as a hard sphere homogeneously coated with a charged thin layer. For anisotropic Au nanorods, the obtained values of ζ-potential were generally ~10% higher than the results from the spherical approximation when theories for cylindrical particles were applied to ζ-potential calculations using the actual dimensions of Au nanorods (determined from electron microscopy measurements).[76] More quantitative determination of accurate ζ-potentials, however, requires the incorporation of additional empirical or semi-empirical parameters, such as the geometric details of the faceted NPs and heterogeneous distribution of adsorbates on various facets, into the theoretical formulas, which is beyond the scope of this paper.

The facets of the overgrown Au nanorods could also be fine tailored through systematic variation of CTAB concentrations while keeping Cu^{2+} at fixed concentrations. The morphological evolution of the faceted Au nanorods as the CTAB concentration varied was tracked using a combination of optical extinction spectroscopy and TEM measurements (Figure 7.5). At relatively low Cu^{2+} concentrations (e.g., $[Cu^{2+}]$ = 10 μM), a structural evolution from TCB to CCB and eventually to ETOH was observed when the CTAB concentration progressively increased in the range from 3 to 51 mM. At relatively high Cu^{2+} concentrations (e.g., $[Cu^{2+}]$ = 100 μM), the NP morphologies gradually changed from EOH to TCB and eventually to CCB NPs as concentration of CTAB increased from 3 to 51 mM. Therefore, it was the molar ratio of Cu^{2+}/CTAB rather than the absolute concentrations of Cu^{2+} and CTAB that determined the surface structures and hence the geometries of the overgrown Au nanorods. The competition between Cu^{+} and CTAB could be further modulated by adding BCA into the overgrowth solutions. The specific and strong chelating interactions between BCA and Cu^{+} ions effectively

inhibited the competition between Cu^{+} and CTAB. Therefore, Au ETOH NPs were always obtained regardless of the relative $[Cu^{2+}]$/[CTAB] ratios when BCA was in excess with respect to Cu^{+}. Analogous to Cu^{+} ions, we found that Pb^{2+} could also compete with CTAB, allowing the ETOH NPs to evolve into CCB NPs. However, Pb^{2+} appeared to be much less effective than Cu^{+} in terms of facet control capability. The formation of CCB NPs required much higher concentrations of Pb^{2+} than those of Cu^{2+} mostly likely due to the much weaker interactions of Pb^{2+} with Au surfaces compared to the Cu^{+}-Au interactions.

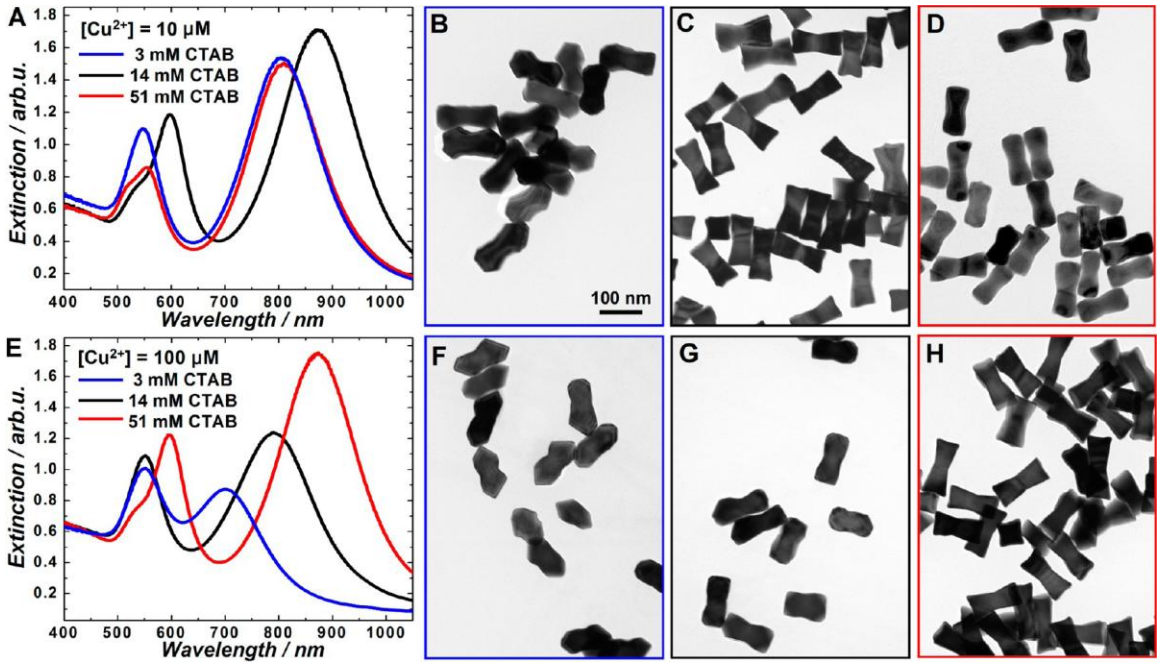

Figure 7.5. Extinction spectra of Au NPs obtained through overgrowth of Au ETHH NPs in the presence of various concentrations of CTAB and fixed Cu^{2+} concentrations: (A) $[Cu^{2+}]$ = 10 μM; (E) $[Cu^{2+}]$ = 100 μM. TEM images of faceted Au nanorods obtained through overgrowth of Au ETHH NPs under various conditions: (B) $[Cu^{2+}]$ = 10 μM, [CTAB] = 3 mM; (C) $[Cu^{2+}]$ = 10 μM, [CTAB] = 14 mM; (D) $[Cu^{2+}]$ = 10 μM, [CTAB] = 51 mM; (F) $[Cu^{2+}]$ = 100 μM, [CTAB] = 3 mM; (G) $[Cu^{2+}]$ = 100 μM, [CTAB] = 14 mM; (H) $[Cu^{2+}]$ = 100 μM, [CTAB] = 51 mM. All TEM images share the scale bar in panel B.

Among various foreign metal ion additives, Ag^+ has been so far most widely used to guide the seed-mediated shape evolution of noble metal nanocrystals. Ag^+ ions can be used in combination with appropriate surfactants to guide the growth of a series of high-index and low-index faceting polyhedral NPs through selective surface passivation induced by underpotential deposition (UPD) of Ag.[15,77] In contrast to those of Ag^+, the roles of Cu^{2+} in seed-mediated nanocrystal growth have been much less explored. A similar mechanism involving UPD of Cu on Au seed surfaces has been proposed to interpret Cu^{2+}-mediated shape evolution of metallic NPs.[78,79] Although the existence of transient, localized Cu UPD layers on Au surfaces during nanorod overgrowth cannot be completely ruled out, the results of ex situ HAADF-STEM, XPS, and ζ-potential measurements provided clear evidence on the absence of metallic Cu UPD layers on the surfaces of the overgrown Au CCB, QCB, TCB, and EOH NPs. Therefore, the facet evolution of Au nanorods observed in this work should not be simply interpreted as a consequence of selective facet passivation guided by Cu UPD. An alternative mechanism involved in Cu^{2+} ion-guided growth of Au nanocrystals has been recently proposed, which is based on Cu^{2+}-catalyzed oxidative etching of Au surface atoms.[56,57,80] The reaction occurring in this oxidative etching process can be described using the following equation:

$$\mathbf{4\,Au^0 + 8\,Br^- + O_2 + 4\,H^+ \xrightarrow{Cu^{2+}} 4\,AuBr_2^- + 2\,H_2O}$$

This Cu^{2+}-catalyzed oxidative etching of Au occurs in strongly acidic environments and involves the participation of bromide anions (from CTAB), the oxygen dissolved in water, protons, and Cu^{2+} ions. The oxidative etching of Au nanorods resulted in decrease of both the aspect ratios and surface curvatures of the nanorods, giving rise to spectral

blue shift of the longitudinal plasmon resonances.[57] When the Cu^{2+} ion-catalyzed oxidative etching dominated the nanorod overgrowth, the overgrowth rates greatly increased due to the etching-induced refreshment of NP surfaces, leading to the formation of thermodynamically stable {111}-faceting octahedral NPs.[56] To achieve precise control over the nanorod facets, the oxidative etching of Au surfaces needs to be suppressed. We observed that Au ETHH NPs underwent a slow etching process when exposed to an aqueous solution containing 300 μM Cu^{2+}, 14 mM CTAB, and 0.1 M HCl under ambient air at 60 ℃, which was in line with previous observations on cylindrical Au nanorods.[57] This etching process was further slowed down when the temperature dropped to 30 ℃, the temperature at which the nanorod overgrowth was carried out. In addition, we found that the presence of excessive reducing agent, AA, in the overgrowth solution suppressed the Cu^{2+}-catalyzed oxidative etching of Au. Although AA is a mild reducing agent, it can effectively suppress oxidation processes, such as galvanic replacement of metallic Ag with $HAuCl_4$, when it is in great excess.[81] Furthermore, the Cu^{2+} ion-catalyzed oxidative etching of Au requires low pH values below 1 and therefore high concentrations (~0.1 M) of strong acids, such as HCl or H_2SO_4, are needed to boost the oxidative etching.[56,57,80] However, under our experimental conditions for nanorod overgrowth, no additional strong acid was added and the pH values of the overgrowth solutions were measured to be around 4. As a consequence, no etching of Au ETHH NPs was observed over time period up to 24 h. While the detailed mechanistic understanding of the roles of Cu^{2+} and CTAB requires further investigations, our results provided strong evidence that the facet evolution of Au nanorods under our experimental conditions was essentially

modulated by the competitive surface capping of various Au facets with Cu^{+} and CTAB rather than the UPD of Cu or Cu^{2+}-catalyzed oxidative etching.

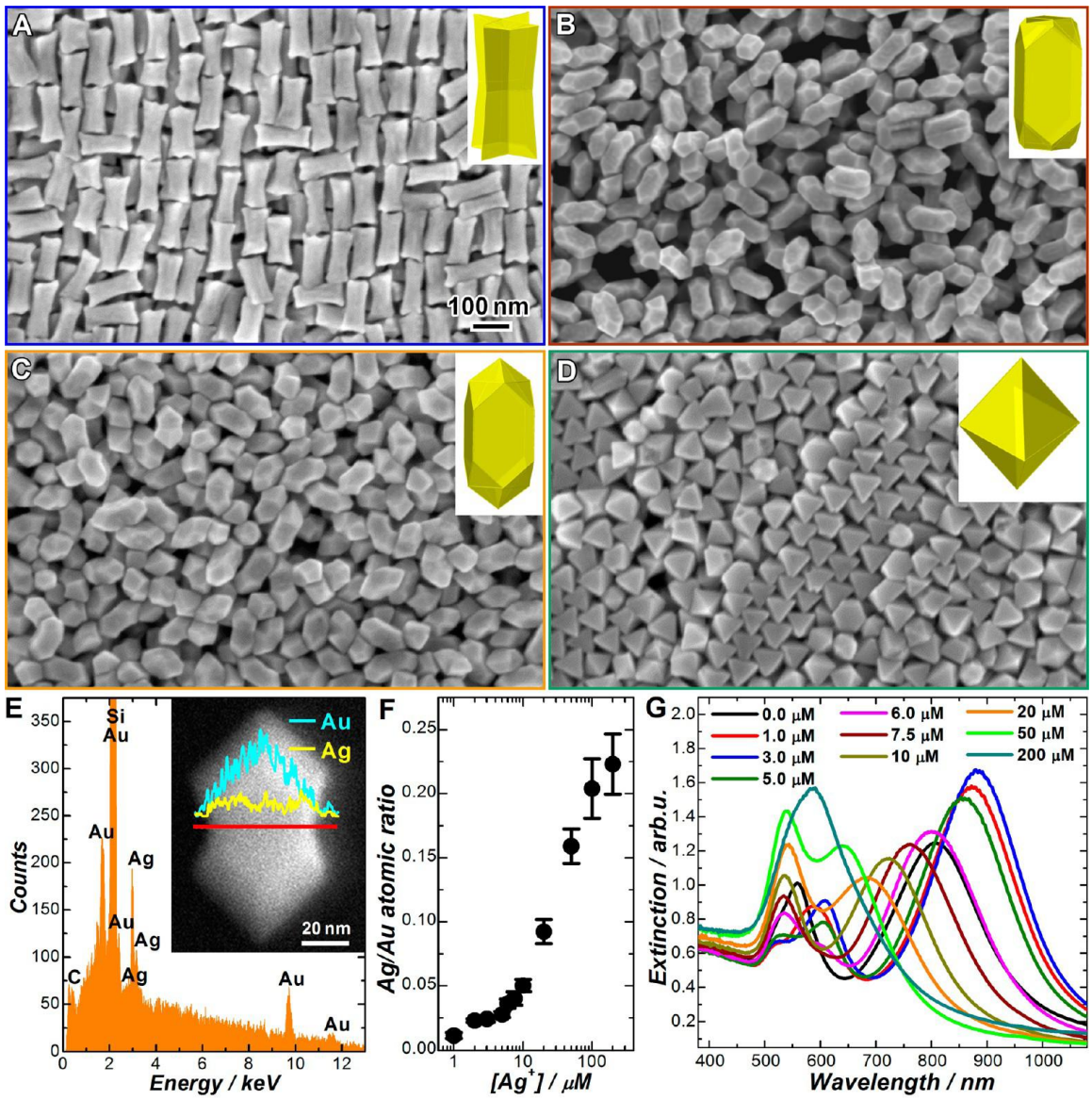

Figure 7.6. SEM images of NPs obtained through overgrowth of Au ETHH NPs in the presence of 14 mM CTAB and various concentrations of Ag^{+} at: (A) 3 μM; (B) 7.5 μM; (C) 20 μM; (D) 200 μM. The inset in each panel shows the geometric model for the NPs. All SEM images share the scale bar in panel A. (E) EDS spectrum of the NPs obtained in the presence of 20 μM Ag^{+}. The inset shows the line-scan profile of elemental distribution overlapped with the SEM image of an individual NP. (F) Atomic ratio of Ag/Au obtained from EDS measurements as a function of the concentration of Ag^{+} in the overgrowth solution. (G) Experimental extinction spectra of colloidal Au NPs obtained through overgrowth of Au ETHH NPs in the presence of various Ag^{+} concentrations as labeled in the figure.

We further demonstrated the capability to fine-tune the particle aspect ratios using this facet-controlled nanorod overgrowth approach. The aspect ratios of Au ETHH NPs could be fine-tuned by exposing the preformed Au ETHH NPs to the same growth solution used for the seed-mediated growth of Au ETHH NPs. The aspect ratio of Au ETHH NPs progressively decreased as the volume of the growth solution increased while the {730} facets and the ETHH geometry were both well preserved. When the Cu^{2+}/CTAB ratios were fixed at the optimal values for each geometry ([CTAB] was fixed at 14 mM and [Cu^{2+}] were 0, 5, 70, and 300 μM for the ETOH, CCB, QCB, and EOH NPs, respectively), varying the amount of $HAuCl_4$ allowed us to systematically tune the particle aspect ratios without changing the characteristic facets and morphological features of each geometry. Each faceted nanorod geometry exhibited its own characteristic aspect ratio-dependent extinction spectral features in terms of plasmon resonance wavelengths and detailed spectral line-shapes. For all the nanostructures, the transverse plasmon peaks became significantly more intense with respect to the longitudinal plasmon peaks as the particle aspect ratios decreased essentially due to the increase of the transverse dimensions of the NPs.

A similar facet and morphological evolution process was observed upon nanorod overgrowth when Ag^+ ions were used instead of Cu^{2+} to compete with CTAB. At a fixed CTAB concentration of 14 mM, the geometry of nanorods evolved from CCB (Figure 7.6A) to TCB (Figure 7.6B) and then to EOH NPs (Figure 7.6C) as the Ag^+ concentration progressively went up. Further increase of Ag^+ concentration eventually led to the formation of octahedral NPs (Figure 7.6D). Apparently, low Ag^+/CTAB ratios facilitated the formation of high-index {hkk} facets whereas high Ag^+/CTAB ratios strongly

favored the formation of {111} facets. Analogous to Cu^{+} ions, Ag^{+} ions served as a surface capping competitor to CTAB in guiding the facet evolution of nanorods. However, the chemistry involved in the Ag^{+}-mediated nanorod overgrowth was found to be strikingly different from that of the Cu^{2+}-mediated overgrowth. During the Ag^{+}-mediated nanorod overgrowth, Ag^{+} was reduced to metallic Ag by AA and thus codeposition of Ag and Au occurred on the surfaces of the Au nanorod cores (Figure 7.6E). In comparison to Cu, Ag has a reduction potential much closer to that of Au, enabling the codeposition of Ag and Au in the presence of AA and CTAB. In addition, the lattice mismatch between Ag and Au (0.34%) is much smaller than that between Cu and Au (11.4%), which favors the atomic interdiffusion and thus the formation of bimetallic alloy structures. The coreduction of Ag and Au under various conditions has been previously demonstrated to be a robust approach to the formation of bimetallic alloy NPs.[82-84] Under our experimental conditions, the atomic ratios of Ag/Au were found to increase with the concentration of Ag^{+} in the overgrowth solutions (Figure 7.6F). As shown in Figure 7.6G, the structural evolution of the faceted nanorods introduced interesting modifications to the extinction spectral features. The surface concavity caused significant red-shifts of both the longitudinal and transverse plasmon resonances while the development of corner truncation blue-shifted and weakened the longitudinal plasmon peak, a similar trend as that observed in the cuprous ion-guided facet evolution.

Despite more than a decade of intensive investigation on the Ag^{+}-assisted nanorod synthesis, the detailed roles of Ag^{+} in guiding the anisotropic growth of Au nanorods still remain controversial.[15-18] Three plausible mechanisms[4,9,18,19] have been proposed regarding the roles of Ag^{+} in controlling the nanorod aspect ratios: (1) the UPD of a

submonolayer quantity of metallic Ag on the longitudinal faces of Au nanorods; (2) the action of a CTAB-Ag^+ complex as a facet-specific capping agent; and (3) the Ag^+- and Br^--guided formation of rod-shaped CTAB micelles, which serve as a soft-template. Characterizing the locations of trace amount of Ag on the Au nanorod surfaces constitute the major challenge associated with the mechanistic studies. Recent studies using combined electron microscopy and advanced EDS revealed that the surface deposition of Ag exhibited no preference for a specific facet or axis of the Au nanorods while the dogbone-like nanostructures developed from nanorod overgrowth showed preferential Ag deposition on the ends and in the crevices.[18] Although further investigations are needed to fully elucidate the synergistic effects of Ag^+ and CTAB on the nanorod facet evolution, our results clearly show that the competitive surface capping of nanorods with Ag^+ and CTAB provides a unique way to fine-tailor the facets of anisotropic Au-Ag bimetallic NPs.

The combination of fine-tailored surface structures and tunable plasmonic properties on the faceted Au nanorods provided a unique opportunity for us to quantitatively study the facet dependence of heterogeneous catalysis on Au nanorods using SERS as a time-resolved spectroscopic tool. As recently demonstrated by our group[62,85,86] and several other groups,[87-93] using SERS to characterize the interfacial molecular transformations during heterogeneous catalysis has several unique advantages, such as real-time monitoring, noninvasive detection, high sensitivity, and detailed molecular finger-printing capability. Here we focused on the catalytic hydrogenation of surface-adsorbed 4-nitrothiophenol (4-NTP) by ammonia borane (AB) as a model reaction to gain quantitative insights on the relationship between atomic surface structures and intrinsic

catalytic activities of various Au facets. It has been shown that aromatic thiolated ligands, such as 4-NTP, can displace the halide-containing cationic surfactants and other physisorbed species on Au nanoparticle surfaces.[94,95] The as-fabricated Au ETHH, ETOH, CCB, QCB, and EOH NPs first underwent a ligand exchange process through which self-assembled monolayers (SAMs) of 4-NTP were immobilized on the NP surfaces via the Au-thiol interactions to displace the surface-adsorbed CTAB and Cu(I) ions. The 4-NTP-coated NPs were then redispersed in water and the characteristic facets and geometric features of the NPs were both well-preserved after the ligand exchange process. We collected SERS spectra on colloidal NPs coated with 4-NTP SAMs at 785 nm excitation. Although the 4-NTP molecules were distributed over the entire NP surfaces, the overall SERS signals were dominated by the signals from the molecules adsorbed on the end facets with negligible contribution from the molecules on the lateral side facets. This is because at 785 nm, the longitudinal plasmon resonances were more effectively excited and the field enhancements were much higher at the ends than on the lateral sides of the nanorods.[20,22,24,65] We estimated the average Raman enhancement factors (EFs) of surface-adsorbed 4-NTP by comparing the SERS signals to normal Raman signals of 4-NTP based on the Raman mode at 1338 cm^{-1}. The estimated Raman EFs were on the order of 10^6 for the various faceted nanorod geometries, approaching 10^7 for Au ETHH NPs.

The catalytic hydrogenation reactions were initiated upon exposure of the 4-NTP-coated NPs to 2 mM AB in 1 mM K_2CO_3 solution at room temperature. The metallic NPs efficiently catalyzed the dehydrogenation of surface-adsorbed AB to generate active hydrogen,[96] which then drove the hydrogenation of surface-adsorbed 4-NTP.[65] We used a

confocal Raman microscope with a laser focal plane ~2 μm × 2 μm in size and an effective excitation volume of ~1.0 × 10^{-16} m^3 to collect the SERS spectra. Exposure of each diffusing colloidal NP to the excitation laser at relatively low power (10 mW) for short time periods (limited by the diffusion time) allowed us to effectively suppress plasmon-driven photoreduction of 4-NTP[97] and the perturbation of reaction kinetics caused by photothermal effects.[62,85,86] As schematically illustrated in Figure 7.7A, this catalytic hydrogenation reaction essentially involved two key steps. 4-NTP and 4-aminothiolphenol (4-ATP) were the reactant and final product, respectively, and 4,4′-dimercaptoazobenzene (DMAB) was identified as the transient intermediate. The detailed assignments of the peaks in SERS spectra[85,87,97,98] are listed. Time-resolved SERS results (Figure 7.7B and 7.7C) clearly showed that the reaction rates decreased in the order of ETHH > CCB > ETOH > QCB > EOH NPs. It is worth mentioning that all the faceted nanorod structures were enclosed by facets larger than 5 nm in size. Therefore, the relative reaction rates well-reflected the characteristic catalytic activities of various facets because the edge and corner atoms at the boundaries between facets only accounted for negligibly small fractions of the total surface atoms.[99,100]

We used the Raman modes at 1338 cm^{-1} (the N-O stretching mode of 4-NTP), 1590 cm^{-1} (the phenol ring mode of 4-ATP), and 1438 cm^{-1} (the N-N stretching mode of DMAB) to quantify the fractions of reactant (θ_R), product (θ_P), and intermediate (θ_I), respectively, as a function of reaction time (t). To obtain $\theta_R(t)$ values, the peak intensities of the 1338 cm^{-1} mode at particular time spots, I(t), were normalized against the initial peak intensities before the reactions started, $I(t=0\ s)$. To obtain $\theta_P(t)$ values, the peak intensities of the 1590 cm^{-1} mode at particular time spots were normalized against the

peak intensities after the reaction was completed, $I(t=\infty)$. This catalytic reaction followed pseudo-first-order kinetics because AB was in great excess with respected to the surface-adsorbed 4-NTP. The pseudo-first-order rate constants for the first step, k_1, were first obtained by performing least-squares curve fitting to the $\theta_R(t)$ trajectories (Figure 7.7D) using the following rate equation:

$$\theta_R = e^{-k_1 \times t} \qquad (1),$$

The pseudo-first-order rate constants for the second step, k_2, were then obtained by fitting the $\theta_P(t)$ trajectories using the following rate equation:

$$\theta_P = 1 + \frac{(k_1 \times e^{-k_2 \times t} - k_2 \times e^{-k_1 \times t})}{k_2 - k_1} \qquad (2),$$

$\theta_I(t)$ was finally calculated based on the curve-fitting results using the following equation:

$$\theta_I = 1 - \theta_R - \theta_P \qquad (3),$$

The experimentally measured $\theta_I(t)$ were plotted after normalization of the maximum peak intensities of the 1438 cm^{-1} mode against the maximum θ_I values of the curve-fitting results.

As shown in Figure 7.7D and 7.7E, the three types of high-index facets were catalytically much more active than the low-index facets toward the catalytic hydrogenation of 4-NTP. The Au ETHH NPs enclosed by {730} facets exhibited the highest catalytic activities among the nanostructures investigated in this work, with k_1 approximately 500 times larger than that of the EOH NPs enclosed by the least active {111} facets (Figure 7.7E). On the EOH NPs, it took more than 90 min for the reaction to go to completion under the current experimental conditions. While both k_1 and k_2 were observed to be facet dependent, decreasing in the order of {730} > {511} > {221} >

{100} > {111}, k_1 was much more sensitively dependent upon the facets than k_2. Interestingly, the k_2 values were always larger than k_1 regardless of nanorod geometries, suggesting that the rate-limiting step was the conversion of 4-NTP to DMAB and the overall reaction kinetics were essentially determined by k_1 rather than k_2. The ratios of k_1/k_2, which were also facet-dependent, determined both the maximum fractions of DMAB, $\theta_{I,max}$, and the reaction time at which the $\theta_{I,max}$ was achieved, t_{max}. As shown in the bottom panel of Figure 7.7D, $\theta_{I,max}$ decreased while tmax increased as k_1/k_2 went down. For ETOH, QCB, and EOH NPs, the fraction of DMAB (θ_I) remained very low throughout the entire reaction processes and the rates of product formation were dominated essentially only by k_1 because k_2 was far greater than k_1 ($k_2 > 10k_1$). As a consequence, the overall kinetics could be further simplified as a one-step first order reaction and the θP trajectories could be well described by a single-exponential function:

$$\theta_P = 1 - e^{-k_1 \times t} \qquad (4)$$

The observed facet-dependent catalytic activities correlated well with the characteristic distributions of undercoordinated surface atoms on various facets (Figure 7.7F). The surface atoms on the low-index {100} and {111} facets are close-packed with coordination numbers of 8 and 9, respectively, and are thus catalytically less active than the high-index facets. The {730} facet possess 44% of its surface atoms with coordination number of 6, which served as highly active sites for the catalytic hydrogenation reaction. The {511} and {221} facets possess 50% and 33% undercoordinated surface atoms, respectively, with a coordination number of 7. The {511} facets were more active than the {221} facets largely due to the higher fraction of surface atoms with coordination number of 7. Our results provided clear experimental

evidence on the crucial roles of undercoordinated surface atoms in Au-based heterogeneous catalysis, which were originally proposed based on the results obtained from CO oxidation catalyzed by oxide-supported sub-5 nm Au NPs.[99,100] The SERS-based kinetic measurements on Au nanorods enclosed by well-defined facets allowed us to quantitatively correlate the intrinsic activities with the atomic-level surface structures of Au nanocatalysts with no complication from the synergy between the Au NPs and the high surface-area oxide supports.

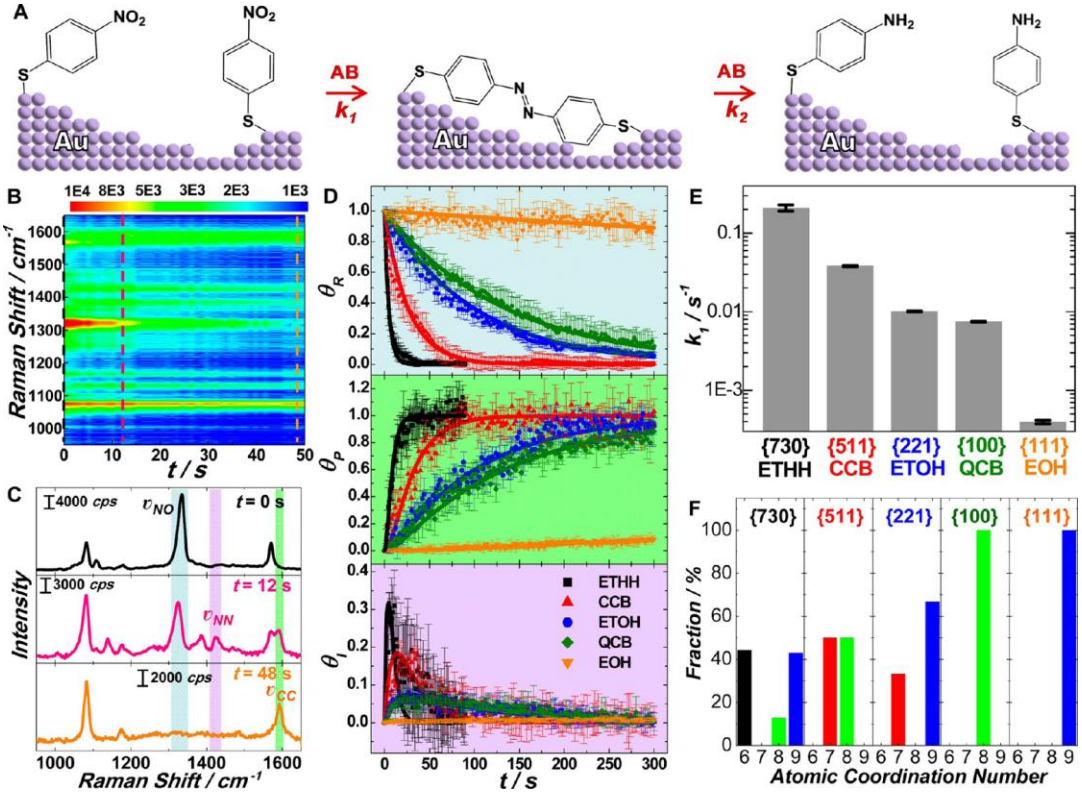

Figure 7.7. (A) Schematic illustration of the two-step hydrogenation process. (B) Two-dimensional colored code intensity map of time-resolved SERS spectra collected from 4-NTP molecules adsorbed on the surfaces of Au ETHH NPs at different reaction times upon exposure to 2 mM AB. (C) Representative SERS spectra collected at reaction times of 0, 12, and 48 s. (D) Fraction of reactant (θ_R) (top panel), product (θ_P) (middle panel), and intermediate (θ_I) (bottom panel) as a function of reaction time (t) during the reactions catalyzed by Au ETHH, CCB, ETOH, QCB, and EOH NPs. The error bars show the standard deviations obtained from 5 experimental runs. The results of the least-squares fitting are shown as solid curves. (E) k_1 values on Au ETHH, CCB, ETOH, QCB, and EOH NPs. (F) Fraction of surface atoms with various atomic coordination numbers for {730}, {511}, {221}, {100}, and {111} facets.

7.4 Conclusions

In summary, we have developed a highly robust and versatile facet-controlled nanorod overgrowth approach with unique capabilities to selectively create an entire family of well-defined facets on the surfaces of single-crystalline Au nanorods, including high-index {hk0} facets on ETHH NPs, high-index {hhk} facets on ETOH NPs, high-index {hkk} facets on CCB NPs, low-index {100} facets on QCB NPs, and low-index {111} facets on EOH NPs. Our success in precise facet control of Au nanorods essentially relies on the utilization of cuprous ions and CTAB as a unique pair of surface capping competitors to fine-control the facet evolution during nanorod overgrowth. This approach also allows for the fine-tuning of the particle aspect ratios while still retaining the characteristic surface structures and morphological features of each nanorod geometry. This work represents a significant advancement in nanorod synthesis and provides new mechanistic insights on the roles of foreign ions and surface-capping surfactants in guiding the facet evolution of anisotropic nanocrystals, thereby promoting the geometry control of anisotropic nanostructures toward an unprecedented level of precision and versatility. The faceted Au nanorods, which exhibit fine-tailored atomic level surface structures while still inheriting the plasmonic tunability of the conventional cylindrical Au nanorods, serve as a unique multifunctional nanomaterials system that allows us to quantitatively correlate the intrinsic catalytic activities with the atomic-level surface structures of Au nanocatalysts using SERS as a time-resolved plasmon-enhanced spectroscopic tool.

7.5 References

(1) Yu, Y. Y.; Chang, S. S.; Lee, C. L.; Wang, C. R. C., *J. Phys. Chem. B* **1997,** *101*, 6661-6664.

(2) Jana, N. R.; Gearheart, L.; Murphy, C. J., *J. Phys. Chem. B* **2001,** *105*, 4065-4067.

(3) Nikoobakht, B.; El-Sayed, M. A., *Chem. Mater.* **2003,** *15*, 1957-1962.

(4) Murphy, C. J.; San, T. K.; Gole, A. M.; Orendorff, C. J.; Gao, J. X.; Gou, L.; Hunyadi, S. E.; Li, T., *J. Phys. Chem. B* **2005,** *109*, 13857-13870.

(5) Grzelczak, M.; Perez-Juste, J.; Mulvaney, P.; Liz-Marzan, L. M., *Chem. Soc. Rev.* **2008,** *37*, 1783-1791.

(6) Sau, T. K.; Murphy, C. J., *Langmuir* **2004,** *20*, 6414-6420.

(7) Perez-Juste, J.; Pastoriza-Santos, I.; Liz-Marzan, L. M.; Mulvaney, P., *Coord. Chem. Rev.* **2005,** *249*, 1870-1901.

(8) Jain, P. K.; Huang, X. H.; El-Sayed, I. H.; El-Sayed, M. A., *Acc. Chem. Res.* **2008,** *41*, 1578-1586.

(9) Murphy, C. J.; Thompson, L. B.; Alkilany, A. M.; Sisco, P. N.; Boulos, S. P.; Sivapalan, S. T.; Yang, J. A.; Chernak, D. J.; Huang, J. Y., *J. Phys. Chem. Lett.* **2010,** *1*, 2867-2875.

(10) Lohse, S. E.; Murphy, C. J., *Chem. Mater.* **2013,** *25*, 1250-1261.

(11) Chen, H. J.; Shao, L.; Li, Q.; Wang, J. F., *Chem. Soc. Rev.* **2013,** *42*, 2679-2724.

(12) Johnson, C. J.; Dujardin, E.; Davis, S. A.; Murphy, C. J.; Mann, S., *J. Mater. Chem.* **2002,** *12*, 1765-1770.

(13) Vigderman, L.; Zubarev, E. R., *Chem. Mater.* **2013,** *25*, 1450-1457.

(14) Ye, X. C.; Jin, L. H.; Caglayan, H.; Chen, J.; Xing, G. Z.; Zheng, C.; Doan-Nguyen, V.; Kang, Y. J.; Engheta, N.; Kagan, C. R.; Murray, C. B., *ACS Nano* **2012,** *6*, 2804-2817.

(15) Liu, M. Z.; Guyot-Sionnest, P., *J. Phys. Chem. B* **2005,** *109*, 22192-22200.

(16) Edgar, J. A.; McDonagh, A. M.; Cortie, M. B., *ACS Nano* **2012,** *6*, 1116-1125.

(17) Walsh, M. J.; Barrow, S. J.; Tong, W. M.; Funston, A. M.; Etheridge, J., *ACS Nano* **2015,** *9*, 715-724.

(18) Jackson, S. R.; McBride, J. R.; Rosenthal, S. J.; Wright, D. W., *J. Am. Chem. Soc.* **2014,** *136*, 5261-5263.

(19) Almora-Barrios, N.; Novell-Leruth, G.; Whiting, P.; Liz-Marzan, L. M.; Lopez, N., *Nano Lett.* **2014,** *14*, 871-875.

(20) Nikoobakht, B.; Wang, J. P.; El-Sayed, M. A., *Chem. Phys. Lett.* **2002,** *366*, 17-23.

(21) Alvarez-Puebla, R. A.; Agarwal, A.; Manna, P.; Khanal, B. P.; Aldeanueva-Potel, P.; Carbo-Argibay, E.; Pazos-Perez, N.; Vigderman, L.; Zubarev, E. R.; Kotov, N. A.; Liz-Marzan, L. M., *Proc. Natl. Acad. Sci. U. S. A.* **2011,** *108*, 8157-8161.

(22) Sivapalan, S. T.; DeVetter, B. M.; Yang, T. K.; van Dijk, T.; Schulmerich, M. V.; Carney, P. S.; Bhargava, R.; Murphy, C. J., *ACS Nano* **2013,** *7*, 2099-2105.

(23) Abadeer, N. S.; Brennan, M. R.; Wilson, W. L.; Murphy, C. J., *ACS Nano* **2014,** *8*, 8392-8406.

(24) Fu, Y.; Zhang, J.; Lakowicz, J. R., *J. Am. Chem. Soc.* **2010,** *132*, 5540-5541.

(25) Nepal, D.; Drummy, L. F.; Biswas, S.; Park, K.; Vaia, R. A., *ACS Nano* **2013,** *7*, 9064-9074.

(26) Mayer, K. M.; Hafner, J. H., *Chem. Rev.* **2011,** *111*, 3828-3857.

(27) Lee, K. S.; El-Sayed, M. A., *J. Phys. Chem. B* **2006,** *110*, 19220-19225.

(28) Murphy, C. J.; Gole, A. M.; Hunyadi, S. E.; Stone, J. W.; Sisco, P. N.; Alkilany, A.; Kinard, B. E.; Hankins, P., *Chem. Commun.* **2008,** 544-557.

(29) Huang, X. H.; El-Sayed, I. H.; Qian, W.; El-Sayed, M. A., *J. Am. Chem. Soc.* **2006,** *128*, 2115-2120.

(30) Huang, X. H.; Neretina, S.; El-Sayed, M. A., *Adv. Mater.* **2009,** *21*, 4880-4910.

(31) Wang, H. F.; Huff, T. B.; Zweifel, D. A.; He, W.; Low, P. S.; Wei, A.; Cheng, J. X., *Proc. Natl. Acad. Sci. U. S. A.* **2005,** *102*, 15752-15756.

(32) Tong, L.; Wei, Q. S.; Wei, A.; Cheng, J. X., *Photochem. Photobiol.* **2009,** *85*, 21-32.

(33) Ding, H.; Yong, K. T.; Roy, I.; Pudavar, H. E.; Law, W. C.; Bergey, E. J.; Prasad, P. N., *J. Phys. Chem. C* **2007,** *111*, 12552-12557.

(34) Bonoiu, A. C.; Mahajan, S. D.; Ding, H.; Roy, I.; Yong, K. T.; Kumar, R.; Hu, R.; Bergey, E. J.; Schwartz, S. A.; Prasad, P. N., *Proc. Natl. Acad. Sci. U. S. A.* **2009,** *106*, 5546-5550.

(35) Wijaya, A.; Schaffer, S. B.; Pallares, I. G.; Hamad-Schifferli, K., *ACS Nano* **2009,** *3*, 80-86.

(36) Huang, X. H.; Jain, P. K.; El-Sayed, I. H.; El-Sayed, M. A., *Nanomedicine* **2007,** *2*, 681-693.

(37) Sun, Z. H.; Ni, W. H.; Yang, Z.; Kou, X. S.; Li, L.; Wang, J. F., *Small* **2008,** *4*, 1287-1292.

(38) Liu, K.; Nie, Z. H.; Zhao, N. N.; Li, W.; Rubinstein, M.; Kumacheva, E., *Science* **2010,** *329*, 197-200.

(39) Nie, Z. H.; Fava, D.; Rubinstein, M.; Kumacheva, E., *J. Am. Chem. Soc.* **2008,** *130*, 3683-3689.

(40) Joseph, S. T. S.; Ipe, B. I.; Pramod, P.; Thomas, K. G., *J. Phys. Chem. B* **2006,** *110*, 150-157.

(41) Nie, Z. H.; Fava, D.; Kumacheva, E.; Zou, S.; Walker, G. C.; Rubinstein, M., *Nat. Mater.* **2007,** *6*, 609-614.

(42) Zhou, X. C.; Andoy, N. M.; Liu, G. K.; Choudhary, E.; Han, K. S.; Shen, H.; Chen, P., *Nat. Nanotechnol.* **2012,** *7*, 237-241.

(43) Katz-Boon, H.; Rossouw, C. J.; Weyland, M.; Funston, A. M.; Mulvaney, P.; Etheridge, J., *Nano Lett.* **2011,** *11*, 273-278.

(44) Carbo-Argibay, E.; Rodriguez-Gonzalez, B.; Gomez-Grana, S.; Guerrero-Martinez, A.; Pastoriza-Santos, I.; Perez-Juste, J.; Liz-Marzan, L. M., *Angew. Chem.-Int. Edit.* **2010,** *49*, 9397-9400.

(45) Gai, P. L.; Harmer, M. A., *Nano Lett.* **2002,** *2*, 771-774.

(46) Sohn, K.; Kim, F.; Pradel, K. C.; Wu, J. S.; Peng, Y.; Zhou, F. M.; Huang, J. X., *ACS Nano* **2009,** *3*, 2191-2198.

(47) Huang, Y. J.; Wu, L.; Chen, X. D.; Bai, P.; Kim, D. H., *Chem. Mater.* **2013,** *25*, 2470-2475.

(48) Zhang, L. F.; Zhang, C. Y., *Nanoscale* **2013,** *5*, 5794-5800.

(49) Goris, B.; Bals, S.; Van den Broek, W.; Carbo-Argibay, E.; Gomez-Grana, S.; Liz-Marzan, L. M.; Van Tendeloo, G., *Nat. Mater.* **2012,** *11*, 930-935.

(50) Wang, Z. L.; Gao, R. P.; Nikoobakht, B.; El-Sayed, M. A., *J. Phys. Chem. B* **2000,** *104*, 5417-5420.

(51) Katz-Boon, H.; Walsh, M.; Dwyer, C.; Mulvaney, P.; Funston, A. M.; Etheridge, J., *Nano Lett.* **2015,** *15*, 1635-41.

(52) Gou, L. F.; Murphy, C. J., *Chem. Mater.* **2005,** *17*, 3668-3672.

(53) Song, J. H.; Kim, F.; Kim, D.; Yang, P. D., *Chem.-Eur. J.* **2005,** *11*, 910-916.

(54) Kou, X. S.; Zhang, S. Z.; Yang, Z.; Tsung, C. K.; Stucky, G. D.; Sun, L. D.; Wang, J. F.; Yan, C. H., *J. Am. Chem. Soc.* **2007,** *129*, 6402-6404.

(55) Khlebtsov, B. N.; Ithanadeev, V. A.; Ye, J.; Sukhorukov, G. B.; Khlebtsov, N. G., *Langmuir* **2014,** *30*, 1696-1703.

(56) Liu, W. Q.; Zhang, H.; Wen, T.; Yan, J.; Hou, S.; Shi, X. W.; Hu, Z. J.; Ji, Y. L.; Wu, X. C., *Langmuir* **2014,** *30*, 12376-12383.

(57) Wen, T.; Zhang, H.; Tang, X. P.; Chu, W. G.; Liu, W. Q.; Ji, Y. L.; Hu, Z. J.; Hou, S.; Hu, X. N.; Wu, X. C., *J. Phys. Chem. C* **2013,** *117*, 25769-25777.

(58) Tsung, C. K.; Kou, X. S.; Shi, Q. H.; Zhang, J. P.; Yeung, M. H.; Wang, J. F.; Stucky, G. D., *J. Am. Chem. Soc.* **2006,** *128*, 5352-5353.

(59) Ye, X. C.; Zheng, C.; Chen, J.; Gao, Y. Z.; Murray, C. B., *Nano Lett.* **2013,** *13*, 765-771.

(60) Ye, X. C.; Gao, Y. Z.; Chen, J.; Reifsnyder, D. C.; Zheng, C.; Murray, C. B., *Nano Lett.* **2013,** *13*, 2163-2171.

(61) Ming, T.; Feng, W.; Tang, Q.; Wang, F.; Sun, L. D.; Wang, J. F.; Yan, C. H., *J. Am. Chem. Soc.* **2009,** *131*, 16350-16351.

(62) Zhang, Q. F.; Wang, H., *ACS Catal.* **2014,** *4*, 4027-4033.

(63) Tian, N.; Zhou, Z. Y.; Sun, S. G.; Ding, Y.; Wang, Z. L., *Science* **2007,** *316*, 732-735.

(64) Quan, Z. W.; Wang, Y. X.; Fang, J. Y., *Acc. Chem. Res.* **2013,** *46*, 191-202.

(65) Zhang, Q. F.; Zhou, Y. D.; Villarreal, E.; Lin, Y.; Zou, S. L.; Wang, H., *Nano Lett.* **2015,** *15*, 4161-4169.

(66) Xia, X. H.; Zeng, J.; McDearmon, B.; Zheng, Y. Q.; Li, Q. G.; Xia, Y. N., *Angew. Chem.-Int. Edit.* **2011,** *50*, 12542-12546.

(67) Zhang, J. A.; Langille, M. R.; Personick, M. L.; Zhang, K.; Li, S. Y.; Mirkin, C. A., *J. Am. Chem. Soc.* **2010,** *132*, 14012-14014.

(68) Tran, T. T.; Lu, X. M., *J. Phys. Chem. C* **2011,** *115*, 3638-3645.

(69) Ma, Y. Y.; Kuang, Q.; Jiang, Z. Y.; Xie, Z. X.; Huang, R. B.; Zheng, L. S., *Angew. Chem.-Int. Edit.* **2008,** *47*, 8901-8904.

(70) Niu, W. X.; Zhang, W. Q.; Firdoz, S.; Lu, X. M., *Chem. Mater.* **2014,** *26*, 2180-2186.

(71) O'Brien, M. N.; Jones, M. R.; Brown, K. A.; Mirkin, C. A., *J. Am. Chem. Soc.* **2014,** *136*, 7603-7606.

(72) Lu, C. L.; Prasad, K. S.; Wu, H. L.; Ho, J. A. A.; Huang, M. H., *J. Am. Chem. Soc.* **2010,** *132*, 14546-14553.

(73) Lin, H. X.; Lei, Z. C.; Jiang, Z. Y.; Hou, C. P.; Liu, D. Y.; Xu, M. M.; Tian, Z. Q.; Xie, Z. X., *J. Am. Chem. Soc.* **2013,** *135*, 9311-9314.

(74) Gou, L. F.; Murphy, C. J., *Nano Lett.* **2003,** *3*, 231-234.

(75) Personick, M. L.; Langille, M. R.; Zhang, J.; Mirkin, C. A., *Nano Lett.* **2011,** *11*, 3394-3398.

(76) Brenner, A. J.; Harris, E. D. A *Acid. Anal. Biochem.* **1995**, *226*, 80-84.

(77) Park, S.; Sinha, N.; Hamad-Schifferli, K. *Langmuir* **2010**, *26*, 13071-13075.

(78) Zhang, L.; Zhang, J. W.; Kuang, Q.; Xie, S. F.; Jiang, Z. Y.; Xie, Z. X.; Zheng, L. S., *J. Am. Chem. Soc.* **2011,** *133*, 17114-17117.

(79) Zhang, L.; Chen, Q. L.; Jiang, Z. Y.; Xie, Z. X.; Zheng, L. S., *CrystEngComm* **2015,** *17*, 5556-5561.

(80) Wen, T.; Hu, Z. J.; Liu, W. Q.; Zhang, H.; Hou, S.; Hu, X. N.; Wu, X. C., *Langmuir* **2012,** *28*, 17517-17523.

(81) Yang, Y.; Liu, J. Y.; Fu, Z. W.; Qin, D., *J. Am. Chem. Soc.* **2014,** *136*, 8153-8156.

(82) Raveendran, P.; Fu, J.; Wallen, S. L., *Green Chem.* **2006,** *8*, 34-38.

(83) Bai, T. L.; Sun, J. F.; Che, R. C.; Xu, L. N.; Yin, C. Y.; Guo, Z. R.; Gu, N., *ACS Appl. Mater. Interfaces* **2014,** *6*, 3331-3340.

(84) Park, K.; Vaia, R. A., *Adv. Mater.* **2008,** *20*, 3882-3886.

(85) Jing, H.; Zhang, Q. F.; Large, N.; Yu, C. M.; Blom, D. A.; Nordlander, P.; Wang, H., *Nano Lett.* **2014,** *14*, 3674-3682.

(86) Zhang, Q. F.; Blom, D. A.; Wang, H., *Chem. Mater.* **2014,** *26*, 5131-5142.

(87) Huang, J. F.; Zhu, Y. H.; Lin, M.; Wang, Q. X.; Zhao, L.; Yang, Y.; Yao, K. X.; Han, Y., *J. Am. Chem. Soc.* **2013,** *135*, 8552-8561.

(88) Heck, K. N.; Janesko, B. G.; Scuseria, G. E.; Halas, N. J.; Wong, M. S., *J. Am. Chem. Soc.* **2008,** *130*, 16592-16600.

(89) Joseph, V.; Engelbrekt, C.; Zhang, J. D.; Gernert, U.; Ulstrup, J.; Kneipp, J., *Angew. Chem.-Int. Edit.* **2012,** *51*, 7592-7596.

(90) Xie, W.; Herrmann, C.; Kompe, K.; Haase, M.; Schlucker, S., *J. Am. Chem. Soc.* **2011,** *133*, 19302-19305.

(91) Xie, W.; Walkenfort, B.; Schlucker, S., *J. Am. Chem. Soc.* **2013,** *135*, 1657-1660.

(92) Liu, R.; Liu, J. F.; Zhang, Z. M.; Zhang, L. Q.; Sun, J. F.; Sun, M. T.; Jiang, G. B., *J. Phys. Chem. Lett.* **2014,** *5*, 969-975.

(93) Cui, Q. L.; Yashchenok, A.; Zhang, L.; Li, L. D.; Masic, A.; Wienskol, G.; Mohwald, H.; Bargheer, M., *ACS Appl. Mater. Interfaces* **2014,** *6*, 1999-2002.

(94) DeVetter, B. M.; Mukherjee, P.; Murphy, C. J.; Bhargava, R., *Nanoscale* **2015,** *7*, 8766-8775.

(95) Wang, H.; Levin, C. S.; Halas, N. J., *J. Am. Chem. Soc.* **2005,** *127*, 14992-14993.

(96) Goksu, H.; Ho, S. F.; Metin, O.; Korkmaz, K.; Garcia, A. M.; Gultekin, M. S.; Sun, S. H., *ACS Catal.* **2014,** *4*, 1777-1782.

(97) Sun, M. T.; Xu, H. X., *Small* **2012,** *8*, 2777-2786.

(98) Huang, Y. F.; Zhu, H. P.; Liu, G. K.; Wu, D. Y.; Ren, B.; Tian, Z. Q., *J. Am. Chem. Soc.* **2010,** *132*, 9244-9246.

(99) Hvolbaek, B.; Janssens, T. V. W.; Clausen, B. S.; Falsig, H.; Christensen, C. H.; Norskov, J. K., *Nano Today* **2007,** *2*, 14-18.

(100) Janssens, T. V. W.; Clausen, B. S.; Hvolbaek, B.; Falsig, H.; Christensen, C. H.; Bligaard, T.; Norskov, J. K., *Top. Catal.* **2007,** *44*, 15-26.

CHAPTER 8

Intertwining Roles of Silver Ions, Surfactants, and Reducing Agents in Gold Nanorod Overgrowth: Pathway Switch between Silver Underpotential Deposition and Gold-Silver Codeposition

8.1 Introduction

Recent advances in colloidal nanoparticle synthesis have greatly enhanced our capabilities of fine-tuning the optical, electronic, and catalytic properties of metallic nanoparticles through deliberate control over the particle shapes and compositions.[1-5] Seed-mediated nanocrystal growth, in particular, provides a highly robust and versatile approach to the precise geometry control of metallic nanoparticles under mild conditions.[5-13] The seed-mediated structural evolution of nanocrystals is synergistically guided by a set of interplaying geometric, kinetic, and thermodynamic factors such as the crystallinity of seeds,[5,10,14] the supersaturation of crystal growth units,[15] the thermodynamic stabilities of various crystallographic facets,[16] and the selective passivation of nanocrystal surfaces.[10] An extensive library of anisotropic nanoparticle geometries, such as nanorods,[6,17-21] nanoprisms,[22] and a series of low-index and high-index faceting nanopolyhedrons,[12,13,16,23-31] have been experimentally realized through kinetically controlled seed-mediated nanocrystal growth processes with the aid of structure-directing surfactants and foreign ion additives. These synthetic protocols, however, have been developed and optimized in a largely empirical fashion, while detailed nanocrystal growth mechanisms often remained ambiguous until recently a coherent mechanistic understanding of shape-controlled growth of Au nanocrystals started to emerge in the literature.[32]

The geometric evolution of Au nanocrystals during seed-mediated growth is essentially governed by two primary pathways: kinetic control of nanocrystal growth and selective passivation of nanoparticle surfaces.[10,32] Under the kinetic control pathway, fast nanocrystal growth facilitates the formation of kinetically favored high-index faceting

nanocrystals, such as {221}-faceting nanotrisoctahedrons,[10,33-35] whereas slower nanocrystal growth generally results in thermodynamically more stable, low-index faceting nanoparticles such as nanocubes enclosed by {100} facets and nanooctahedrons enclosed by {111} facets.[10,32] In contrast, selective passivation of nanoparticle surfaces by capping surfactants or foreign ions offers an alternative pathway that leads to the formation of exotic geometries bound entirely by the passivated facets.[10,27,31] While these two pathways appear divergent at first glance, there is a strong synergy between them. The key components in the nanocrystal growth solutions, including the surfactants, the foreign ions, and the reducing agents, all play multiple intertwining roles in guiding the structural evolution of nanocrystals and may modulate the interswitch between multiple nanocrystal growth pathways. A particularly interesting phenomenon manifesting such mechanistic complexity is the underpotential deposition (UPD) of up to a monolayer of foreign metal adatoms on the Au nanoparticle surfaces during foreign ion-guided Au nanocrystal growth.[10,27,31,32,36-40] The UPD adlayer not only selectively passivates various Au facets, but also fine-regulates the overall nanocrystal growth kinetics, allowing Au nanocrystals to evolve into a variety of low-index and high-index faceting geometries in a highly controllable manner. Under appropriate conditions, the foreign metal ions may also be coreduced with Au through seed-mediated electroless codeposition processes to form heterostructured or homogeneously alloyed multimetallic nanoparticles with further increased architectural and compositional complexity.[41-46]

Among various anisotropic Au nanostructures, single-crystalline cylindrical Au nanorods (NRs) have been of particular interests owing to their intriguing aspect ratio-dependent plasmonic properties.[6,7,19,20] The most popular protocols for NR synthesis

involve seed-mediated growth coguided by a foreign metal ion, Ag^+, and halide-containing cationic surfactants, such as cetyltrimethylammonium bromide (CTAB), in the presence of ascorbic acid (AA), which serves as a mild reducing agent.[6,17-19] While the aspect ratios of Au NRs can be fine-tuned by simply varying the concentration of Ag^+ ions in the growth solution, the exact roles that Ag^+ ions play in the symmetry-breaking of the isotropic seeds and the subsequent anisotropic NR growth still remain elusive and controversial.[36,47-50] In striking contrast to the excellent control over NR aspect ratios, limited success has been achieved so far in the precise facet control of NRs using the seed-mediated growth method. The surface curvature and local facets of Au NRs may change drastically upon even slight variation of the ingredients in the NR growth solutions, and quantitative assignments of the crystallographic facets exposed on the highly curved NR surfaces have long been under intense debate.[17,51-56]

A unique way to further fine-tailor the crystallographic facets and expand the aspect ratio tuning range of Au NRs involves the shape-controlled overgrowth of preformed cylindrical NRs.[57-69] In the absence of foreign metal ions, cylindrical Au NRs may selectively undergo tip overgrowth, isotropic overgrowth, and anisotropic overgrowth to evolve into peanut-shaped NRs, cuboidal NRs, and truncated nanooctahedrons, respectively, depending on the concentrations of CTAB in the overgrowth solutions.[60] Recently, we further demonstrated that more rigorous control of Au NR facets with atomic level precision could be achieved using cuprous (Cu^+) foreign ions and halide-containing surfactants as unique pairs of surface capping competitors to maneuver the facet evolution during NR overgrowth.[68,69] In comparison to Cu^+ ions, Ag^+ ions have been more widely used in combination with various surfactants to guide the morphology-

controlled overgrowth of Au NRs. A large variety of NR-derived anisotropic geometries, such as nanodumbbells, starfruit-shaped NRs, dogbone-like NRs, concave nanocuboids, and arrow-headed NRs, have been obtained through Ag^+- and CTAB-coguided NR overgrowth processes.[57,58,61,63-67] However, it still remains a significant challenge to obtain a unified picture that rigorously interprets the interplay of multiple evolutionary pathways involved in the NR overgrowth processes. In this chapter, we endeavor to pinpoint the intertwining roles of Ag^+ ions, surfactants, and reducing agents in directing the structural and compositional evolution during NR overgrowth with a primary focus on the effects of two interswitchable pathways, specifically Ag UPD and Au-Ag codeposition, on the geometries and compositions of the overgrown NRs.

8.2 Experimental Section

Nanorod Overgrowth. Single-crystalline cylindrical Au NRs were prepared following a previously published protocol[70] with minor modifications. The NR overgrowth was conducted in the presence of Ag^+, $HAuCl_4$, CTAB, and AA at 30 ℃ under ambient air. The NR overgrowth solution was prepared by sequentially adding H_2O, $HAuCl_4$, $AgNO_3$, and AA into a CTAB solution. After the solution was gently mixed for 30 s, the overgrowth of NRs was initiated by the introduction of 100 μL of the preformed cylindrical Au NRs (in 0.1 M CTAB). The reaction solution was gently mixed for 30 s immediately after the addition of Au NRs and then left undisturbed at 30 ℃ for 1 h. The obtained nanoparticles were then washed with H_2O twice through centrifugation/redispersion cycles and finally redispersed in 200 μL of 20 mM CTAB. To investigate the effects of Ag^+, CTAB, and AA, the overall concentrations of Ag^+, CTAB, and AA in the NR overgrowth solutions were systematically varied, while the total

volume of the nanorod overgrowth solutions was always fixed at 5.0 mL. BDAC and CTAC were also used as an alternative surfactant instead of CTAB to compare the effects of different surfactants on the NR overgrowth. The effects of reducing agents were investigated by varying the concentration of AA in the overgrowth solutions or using other mild reducing agents such as HQ and HEPES.

Characterizations. The TEM images were obtained using a Hitachi H-8000 transmission electron microscope operated at an accelerating voltage of 200 kV. All samples for TEM measurements were dispersed in water and drop-dried on 300 mesh Formvar/carbon-coated Cu grids. SEM and EDS measurements were performed using a Zeiss Ultraplus thermal field emission scanning electron microscope. The samples for SEM and EDS measurements were dispersed in water and drop-dried on silicon wafers. The atomic level structures of the nanoparticles were resolved by aberration-corrected HAADF-STEM using a JEOL 2100F 200 kV FEG-STEM/TEM microscopy equipped with a CEOS CS corrector on the illumination system. The samples for HAADF-STEM measurements were dispersed in water and drop-dried on 400 mesh Cu grids with ultrathin carbon support film (Electron Microscopy Science Inc.). The optical extinction spectra of the nanoparticles were measured on aqueous colloidal suspensions at room temperature using a Beckman Coulter Du 640 spectrophotometer. ζ-Potentials of colloidal nanoparticles were measured at room temperature using ZETASIZER nanoseries (Nano-ZS, Malvern). The samples for ζ−potential measurements were all freshly prepared, centrifuged, and redispersed in 10 mM CTAB (pH ~ 7.8). XPS measurements were carried out using a Krato AXIS Ultra DLD XPS system equipped with a monochromatic Al Kα source. The samples for XPS measurements were all

freshly prepared and dried in vacuum before being loaded into the XPS chambers. SERS spectra were obtained on a Bayspec Nomadic confocal Raman microscopy built on an Olympus BX51 microscope equipped with a 785 nm continuous wave diode laser. CV measurements were performed in 0.1 M KNO_3 electrolyte solution at room temperature.

8.3 Results and Discussions

Single-crystalline cylindrical Au NRs were prepared through a seed-mediated growth process in the presence of Ag^+ ions and CTAB/oleate binary surfactant mixtures[70] and were subsequently employed as the seeds for the post-fabrication NR overgrowth. As shown by the scanning electron microscopy (SEM) and transmission electron microscopy (TEM) images, the as-fabricated Au NRs were highly uniform and monodisperse with diameters of 21 $\pm$ 3 nm and lengths of 105 $\pm$ 5 nm. It was previously reported that Ag existed as either a UPD layer of Ag adatoms or arguably as a AgBr adlayer on the NR surfaces, which was further capped with a positively charged, self-assembled bilayer of CTAB.[17] While the bulk composition of the NRs was dominated by Au as shown by the energy dispersive spectroscopy (EDS) results, both Ag and Br signals were well-resolved by X-ray photoelectron spectroscopy (XPS), clearly verifying the presence of both Ag and CTAB on the NR surfaces. Starting with these preformed cylindrical Au NRs, we performed detailed investigations on the structural and compositional transformations upon NR overgrowth as a function of three variables: Ag^+ ions, capping surfactants, and reducing agents.

8.3.1 Effects of Ag^+ Ions.

We symmetrically varied the concentration of Ag^+ ions while keeping $HAuCl_4$ (Au precursor), CTAB, and AA at fixed concentrations of 200 μM, 20 mM, and 10 mM,

respectively. As schematically illustrated in Figure 8.1A, the cylindrical Au NRs transformed into a series of interesting NR-derived anisotropic geometries as the Ag^+ concentration in the overgrowth solution progressively increased. In the absence of Ag^+ ions, the Au NRs transformed into elongated trisoctahedral nanoparticles (ETOH NPs) (Figure 8.1B), which is in line with our previous observations.[69] Detailed electron microscopy characterizations revealed that each ETOH NP was enclosed by four {110} lateral side facets and 24 high-index {221} facets at the two ends.[69] The formation of the kinetically favored, high-index faceting ETOH NPs was a direct consequence of fast NR overgrowth at sufficiently high [AA]/[$HAuCl_4$] ratios ([AA]/[$HAuCl_4$] = 50 in this case). Overgrowth of quasi-spherical Au nanoparticles under similar conditions resulted in the formation of high-index faceting nanotrisoctahedrons each of which was enclosed by 24 {221} facets.[34] In the presence of Ag^+ ions, strikingly different geometric transformations were observed upon NR overgrowth. As shown in Figure 8.1, panel C, surface concavity was developed on the NR surfaces at relatively low [Ag^+]/[$HAuCl_4$] ratios below 0.02, forming dog bone-like nanorods (DBLNRs) with eight sharp tips. Upon further increase of the [Ag^+]/[$HAuCl_4$] ratio, however, the surface indentation and tip sharpness of the DBLNRs both gradually decreased, while the transverse dimensions of the overgrown NRs progressively increased (Figure 8.1D,E), eventually leading to the formation of arrow-headed NRs (AHNRs) with two sharp tips, each of which was enclosed by four thermodynamically stable {111} facets (Figure 8.1F,G). Apparently, Ag^+ ions played crucial roles in directing the shape evolution of NRs under the overgrowth conditions.

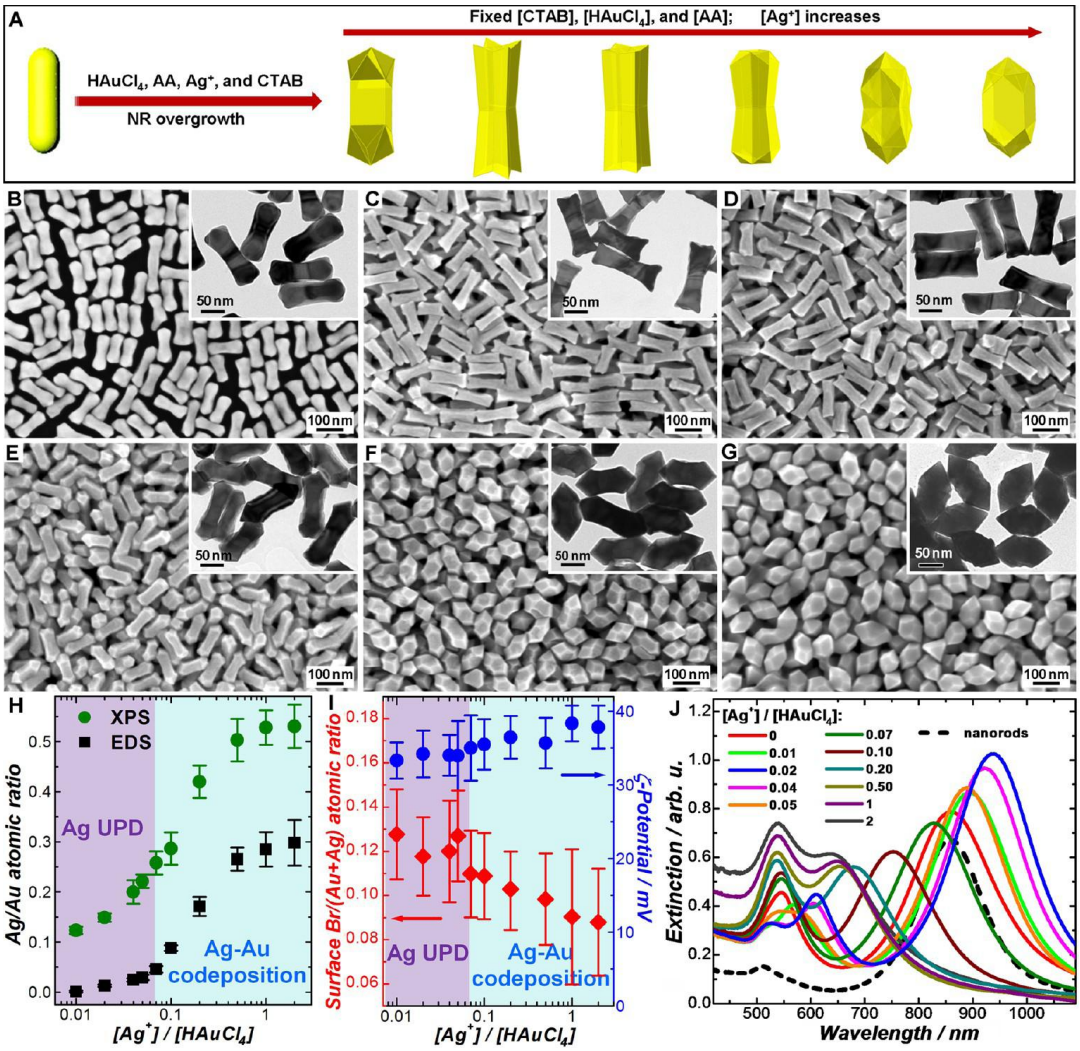

Figure 8.1. (A) Schematic illustration of geometric evolution during NR overgrowth in the presence of fixed concentrations of HAuCl4, AA, and CTAB but varying concentrations of Ag^+ ions. SEM and TEM (inset) images of the overgrown NRs obtained at various $[Ag^+]/[HAuCl_4]$ ratios of (B) 0, (C) 0.02, (D) 0.05, (E) 0.07, (F) 0.50, and (G) 2.0. The concentrations of CTAB, HAuCl4, and AA were 20 mM, 200 μM, and 10 mM, respectively. (H) Ag/Au atomic ratios of the overgrown NRs obtained at various $[Ag^+]/[HAuCl_4]$ ratios. The bulk and surface Ag/Au atomic ratios were quantified by EDS and XPS, respectively. (I) Surface atomic ratios of Br/(Au + Ag) quantified by XPS and apparent ζ-potentials of the overgrown NRs obtained at various $[Ag^+]/[HAuCl_4]$ ratios. The error bars in panels H and I represent the standard deviations of three samples fabricated under identical conditions. (J) Optical extinction spectra of the overgrown NRs obtained at various $[Ag^+]/[HAuCl_4]$ ratios as labeled in the figure.

To further elucidate the exact roles of Ag^+ ions, we used EDS and XPS to characterize the bulk and surface compositions of the overgrown NRs, respectively. Both EDS and XPS results showed the absence of Ag on the ETOH NPs, verifying that the formation of

ETOH NPs was purely a CTAB-mediated, kinetically controlled process without the involvement of Ag^+ foreign ions. At low $[Ag^+]/[HAuCl_4]$ ratios below 0.07, the bulk compositions of the overgrowth NRs were essentially dominated by Au with Ag signals almost undetectable by EDS. However, strong Ag signals were clearly resolved in XPS, and the surface Ag/Au atomic ratios measured by XPS exhibited much higher values than the bulk Ag/Au atomic ratios obtained from EDS. The sample penetration depth of the XPS measurements under the current experimental conditions was calibrated to be ~1 nm, which roughly corresponded to five atomic layers from the outer surface of the nanoparticles. Therefore, a Ag/Au atomic ratio of ~0.25 corresponded to a saturated monolayer coverage of Ag UPD adatoms on the Au nanoparticle surfaces. As the $[Ag^+]/[HAuCl_4]$ ratio increased from 0.01 to 0.07, the surface Ag/Au atomic ratios (measured by XPS) progressively increased from ~0.12 to ~0.26, while the bulk Ag/Au atomic ratios (measured by EDS) remained below 0.03 (Figure 8.1H), well reflecting the transition of a submonolayer to a fully saturated monolayer of Ag UPD adatoms on the surfaces of the overgrown NRs. Both the EDS and XPS results strongly indicated that the transformation of cylindrical Au NRs into the DBLNRs was governed by a Ag UPD-dominated overgrowth pathway.

As the $[Ag^+]/[HAuCl_4]$ ratio further increased to above 0.07, Ag^+ and $HAuCl_4$ started to be coreduced by AA to form Au-Ag alloy shells surrounding the Au NR cores, resulting in the formation of Au-Ag bimetallic AHNRs. EDS and XPS results clearly verified the Au NR-core and Au−Ag alloy-shell heterostructure of the AHNRs. Much higher Ag content was detected by both EDS and XPS on the AHNRs than on the DBLNRs, and a sharp increase of both the bulk and surface Ag/Au atomic ratios was

observed over a narrow $[Ag^+]/[HAuCl_4]$ window (Figure 8.1H). In the high $[Ag^+]/[HAuCl_4]$ ratio regime, the NR overgrowth was dominated by Au-Ag electroless codeposition, a pathway fundamentally different from the Ag UPD. The Ag atoms in the AHNRs were intermixed with Au atoms far beyond the surface atomic layer to form alloy structures. We also performed angle-dependent XPS measurements to further contrast the compositional difference between DBLNRs and AHNRs. The maximal probe penetration depth (~1 nm) was achieved at normal incidence, while the probe penetration depth decreased as the detector was shifted away from normal incidence with respect to the sample surfaces. The surface Ag/Au atomic ratios of DBLNRs progressively increased as the probe penetration depth decreased, whereas the AHNRs exhibited surface Ag/Au atomic ratios that were almost independent of the probe penetration depth. Meanwhile, both the DBLNRs and AHNRs exhibited surface Br/Au atomic ratios that progressively increased with decrease in probe penetration depth, verifying that the CTAB surfactant molecules existed on the surfaces of the overgrown NRs. The angle-dependent XPS results provided strong evidence that Ag UPD adatoms were present on the surface of DBLNRs, while an AHNR was composed of a Au NR core surrounded by a Ag-Au alloy shell. Therefore, DBLNRs can be considered as a product of Ag UPD-guided NR overgrowth, while the transformation of Au NRs into AHNRs was dominated by Ag-Au codeposition. More interestingly, the pathway interswitch between the Ag UPD and Ag-Au codeposition can be modulated by simply tuning the $[Ag^+]/[HAuCl_4]$ ratios with a threshold value around 0.07 for the pathway switch (Figure 8.1H).

Under all the experimental conditions mentioned above ($[Ag^+]/[HAuCl_4] < 2$), no precipitation of AgBr was observed during the NR overgrowth. However, when the

$[Ag^+]/[HAuCl_4]$ ratio further increased to 4, insoluble AgBr started to form, which resulted in mixtures of AHNRs and irregularly shaped, micron-sized AgBr. To avoid the complication due to AgBr precipitation, the structural evolution during NR overgrowth at $[Ag^+]/[HAuCl_4]$ ratio higher than 2 was not further explored.

We qualitatively assessed the surface packing density of CTAB on the overgrown NRs by plotting surface atomic ratio of Br/(Au+Ag) (quantified by XPS) as a function of the $[Ag^+]/[HAuCl_4]$ ratio in the overgrowth solutions. As shown in Figure 8.1, panel I, the CTAB packing densities on the DBLNRs appeared higher than those on AHNRs. The XPS results also showed that the Br/(Au+Ag) ratio was independent of the Ag/ (Au+Ag) ratio of the DBLNRs, suggesting that the surface of a DBLNR was capping with a CTAB surfactant layer rather than a AgBr adlayer. However, XPS was incapable of further distinguishing the Ag(0) from Ag(I) species because of the spectral overlap between Ag(0) and Ag(I). To gain further insights into the nature of surface-deposited Ag, we correlated the XPS results with the nanoparticle surface charges characterized by ζ-potential measurements. In our ζ-potential measurements, a commercial ζ-potentiometer was used to measure the free mobility and effective hydrodynamic sizes of the colloidal nanoparticles, which were then converted into apparent ζ-potentials using simple theoretical formulas approximating each particle as a hard sphere homogeneously coated with a charged thin layer. Although more accurate determination of ζ-potentials requires the incorporation of additional empirical or semi-empirical parameters, such as the geometric anisotropy and heterogeneous distribution of adsorbates on various facets,[71] into the theoretical formulas, the apparent ζ-potentials reported here allowed us to qualitatively compare the relative surface charges of the nanoparticles of various NR-like

geometries. Interestingly, the apparent ζ-potentials of the DBLNRs remained essentially unchanged regardless of the variation of the $[Ag^+]/[HAuCl_4]$ ratios (Figure 8.1I). Both the XPS and ζ-potential results suggested that the surface packing density of CTAB on the overgrown DBLNRs was independent of the $[Ag^+]/[HAuCl_4]$ ratios in the NR overgrowth solutions. When the Au-Ag codeposition dominated the NR overgrowth, however, the apparent ζ-potentials started to increase with the $[Ag^+]/[HAuCl_4]$ ratios despite the decrease in the surface packing density of CTAB, suggesting that additional Ag^+ ions may be physisorbed on the surfaces of AHNRs when the Ag^+ concentration is sufficiently high. More quantitative assessment of Ag(0) and Ag(I) species on the nanoparticle surfaces, however, requires detailed investigations using advanced structural characterization techniques such as synchrotron Ag K-edge extended X-ray absorption fine-structure (EXAFS)[40] and small-angle neutron scattering (SANS)[72] measurements.

Complementary to the SEM and TEM measurements, the structural transformations of NRs upon their overgrowth can also be monitored using optical extinction spectroscopy owing to the geometry-dependent plasmonic characteristics of the nanoparticles (Figure 8.1J). The cylindrical Au NRs displayed a strong longitudinal plasmon resonance at ~860 nm and a much weaker transverse plasmon resonance at ~510 nm, respectively. In the low $[Ag^+]/[HAuCl_4]$ ratio regime where Ag UPD dominated the NR overgrowth, both the longitudinal and transverse plasmon resonances red-shifted and became stronger as the Au NRs evolved into DBLNRs largely due to the formation of surface concavity. We also found that the transverse plasmon mode of DBLNRs split into two peaks, which is a spectral signature of NRs with surface indentations.[63,68] As the degree of surface indentation of the DBLNRs decreased, both the longitudinal and transverse plasmon

peaks gradually blue-shifted accompanied by decrease in peak intensities. When the Au-Ag codeposition started to dominate the NR overgrowth at higher $[Ag^+]/[HAuCl_4]$ ratios, corner truncation of the DBLNRs led to further blue-shift and weakening of the longitudinal plasmon peak, while the transverse plasmon peak remained robust at essentially fixed wavelengths. The transverse plasmon peak became much stronger than the longitudinal plasmon peak when the NRs eventually evolved into AHNRs at sufficiently high $[Ag^+]/[HAuCl_4]$ ratios.

We used high-angle annular dark-field scanning transmission electron microscopy (HAADF-STEM) to further characterize the atomic-level structures of the DBLNRs and AHNRs (Figure 8.2). The relative orientation of each DBLNR or AHNR with respect to the electron beam was verified by the crystalline lattices in the high-resolution HAADF-STEM images and the fast-Fourier transform (FFT) patterns of the images. Figure 8.2, panel A shows the geometric model and HAADF-STEM image of a single-crystalline DBLNR projected along the [001] zone axis. The surface indentation of the DBLNR was well reflected by the line-scan image intensity profiles (the image intensity was roughly proportional to the thickness of the specimen). Figure 8.2, panels B and C show the high-resolution HAADFSTEM images of the regions i and ii labeled in Figure 8.2, panel A, respectively. Because of the small lattice mismatch between Au and Ag (<0.2%), only one set of face centered cubic lattices was resolved in the high resolution HAADF-STEM image. The concave surfaces of a DBLNR were essentially enclosed by various types of high-index facets whose Miller indices were determined by the local surface curvatures. Figure 8.2, panels D and E show the HAADF-STEM images and geometric models of individual AHNRs projected along the [001] and [011] zone axis, respectively. The 3D

geometries of the AHNRs were qualitatively confirmed by the orientation-dependent line-scan intensity profiles. The (100) crystalline lattices were clearly resolved in the high resolution HAADF-STEM image when an AHNR was projected along the [001] zone axis (Figure 8.2F). The lateral side facets of an AHNR were dominated by low-index {100} facets, while the longitudinal tips of an AHNR were enclosed by low-index {111} facets. Under the Ag UPD pathway, the side facets were selectively passivated by the UPD adlayers, while the growth of corners was facilitated, resulting in the formation of high-index faceting DBLNRs with concave surfaces and increased longitudinal dimensions. In contrast, Ag-Au codeposition preferentially occurred on the lateral side facets to form thermodynamically more stable, low-index faceting AHNRs with significantly increased transverse dimensions.

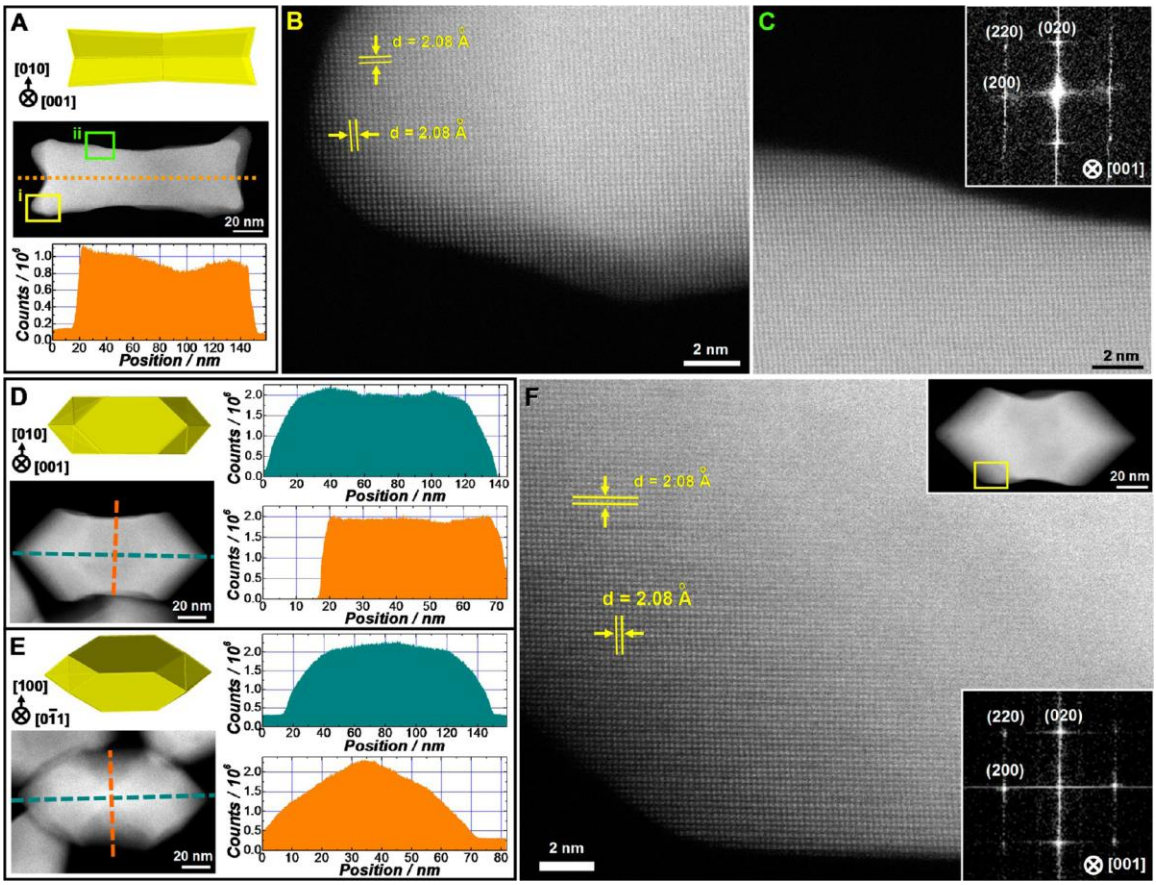

Figure 8.2. (A) HAADF-STEM image and the corresponding geometric model of an individual Au DBLNR projected along the [001] zone axis, together with the intensity profiles along the line labeled in panel A. High-resolution HAADF-STEM images of (B) region i and (C) region ii labeled in panel A. The inset in panel C is the fast Fourier transform (FFT) pattern of the image. HAADF-STEM images and the corresponding geometric models of individual AHNRs projected along (D) [001] and (E) [011] zone axes. The intensity profiles along the lines labeled in each panel were also shown. (F) High-resolution HAADF-STEM images of a portion of an individual AHNR. The HAADF-STEM image of the entire AHNR and the specific region in the high resolution image are shown in the upright inset. The bottom right inset is the corresponding FFT pattern of the high-resolution HAADF-STEM image.

8.3.2 Effects of Surface Capping Surfactants.

The pathway switch between Ag UPD and Au-Ag codeposition could also be maneuvered by varying the concentration of the CTAB surfactants while keeping Ag^+, $HAuCl_4$, and AA at fixed concentrations. Figure 8.3, panels A-F show the SEM and TEM images of the nanoparticles obtained upon NR overgrowth in the presence of 200 μM $HAuCl_4$, 10 mM AA, 14 μM Ag^+, and various concentrations of CTAB. At relatively low CTAB concentrations (e.g., [CTAB] = 10 mM), AHNRs were obtained. As the concentration of CTAB progressively increased, surface indentation and corner protrusion gradually emerged, eventually leading to the formation of DBLNRs with shape tips and highly indented surfaces at CTAB concentrations above 80 mM. The structural transition from AHNRs to DBLNRs was essentially caused by the pathway switch from Ag-Au codeposition to Ag UPD, which was further verified by EDS (Figure 8.3G). As the concentration of CTAB increased, both the longitudinal and transverse plasmon resonances progressively red-shifted and became increasingly more intense (Figure 3H), well-reflecting the transition from AHNRs to DBLNRs with increasing degrees of surface indentation. Under the current NR overgrowth conditions, CTAB served as a surface-capping competitor to the Ag^+ foreign ions, providing another key knob for the pathway interswitch. Therefore, it is the ratio of $[Ag^+]$/[CTAB] rather than

the absolute concentrations of Ag^+ and CTAB that modulates the pathway switch between Ag UPD and Ag-Au codeposition.

To gain more detailed insights into the effects of Ag UPD layers on the surface indentation of DBLNRs, we systematically varied the concentration of Ag^+ ions in the NR overgrowth solutions while keeping CTAB at a sufficiently high concentration (150 mM) such that the pathway switch from Ag UPD to Au-Ag codeposition was effectively suppressed. In the presence of 150 mM CTAB, the NR overgrowth was always dominated by the Ag UPD pathway when the $[Ag^+]$/[CTAB] ratio was varied over a broad range from 0.1-0.75. The degree of surface indentation and the sharpness of the tips of the DBLNRs progressively decreased as the $[Ag^+]$/[CTAB] ratio increased (Figure 8.4A-D). While the Ag signals were very low in EDS, the surface Ag/Au atomic ratios were measured to be in the range of 0.2-0.25 by XPS for the DBLNRs with various degrees of surface indentation (Figure 8.4E), verifying the presence of a Ag UPD adlayer on the nanoparticle surfaces. The capability of tuning the surface indentation and tip sharpness of the DBLNRs, when combined with the fine-control over aspect ratios, enables the tuning of the plasmon resonance frequencies and extinction spectral line-shapes of NRs with greater detail and precision. As shown in Figure 8.4, panel F, sharper tips and more significant surface indentation gave rise to larger spectral red-shifts of both the transverse and longitudinal plasmon resonances.

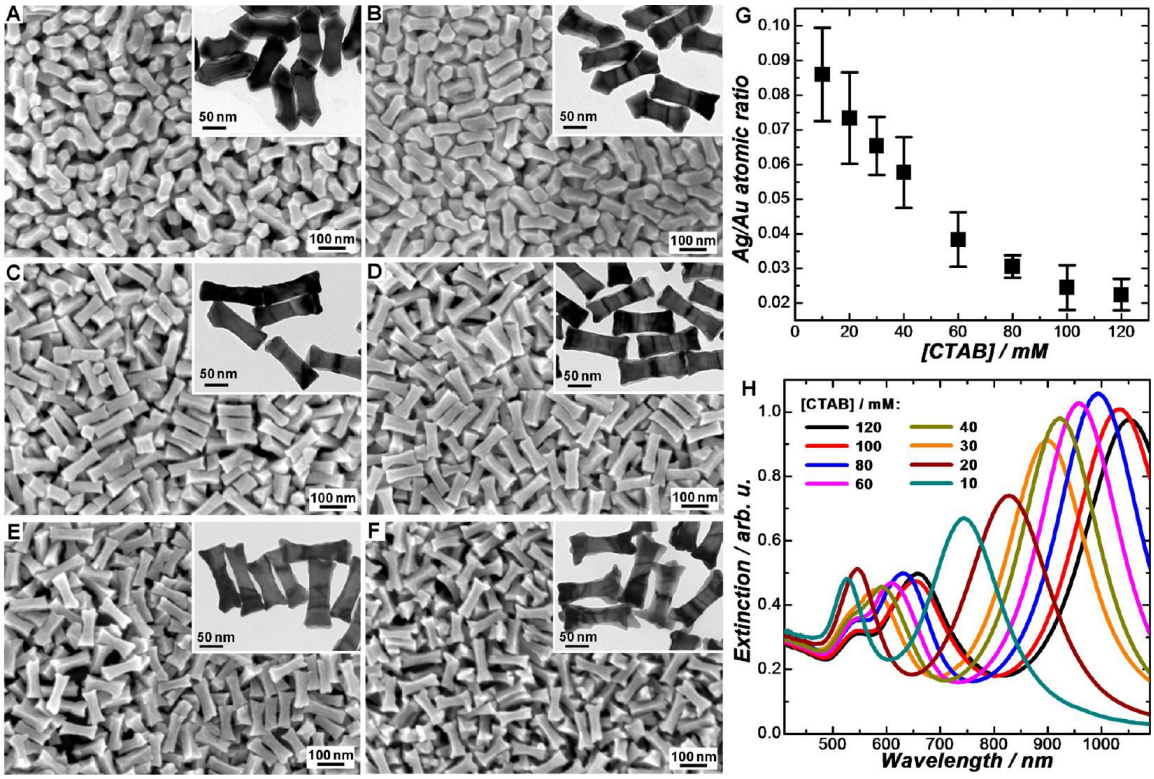

Figure 8.3. SEM and TEM (inset) images of overgrown NRs obtained in (A) 10 mM, (B) 20 mM, (C) 30 mM, (D) 60 mM, (E) 80 mM, and (F) 120 mM CTAB. The Ag^+, AA, and $HAuCl_4$ concentrations were kept at 14 μM, 10 mM, and 200 μM, respectively. (G) Ag/Au atomic ratios (quantified by EDS) of the overgrown NRs obtained at various CTAB concentrations. The error bars represent the standard deviations of three samples fabricated under identical conditions. (H) Optical extinction spectra of the overgrown NRs obtained in various concentrations of CTAB as labeled in the figure.

To further test the hypothesis that the pathway switch was maneuvered by the competition between Ag^+ ions and capping surfactants, we used benzyldimethylhexadecylammonium chloride (BDAC) instead of CTAB as the capping surfactants to guide the NR overgrowth. At a $[Ag^+]/[HAuCl_4]$ ratio of 0.05, AHNRs were obtained in the presence of 30 mM BDAC (Figure 8.5A), while DBLNRs were obtained in 30 mM CTAB under otherwise identical NR overgrowth conditions. Apparently, the substitution of CTAB with BDAC switched the NR overgrowth pathway from Ag UPD

to the Ag-Au codeposition. Such pathway switch could be interpreted as a consequence of the weaker interactions of BDAC than those of CTAB with Au surfaces.[10,73] The relative binding affinities of CTAB and BDAC on Au surfaces were further verified by the surfactant exchange between CTAB and BDAC monitored by surface-enhanced Raman spectroscopy (SERS) measurements. In the presence of 30 mM BDAC, nanoscale roughness started to develop on the lateral side surfaces of the AHNRs as the $[Ag^+]/[HAuCl_4]$ ratio increased, while the {111} facets at the tips were preserved (Figure 8.5B-D), leading to the formation of a unique structure resembling momordica charantia, inspiring the name momordica charantia-like nanorods (MCLNRs) (Figure 8.5E,F). The EDS results clearly showed that each MCLNR was composed of a Au NR core and a Ag-Au alloy shell. The Ag/Au atomic ratios obtained from EDS progressively went up to ~0.40 with the increase of the $[Ag^+]/[HAuCl_4]$ ratios, indicating that the transformation of Au NRs into MCLNRs was dominated by Ag-Au electroless codeposition (Figure 8.5G). As shown in Figure 8.5, panel H, the structural evolution from AHNRs to MCLNRs caused significant blue-shift and weakening of the longitudinal plasmon resonance largely due to the increased transverse dimensions and Ag content of the particles.

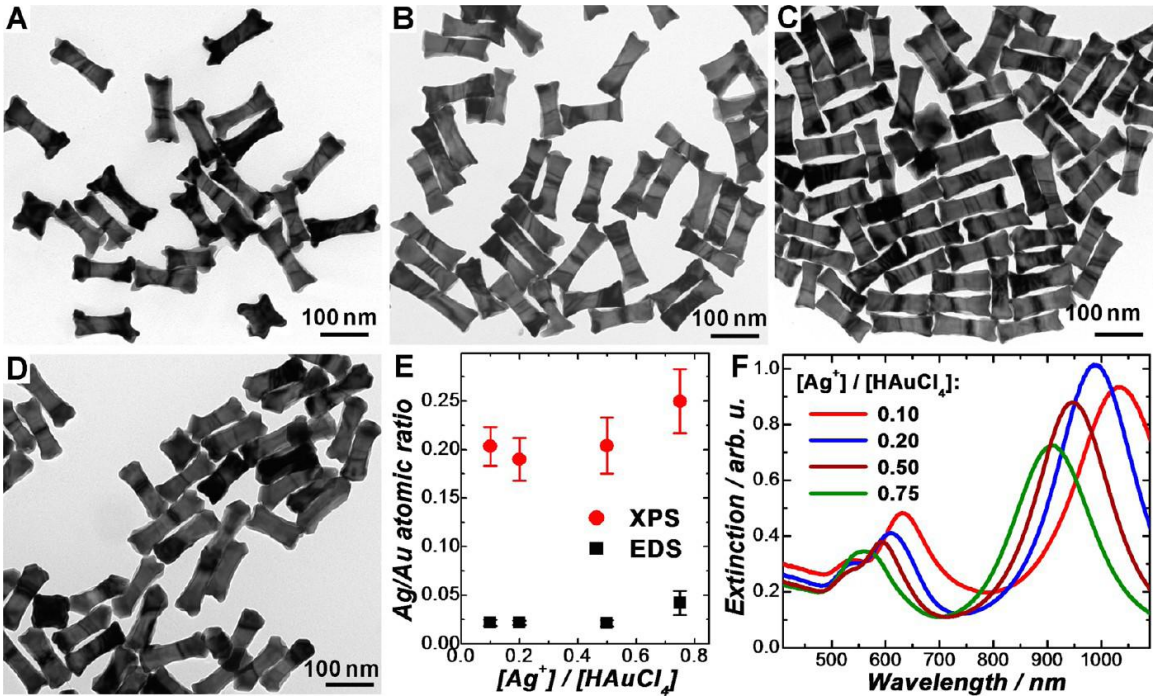

Figure 8.4. TEM images of overgrown NPs obtained in the presence of 150 mM CTAB at various $[Ag^+]/[HAuCl_4]$ ratios of (A) 0.10, (B) 0.20, (C) 0.50, and (D) 0.75. The concentrations of HAuCl4 and AA were 200 μM and 10 mM, respectively. (E) Ag/Au atomic ratios determined by EDS and XPS for the overgrown NRs obtained at various $[Ag^+]/[HAuCl_4]$ ratios. The error bars represent the standard deviations of three samples fabricated under identical conditions. (F) Optical extinction spectra of the overgrown NRs obtained in the presence of 150 mM CTAB and various $[Ag^+]/ [HAuCl_4]$ ratios as labeled in the figure.

The morphological interconversions between MCLNRs and AHNRs could also be achieved through variation of the BDAC concentration while keeping Ag^+, $HAuCl_4$, and AA at fixed concentrations. As shown in Figure 8.6, panels A-D, the MCLNRs gradually became less rough on their lateral side surfaces as the concentration of BDAC increased, eventually transforming into AHNRs at sufficiently high BDAC concentrations. The Ag/Au atomic ratios of MCLNRs were significantly higher than those of the AHNRs, though the $[Ag^+]/[HAuCl_4]$ ratio in the NR overgrowth solutions was kept the same (Figure 8.6E). During the geometric transition from MCLNRs to AHNRs, the longitudinal plasmon resonance progressively blue-shifted, and the peak width

significantly decreased as a consequence of decrease in aspect ratios, while the transverse plasmon resonance wavelength remained essentially unchanged (Figure 8.6F).

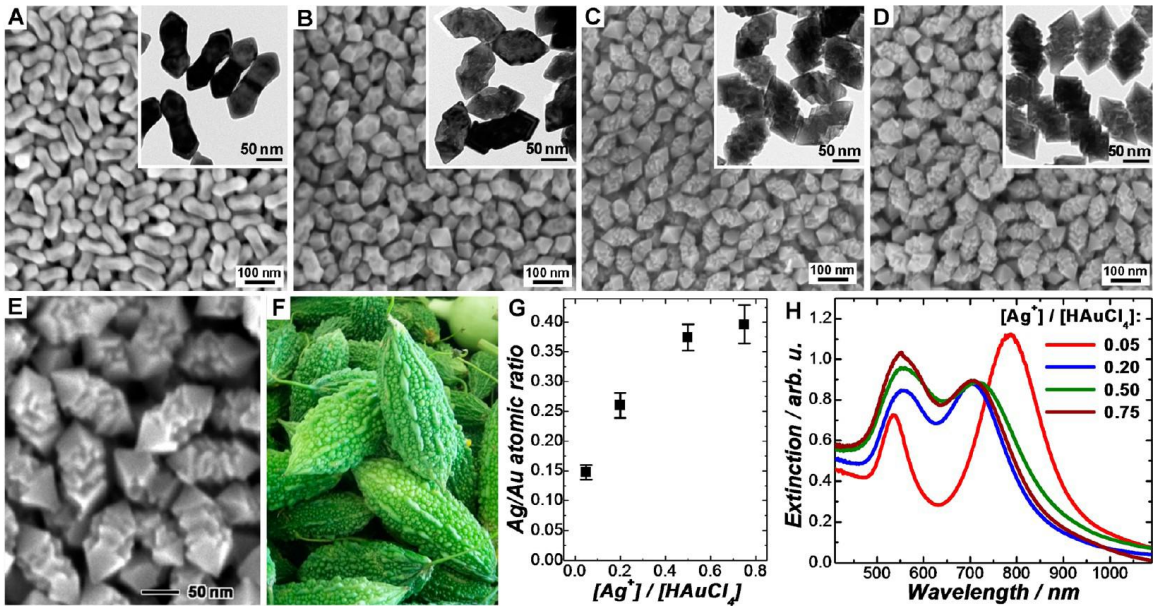

Figure 8.5. SEM and TEM (inset) images of overgrown NRs obtained in the presence of 30 mM BDAC at various $[Ag^+]/[HAuCl_4]$ ratios of (A) 0.05, (B) 0.20, (C) 0.50, and (D) 0.75. The concentrations of HAuCl4 and AA were fixed at 200 μM and 10 mM, respectively. (E) High-magnification SEM image of Au@Ag-Au MCLNRs obtained at $[Ag^+]/[HAuCl_4]$ ratio of 0.75. (F) Photograph of momordica charantias. (G) Ag/Au atomic ratios, determined by EDS, of NPs obtained at various $[Ag^+]/[HAuCl_4]$ ratios. The error bars represent the standard deviations of three samples fabricated under identical conditions. (H) Optical extinction spectra of NPs obtained through NR overgrowth in the presence of 30 mM BDAC and various $[Ag^+]/[HAuCl_4]$ ratios as labeled in the figure.

Both the cationic amphiphilic chain and the halide anion of the surfactant molecules play crucial roles in guiding the NR structural evolution. The surfactants interact with the nanoparticle surfaces primarily through metal-halide interactions. During surfactant-guided, seed-mediated nanocrystal growth, the presence of additional halide anions may drastically modify the geometries of the resulting Au nanoparticles due to the metal-halide interactions.[74-76] However, we found that the halide anions alone without the surfactants were incapable of controlling the geometry of overgrown NRs. In the

presence of the halide-containing cationic surfactants, the Au(III) precursor is reduced to Au(I) by AA, which forms Au(I)-surfactant complexes that are soluble in water.[18] Upon addition of Au NR seeds into the overgrowth solution, a surface-catalyzed electroless plating process occurs, through which Au(I) is further reduced to metallic Au on the surfaces of Au NRs.[18] Without any surfactants, Au(III) was rapidly reduced to metallic Au, while Ag(I) was coreduced to metallic Ag in the presence of KBr or KCl even before the introduction of Au NR seeds, resulting in the formation of highly aggregated Au-Ag bimetallic nanoparticles. To further elucidate the roles of the halide anions in the surfactants, we substituted CTAB with cetyltrimethylammonium chloride (CTAC), a chloride-containing surfactant with exactly the same amphiphilic chain as that of CTAB, to guide the NR overgrowth under otherwise identical experimental conditions. It is found that substitution of 20 mM CTAB with 20 mM CTAC resulted in a morphological change from DBLNRs to AHNRs primarily because chloride anions have weaker interactions with Au than bromide anions and thus are less efficient to compete with Ag^+ ions. On the other hand, the packing density of the surfactants on the nanoparticle surfaces is intimately tied to the structures of the amphiphilic chains. Although both CTAC and BDAC contain the same anion, the cationic chain of BDAC is bulkier than that of CTAC due to the presence of benzene ring. As a result, substitution of 30 mM BDAC with 30 mM CTAC switched the morphology of the overgrown NRs from MCLNRs to AHNRs possibly due to denser packing of CTAC on the nanoparticle surfaces than that of BDAC.

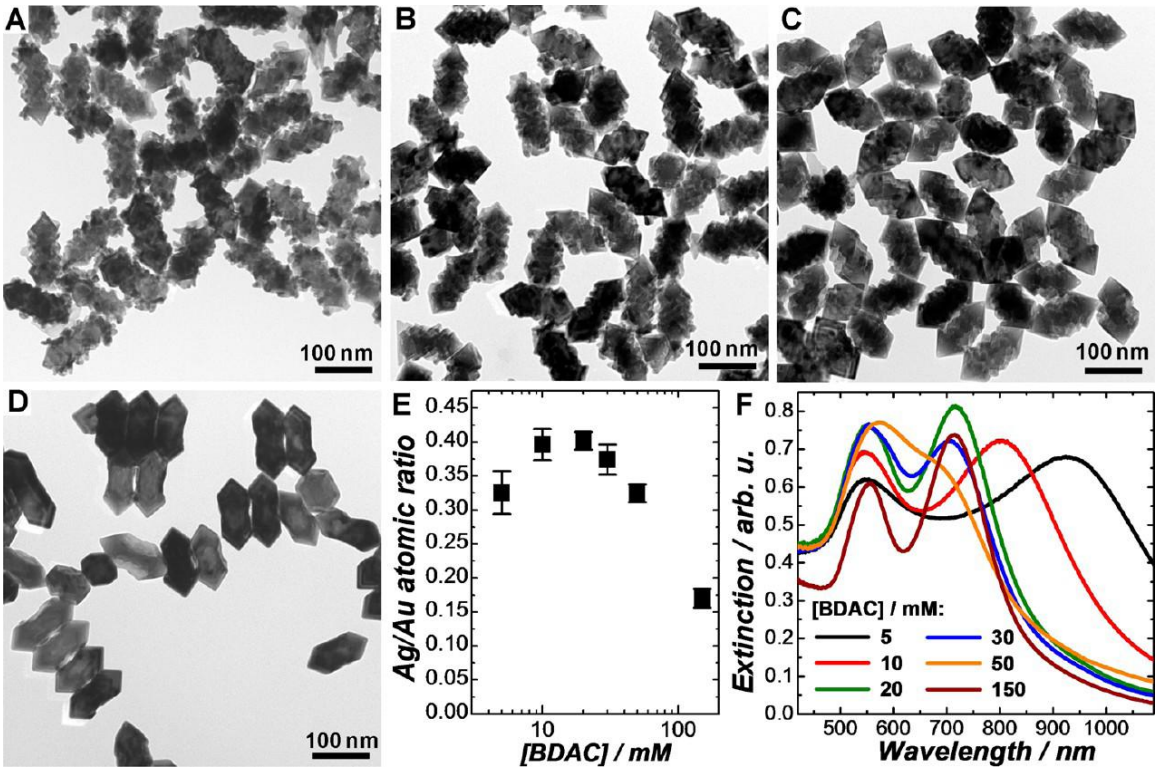

Figure 8.6. TEM images of overgrown NRs obtained in (A) 5 mM, (B) 10 mM, (C) 50 mM, and (D) 150 mM BDAC. The concentrations of Ag^+, $HAuCl_4$, and AA were fixed at 20 μM, 200 μM, and 10 mM, respectively. (E) Ag/Au atomic ratios, determined by EDS, of NPs obtained at various BDAC concentrations. The error bars represent the standard deviations of three samples fabricated under identical conditions. (F) Optical extinction spectra of the overgrown NRs obtained in the presence of various concentrations of BDAC as labeled in the figure.

We analyzed the detailed XPS spectral features of the Au 4f and Ag 3d peaks of the overgrown NRs of various geometries and compositions. On the bulk Ag foil, two well separated spin-orbital components were observed at 368.2 eV (Ag $3d_{5/2}$) and 374.2 eV (Ag $3d_{3/2}$), respectively, and weak loss features were also observed to the higher binding energy side of each spin-orbit component for Ag. The loss features, however, became undetectable on the Ag-containing overgrown NR samples due to the change of atomic coordination environment of Ag atoms upon the formation of either a Ag UPD layer or a Ag-Au alloy shell. While the Au 4f peaks only slightly shifted within ±0.1 eV, the Ag 3d peaks exhibited significantly more pronounced spectral down-shifts up to -0.5 eV upon

the formation of a Ag UPD layer or a Ag−Au alloy shell, which is in excellent agreement with previously reported XPS results on Ag UPD layer-coated Au nanoparticles[27] and Au-Ag alloy nanoparticles.[77,78]

8.3.3 Effects of Reducing Agents.

In addition to the interplay between Ag^+ ions and surfactants, the reducing agents also played a key role in maneuvering pathway interswitch between Ag UPD and Ag-Au codeposition. To further investigate the effects of reducing agents, we fixed the concentrations of CTAB, $AgNO_3$, and $HAuCl_4$ at 20 mM, 100 μM, and 200 μM, respectively, while systematically varying the AA concentrations. At relatively high [AA]/[$HAuCl_4$] ratios, the preferential codeposition of Ag and Au resulted in the formation of Au@Ag-Au AHNRs (Figure 8.7A). As the [AA]/[$HAuCl_4$] ratios gradually decreased, and Ag UPD began to dominate the NR overgrowth process, giving rise to the formation of DBLNRs with truncated corners, which further evolved into DBLNRs with sharper tips and more significant surface indentation (Figures 8.7B-D). The evolution of Ag/Au atomic ratios (Figure 8.7E) and optical extinction spectral features (Figure 8.7F) provided additional evidence on the pathway switch from Ag-Au codeposition to Ag UPD as AA concentration decreased. This strongly indicated that fast NR overgrowth in the presence of high concentrations of AA favored the Au-Ag codeposition. The NR overgrowth was slowed down when decreasing the AA concentrations, which caused the pathway switch from Au-Ag codeposition to Ag UPD.

To better understand the effects of reducing agents, we also used other mild reducing agents, such as hydroquinone (HQ) and 4-(2-hydroxyethyl)-1-piperazineethanesulfonic acid (HEPES), to initiate the NR overgrowth. Because the reducing capabilities of both

HQ and HEPES are significantly weaker than those of AA,[79,80] the NR overgrowth became much slower when using HQ and HEPES instead of AA under otherwise identical conditions. By keeping the molar ratio of reducing agents to $HAuCl_4$ fixed at 50, AHNRs were obtained in the presence of AA, whereas the use of HQ and HEPES resulted in the formation of DBLNRs. Therefore, the NR overgrowth kinetics controlled by the reducing agents is also a key factor determining the pathway interswitch between Ag UPD and Au-Ag codeposition.

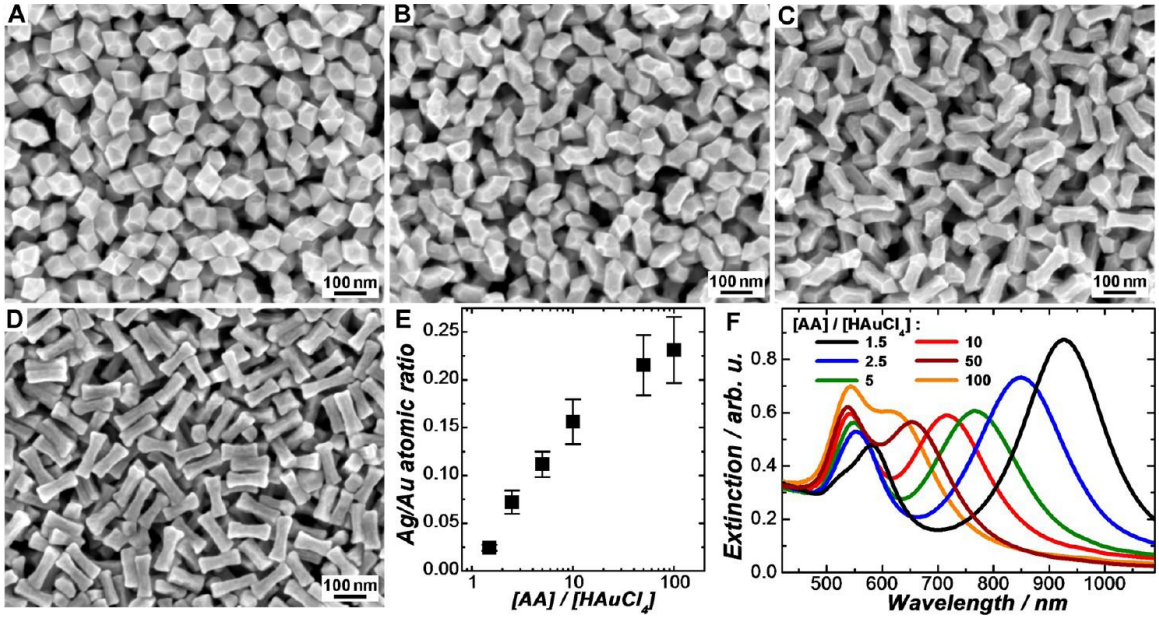

Figure 8.7. SEM images of overgrown NRs obtained at various [AA]/[$HAuCl_4$] ratios of (A) 100, (B) 10, (C) 2.5, and (D) 1.5. The concentrations of Ag^+, CTAB, and $HAuCl_4$ were kept at 100 μM, 20 mM, and 200 μM, respectively. (E) Ag/Au atomic ratios (quantified by EDS) of the overgrown NRs obtained at various [AA]/[$HAuCl_4$] ratios. The error bars represent the standard deviations of three samples fabricated under identical conditions. (F) Optical extinction spectra of the overgrown NRs obtained at various [AA]/[$HAuCl_4$] ratios as labeled in the figure.

As summarized in the literature, the geometric evolution of Au nanocrystals during seed-mediated growth is primarily governed by two pathways: kinetic control and selective surface passivation.[32] In absence of foreign metal ions, high-index faceting nanoparticles were typically the major products of fast nanocrystal growth processes,

while slow growth kinetics favored the formation of thermodynamically stable low-index faceting nanoparticles. In the presence of Ag^+ foreign ions, the surfaces of Au nanoparticle were selectively passivated by Ag UPD adlayers, guiding the transformation of Au nanocrystals into a variety of high-index faceting geometries.[10,27] Higher Ag^+ concentrations resulted in the formation of facets with higher-order Miller indices.[27] In striking contrast to these previous observations, we found that slow NR overgrowth allowed the cylindrical Au NRs to transform into high-index faceting DBLNRs, whereas fast NR overgrowth led to the formation of low-index faceting AHNRs. Apparently, the geometric evolution of NRs observed in this work should not be simply interpreted as the consequence of either a kinetically controlled or a surface passivation-dominated nanocrystal growth process. It was essentially the pathway interswitch between Ag UPD and Au-Ag codeposition that underpinned the intriguing structural evolution of cylindrical Au NRs into various Au-Ag bimetallic nanoparticle geometries.

8.3.4 Structural Stability of Ag-Au Bimetallic AHNRs and MCLNRs.

Ag nanostructures exhibit highly desired plasmonic properties for widespread applications; however, they are chemically much less stable than the other noble metal counterparts such as Au, Pt, and Pd nanoparticles. An effective way to stabilize the Ag nanoparticles while retaining their key plasmonic characteristics is to homogeneously alloy elemental Ag with elemental Au in nanocrystals. As previously demonstrated in various Ag-Au alloy nanoparticles, the interdiffusion of Ag atoms into Au matrix through alloying greatly enhanced the stability of Ag elements, and higher oxidation potentials were required to trigger the oxidation of Ag when it was alloyed.[65,66,81] While nanostructures similar to the AHNRs can be fabricated through NR overgrowth under

various conditions,[37,65,66,82] there has long been lack of consensus on the exact compositions of the AHNRs. An AHNR was initially identified to be a Au NR core coated with either a Ag UPD adlayer[37] or a monometallic Ag nanoshell.[82] However, more recent studies revealed that each AHNR was essentially a heteronanostructure composed of a Au-core and a Ag-Au alloy shell,[65,66] which well interpreted the structural robustness of the AHNRs against chemical etching.[65,66] As demonstrated in this work, the Au-Ag codeposition-controlled NR overgrowth provided a unique way to electrolessly deposit Ag-Au alloy shells on Au NR cores.

We systematically compared the structural changes of three representative Ag-Au bimetallic heteronanostructures, Au@Ag core-shell nanocuboids (NCBs), Au@Au-Ag core-shell AHNRs, and Au@Au-Ag core-shell MCLNRs, upon oxidative etching by Fe^{3+}, sulfidation with Na_2S, and galvanic replacement with $HAuCl_4$ (Figure 8.8). The monometallic Ag shells were completely etched upon exposure of the NCBs to Fe^{3+}, whereas both the AHNRs and MCLNRs were extremely robust against oxidative etching (Figure 8B,G,L). The relative resistivities of various nanoparticles toward oxidative etching were further evaluated by electrochemical measurements. A strong anodic peak was observed at ~0.56 V versus SCE in the cyclic voltamogram (CV) of Au@Ag core-shell NCBs, which was attributed to the oxidation of the metallic Ag shells. In contrast, much weaker anodic peaks were observed for both AHNRs and MCLNRs at significantly more positive potentials, indicating that alloying of Ag with Au shifted the Ag oxidation potential to much higher values and the oxidation of Ag also became kinetically inhibited. The structural robustness of Ag-Au alloys was further confirmed by the sulfidation reactions with Na_2S. While the Au@Ag core-shell NCBs completely

transformed into Au@Ag_2S core-shell nanoparticles upon sulfidation (Figure 8.8C), no significant morphological or compositional change was observed on AHNRs and MCLNRs (Figure 8.8H,M). Upon the exposure of the NCBs to $HAuCl_4$, fast galvanic replacement reactions occurred, which gave rise to the formation of Au@Ag-Au yolk−shell particles with interior cavities[83,84] (Figure 8.8D). For AHNRs, the sharpness of the tips and edges decreased, while all the facet were well-preserved because the undercoordinated corner and edge atoms were less stable than the surface atoms on the low-index facets of the AHNRs (Figure 8.8I). The MCLNRs appeared to be more reactive than AHNRs as evident by the formation of nanoscale porosity upon galvanic replacement (Figure 8.8N) mostly likely due to the fact that the Ag/Au atomic ratios of MCLNRs were higher than those of AHNRs and BDAC provided less effective surface protection in comparison to CTAB.

All the above-mentioned structural transformation processes could be tracked by optical extinction spectroscopy. As shown in Figure 8.8, panel E, Au@Ag core−shell NCBs exhibited four distinct plasmon resonance bands, which could be assigned to the longitudinal dipole, transverse dipole, transverse octupole, and even high-order multipole resonances, respectively.[85-88] Upon complete etching of the Ag shells with $Fe(NO_3)_3$, only the spectral features of pure Au NR cores were preserved. Interestingly, significant plasmon damping was observed upon the sulfidation of the Ag shells into Ag_2S shells due to the spectral overlap between interband transitions of Ag_2S with the plasmon resonances of Au.[89] The galvanic replacement of NCBs gave rise to significant red-shift and broadening of both the transverse and longitudinal plasmon band upon the formation of the yolk-shell structures, which was in line with previous observations.[83,84] For

AHNRs and MCLNRs, no obvious spectral changes were observed due to the structural robustness of these two structures against the oxidative etching, sulfidation, and galvanic replacement treatments (Figure 8.8J,O).

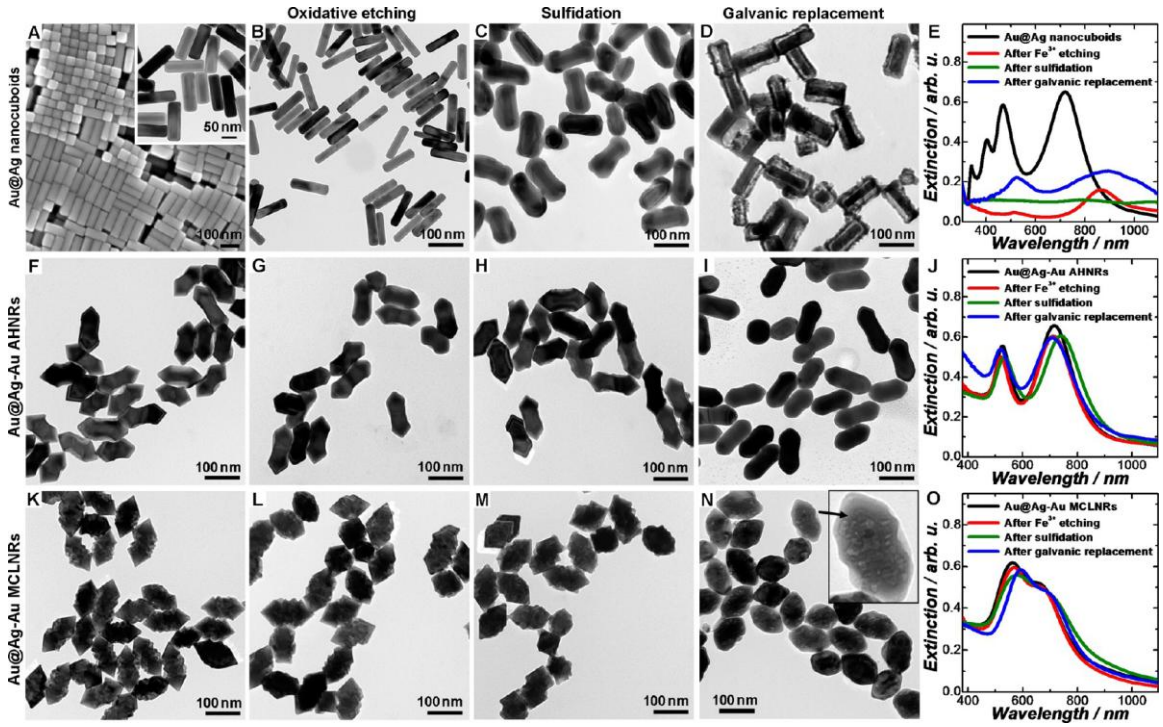

Figure 8.8. (A) SEM and TEM (inset) images of Au@Ag core-shell NCBs. TEM images of Au@Ag core-shell NCBs after (B) oxidative etching by Fe^{3+}, (C) sulfidation with Na_2S, and (D) galvanic replacement with $HAuCl_4$. (E) Optical extinction spectra of the NPs shown in panels A-D. TEM images of (F) AHNRs, (G) AHNRs after oxidative etching by Fe^{3+}, (H) AHNRs after sulfidation with Na_2S, and (I) AHNRs after galvanic replacement with $HAuCl_4$. (J) Optical extinction spectra of the NPs shown in panels F-I. TEM images of (K) MCLNRs, (L) MCLNRs after oxidative etching by Fe^{3+}, (M) MCLNRs after sulfidation with Na_2S, and (N) MCLNRs after galvanic replacement with $HAuCl_4$. The inset of panel N shows a high-magnification TEM of one particle indicated by an arrow. (O) Optical extinction spectra of the NPs shown in panels K-N.

8.4 Conclusions

This work highlights the intertwining roles of Ag^+ foreign ions, surface-capping surfactants, and reducing agents that underpin the intriguing geometric and compositional evolution of single-crystalline Au NRs upon their overgrowth. The interplay of Ag^+ ions, surfactants, and reducing agents modulates the switch between two underlying NR

overgrowth pathways, Ag UPD and Au-Ag electroless codeposition. The interswitch between the two pathways allows cylindrical Au NRs to selectively evolve into a variety of NR-derived anisotropic geometries with interesting structural, compositional, and plasmonic characteristics. The selective surface passivation of Au NRs by Ag UPD adlayers leads to the transformation of cylindrical Au NRs into DBLNRs with concave surfaces enclosed by high-index facets, whereas the Au-Ag codeposition-dominated NR overgrowth processes result in the formation of low-index faceting AHNRs and MCLNRs with Au-Ag alloy shell structures. The homogeneous alloying of Ag with Au in the AHNRs and MCLNRs greatly enhances the stability of the Ag elements in the particles, which makes the AHNRs and MCLNRs remarkably more resistive to oxidative etching, sulfidation, and galvanic replacement than their heterostructured Au-Ag core-shell counterparts. The new insights gained from this work provide important information that may guide the rational design and development of new synthetic approaches to architecturally more sophisticated metallic nanostructures, further enhancing our capabilities to fine-tune the optical, electronic, and catalytic properties of metallic nanoparticles through more deliberate and precise control over the particle geometries and compositions.

8.5 References

(1) Burda, C.; Chen, X. B.; Narayanan, R.; El-Sayed, M. A. *Chem. Rev.* **2005**, *105*, 1025-1102.

(2) Jain, P. K.; Huang, X. H.; El-Sayed, I. H.; El-Sayed, M. A. *Acc. Chem. Res.* **2008**, *41*, 1578-1586.

(3) Tao, A. R.; Habas, S.; Yang, P. D. *Small* **2008**, *4*, 310-325.

(4) Grzelczak, M.; Perez-Juste, J.; Mulvaney, P.; Liz-Marzan, L. M. *Chem. Soc. Rev.* **2008**, *37*, 1783-1791.

(5) Xia, Y. N.; Xiong, Y. J.; Lim, B.; Skrabalak, S. E. *Angew. Chem. Int. Edit.* **2009**, *48*, 60-103.

(6) Murphy, C. J.; San, T. K.; Gole, A. M.; Orendorff, C. J.; Gao, J. X.; Gou, L.; Hunyadi, S. E.; Li, T. *J. Phys. Chem. B* **2005**, *109*, 13857-13870.

(7) Perez-Juste, J.; Pastoriza-Santos, I.; Liz-Marzan, L. M.; Mulvaney, P. *Coord. Chem. Rev.* **2005**, *249*, 1870-1901.

(8) Jones, M. R.; Osberg, K. D.; Macfarlane, R. J.; Langille, M. R.; Mirkin, C. A. *Chem. Rev.* **2011**, *111*, 3736-3827.

(9) Sau, T. K.; Rogach, A. L. *Adv. Mater.* **2010**, *22*, 1781-1804.

(10) Langille, M. R.; Personick, M. L.; Zhang, J.; Mirkin, C. A. *J. Am. Chem. Soc.* **2012**, *134*, 14542-14554.

(11) Sau, T. K.; Murphy, C. J. *Langmuir* **2004**, *20*, 6414-6420.

(12) Wang, Y. S.; Sentosun, K.; Li, A.; Coronado-Puchau, M.; Sánchez-Iglesias, A.; Li, S. Z.; Su, X. D.; Bals, S.; Liz-Marzán, L. M. *Chem. Mater.* **2015**, *27*, DOI: 10.1021/acs.chemmater.5b03600.

(13) Tsao, Y. C.; Rej, S.; Chiu, C. Y.; Huang, M. H. *J. Am. Chem. Soc.* **2014**, *136*, 396-404.

(14) O'Brien, M. N.; Jones, M. R.; Brown, K. A.; Mirkin, C. A. *J. Am. Chem. Soc.* **2014**, *136*, 7603-7606.

(15) Lin, H. X.; Lei, Z. C.; Jiang, Z. Y.; Hou, C. P.; Liu, D. Y.; Xu, M. M.; Tian, Z. Q.; Xie, Z. X. *J. Am. Chem. Soc.* **2013**, *135*, 9311-9314.

(16) Quan, Z. W.; Wang, Y. X.; Fang, J. Y. *Acc. Chem. Res.* **2013**, *46*, 191-202.

(17) Murphy, C. J.; Thompson, L. B.; Alkilany, A. M.; Sisco, P. N.; Boulos, S. P.; Sivapalan, S. T.; Yang, J. A.; Chernak, D. J.; Huang, J. Y. *J. Phys. Chem. Lett.* **2010**, *1*, 2867-2875.

(18) Lohse, S. E.; Murphy, C. J. *Chem. Mater.* **2013**, *25*, 1250-1261.

(19) Chen, H. J.; Shao, L.; Li, Q.; Wang, J. F. *Chem. Soc. Rev.* **2013**, *42*, 2679-2724.

(20) Huang, X. H.; Neretina, S.; El-Sayed, M. A. *Adv. Mater.* **2009**, *21*, 4880-4910.

(21) Nikoobakht, B.; El-Sayed, M. A. *Chem. Mater.* **2003**, *15*, 1957-1962.

(22) Millstone, J. E.; Hurst, S. J.; Metraux, G. S.; Cutler, J. I.; Mirkin, C. A. *Small* **2009**, *5*, 646-664.

(23) Chiu, C. Y.; Chung, P. J.; Lao, K. U.; Liao, C. W.; Huang, M. H. *J. Phys. Chem. C* **2012**, *116*, 23757-23763.

(24) Lu, C. L.; Prasad, K. S.; Wu, H. L.; Ho, J. A. A.; Huang, M. H. *J. Am. Chem. Soc.* **2010**, *132*, 14546-14553.

(25) Ming, T.; Feng, W.; Tang, Q.; Wang, F.; Sun, L. D.; Wang, J. F.; Yan, C. H. *J. Am. Chem. Soc.* **2009**, *131*, 16350-16351.

(26) Niu, W. X.; Zhang, W. Q.; Firdoz, S.; Lu, X. M. *Chem. Mater.* **2014**, *26*, 2180-2186.

(27) Personick, M. L.; Langille, M. R.; Zhang, J.; Mirkin, C. A. *Nano Lett.* **2011**, *11*, 3394-3398.

(28) Tao, A.; Sinsermsuksakul, P.; Yang, P. D. *Angew. Chem. Int. Edit.* **2006**, *45*, 4597-4601.

(29) Xia, X. H.; Zeng, J.; McDearmon, B.; Zheng, Y. Q.; Li, Q. G.; Xia, Y. N. *Angew. Chem. Int. Edit.* **2011**, *50*, 12542-12546.

(30) Zhang, Q. F.; Wang, H. *ACS Catal.* **2014**, *4*, 4027-4033.

(31) Zhang, J. A.; Langille, M. R.; Personick, M. L.; Zhang, K.; Li, S. Y.; Mirkin, C. A. *J. Am. Chem. Soc.* **2010**, *132*, 14012-14014.

(32) Personick, M. L.; Mirkin, C. A. *J. Am. Chem. Soc.* **2013**, *135*, 18238-18247.

(33) Ma, Y. Y.; Kuang, Q.; Jiang, Z. Y.; Xie, Z. X.; Huang, R. B.; Zheng, L. S. *Angew. Chem. Int. Edit.* **2008**, *47*, 8901-8904.

(34) Zhang, Q. F.; Large, N.; Nordlander, P.; Wang, H. *J. Phys. Chem. Lett.* **2014**, *5*, 370-374.

(35) Yu, Y.; Zhang, Q. B.; Lu, X. M.; Lee, J. Y. *J. Phys. Chem. C* **2010**, *114*, 11119-11126.

(36) Liu, M. Z.; Guyot-Sionnest, P. *J. Phys. Chem. B* **2005**, *109*, 22192-22200.

(37) Xiang, Y. J.; Wu, X. C.; Liu, D. F.; Feng, L. L.; Zhang, K.; Chu, W. G.; Zhou, W. Y.; Xie, S. S. *J. Phys. Chem. C* **2008**, *112*, 3203-3208.

(38) Zhang, L.; Chen, Q. L.; Jiang, Z. Y.; Xie, Z. X.; Zheng, L. S. *CrystEngComm* **2015**, *17*, 5556-5561.

(39) Zhang, L.; Zhang, J. W.; Kuang, Q.; Xie, S. F.; Jiang, Z. Y.; Xie, Z. X.; Zheng, L. S. *J. Am. Chem. Soc.* **2011**, *133*, 17114-17117.

(40) Padmos, J. D.; Personick, M. L.; Tang, Q.; Duchesne, P. N.; Jiang, D.-E.; Mirkin, C. A.; Zhang, P.. *Nat. Commun.* **2015**, *6*, 7664.

(41) Mallin, M. P.; Murphy, C. J. *Nano Lett.* **2002**, *2*, 1235-1237.

(42) DeSantis, C. J.; Weiner, R. G.; Radmilovic, A.; Bower, M. M.; Skrabalak, S. E. *J. Phys. Chem. Lett.* **2013**, *4*, 3072-3082.

(43) Huang, J. F.; Zhu, Y. H.; Lin, M.; Wang, Q. X.; Zhao, L.; Yang, Y.; Yao, K. X.; Han, Y. *J. Am. Chem. Soc.* **2013**, *135*, 8552-8561.

(44) DeSantis, C. J.; Peverly, A. A.; Peters, D. G.; Skrabalak, S. E. *Nano Lett.* **2011**, *11*, 2164-2168.

(45) DeSantis, C. J.; Sue, A. C.; Bower, M. M.; Skrabalak, S. E. *ACS Nano* **2012**, *6*, 2617-2628.

(46) Shibata, T.; Bunker, B. A.; Zhang, Z. Y.; Meisel, D.; Vardeman, C. F.; Gezelter, J. D. *J. Am. Chem. Soc.* **2002**, *124*, 11989-11996.

(47) Edgar, J. A.; McDonagh, A. M.; Cortie, M. B. *ACS Nano* **2012**, *6*, 1116-1125.

(48) Walsh, M. J.; Barrow, S. J.; Tong, W. M.; Funston, A. M.; Etheridge, J. *ACS Nano* **2015**, *9*, 715-724.

(49) Jackson, S. R.; McBride, J. R.; Rosenthal, S. J.; Wright, D. W. *J. Am. Chem. Soc.* **2014**, *136*, 5261-5263.

(50) Almora-Barrios, N.; Novell-Leruth, G.; Whiting, P.; Liz-Marzan, L. M.; Lopez, N. *Nano Lett.* **2014**, *14*, 871-875.

(51) Katz-Boon, H.; Rossouw, C. J.; Weyland, M.; Funston, A. M.; Mulvaney, P.; Etheridge, J. *Nano Lett.* **2011**, *11*, 273-278.

(52) Carbo-Argibay, E.; Rodriguez-Gonzalez, B.; Gomez-Grana, S.; Guerrero-Martinez, A.; Pastoriza-Santos, I.; Perez-Juste, J.; Liz-Marzan, L. M. *Angew. Chem. Int. Edit.* **2010**, *49*, 9397-9400.

(53) Goris, B.; Bals, S.; Van den Broek, W.; Carbo-Argibay, E.; Gomez-Grana, S.; Liz-Marzan, L. M.; Van Tendeloo, G. *Nat. Mater.* **2012**, *11*, 930-935.

(54) Gai, P. L.; Harmer, M. A. *Nano Lett.* **2002**, *2*, 771-774.

(55) Wang, Z. L.; Gao, R. P.; Nikoobakht, B.; El-Sayed, M. A. *J. Phys. Chem. B* **2000**, *104*, 5417-5420.

(56) Katz-Boon, H.; Walsh, M.; Dwyer, C.; Mulvaney, P.; Funston, A. M.; Etheridge, J. *Nano Lett.* **2015**, *15*, 1635-41.

(57) Gou, L. F.; Murphy, C. J. *Chem. Mater.* **2005**, *17*, 3668-3672.

(58) Song, J. H.; Kim, F.; Kim, D.; Yang, P. D. *Chem. Eur. J.* **2005**, *11*, 910-916.

(59) Kou, X. S.; Zhang, S. Z.; Yang, Z.; Tsung, C. K.; Stucky, G. D.; Sun, L. D.; Wang, J. F.; Yan, C. H. *J. Am. Chem. Soc.* **2007**, *129*, 6402-6404.

(60) Sohn, K.; Kim, F.; Pradel, K. C.; Wu, J. S.; Peng, Y.; Zhou, F. M.; Huang, J. X. *ACS Nano* **2009**, *3*, 2191-2198.

(61) Khlebtsov, B. N.; Ithanadeev, V. A.; Ye, J.; Sukhorukov, G. B.; Khlebtsov, N. G. *Langmuir* **2014**, *30*, 1696-1703.

(62) Liu, W. Q.; Zhang, H.; Wen, T.; Yan, J.; Hou, S.; Shi, X. W.; Hu, Z. J.; Ji, Y. L.; Wu, X. C. *Langmuir* **2014**, *30*, 12376-12383.

(63) Huang, Y. J.; Wu, L.; Chen, X. D.; Bai, P.; Kim, D. H. *Chem. Mater.* **2013**, *25*, 2470-2475.

(64) Zhang, L. F.; Zhang, C. Y. *Nanoscale* **2013**, *5*, 5794-5800.

(65) Huang, J. F.; Zhu, Y. H.; Liu, C. X.; Zhao, Y. F.; Liu, Z. H.; Hedhili, M. N.; Fratalocchi, A.; Han, Y. *Small* **2015**, *11*, 5214-5221.

(66) Bai, T. L.; Sun, J. F.; Che, R. C.; Xu, L. N.; Yin, C. Y.; Guo, Z. R.; Gu, N. *ACS Appl. Mater. Interfaces* **2014**, *6*, 3331-3340.

(67) Vigderman, L.; Zubarev, E. R. *Langmuir* **2012**, *28*, 9034-9040.

(68) Zhang, Q. F.; Zhou, Y. D.; Villarreal, E.; Lin, Y.; Zou, S. L.; Wang, H. *Nano Lett.* **2015**, *15*, 4161-4169.

(69) Zhang, Q. F.; Han, L. L.; Jing, H.; Blom, D. A.; Lin, Y.; Xin, H. L.; Wang, H. *ACS Nano* **2016**, *10*, 2960-2974.

(70) Ye, X. C.; Zheng, C.; Chen, J.; Gao, Y. Z.; Murray, C. B. *Nano Lett* **2013**, *13*, 765-771.

(71) Park, S.; Sinha, N.; Hamad-Schifferli, K. *Langmuir* **2010**, *26*, 13071-13075.

(72) Hore, M. J. A.; Ye, X. C.; Ford, J.; Gao, Y. Z.; Fei, J. Y.; Wu, Q.; Rowan, S. J.; Composto, R. J.; Murray, C. B.; Hammouda, B. Probing the Structure, Composition, and Spatial Distribution of Ligands on Gold Nanorods. *Nano Lett.* **2015**, *15*, 5730-5738.

(73) Lee, J. H.; Gibson, K. J.; Chen, G.; Weizmann, Y. *Nat. Commun.* **2015**, *6*, 7571.

(74) DuChene, J. S.; Niu, W. X.; Abendroth, J. M.; Sun, Q.; Zhao, W. B.; Huo, F. W.; Wei, W. D. Halide Anions as Shape-Directing Agents for Obtaining High-Quality Anisotropic Gold Nanostructures. *Chem. Mater.* **2013**, *25*, 1392-1399.

(75) Millstone, J. E.; Wei, W.; Jones, M. R.; Yoo, H. J.; Mirkin, C. A. Iodide Ions Control Seed-Mediated Growth of Anisotropic Gold Nanoparticles. *Nano Lett.* **2008**, *8*, 2526-2529.

(76) Pallares, R. M.; Su, X. D.; Lim, S. H.; Thanh, N. T. K. Fine-Tuning of Gold Nanorod Dimensions and Plasmonic Properties Using the Hofmeister Effects. *J. Mater. Chem. C* **2016**, *4*, 53-61.

(77) Nishimura, S.; Dao, A. T. N.; Mott, D.; Ebitani, K.; Maenosono, S. X-Ray Absorption Near-Edge Structure and X-ray Photoelectron Spectroscopy Studies of Interfacial Charge Transfer in Gold-Silver-Gold Double-Shell Nanoparticles. *J. Phys. Chem. C* **2012**, *116*, 4511-4516.

(78) Srnova-Sloufova, I.; Vlckova, B.; Bastl, Z.; Hasslett, T. L. Bimetallic (Ag)Au Nanoparticles Prepared by the Seed Growth Method: Two-Dimensional Assembling, Characterization by Energy Dispersive X-Ray Analysis, X-Ray Photoelectron Spectroscopy, and Surface Enhanced Raman Spectroscopy, and Proposed Mechanism of Growth. *Langmuir* **2004**, *20*, 3407-3415.

(79) Vigderman, L.; Zubarev, E. R. *Chem. Mater.* **2013**, *25*, 1450-1457.

(80) Xie, J. P.; Lee, J. Y.; Wang, D. I. C. *Chem. Mater.* **2007**, *19*, 2823-2830.

(81) Gao, C. B.; Hu, Y. X.; Wang, M. S.; Chi, M. F.; Yin, Y. D. *J. Am. Chem. Soc.* **2014**, *136*, 7474−7479.

(82) Park, K.; Vaia, R. A. *Adv. Mater.* **2008**, *20*, 3882-3886.

(83) Liu, K. K.; Tadepalli, S.; Tian, L. M.; Singamaneni, S. *Chem. Mater.* **2015**, *27*, 5261-5270.

(84) Xiong, W.; Sikdar, D.; Yap, L. W.; Premaratne, M.; Li, X. Y.; Cheng, W. L. *Nanoscale* **2015**, *7*, 3445-3452.

(85) Jing, H.; Zhang, Q. F.; Large, N.; Yu, C. M.; Blom, D. A.; Nordlander, P.; Wang, H. *Nano Lett.* **2014**, *14*, 3674-3682.

(86) Jiang, R. B.; Chen, H. J.; Shao, L.; Li, Q.; Wang, J. F. *Adv. Mater.* **2012**, *24*, OP200-OP207.

(87) Okuno, Y.; Nishioka, K.; Kiya, A.; Nakashima, N.; Ishibashi, A.; Niidome, Y. *Nanoscale* **2010**, *2*, 1489-1493.

(88) Jing, H.; Large, N.; Zhang, Q. F.; Wang, H. *J. Phys. Chem. C* **2014**, *118*, 19948-19963.

(89) Fang, C. H.; Lee, Y. H.; Shao, L.; Jiang, R. B.; Wang, J. F.; Xu, Q. H. *ACS Nano* **2013**, *7*, 9354-9365.

CHAPTER 9

Insights on Plasmon-Driven Oxidative Coupling of Thiophenol-Derivates: Evidence on Steady-State Active Oxygen Species

9.1 Introduction

Plasmonics is an emerging field that has profound impacts on energy storage and conversion, sub-wavelength light manipulation, plasmon-enhanced spectroscopic studies, photothermal cancer therapy, and ultrasensitive biomolecular sensing.[1-7] The excitation of collective oscillations of the surface electrons on metallic thin films or nanostructures is known as surface plasmon resonance (SPR). Surface plasmons can either be propagating, for example on the surface of metallic thin film, or localized, for example on the surface of a metallic nanostructure.[1] It has been recently observed that the surface plasmons supported by metallic nanostructures play a key role in guiding photo-chemical reactions, such as photochromic reactions,[8] photopolymerization,[9] oxidative dimerization of 4-aminothiophenol (4-ATP),[10,11] and reductive dimerization of 4-nitrothiophenol (4-NTP).[12] Moreover, some important catalytic reactions, such as ethylene epoxidation,[13-15] dissociation of H_2,[16] styrene hydrogenation,[17] and generation of H_2 via water-splitting,[5] were also found to be either induced or enhanced by the plasmon-driven hot carriers injection into the surface molecular adsorbates upon exposure to light excitation. The mechanisms of plasmon-driven photoreactions, however, still remain unclear and under intense debate.[6,18,19] Therefore, it is imperative to gain quantitative new insights into the reaction kinetics and underlying pathways of these plasmon-driven photoreactions to fully understand the obstacles that might limit the wide applications of plasmonic nanostructures as high-performance photocatalysts.

In Recent years, the peculiar role of active molecular O_2 in plasmonic heterogeneous photocatalysis has been proposed and investigated in some important catalytic oxidation reactions, such as, ethylene epoxidation,[4,13-15] CO oxidation,[13] NH_3 oxidation,[13] and

oxidative dimerization of 4-ATP.[10,11,20,21] Particularly, Linic and co-workers[4] demonstrated that plasmonic silver nanostructures with superior visible light absorption and scattering properties, can utilize concurrently photons and thermal energy to drive catalytic oxidation reactions at drastically lower temperatures comparing to those associated with conventional thermal processes. More importantly, they also found that energetic hot electrons, formed via the decay of surface plasmon resonance on illuminated silver nanoparticles, are transferred from the silver to adsorbed molecular O_2, allowing for activation of the O-O bond for oxidation of surface molecular adsorbates, for example, a commercially important epoxidation of ethylene to form ethylene oxide.[13] A steady-state reaction kinetics model was also proposed to support their experimental findings, that is, the steady-state rate of O_2 dissociation on plasmonic Ag nanostructures were measured as a function of temperature and illumination intensity under their experimental conditions.[22] Their work strongly impacted and stimulated the field of plasmonic photocatalysis, allowing one to better understand the underlying mechanisms of plasmonic photocatalysis, as well as the unique role of active molecular O_2 species in oxidative photocatalysis. Inspired by the above work, interesting work on studying the plasmon-driven photocatalytic reactions were continually reported to further unravel the real face of plasmonic photocatalysis.[6,21,23-29]

Our enthusiasm for plasmon-driven oxidative coupling of thiophenol-derivates stems from the unique combination of exceptional important industrial catalytic application with their intense, ultrasensitive, and finger-printing molecular Raman scattering signal when adsorbed on the surface of plasmonic metallic nanostructures. Taking the plasmon-driven oxidative coupling of 4-ATP as a model example.[10,11,30] The plasmon-driven

oxidative coupling of 4-ATP during the SERS measurement was first experimentally demonstrated by Huang and co-authors in 2010, unraveling an interesting scientific question of SERS on distinguishing between chemical enhancement mechanism and photochemical transformation.[10] The complicated mechanisms of this reaction were further explored in next a few years both experimentally and theoretically,[11,12,27,29,31-34] in which the effects of surroundings, especially the role of active molecular O_2 were proposed.[20,21] As schematically illustrated in Figure 9.1, we proposed a two-step reaction pathway to show how molecular O_2 was activated upon light excitation based on our understandings of previously published reports.[10,20,21,29] The first step is that hot electron-hole pairs are generated on the surface of metallic nanostructures via surface plasmon resonance decay upon light excitation. Secondly, surface physisorbed molecular O_2 was activated by the injection of energetic hot electrons into the lowest unoccupied molecular orbital (LUMO) of physisorbed molecular O_2, following by driving the oxidative coupling of 4-ATP into 4,4'-dimercaptoazobenzene (DMAB). While suitable energetic gap between the energy of hot electrons and LUMO of physisorbed molecular O_2 facilitates the hot electrons injection processes, it was found that the injection of hot electrons into LUMO of 4-ATP is unable to realize due to the large energetic gap, as shown in Figure 9.1. Therefore, it was reasonable that the molecular O_2 species are firstly activated upon receiving the hot electrons, then the active molecular O_2 will transfer the electrons to surface-adsorbed 4-ATP and induce the oxidative coupling into the formation of azobenzene compound. While the effect of O_2 species in this hot electrons driven oxidative coupling photoreaction were clearly explained,[20,21] it remains significant more challenging to elucidate the detailed mechanisms and reaction kinetics. A couple of key

questions concerning about the detailed mechanisms and reaction kinetics are still less explored and poorly understood: (1) What is the rate-limiting step and the reaction kinetics model? (2) What is the hot electron injection pathway: Landau damping or chemical interface damping? (3) What is the correlation between near electromagnetic field enhancement and reaction kinetics? (4) The entangled role of photothermal/thermal effect? (5) The molecular structure effect of 4-ATP on this reaction?

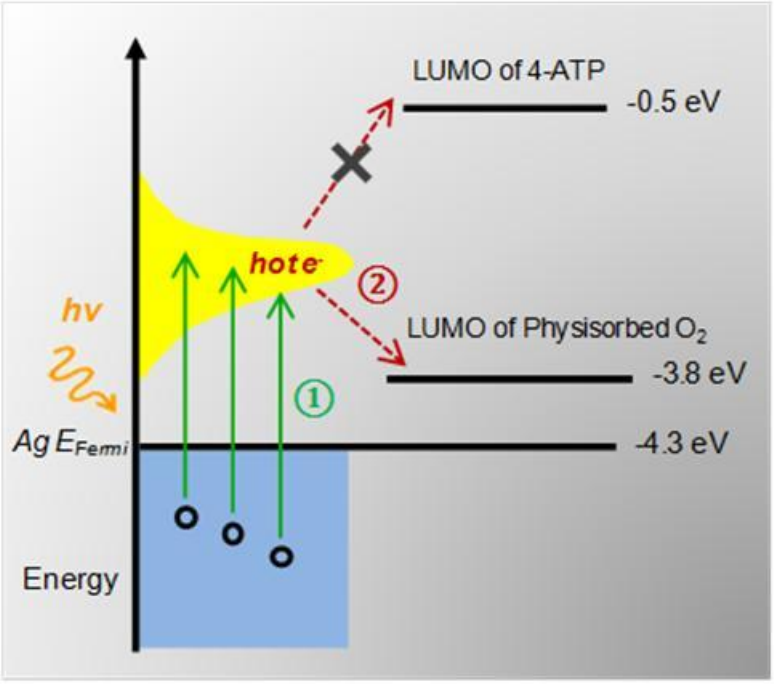

Figure 9.1. Schematic illustration of plasmon-driven activation of molecular oxygen species toward oxidative coupling of 4-ATP. 1st Step: The formation of hot electron-hole pairs induced by the surface plasmon resonance decay under light excitation. 2nd Step: Physisorbed oxygen molecules were activated by hot electron injection, following by driving the oxidative coupling of 4-ATP.

In this chapter, we chose the plasmon-driven oxidative coupling of 4-ATP as a model reaction to explore those challenging questions, that is, investigate the plasmonic and molecular effects on photoreaction kinetics and yield, using time-resolved SERS as an ultrasensitive spectroscopic tool with unique molecular finger-printing capabilities. A

unique three-dimensional hierarchical nanostructure composed of a SiO_2 bead decorated with Ag nanocubes (SiO_2@Ag nanocubes) was used as a plasmonically addressable substrate for SERS measurement. The time-resolved SERS measurement on one-particle-at-a-time enables us to quantitatively analyze the reaction kinetics of this photoreaction via building statistically distributions over a large amount of reaction trajectories. We further demonstrate that the reaction kinetics and yields of plasmon-driven oxidative coupling of thiophenol-derivates were sensitively dependent on the local electromagnetic field enhancement, surrounding accessible amount of oxygen species, molecular structure of thiophenol-derivates, thermal annealing, and photothermal processes. Moreover, a steady-state reaction kinetics model was proposed, that is, active molecular oxygen species is at steady state, to explain and support our experimental findings on the reaction kinetics as a function of laser power, concentration of oxygen gas, thiophenol-derivates with different molecular structures, and thermal/photothermal annealing. In addition, a concept of "pre-activating" of thiophenol-derivates was proposed to understand the reason why the reaction yield was varying when different reaction condition was employed.

9.2 Experimental Section

Chemicals and Materials. Ethylene glycol (EG) was obtained from VWR International. Poly(vinylpyrrolidone) (PVP58 with Mw~58000), and 4-aminothiophenol (C_6H_7NS, 4-ATP, 97%) were all obtained from Alfa Aesar. Silver trifluoroacetate (CF_3COOAg, ≥ 99.99%), sodium hydrosulfide hydrate ($NaHS \cdot xH_2O$), hydrochloric acid (HCl, 37% in water), poly(4-vinylpyridine) (PVP, Mw~60,000), poly(diallyldimethylammonium chloride) (PDDA, 20%, w/w in water, Mw=200,000-350,000), 4-

(dimethylamino)thiophenol ($C_8H_{11}NS$, 4-DMATP), and 4-Acetamidothiophenol (C8H9NOS, 4-AATP, 95%) were all purchased from Sigma-Aldrich. Silica beads (SiO_2) was obtained from nanoComposix. Hydrogen peroxide (H_2O_2, 30%), sulfuric acid (H_2SO_4, 96.10%), and ethanol (200 proof) were purchased from Fisher Scientific. Acetone was purchased from Honeywell. All reagents were used as received without further purification. Ultrapure water (18.2 MΩ resistivity, Barnstead EasyPure II 7138) was used for all experiments. Silicon wafers were obtained from University Wafers.

Synthesis of Ag Nanocubes. Ag nanocubes were synthesized following a previous protocol with minor modification.[35] In a typical procedure, 20 mL of EG was added into a 100 mL flask and preheated for 40 min under magnetic stir in an oil bath set to 150 ℃. Other reagents dissolved in EG were sequentially added into the flask using a pipette. 0.25 mL of NaHS solution (3 mM) was first added, and after 2 min 1.5 mL of HCl (3 mM) was added, followed by the addition of 5.0 mL of PVP58 (150 mg/mL). After another 2 min, 1.5 mL of CF_3COOAg solution (282 mM) was added. During the entire process, the flask was capped with a glass stopper except during the addition of reagents. The Ag nanocubes of ~ 30 nm edge lengths were obtained by quenching the reaction with an ice-water bath when the suspension had reached a brown color with a well-defined localized surface plasmon resonance peak at around 415 nm. After centrifugation and wash with acetone once and water twice, the Ag nanocubes were redispersed in 2 mL of EG for further use.

Synthesis of SiO_2@Ag Nanocubes Core-Satellite Particles. SiO_2@Ag nanocubes hybrid particles were prepared via a layer-by-layer assembly approach.[36] A colloidal suspension of SiO_2 beads (9.8 mg/mL water) was added to 1 mL of PDDA solution (1%).

After sonication for 30 min, the suspension was collected by centrifugation and washed three times with pure water. 0.1 mL of the as-prepared Ag nanocubes was then added to the SiO_2/PDDA nanocomposites under mechanical stirring for 1 h. The final product was centrifuged and then redispersed in pure water. During this process, Ag nanocubes were attached to the surface of the SiO_2/PDDA nanocomposites through electrostatic interactions. Then the products were removed from the solution by centrifugation. This process was repeated multiple times until the color of added Ag nanocubes no longer changed, indicating a saturating coverage of Ag nanocubes on the PDDA-functionalized SiO_2 beads.

Time-Resolved Single-Particle SERS Measurements. Sub-monolayer films of isolated SiO_2@Ag nanocubes hybrid particles were prepared by immobilizing the particles onto PVP (polyvinylpyridine)-functionalized silicon substrates.[37] In a typical procedure, silicon substrates were cleaned in a piranha solution (sulfuric acid : hydrogen peroxide, 7:3) for 15 min, and then immersed in a 1.0 % wt. of PVP ethanolic solution for 24 h. The silicon substrates were thoroughly rinsed with ethanol, dried with N_2 gas before use. SiO_2@Ag hybrid particles were incubated in 4-ATP ethanolic solution for overnight, and then washed with ethanol and water. Then the silicon substrate were immersed in an aqueous solution of SiO_2@Ag hybrid particles for 1 h. The silicon substrates were thoroughly rinsed with ethanol and dried with N_2 gas after they were removed from the solution of SiO_2@Ag hybrid particles.

Time-resolved SERS spectra were obtained on a Bayspec *Nomadic*^{TM} Raman microscopy built on an Olympus BX51 reflected optical system under 785 nm laser excitation in the confocal mode (focal area of 2 μm diameter). A 50× dark field objective

(NA=0.5, WD=10.6 mm, Olympus LMPLFLN-BD) was used for both Raman signal collection and dark field scattering imaging. The laser beam was focused on one particle each time for Raman spectrum collection. In a typical procedure, the laser power focused on the samples was measured to be 0.45 mW and the spectrum acquisition time was 2 s under condition. For the laser power-dependant experiments, we tested the samples under various laser powers. The gas atmosphere experiment were conducted by using pure oxygen gas, nitrogen gas, and their combination gas flow. The pre-thermal annealing experiments were carried out by incubating the SiO_2@Ag hybrid particles (sealed silicon substrates into a plastic tube) into water bath of 90 ^oC for 60 min. And then, the samples were measured after cooling down to room temperature. Normal Raman spectra were obtained on solid thin film of 4-ATP, 4-DMATP, and 4-AATP on silicon substrate, respectively.

Characterizations. The TEM images were obtained using a Hitachi H-8000 transmission electron microscope operated at an accelerating voltage of 200 kV. All samples for TEM measurements were dispersed in water and drop-dried on 300 mesh Formvar/carbon-coated Cu grids. SEM and EDS measurements were performed using a Zeiss Ultraplus thermal field emission scanning electron microscope. The samples for SEM and EDS measurements were dispersed in water and drop-dried on silicon wafers. The optical extinction spectra of the nanoparticles were measured on aqueous colloidal suspensions at room temperature using a Beckman Coulter Du 640 spectrophotometer. ζ-Potentials of colloidal nanoparticles were measured at room temperature using ZETASIZER nanoseries (Nano-ZS, Malvern). Raman spectra were obtained on a

Bayspec *Nomadic*^{TM} Raman microscopy built on an Olympus BX51 microscope equipped with a 785 nm CW diode laser.

Reaction Kinetics and Percentage Analysis. To quantitatively analyze the kinetic data, we used the ratio between the SERS intensities of 1440 cm^{-1} Raman mode (N=N stretching mode of DMAB) and 1078 cm^{-1} Raman mode (C-S stretching mode of both 4-ATP and DMAB) as being representative of product grow kinetics, which can be described as: $Y=I_{1440(experiment)}/I_{1078(experiment)}$. Because the C-S stretching mode during the photoreaction process actually included two part of contributions: one is from 4-ATP, another one is from DMAB, so it is very difficult for us to separate them from the experimental Raman spectra (1078 cm^{-1} for 4-ATP, 1072 cm^{-1} for DMAB). To address this problem, we calculated the ratio between I_{1078} of 4-ATP (in nitrogen gas) and I_{1072} of DMAB (4-ATP in oxygen gas) under 785 nm laser of same laser power of 0.90 mW. The results can be marked as $X=I_{1078(ATP)}/I_{1072(DMAB)}$, and then we were able to obtain the values of X for three different molecules: $X_{4\text{-}ATP}=0.40\pm0.02$, $X_{4\text{-}DMATP}=0.24\pm0.02$, $X_{4\text{-}AATP}=0.75\pm0.03$. The variable X values for different molecule is probably due to their significant difference in Raman scattering cross-sections.

We further calculated the value of I_{1440}/I_{1078} in pure DMAB, which are available from our experimental data and also previously published reports,[10] in which the value was determined to be I_{1440}/I_{1078} (DMAB) $=1.07\pm0.05$. By taking into account the above results, we were able to calculate the fraction of product DMAB (θ_{DMAB}) using the following equations:

$$Y=\frac{I_{1440(\text{experiment})}}{I_{1078(\text{experiment})}}=\frac{I_{1440(DMAB)}\times\theta_{DMAB}}{I_{1078(DMAB)}\times\theta_{DMAB}+I_{1078(DMAB)}\times X_{ATP}\times(1-\theta_{DMAB})}=\frac{I_{1440(DMAB)}}{I_{1078(DMAB)}}\times\frac{\theta_{DMAB}}{\theta_{DMAB}+X_{ATP}\times(1-\theta_{DMAB})}$$

So for 4-ATP,

$$Y_{4-ATP}=\frac{I_{1440(experiment)}}{I_{1078(experiment)}}=1.07\times\frac{\theta_{DMAB}}{\theta_{DMAB}+0.40\times(1-\theta_{DMAB})}$$

Then,

$$\theta_{DMAB}=\frac{0.40\times Y_{4-ATP}}{1.07-0.60\times Y_{4-ATP}}$$

For 4-DMATP,

$$Y_{4-DMATP}=\frac{I_{1440(experiment)}}{I_{1078(experiment)}}=1.07\times\frac{\theta_{DMAB}}{\theta_{DMAB}+0.24\times(1-\theta_{DMAB})}$$

$$\theta_{DMAB}=\frac{0.24\times Y_{4-DMATP}}{1.07-0.76\times Y_{4-DMATP}}$$

For 4-AATP,

$$Y_{4-AATP}=\frac{I_{1440(experiment)}}{I_{1078(experiment)}}=1.07\times\frac{\theta_{DMAB}}{\theta_{DMAB}+0.75\times(1-\theta_{DMAB})}$$

$$\theta_{DMAB}=\frac{0.75\times Y_{4-DMATP}}{1.07-0.25\times Y_{4-DMATP}}$$

We experimentally collected the Y values from time resolved SERS spectra during the reaction process, then the fraction of product DMAB (θ_{DMAB}) can be calculated using the above equations. We further plotted the fraction of product DMAB (θ_{DMAB}) verse the reaction time (t) for each individual reaction trajectory (one trajectory on one particle at one time). The rate constant (k) and reaction percentage ($\theta_{t=\infty}$) for each individual trajectory can be obtained by fitting the reaction trajectory using the following rate equation:

$$\theta_{DMAB}=\theta_{t=\infty}\times(1-e^{-kt})$$

Then we plotted the rate constant (k) and reaction percentage ($\theta_{t=\infty}$) versus the initial peak intensities at 1078 cm^{-1} (C-S stretching mode of 4-ATP) on the excitation of 785 nm laser with various laser powers.

9.3 Results and Discussions

A layer-by-layer (LBL) assembly approach was developed for the fabrication of the SiO_2@Ag nanocubes core-satellites hybrid nanostructure. As schematically illustrated in Figure 9.2A, the SiO_2@Ag nanocubes hybrid particles were prepared through a stepwise LBL process. SiO_2 beads of uniform size (~ 1 ± 0.1 μm) are used as the core on which Ag nanocubes (~ 30 ± 3.2 nm), enclosed exclusively by 6 low-index {100} facets,[35] are assembled electrostatically. The surfaces of the initial SiO_2 beads, which are terminated by carboxyl group, are negatively charged at neutral and basic pHs. A thin layer of polydiallyldimethylammonium chloride (PDDA) is then adsorbed onto the SiO_2 surface to generate a positively charged particle surface. Since the Ag nanocubes are negatively charged, they can be attached onto the PDDA-functionalized SiO_2 beads through electrostatic interactions. The mechanism of this LBL assembly process can be clearly seen from the evolution of the ζ-potentials. We further used a combination of scanning electron microscopy (SEM), transmission electron microscopy (TEM), energy-dispersive spectroscopy (EDS), and UV-Vis spectroscopy to fully characterize the SiO_2@Ag nanocubes hybrid particles. As shown in Figure 9.2B, the SEM images clearly show that each individual SiO_2 bead was almost fully packed by monolayer or up to several layers of Ag nanocubes. EDS-elemental mapping images of individual SiO_2@Ag nanocubes hybrid particle further demonstrated the 3D core-satellites hybrid nanostructure (Figure 9.2C). Close-packing of Ag nanocubes with ultra small interparticle gaps on the surface

of SiO_2 bead were clearly observed in the high-magnification TEM images (Figure 9.2D), showing our capability of producing high density of "hot-spots" on individual bead for single particle SERS measurement. The strong SERS signal is also essentially relied on the optical properties of the assembled Ag nanocubes, including not only the enhanced plasmonic coupling, but also the specific extinction peak and range. Figure 9.2E shows the optical extinction spectra of SiO_2 beads, Ag nanocubes, and SiO_2@Ag nanocubes hybrid particle. While no obvious extinction peak were observed for SiO_2 beads, Ag nanocubes exhibited a strong plasmonic peak located at ~415 nm and a tiny peak at ~354 nm, which is in line with previous report.[35] Large red shifts and significant broadening of plasmon bands were observed when Ag nanocubes were assembled onto the surface of SiO_2 beads. The strong optical extinction in the visible and near IR range allows us to use SiO_2@Ag nanocubes hybrid particle as a robust SERS substrate at 785 nm laser excitation, as well as a potential plasmonic photocatalyst under visible light irradiation. The plasmon coupling between the neighboring Ag nanocubes leads to the formation of plasmon "hot-spots" in the interparticle gaps where the local electromagnetic fields are drastically enhanced upon plasmonic excitation in the near-IR.[1] This LBL self assembly approach allows us to fine-control the Ag nanocube coverage on each SiO_2 bead, providing a unique way to tune the density, size, and intensity of the plasmon "hot-spots" on the particle surfaces. Overall, this method provides a robust way to fabricate uniform 3D core-satellites nanostructures with extremely strong plasmonic properties that are highly desirable for SERS and plasmonic photocatalysis.

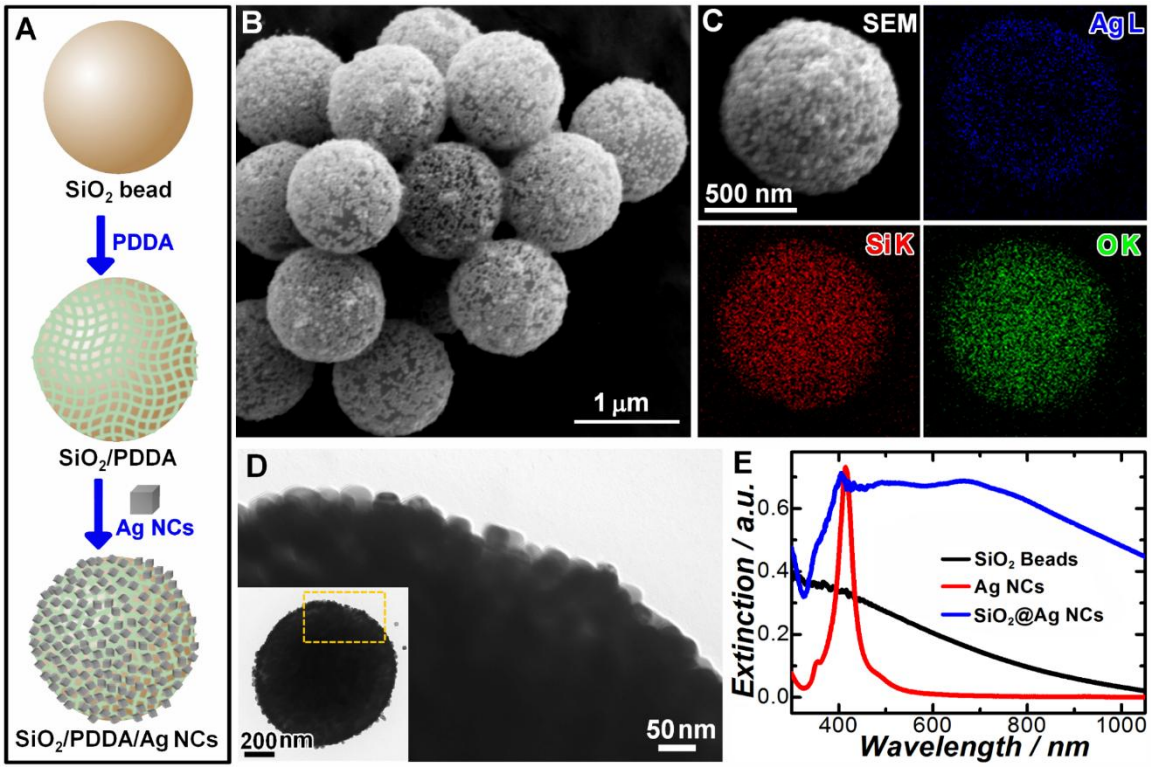

Figure 9.2. (A) Schematic illustration of the fabrication of SiO_2/Ag nanocubes hybrid structures. (B) SEM image of SiO_2/Ag nanocubes hybrid particles. (C) SEM image of an individual SiO_2/Ag nanocubes hybrid particle and the corresponding elemental mapping images of Ag-L, O-K, and Si-K. (D) High-magnification TEM image of the assembled Ag nanocubes on the surface of SiO_2 bead, which was magnified from the TEM image of an individual SiO_2/Ag nanocubes hybrid particle in the inset. (E) Experimental extinction spectra of SiO_2 beads, Ag nanocubes, and SiO_2/Ag nanocubes hybrid particles.

We used time-resolved SERS to monitor the plasmon-driven oxidative coupling of 4-ATP into DMAB that are adsorbed on the surface of SiO_2@Ag nanocubes hybrid particle. To form a self-assembled monolayer of 4-ATP on the nanoparticle surfaces, SiO_2@Ag nanocubes hybrid particles were first immersed in 4-ATP solution, then separated from the mixture by centrifugation, and finally dried on silicon substrates for SERS measurements. Well-dispersed sub-monolayer of SiO_2@Ag nanocubes particle were observed on the surface of silicon substrate, which is used for building the experimental setup for ambient single-particle SERS measurement at room temperature. The confocal

Raman microscope setup with a laser focal plane ~2 μm × 2 μm in size and an effective excitation volume of ~1.0 × 10^{-16} m^3, when combined with the sub-monolayer particle substrate geometry, allows us to collect SERS trajectories one-particle-at-a-time and subsequently build statistics on the reaction kinetics by analyzing the ensemble of large numbers of trajectories. The oxidative photoreaction was initiated upon exposure of the 4-ATP-coated SiO_2@Ag particle to 785 nm laser in ambient air at room temperature. As schematically illustrated in Figure 9.3A, 4-ATP are firstly oxidized and then formed azobenzene dimers on the Ag surface, named as DMAB. Figure 9.3B,C show SERS spectra of 4-ATP monolayer molecules adsorbed on individual SiO_2@Ag hybrid particle at various reaction times upon the excitation of 785 nm laser of 0.45 mW. The Raman bands at 1078, and 1595 cm^{-1} mode are assigned to the reactant (4-ATP), and the characteristic Raman bands at 1072, 1142, 1390, 1440, and 1575 cm^{-1} are assigned to the newly forming product (DMAB).[10,21] Once the photoreaction started, the intensities of 1595 cm^{-1} Raman bands of 4-ATP were observed to decrease progressively with the concomitant emergence of new bands corresponding to the N-N stretching modes of DMAB at 1390 and 1440 cm^{-1}. Meanwhile, the C-S stretching mode of 4-ATP at 1078 cm^{-1} gradually downshifted to 1072 cm^{-1} (C-S stretching mode of DMAB) with the concomitant significant enhanced of Raman intensities which might due to the large difference of Raman scattering cross section between 4-ATP and DMAB.[10,21,29]

The ratios between Raman modes at 1440 cm^{-1} (N-N stretching mode of DMAB) and 1078 cm^{-1} (C-S stretching mode of 4-ATP and DMAB) modes were used as being representative of product grow kinetics to quantify the fraction of DMAB (θ_{DMAB}), as a function of reaction time (t). As shown in Figure 9.3D, we plotted the trajectories of

θ_{DMAB} as a function of reaction time (t) under 785 nm laser of 0.45 mW. This photoreaction kinetics followed first order kinetics very well when single exponential reaction kinetics equation was used to fit the kinetic curves. The first order rate constant k were obtained by performing least-squares curve fitting to the $\theta_{DMAB}(t)$ trajectories using the following rate equation:

$$\theta_{DMAB} = \theta_{t=\infty} \times (1 - e^{-kt}) \qquad (1),$$

The reaction percentage, marked as $\theta_{t=\infty,}$ can be also obtained from the curve-fitting, showing the variable reaction percentages from different individual reaction trajectories. We then systematically collected the time-resolved SERS spectra on 10 different individual particles under same condition to build the statistical distribution, as shown in Figure 9.3E. Variable rate constant (k) and reaction percentage ($\theta_{t=\infty}$) from the curve fitting on each $\theta_{DMAB}(t)$ trajectories were obtained under same experimental conditions, enabling us to build the reliable statistical analysis in consideration of the deviation of the coverage of Ag nanocubes and 4-ATP molecules on different SiO_2@Ag nanocubes particles. Because of the excellent fitting of experimental trajectories using single exponential kinetic equation, we proposed that the active molecular O_2 is at steady state and the activation of 4-ATP is the rate-limiting step in comparison to the dimerization of two 4-ATP molecules into one DMAB molecule in this photoreaction. To further clarify that, we firstly expressed this reaction as a two-step photochemical reaction:

1) $O_2^{ad} + h\nu \underset{k_{-1}}{\overset{k_1}{\rightleftarrows}} O_2^-$

2) $O_2^- + 4\text{-ATP} \xrightarrow{k_2} \text{TI}^* \xrightarrow{fast} 1/2\text{DMAB}$ (TI*: Transient Intermediate)

The first step is the injection of energetic hot electrons from Ag to adsorbed molecular O_2 on light excitation, which is a ultrafast step, typically at ~*fs* time level,[19] so we used k_1 to define the formation kinetics of active molecular O_2. On the other hand, we assumed the first step is reversible, which means the active molecular O_2 might transfer electrons back to Ag in some cases, so k_{-1} was used to define the decay kinetics of active molecular O_2. Because we proposed that active molecular O_2 is at steady state, so the value of k_1/k_{-1} and concentration of active molecular O_2 are constants when the experimental conditions are fixed, such as, laser power, the near electromagnetic field enhancement, and concentration of surrounding molecular O_2 (gas phase). The second step is the oxidative coupling of 4-ATP induced by surface active molecular O_2, which is much slower than the first step because multiple molecular bond breaking and forming are involved in this complicated molecular dimerization. In addition, both previous reports[10,12,33] and our time-resolved SERS data demonstrated that the second step can be monitored by time-resolved SERS measurement, which is obviously at ~ms to ~s time level, strongly indicating that the second step is the rate-limiting step. We were able to identify and track the reactant, intermediates, and product during the photoreaction process using SERS as an ultrasensitive spectroscopic tool with unique time-resolving and molecular finger-printing capabilities. While unknown transient intermediates (TI*) might be involved during the second step, it won't have any effect on the reaction kinetics because no clear and stable transient intermediate can be observed during our time-resolved SERS measurement, indicating the lifetime of transient intermediate might be too short to be detected under our experimental conditions. Therefore, we used k_2 to reveal the reaction kinetics of oxidative coupling of 4-ATP, which can be described as first order reaction

model because the concentration of active molecular O_2 is a constant at steady state and the activation of 4-ATP is the rate-limiting step.

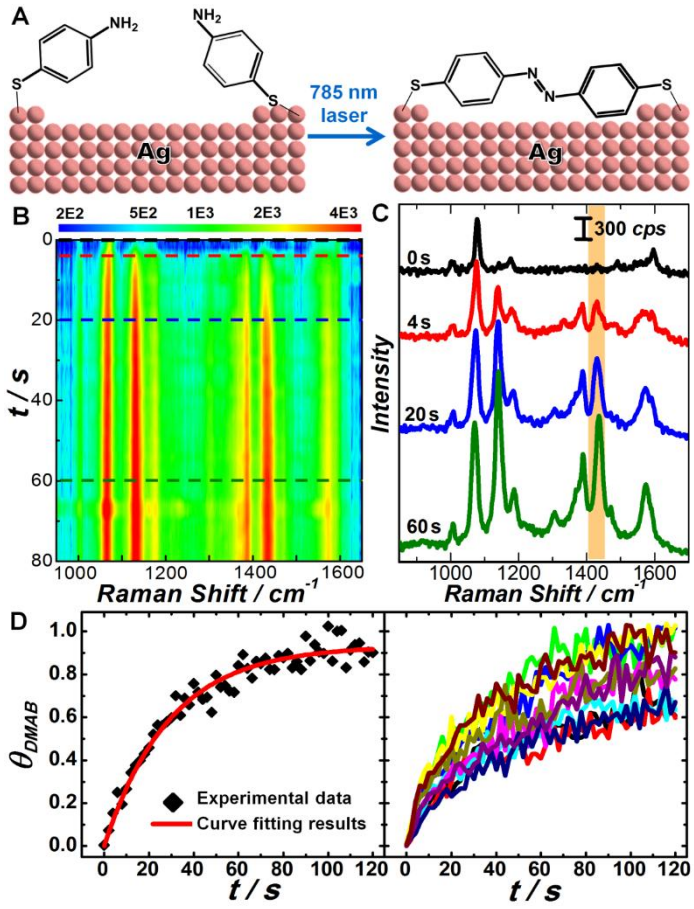

Figure 9.3. (A) Schematic illustration of plasmon-driven oxidative coupling of 4-ATP adsorbed on the surfaces of Ag nanocubes under 785 nm laser excitation. (B) Two-dimensional colored code intensity map of time-resolved SERS spectra collected from 4-ATP molecules adsorbed on the surfaces of Ag nanocubes at different reaction times upon exposure to 785 nm laser. (C) Representative SERS spectra collected at reaction times of 0, 4, 20, and 60 s. The 1440 cm^{-1} Raman band was highlighted for showing the evolution process of SERS spectral line-shape as a function of time. (D-E) A trajectory (D), and all trajectories (E) of fraction of product (θ_{DMAB}) as a function of reaction time (t) under 785 nm laser of 0.45 mW excitation. The acquisition time for each spectra was 2 s. The results of least-squares curve fitting are shown as solid curve in panel D.

According the two-step photoreaction model and the above discussions, the kinetics model of this reaction can be mathematically described as following:

$$\frac{d[O_2^-]}{dt} = k_1[O_2^{ad}] - k_{-1}[O_2^-] - k_2[O_2^-][4-ATP] \quad (2),$$

$$\frac{d[DMAB]}{dt} = k_2[O_2^-][4-ATP] \quad (3),$$

Because the active molecular O_2 is at steady state (ss), so: $\frac{d[O_2^-]_{ss}}{dt} = 0$ (4),

$$\frac{d[O_2^-]_{ss}}{dt} = k_1[O_2^{ad}] - k_{-1}[O_2^-]_{ss} - k_2[O_2^-]_{ss}[4-ATP] = 0 \quad (5),$$

The concentration of active molecular O_2 at steady state can be obtained via calculation and also according to the relationship between k_1, k_{-1} , and k_2, $k_1 >> k_2$, $k_{-1} >> k_2$, so:

$$[O_2^-]_{ss} = \frac{k_1[O_2^{ad}]}{k_{-1} + k_2[ATP]} \approx \frac{k_1}{k_{-1}}[O_2^{ad}] \quad (6),$$

Then the formation kinetics of DMAB can be expressed as:

$$\frac{d[DMAB]}{dt} = k_2[O_2^-]_{ss}[4-ATP] = k_2\frac{k_1}{k_{-1}}[O_2^{ad}][4-ATP] \quad (7),$$

Then we correlated this rate constant equation with our experimental kinetics data to obtain the equation of experimentally defined rate constant *k*, more details about the experimental kinetics analysis were discussed in Supporting Information and will be also discussed later. The rate constant *k* we obtained from experimental trajectory fitting can be described as equation (8), and then we can obtain *k* via inputting *k* of equation (8) into the equation (7):

$$\frac{d[DMAB]}{dt} = k[4-ATP] \quad (8),$$

$$k = k_2[O_2^-]_{ss} = k_2 \frac{k_1}{k_{-1}}[O_2^{ad}] \quad (9),$$

According to the equation (9), the experimentally defined rate constant k was affected by a couple of variables, such as, k_1, k_{-1}, $[O_2^{ad}]$, and k_2. This as-discussed reaction model is based on our initial proposal that active molecular O_2 is at steady state, so we will be able to further demonstrate our idea by providing more experimental evidence to test this reaction kinetic model later on. Therefore, we aim to use the plasmon-driven oxidative coupling of thiophenol-derivates as model reactions to explore the effects of near electromagnetic field enhancement (k_1), concentration of surrounding O_2 gas molecules ($[O_2^{ad}]$), molecular structure of ATP (k_2), thermal annealing (k_2), and photothermal processes (k_2), on the plasmon-driven photoreaction kinetics and yield.

We systematically investigated the effect of laser power on this photoreaction without modifying other experimental conditions. Increasing the laser power means that the density of photons will be increased in per unit area, which will significantly improve the concentration of the active molecular O_2 because the probability in forming active molecular O_2 is fixed when the energy of incident light is unchanging. The increase in laser power will also give rise to the modulation of local electromagnetic field enhancement, expressed as E/E_0, which is because of the correlation between laser power P and local electromagnetic field E is $P \propto \mathcal{E}E^2$. Thus, when laser power is changing, the synergy between variable density of incident photons and tunable local electromagnetic field enhancement will dramatically affect the photoreaction kinetics via modulating the rate constant k_1 for the formation of active molecular O_2. We performed the time-resolved SERS measurements under excitation at a series of different laser power to build the

correlation between the excitation laser power and reaction kinetics and yield. Figure 9.4A,B show plots of rate constant (k) and reaction yield ($\theta_{t=\infty}$) as a function of the initial Raman peak intensities at 1078 cm^{-1} of 4-ATP (I_{1078}) on the excitation of 785 nm laser with various laser powers of 0.21, 0.32, 0.45, 0.56, and 0.90 mW. To better address the underlying meaning of the as-plotted figures (Figure 9.4A,B), we plotted the ensemble-averaged Raman peak intensities at 1078 cm^{-1} of 4-ATP (I_{1078}) as a function of laser power square, as shown in the inset of Figure 9.4C. Interestingly, well-fitted linear relationship between I_{1078} and laser power square was observed, when combined with the linear relationship between laser power and $(E/E_0)^2$, further demonstrating that the correlation between I_{1078} and near field enhancement E/E_0 is that, $I_{1078} \propto (E/E_0)^4$. Thus, we tactfully employed the initial Raman peak intensities of 4-ATP (I_{1078}) to quantify the near field enhancement E/E_0 instead of laser power, clearly showing the correlation between rate constant (k) and near field enhancement (E/E_0) (Figure 9.4A).

Remarkably, we observed very good linear relationship between k and I_{1078} at relatively low laser power, and the super linear deviation start to dominate at relatively high laser power, as shown in Figure 9.4A. As previously demonstrated, the Raman peak intensities is proportional to the fourth power of near field enhancement ($(E/E_0)^4$), that is, $I_{1078} \propto (E/E_0)^4$. Therefore, linear correlation between k and I_{1078} from our experimental results strongly indicating that the relationship between rate constant (k) and near field enhancement $(E/E0)^4$ is $k \propto (E/E_0)^4$. The as-demonstrated well-fitted linear correlation between k and $(E/E_0)^4$ provide us an unique opportunity to explore the mechanism of plasmonic hot electron injection pathway that involved in this photoreaction. Two main mechanisms on plasmonic hot electron excitation were widely known currently: indirect,

and direct hot electron injection.[19,28,38] The indirect process, which is also known as Landau damping, that is, the energetic hot electrons formed by plasmonic decay generate an wide energy distribution within the metal nanostructure, then hot electrons with suitable energetic gap can scatter into nearby adsorbate molecular orbitals. On the other hand, the direct process is known as chemical interface damping, during which the hot electrons are directly injected into unoccupied molecular orbitals of nearby adsorbate with suitable energetic gaps. A key difference between this two mechanisms is the correlation between rate constant k and near field enhancement E/E_0, which will allow us to experimentally distinguish these two mechanisms though the underlying mechanisms might be much more complicated. $k \propto (E/E_0)^4$ is found to be Landau damping, and $k \propto (E/E_0)^2$ is verified as chemical interface damping due to their different photon absorption and scattering processes. Therefore, while the mechanism of the hot electron injection process on excited plasmonic nanostructures are still unclear and poorly understood, our experimental results strongly demonstrated that this photoreaction is driven by Landau damping rather than chemical interface damping because direct chemical interface damping typically show the linear correlation between rate constant (k) and $(E/E_0)^2$. In addition, we also proposed that the super linear deviation of k from linear relationship might due to the significant enhanced photothermal effect at relatively high laser power, which will be discussed in great details later.

On the other hand, the reaction yield ($\theta_{t=\infty}$) increases at first beginning and then reaches at an equilibrium when laser power increases to be around 0.56 mW, as shown in Figure 9.4B. While tunable photochemical transformation from 4-ATP to DMAB under different laser power excitation condition has been previously observed,[39] the reason why

the photoreaction yield is laser power-dependent is still unclear because the laser power can only modify the density of incident photons rather than the energy of incident photons. Based on our reaction model, changing laser power will just affect the reaction kinetics except for there are other side effects from changing laser power, such as enhanced photothermal effect. Very recently, Takeyasu and co-authors reported that a threshold value of laser power was observed for the photoreaction of 4-ATP to be initiated, which is in line with our experimental findings partially, however, none of detailed mechanism were further discussed.[40] Our understanding on this question is that the laser power dependent photothermal effect will induce the local heating near the surrounding of the adsorbed molecular 4-ATP, and further pre-activate 4-ATP toward accepting hot electrons and then oxidation coupling. Thus, more and more adsorbed molecular 4-ATP can overcome the energy barrier and be pre-activated by photothermal effect as the laser power increase, resulting in the increase of reaction yield. More evidence on pre-activating of adsorbed molecular 4-ATP by thermal and photothermal effect will be discussed later. Moreover, we also demonstrated that photochemical transformation from 4-ATP to DMAB is irreversible via tuning the laser power during the photoreaction. While all the peak intensities decreased when the laser power is decreasing during the photoreaction process, almost identical line shape of SERS spectra were observed before and after changing laser power, indicating the irreversible photoreaction under our current experimental conditions, which also agrees with previously published reports.[40]

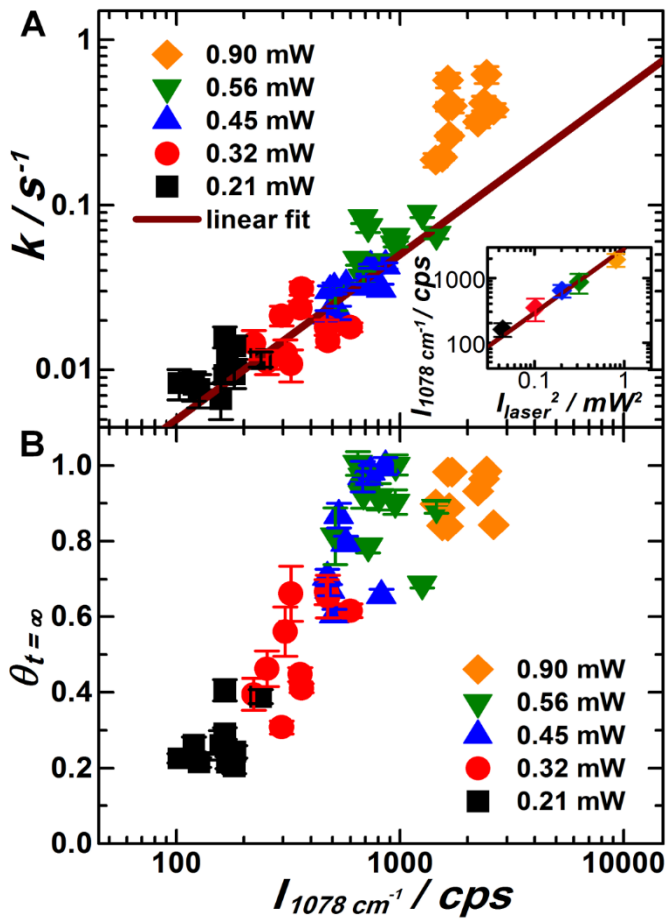

Figure 9.4. Effect of laser power on plasmon-driven oxidative coupling of 4-ATP. (A-B) Plots of (A) rate constant (k), and (B) reaction yield ($\theta_{t=\infty}$) versus the initial SERS peak intensities at 1078 cm^{-1} (4-ATP) on the excitation of 785 nm laser with various laser power of 0.21, 0.32, 0.45, 0.56, and 0.90 mW. Inset: plots of the ensemble averaged initial SERS peak intensities at 1078 cm^{-1} (4-ATP) as a function of laser power square on the excitation of 785 nm laser with various laser power of 0.21, 0.32, 0.45, 0.56, and 0.90 mW. The results of linear fitting are shown as solid curves in panel A and the inset.

We correlated the laser power experiment with the rate constant equation according to the proposed reaction kinetics model. Basically, the near electromagnetic field enhancement is modulated by changing the laser power, which will also affect the amount of active molecular O_2 at steady state. Therefore, the laser power experiment provides us an unique opportunity to modulate the activation of surface molecular O_2, in which k_1 is modulated. Other ways to modulate the near field enhancement includes

varying the coverage of Ag nanocubes on the SiO_2 surfaces, that is, tuning the interparticle gaps between Ag nanocubes, and so on. Therefore, tuning the near electromagnetic field enhancement represents an unique way to tune the kinetics of plasmon-driven oxidative coupling reaction via modulating the concentration of active molecular O_2 at steady state.

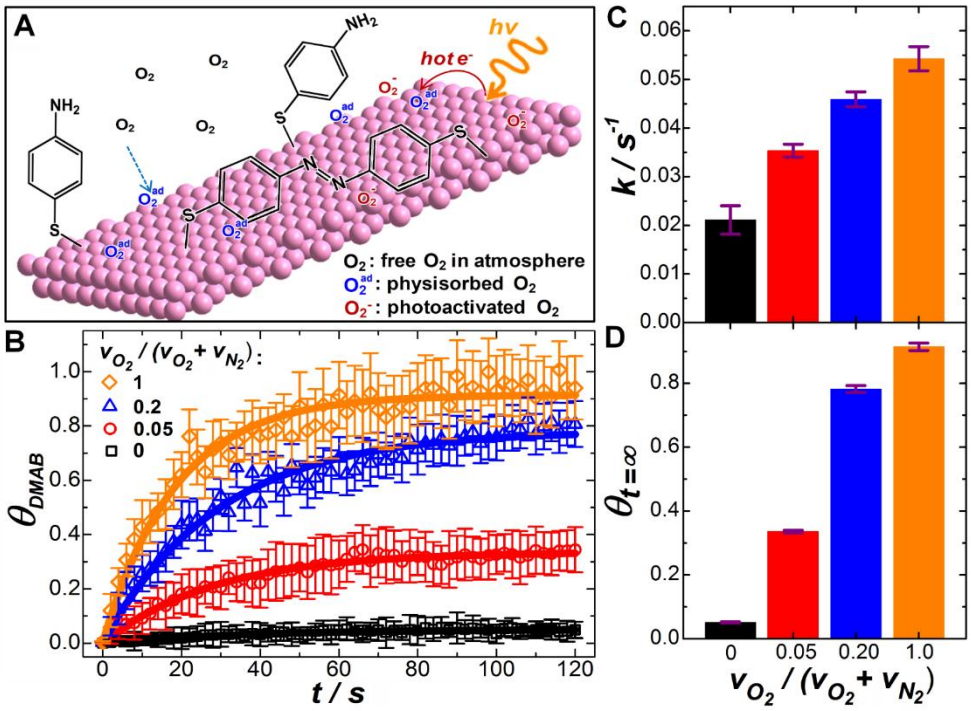

Figure 9.5. Effect of concentration of oxygen gas on plasmon-driven oxidative coupling of 4-ATP. (A) Schematic illustration of the roles of oxygen species during plasmon-driven oxidative coupling of 4-ATP at 785 nm laser excitation. (B) Fraction of product (θ_{DMAB}) as a function of reaction time (t) under 785 nm laser of 0.45 mW in the presence of varying gas atmosphere: 0%, 5%, 20%, and 100% of oxygen gas. The acquisition time for each time-resolved SERS spectra was 2 s. The results of least-squares fitting are shown as solid curves in panel B. (C-D) Comparison of rate constant (k) and reaction yield ($\theta_{t=\infty}$) among in the presence of different volume ratios of oxygen gas.

Another way to modulate the concentration of steady-state active molecular O_2 is to vary the concentration of O_2 gas in the surrounding of reaction according to the rate constant equation. As schematically illustrating in Figure 9.5A, O_2 in gas phase will

affect the photoreaction via firstly adsorbing onto the surface of Ag nanocubes, and then being activated by the injection of hot electrons, followed by oxidizing the 4-ATP to form DMAB. While the concentration of adsorbed molecular O_2 in the rate constant equation is different from the concentration of O_2 gas in our experiments, the reaction kinetics model are still applicable because the adsorption of O_2 onto the surface of Ag nanocubes is a very fast step comparing to the photoreaction process under our current experimental conditions, and the corresponding adsorption kinetics can be ignored in this case. Therefore, we used the gas flow system with variable O_2 concentrations to investigate the effect of O_2 on this photoreaction. As shown in Figure 9.5B-D, both the rate constant *k* and reaction yield $\theta_{t=\infty}$ increase as the concentration of O_2 gas increases. The change of *k*, responding to the variable O_2 concentration, can be explained using the proposed rate constant equation: varying the concentration of O_2 gas will change the concentration of active molecular O_2 at steady state, and further affect the rate constant *k*. On the other hand, the increase in reaction yield $\theta_{t=\infty}$ can be explained using the concept of pre-activating of adsorbed molecular 4-ATP: higher concentration of O_2 gas will facilitate the activation of adsorbed molecular 4-ATP toward acceptance of hot electrons. Tiny DMAB were also observed when the concentration of O_2 gas was 0%, which might be attributed to the surface pre-adsorbed O_2 species that were not totally removed before the photoreaction was initiated.[21] More importantly, the reaction trajectories under different concentration of O_2 gas was also well-fitted by using the first order rate equation, strongly supporting our first order reaction kinetics model. While the essential role of O_2 in this reaction has been previously demonstrated,[20,21] our experimental findings provide

more quantitative and strong evidence on the peculiar role of steady state active molecular O_2 in this plasmon-driven oxidative coupling reaction of 4-ATP.

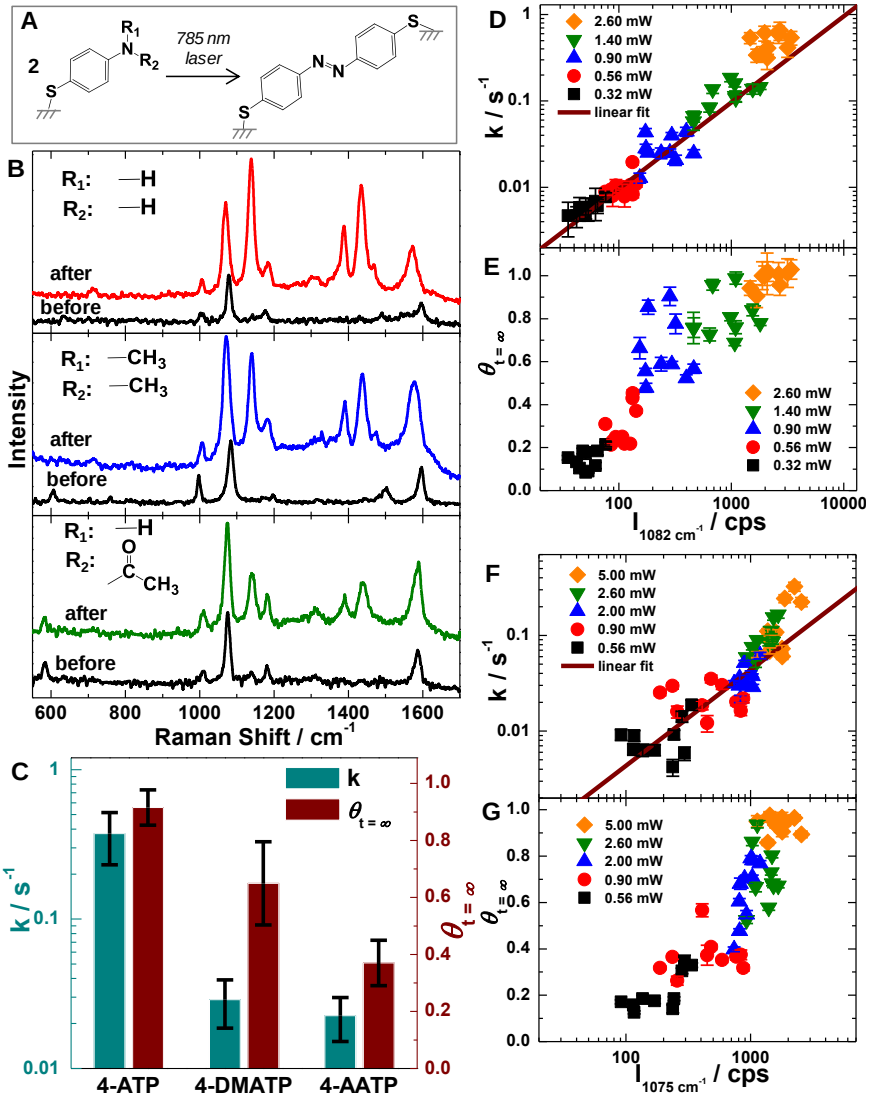

Figure 9.6. Effect of molecular structure on plasmon-driven oxidative coupling of thiophenol-derivates. (A) Schematic illustration of the plasmon-driven oxidative coupling of thiophenol-derivates at 785 nm laser excitation. (B) SERS spectra of 4-ATP, 4-DMATP, and 4-AATP before and after the oxidative coupling reaction under 785 nm laser of 0.90 mW excitation. The spectra acquisition time was 1 s for 4-ATP, and 2 s for 4-DMATP and 4-AATP, respectively. (C) Comparison of rate constant (k) and reaction yield ($\theta_{t=\infty}$) among different molecules as marked in the figure under 785 nm laser of 0.90 mW excitation. (D-E) Plots of (D) rate constant (k), and (E) reaction yield ($\theta_{t=\infty}$) versus the initial peak intensities at 1082 cm^{-1} (4-DMATP) on the excitation of 785 nm laser with various laser power of 0.32, 0.56, 0.90, 1.40, and 2.60 mW. (F-G) Plots of (F) rate constant (k), and (G) reaction yield ($\theta_{t=\infty}$) versus the initial peak intensities at 1075 cm^{-1} (4-AATP) on the excitation of 785 nm laser with various laser power of 0.56, 0.90, 2.00, 2.60, and 5.00 mW. The results of linear fitting are shown as solid curves.

We further investigated the effect of molecular strucutre on the plasmon-driven oxidative coupling of thiophenol-derivates (4-ATP is one of the examples). As schematically illustrating in Figure 9.6A, thiophenol-derivates with two different molecular group (marked as R_1 and R_2) that attached to the N atom might undergo plasmon-driven oxidative coupling to form DMAB on the surface of Ag nanocubes upon exposure to 785 nm laser. We chose three thiophenol-derivates with various R_1 and R_2, includes 4-ATP (R_1: H, and R_2: H), 4-(dimethylamino)thiophenol (4-DMATP, R_1: CH_3, and R_2: CH_3), 4-Acetamidothiophenol (4-AATP, R_1: H, and R_2: $COCH_3$), to study the effect of molecular structure on both reaction kinetics and yield. Interestingly, we observed that plasmon-driven oxidative coupling of both 4-DMATP and 4-AATP into DMAB were also feasible though the significant difference in molecular strucutre of 4-DMATP and 4-AATP in comparison to 4-ATP. Although similar reaction mechanism and pathway was observed for these three molecules, the reactivity toward oxidative coupling is drastically different. We conducted the photoreaction on these three molecules under identical experimental conditions, especially on the excitation of 785 nm laser with same laser power of 0.90 mW. As shown in Figure 6B, 4-ATP with two H groups exhibited the highest reaction yield among these three molecules, and 4-DMATP showed higher reaction yield and 4-AATP. To more quantitatively compare the reaction kinetics and yield, we used the as-proposed single exponential rate constant equation to obtain the rate constant k and reaction yield $\theta_{t=\infty}$ via fitting each reaction trajectories, which also showed very high quality of curve fitting. As shown in Figure 9.6C, 4-ATP showed the highest k and $\theta_{t=\infty}$ in comparison to 4-DMATP and 4-AATP, which might due to the weakest bonding energy of N-H, as well as the minimum of the steric hindrance

effect for 4-ATP. Moreover, 4-AATP exhibited lower k and $\theta_{t=\infty}$ than 4-DMATP, which can be attributed to the stability of local conjugation forming through the N-$COCH_3$ and phenol conjugated ring. The trend of the photoreaction reactivity among 4-ATP, 4-DMATP, and 4-AATP was further confirmed by conducting this experiment in another laser power of 0.56 mW. This experiment provides us to an unique opportunity to understand the photoreaction through correlating the experimental results with the proposed rate constant equation. Changing the reactivity of 4-ATP via molecular modification actually affects the k_2 in the respect of reaction kinetics, and modulates the energy barrier of pre-activation of 4-ATP when the bonding situation is varying in the respect of reaction yield. While the detailed mechanism toward the effect of molecular structure on oxidative coupling of 4-ATP might be even more complicated, our experiment results on tuning the molecular structure of 4-ATP strongly supported the steady state reaction kinetics model and the concept of pre-activation of surface adsorbed molecular 4-ATP for plasmon-driven oxidative coupling reaction.

We further carried out the laser power-dependent experiments on both 4-DMATP and 4-AATP. It is interestingly to observe that the both reaction kinetics and yield can be modulated by varying the incident laser power for 4-DMATP and 4-AATP, which further confirmed our experimental findings on 4-ATP. As shown in Figure 9.6D,E, both rate constant k and reaction yield $\theta_{t=\infty}$ increase as the initial Raman peak intensities of 4-DMATP (I_{1082}) increase when the incident laser power was fine-tuned from 0.32 mW to 2.60 mW. Remarkably, we also found good linear correlation between k and I_{1082} at relatively low laser power, and the super linear deviation at relatively high laser power around 1.4 mW for 4-DMATP. As shown in Figure 9.6F,G, the super linear deviation of

k from linear relationship at relatively high laser power were further confirmed by the experimental results on 4-AATP, which might due to the enhanced photothermal effect. While similar results and correlation were also observed for 4-AATP, higher laser power is required for reaching the 100% photoreaction due to relatively stable of localized molecular conjugation system in 4-AATP. In a word, laser power-dependent experimental results further demonstrated our discovery that the plasmon-induced oxidative coupling of 4-ATP is driven by Landau damping due to the linear correlation between *k* and $(E/E_0)^4$.

Remarkably, photothermal effect plays a key role in mediating plasmon-driven photoreaction because most of energetic hot electrons would undergo thermally dissipation to heat up the metal lattice via electron-phonon coupling.[41] The pre-activation of surface adsorbed 4-ATP might be affected by the local heating due to the gradual enhanced photothermal effect when the laser power is increased. To investigate the photothermal effect on the reaction kinetics and yield, we collected the time-resolved SERS spectra with varying time intervals without changing other experimental conditions, which will allow the reaction substrates to be cooling down during the interval to minimize the local heating from photothermal effect. Interestingly, while only tiny difference were observed for 4-ATP with interval time of 0 s and 60 s when using laser power of 0.45 mW, obvious increase in both rate constant *k* and reaction yield $\theta_{t=\infty}$ were found when using laser power of 0.90 mW. The results can be attributed to the enhanced photothermally pre-activation of 4-ATP under laser power of 0.90 mW in comparison to 0.45 mW, which is in very good agreement with our previous laser power-dependent experiments of 4-ATP. The super linear correlation is prominent under the laser power of

0.90 mW, however, linear correlation is still observed when the laser power is at 0.45 mW. The photothermal effect can also result in the increase of Raman peak intensities via modifying the adsorption states or molecular orientation of 4-ATP, which has been previously reported.[42,43] To gain more evidence on the effect photothermal annealing during the laser irradiation, we compared the SERS spectra of 4-ATP, 4-DMATP, and 4-AATP at 0 s, and 60 s after laser irradiation in the presence of nitrogen gas. While no DMAB were observed for all three molecules, all their SERS peak intensities were significantly increased, ranging from 150% to 200% for the increasing percentage, clearly indicating the effect of photothermal annealing on the surface adsorbed molecules on Ag nanocubes.

To gain more new insights on the effect of photothermal annealing, we further investigated the effect of pre-thermal annealing on the surface adsorbed 4-ATP at molecule-nanoparticle interface via comparing initial SERS peak intensities, rate constant, and reaction yield of 4-ATP between without and with preheating samples for 60 min at 90 ℃. None of obvious modification to the spectral line shape of initial SERS spectra were found after the pre-thermal annealing, strongly demonstrating that no molecular damage were occurred to 4-ATP under our preheating experimental conditions. Moreover, SERS peak intensities were found to be increased after pre-thermal annealing, indicating that the adsorption states of surface adsorbed 4-ATP were modified by thermal annealing, which is line with the previous results from photothermal annealing. We moved forward to compare the reaction kinetics and yield of plasmon-driven oxidative coupling of 4-ATP between without and with preheating (Figure 9.7). After being preheated, the initial SERS peak intensities, rate constant, and reaction yield were all significantly increased

under two different laser powers, which can be clearly observed from the data point distribution as shown in Figure 9.7. The experimental findings on 4-ATP can be further confirmed by experimental results from both 4-DMATP and 4-AATP. Thus, the photothermal and thermal annealing experiments strongly clarify the issues of super linear deviation of rate constant and varying reaction yield in laser power-dependent experiments. A concept of pre-activation of surface adsorbed 4-ATP were proposed to understand our experimental findings on the effect of laser power, photothermal, thermal annealing on this photoreaction.

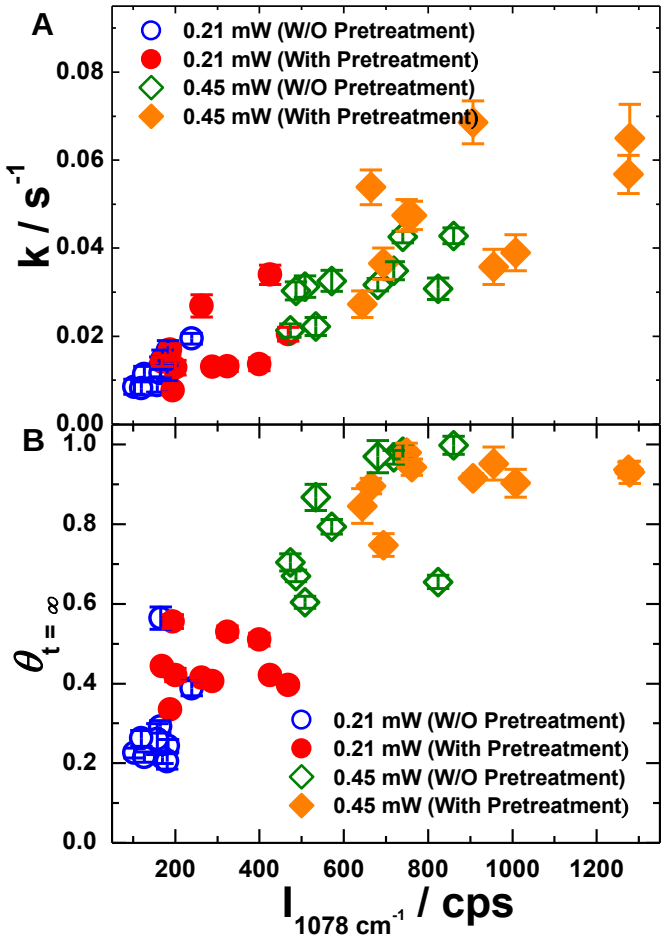

Figure 9.7. Effect of pre-thermal annealing on plasmon-driven oxidative coupling of 4-ATP. (A-B) Plots of (A) rate constant (k), and (B) reaction yield ($\theta_{t=\infty}$) versus the initial peak intensities at 1078 cm^{-1} (4-ATP) on the excitation of 785 nm laser with and without thermal pretreatment.

9.4 Conclusions

In summary, we demonstrated our ability to tackle a couple of key questions toward the detailed mechanisms and reaction kinetics of plasmon-driven oxidative coupling of 4-ATP (thiophenol-derivates):

(1) What is the rate-limiting step and the reaction kinetics model?

We proposed that the activation of surface adsorbed 4-ATP is the rate-limiting step in this photoreaction, and also the steady state kinetics behavior of active molecular O_2, and thus, single exponential equation are used to fit this first order photoreaction.

(2) What is the hot electron injection pathway: Landau damping or direct charge transfer?

We demonstrated that plasmon-induced oxidative coupling of 4-ATP is driven by Landau damping based on the linear correlation between k and $(E/E_0)^4$.

(3) What is the correlation between near electromagnetic field enhancement and reaction kinetics?

We observed good linear relationship between near electromagnetic field enhancement $(E/E_0)^4$ and rate constant k at relatively low laser power, and the super linear deviation start to dominate at relatively high laser power due to enhanced photothermal effect.

(4) The entangled role of photothermal/thermal effect?

We proposed a novel concept of pre-activation of surface adsorbed 4-ATP to understand our experimental findings on the effect of laser power, photothermal, thermal annealing on this photoreaction.

(5) The molecular structure effect of 4-ATP on this reaction?

We demonstrated that changing the reactivity of 4-ATP via modifying the molecular structure actually affects the rate constant of the rate-limiting step, that is, the activation of surface adsorbed 4-ATP, in the respect of reaction kinetics, and also modulating the energy barrier of pre-activation of 4-ATP when the bonding situation is varying in the respect of reaction yield.

While the detailed mechanism might be even more complicated, our experimental findings strongly support our above discussion toward detailed mechanism and reaction kinetics model of plasmon-driven oxidative coupling of thiophenol-derivates. Our success in unraveling the detailed mechanisms and the role of steady state of active molecular oxygen species in plasmon-driven photoreaction would open up a new opportunities for wide investigations and applications of plasmonic metallic and semiconductor nanostructures as high-performance photocatalysts.

9.5 References

(1) Halas, N. J.; Lal, S.; Chang, W. S.; Link, S.; Nordlander, P. *Chem Rev* **2011**, *111*, 3913-3961.

(2) Rycenga, M.; Cobley, C. M.; Zeng, J.; Li, W. Y.; Moran, C. H.; Zhang, Q.; Qin, D.; Xia, Y. N. *Chem Rev* **2011**, *111*, 3669-3712.

(3) Hou, W. B.; Cronin, S. B. *Advanced Functional Materials* **2013**, *23*, 1612-1619.

(4) Linic, S.; Christopher, P.; Xin, H. L.; Marimuthu, A. *Accounts of Chemical Research* **2013**, *46*, 1890-1899.

(5) Mubeen, S.; Lee, J.; Singh, N.; Kramer, S.; Stucky, G. D.; Moskovits, M. *Nat Nanotechnol* **2013**, *8*, 247-251.

(6) Govorov, A. O.; Zhang, H.; Demir, H. V.; Gun'ko, Y. K. *Nano Today* **2014**, *9*, 85-101.

(7) Knight, M. W.; Sobhani, H.; Nordlander, P.; Halas, N. J. *Science* **2011**, *332*, 702-704.

(8) Tsuboi, Y.; Shimizu, R.; Shoji, T.; Kitamura, N. *J Am Chem Soc* **2009**, *131*, 12623-12627.

(9) Deeb, C.; Ecoffet, C.; Bachelot, R.; Plain, J.; Bouhelier, A.; Soppera, O. *J Am Chem Soc* **2011**, *133*, 10535-10542.

(10) Huang, Y. F.; Zhu, H. P.; Liu, G. K.; Wu, D. Y.; Ren, B.; Tian, Z. Q. *J Am Chem Soc* **2010**, *132*, 9244-9246.

(11) Sun, M. T.; Huang, Y. Z.; Xia, L. X.; Chen, X. W.; Xu, H. X. *J Phys Chem C* **2011**, *115*, 9629-9636.

(12) Fang, Y. R.; Li, Y. Z.; Xu, H. X.; Sun, M. T. *Langmuir* **2010**, *26*, 7737-7746.

(13) Christopher, P.; Xin, H. L.; Linic, S. *Nature Chemistry* **2011**, *3*, 467-472.

(14) Linic, S.; Christopher, P.; Ingram, D. B. *Nature Materials* **2011**, *10*, 911-921.

(15) Christopher, P.; Xin, H. L.; Marimuthu, A.; Linic, S. *Nature Materials* **2012**, *11*, 1044-1050.

(16) Mukherjee, S.; Libisch, F.; Large, N.; Neumann, O.; Brown, L. V.; Cheng, J.; Lassiter, J. B.; Carter, E. A.; Nordlander, P.; Halas, N. J. *Nano Lett* **2013**, *13*, 240-247.

(17) Huang, H.; Zhang, L.; Lv, Z.; Long, R.; Zhang, C.; Lin, Y.; Wei, K.; Wang, C.; Chen, L.; Li, Z. Y.; Zhang, Q.; Luo, Y.; Xiong, Y. *J Am Chem Soc* **2016**, *138*, 6822-6828.

(18) Kale, M. J.; Avanesian, T.; Christopher, P. *Acs Catalysis* **2014**, *4*, 116-128.

(19) Manjavacas, A.; Liu, J. G.; Kulkarni, V.; Nordlander, P. *Acs Nano* **2014**, *8*, 7630-7638.

(20) Xu, P.; Kang, L. L.; Mack, N. H.; Schanze, K. S.; Han, X. J.; Wang, H. L. *Scientific Reports* **2013**, *3*.

(21) Huang, Y. F.; Zhang, M.; Zhao, L. B.; Feng, J. M.; Wu, D. Y.; Ren, B.; Tian, Z. Q. *Angewandte Chemie-International Edition* **2014**, *53*, 2353-2357.

(22) Linic, S.; Barteau, M. A. *Journal of Catalysis* **2003**, *214*, 200-212.

(23) Ueno, K.; Misawa, H. *Journal of Photochemistry and Photobiology C-Photochemistry Reviews* **2013**, *15*, 31-52.

(24) Vazquez-Vazquez, C.; Vaz, B.; Giannini, V.; Perez-Lorenzo, M.; Alvarez-Puebla, R. A.; Correa-Duarte, M. A. *J Am Chem Soc* **2013**, *135*, 13616-13619.

(25) Wang, H.; Liu, T.; Huang, Y. Z.; Fang, Y. R.; Liu, R. C.; Wang, S. X.; Wen, W. J.; Sun, M. T. *Scientific Reports* **2014**, *4*.

(26) da Silva, A. G. M.; Rodrigues, T. S.; Wang, J. L.; Yamada, L. K.; Alves, T. V.; Ornellas, F. R.; Ando, R. A.; Camargo, P. H. C. *Langmuir* **2015**, *31*, 10272-10278.

(27) Wang, J. L.; Ando, R. A.; Camargo, P. H. C. *Angewandte Chemie-International Edition* **2015**, *54*, 6909-6912.

(28) Wu, K.; Chen, J.; McBride, J. R.; Lian, T. *Science* **2015**, *349*, 632-635.

(29) Zhao, L. B.; Liu, X. X.; Zhang, M.; Liu, Z. F.; Wu, D. Y.; Tian, Z. Q. *J Phys Chem C* **2016**, *120*, 944-955.

(30) Osawa, M.; Matsuda, N.; Yoshii, K.; Uchida, I. *Journal of Physical Chemistry* **1994**, *98*, 12702-12707.

(31) Wu, D. Y.; Liu, X. M.; Huang, Y. F.; Ren, B.; Xu, X.; Tian, Z. Q. *J Phys Chem C* **2009**, *113*, 18212-18222.

(32) Zong, S. F.; Wang, Z. Y.; Yang, J.; Cui, Y. P. *Anal Chem* **2011**, *83*, 4178-4183.

(33) Dendisova, M.; Havranek, L.; Oncak, M.; Matejka, P. *J Phys Chem C* **2013**, *117*, 21245-21253.

(34) Zhao, L. B.; Zhang, M.; Huang, Y. F.; Williams, C. T.; Wu, D. Y.; Ren, B.; Tian, Z. Q. *Journal of Physical Chemistry Letters* **2014**, *5*, 1259-1266.

(35) Xia, X.; Zeng, J.; Oetjen, L. K.; Li, Q.; Xia, Y. *J Am Chem Soc* **2012**, *134*, 1793-1801.

(36) Zheng, T. T.; Zhang, Q. F.; Feng, S.; Zhu, J. J.; Wang, Q.; Wang, H. *J Am Chem Soc* **2014**, *136*, 2288-2291.

(37) Wang, H.; Halas, N. J. *Adv Mater* **2008**, *20*, 820-+.

(38) Boerigter, C.; Campana, R.; Morabito, M.; Linic, S. *Nat Commun* **2016**, *7*, 10545.

(39) Liu, G. K.; Hu, J.; Zheng, P. C.; Shen, G. L.; Jiang, J. H.; Yu, R. Q.; Cui, Y.; Ren, B. *J Phys Chem C* **2008**, *112*, 6499-6508.

(40) Takeyasu, N.; Kagawa, R.; Sakata, K.; Kaneta, T. *J Phys Chem C* **2016**, *120*, 12163-12169.

(41) Brongersma, M. L.; Halas, N. J.; Nordlander, P. *Nat Nanotechnol* **2015**, *10*, 25-34.

(42) Aggarwal, R. L.; Farrar, L. W.; Saikin, S. K. *J Phys Chem C* **2012**, *116*, 16656-16659.

(43) Canpean, V.; Astilean, S. *Spectrochim Acta A* **2012**, *96*, 862-867.

CHAPTER 10

Plasmonic Hot Electron Driven Photocatalytic Reactions: New insights Gained from Plasmon-Enhanced Spectroscopic Studies

10.1 Introduction

Localized surface plasmon resonance (LSPR) generally refers to the collective oscillations of conduction electrons on surfaces of metallic nanoparticles.[1,2] When a metal nanoparticle is excited to generate surface plasmons at its eigenfrequency upon light excitation, the incident light is both absorbed and scattered, giving rise to vivid colors. The unique features of LSPR can be well displayed by far-field extinction spectral feature and the near-field enhancement.[1,3] The far-field extinction properties are measured by optical extinction spectroscopy to show the maximized excitation of surface plasmons at specific frequencies/wavelengths. Fine control over the size, shape, and composition of plasmonic nanoparticles allows one to achieve highly tunable optical extinction from UV-vis to near Infrared,[4-9] leading to many interesting applications, such as, biomolecular sensing, photothermal cancer therapy, energy storage and conversion.[3,10-16] On the other hand, the significant enhanced local electric field formed by collective oscillation of free electrons would greatly increase the molecular optical cross-section when molecules are adsorbed onto the surfaces of metallic nanoparticles.[1,11,13] Particularly, the enhanced Raman scattering of surface-adsorbed molecules provides an unique opportunity for us to using surface-enhanced Raman spectroscopy (SERS) as *in situ* spectroscopic tool with unprecedented sensitivity to monitor the interfacial molecular transformation at nanoparticle-molecule interface.[9,17-24]

After the excitation of plasmon resonance under light illumination, the energy transferred from light wave to plasmon resonance.[25] Typically, There are three plasmon decay pathways:[25-28] (1) Elastic radiative re-emission of photons, also known as scattering; (2) Landau damping: giving rise to the formation of energetic electrons and

holes pairs in the metal particle; (3) Chemical interface damping (CID): the interaction of excited surface plasmons with unpopulated adsorbate acceptor states, leading to the direct energetic electron injection into the adsorbate acceptor states. In contrast to CID pathway, if none of proper unpopulated adsorbate acceptor states are presented for electron injection, the energetic electrons generated through Landau damping (electron-phonon coupling) would undergo thermal dissipation process, resulting in local heating, also known as photothermal effect. While Landau damping and CID are intrinsically different mechanisms, both of them generate energetic electrons, also known as hot electrons, which can be probably harnessed for energy conversion and catalytic reaction.[29-34] Recently, It has been observed that the hot electrons generated through surface plasmon decay play a key role in guiding interesting photo-chemical reactions, such as photochromic reactions,[35] photopolymerization,[36] photo-reductive dimerization of 4-nitrothiophenol (4-NTP),[37,38] and oxidative coupling of 4-aminothiophenol (4-ATP).[39,40] Moreover, some important catalytic reactions, such as ethylene epoxidation,[29,41,42] dissociation of H_2,[31] styrene hydrogenation,[43] and generation of H_2 via water-splitting,[44] were also found to be either induced or enhanced by the plasmon-driven hot carriers injection into the surface molecular adsorbates upon exposure to light excitation. The mechanisms of plasmon-mediated photoreactions, however, still remain unclear. Therefore, it is imperative to gain quantitative insights into the kinetics and underlying pathways of these plasmon-mediated photoreactions to fully understand the obstacles that might limit the wide applications of plasmonic nanostructures as high-performance photocatalysts.

In this chapter, the plasmon-driven photo-reduction of 4-NTP were chosen as a model reaction to investigate the plasmonic effects on photoreactions. We used time-resolved surface-enhanced Raman spectroscopy (SERS) as an ultrasensitive spectroscopic tool with unique molecular finger-printing capabilities to monitor the photoreaction kinetics. A unique three-dimensional hierarchical nanostructure composed of a Fe_3O_4 bead decorated with Ag nanocubes (Fe_3O_4@Ag NC) was used as a plasmonically addressable substrate for SERS. We demonstrated that the reductive dimerization of 4-NTP to 4,4'-dimercaptoazobenzene (DMAB) is a two-step reaction. The first step is the photothermally induced chemisorption process, which was experimentally observed as induction time. The second step involves the photo-reduced of 4-NTP by plasmon-generated hot electrons, giving arise to the formation of DMAB. By correlating the reaction rates with local field enhancement, we were able to demonstrate that the reductive dimerization of 4-NTP to DMAB is driven by Landau damping mechanism instead of CID. The plasmon-associated local electromagnetic enhancement, which can be modulated by changing the laser power, and the density of Ag nanocubes on Fe_3O_4 bead, was also found to be a key factor on the reaction kinetics and percentage. Furthermore, the peculiar role of active oxygen species in guiding the plasmon-driven photocatalytic reactions was also proposed and discussed in detail, allows us to reveal the underlying reaction mechanism. The knowledge gained through this work would add significant new insights on reaction kinetics and mechanisms of the plasmon-mediated photocatalytic reactions.

10.2 Experimental Section

Chemicals and Materials. Ethylene glycol (EG) was obtained from VWR International. Poly(vinylpyrrolidone) (PVP58 with Mw~58000), Thiophenol (C6H6S, TP, 99+%), 4-aminothiophenol (C6H7NS, 4-ATP, 97%), and 4-nitrothiophenol ($C_6H_5NO_2S$, 4-NTP, 80%) were all obtained from Alfa Aesar. Silver trifluoroacetate (CF3COOAg, ≥99.99%), sodium hydrosulfide hydrate (NaHS ꭓH_2O), hydrochloric acid (HCl, 37% in water), poly(diallyldimethylammonium chloride) (PDDA, 20%, w/w in water, Mw=200,000-350,000), poly(4-vinylpyridine) (PVP, Mw~60,000), were all purchased from Sigma-Aldrich. Fe_3O_4 beads (Dynabeads, carboxyl acid) were obtained from Life Technologies. Silica beads (SiO_2) was obtained from nanoComposix. Hydrogen peroxide (H2O2, 30%), sulfuric acid (H2SO4, 96.10%), and ethanol (200 proof) were purchased from Fisher Scientific. Acetone was purchased from Honeywell. All reagents were used as received without further purification. Ultrapure water (18.2 MΩ resistivity, Barnstead EasyPure II 7138) was used for all experiments.

Synthesis of Ag Nanocubes. Ag nanocubes were synthesized following same protocol as described in chapter 9.

Synthesis of Fe_3O_4@Ag Nanocubes Core-Satellite Particles. Fe_3O_4@Ag nanocubes hybrid particles were prepared via a layer-by-layer assembly approach.[45] A colloidal suspension of Fe_3O_4 beads (10.0 mg/mL water) was added to 1 mL of PDDA solution (1%). After sonication for 30 min, the suspension was collected by sedimentation with the help of an external magnetic field and washed three times with pure water. 0.1 mL of the as-prepared Ag nanocubes was then added to the Fe_3O_4/PDDA nanocomposites under mechanical stirring for 1h. The final product was separated using an external magnetic

field and then redispersed in pure water. During this process, Ag nanocubes were attached to the surface of the Fe_3O_4/PDDA nanocomposites through electrostatic interactions. Then the products were removed from the solution by applying an external magnetic field. This process was repeated multiple times until the color of added Ag nanocubes no longer changed, indicating a saturating (High) coverage of Ag nanocubes on the PDDA-functionalized Fe_3O_4 beads. When PDDA-functionalized Fe_3O_4 beads were mixed with Ag nanocubes with various cycles, Fe_3O_4@Ag nanocubes hybrid particles with high, medium, and low coverages of Ag nanocubes were obtained.

Time-Resolved Single-Particle SERS Measurements. Sub-monolayer films of isolated Fe_3O_4@Ag nanocubes hybrid particles were prepared by immobilizing the particles onto PVP(polyvinylpyridine)-functionalized silicon substrates.[46] In a typical procedure, silicon substrates were cleaned in a piranha solution (sulfuric acid : hydrogen peroxide, 7 : 3) for 15 min, and then immersed in a 1% wt. of PVP ethanolic solution for 24 h. The silicon substrates were thoroughly rinsed with ethanol, dried with N_2 gas before use. Fe_3O_4@Ag hybrid particles were incubated in 4-NTP solution with various concentrations for 1 h, and then washed with ethanol and dried with N_2 gas. The molecular coverage were controlled by incubating Fe_3O_4@Ag hybrid particles in various concentration of 4-NTP (10 μM, 50 μM, 250 μM, and 1 mM). Then the silicon substrate were immersed in an aqueous solution of Fe_3O_4@Ag hybrid particles for 1 h. The silicon substrates were thoroughly rinsed with ethanol and dried with N_2 gas after they were removed from the solution of Fe_3O_4@Ag hybrid particles. The coverage of Fe_3O_4@Ag hybrid particles on the substrates can be controlled by changing the immersion time.

Time-resolved SERS spectra were obtained on a Bayspec *Nomadic*^{TM} Raman microscopy built on an Olympus BX51 reflected optical system under 785 nm laser excitation in the confocal mode (focal area of 2 μm diameter). A 50× dark field objective (NA=0.5, WD=10.6 mm, Olympus LMPLFLN-BD) was used for both Raman signal collection and dark field scattering imaging. The laser beam was focused on one particle each time for Raman spectrum collection. The laser power focused on the samples was measured to be 620 μW and the spectrum acquisition time was varied from 1 s to 30 s under most of conditions. For the laser power-dependant experiments, we tested the samples under various laser powers (240, 370, 620, and 790 μW). The time-resolved SERS measurement on 4-ATP and TP were also done in the same way. The heating effect experiments were carried out by incubating the Fe_3O_4@Ag hybrid particles (silicon substrates) at 90 ^oC for 30 min. And then, the samples were measured after cooling down to room temperature.

Characterizations. The TEM images were obtained using a Hitachi H-8000 transmission electron microscope operated at an accelerating voltage of 200 kV. All samples for TEM measurements were dispersed in water and drop-dried on 300 mesh Formvar/carbon-coated Cu grids. SEM and EDS measurements were performed using a Zeiss Ultraplus thermal field emission scanning electron microscope. The samples for SEM and EDS measurements were dispersed in water and drop-dried on silicon wafers. The optical extinction spectra of the nanoparticles were measured on aqueous colloidal suspensions at room temperature using a Beckman Coulter Du 640 spectrophotometer. ζ-Potentials of colloidal nanoparticles were measured at room temperature using ZETASIZER nanoseries (Nano-ZS, Malvern). Raman spectra were obtained on a

Bayspec *Nomadic*^{TM} Raman microscopy built on an Olympus BX51 microscope equipped with a 785 nm CW diode laser.

10.3 Results and Discussions

We developed a layer-by-layer (LBL) assembly approach to fabricated the Fe_3O_4@Ag nanocubes hybrid particles. The plasmon coupling between the neighboring Ag nanocubes leads to the formation of plasmon "hot-spots" in the interparticle gaps where the local electric fields are drastically enhanced upon plasmonic excitation in the near-IR.[3] This LBL assembly approach allows us to fine-control the Ag nanocube coverage on each magnetic bead, providing a unique way to tune the density, size, and intensity of the plasmon "hot-spots" on the particle surfaces. As shown in Figure 10.1A, the Fe_3O_4@Ag hybrid particles were prepared through a stepwise LBL process. The surfaces of the as-prepared Fe_3O_4 beads, which are terminated by carboxyl group, are negatively charged at neutral and basic pHs. A thin layer of polydiallyldim-ethylammonium chloride (PDDA) is then adsorbed onto the Fe_3O_4 surface to generate a positively charged particle surface. Since the Ag nanocubes are negatively charged, they can be attached onto the PDDA-functionalized Fe_3O_4 beads through electrostatic interactions. Figure 10.1B shows the evolution of the ζ-potentials during the LBL assembly process. We used a combination of scanning electron microscopy (SEM) and transmission electron microscopy (TEM) to fully characterize the Fe_3O_4@Ag nanocubes hybrid particles (Figure 10.1C-10.1J). Fe_3O_4 magnetic beads of uniform size (~ 1 ± 0.1 μm) are used as the core on which Ag nanocubes (~ 36 ± 3.2 nm) are assembled electrostatically. More importantly, the coverage of Ag nanocubes, which determines the number and intensity of the electromagnetic hot spots, on the Fe_3O_4 beads can be fine-controlled by adjusting the

amount ratios between Ag nanocubes and Fe_3O_4 beads during the LBL assembly process (Figures 10.1C-10.1J). This method provides an unique approach for us to fabricate a dual-functional and plasmonically addressable core-satellite nanostructure, which can serve as plasmonic photocatalyst, as well as strong SERS substrate.

We used time-resolved SERS to monitor the plasmon-mediated photochemical conversion of 4-NTP into DMAB that are adsorbed on the surface of Fe_3O_4@Ag hybrid particles. To form a self-assembled monolayer of 4-NTP on the nanoparticle surfaces, Fe_3O_4@Ag hybrid particles are first immersed in 4-NTP solution, then separated from the mixture in an external magnetic field, and finally dried on silicon substrates for SERS measurements. The plasmons of the Fe_3O_4@Ag NC particles are on resonance with the excitation laser (785 nm), which allows us to probe the photoreaction kinetics by collecting the time-resolved SERS spectra. As schematically illustrated in Figure 10.2A, the reductive dimerization of 4-NTP to DMAB was initiated upon exposure of the 4-NTP-coated Fe_3O_4@Ag particle to 785 nm laser in ambient air at room temperature. Moreover, the confocal Raman microscope setup with a laser focal plane ~2 μm × 2 μm in size, when combined with the sub-monolayer particle substrate geometry, allows us to collect SERS trajectories one-particle-at-a-time and subsequently build statistics on the reaction kinetics by analyzing the ensemble of large numbers of trajectories.

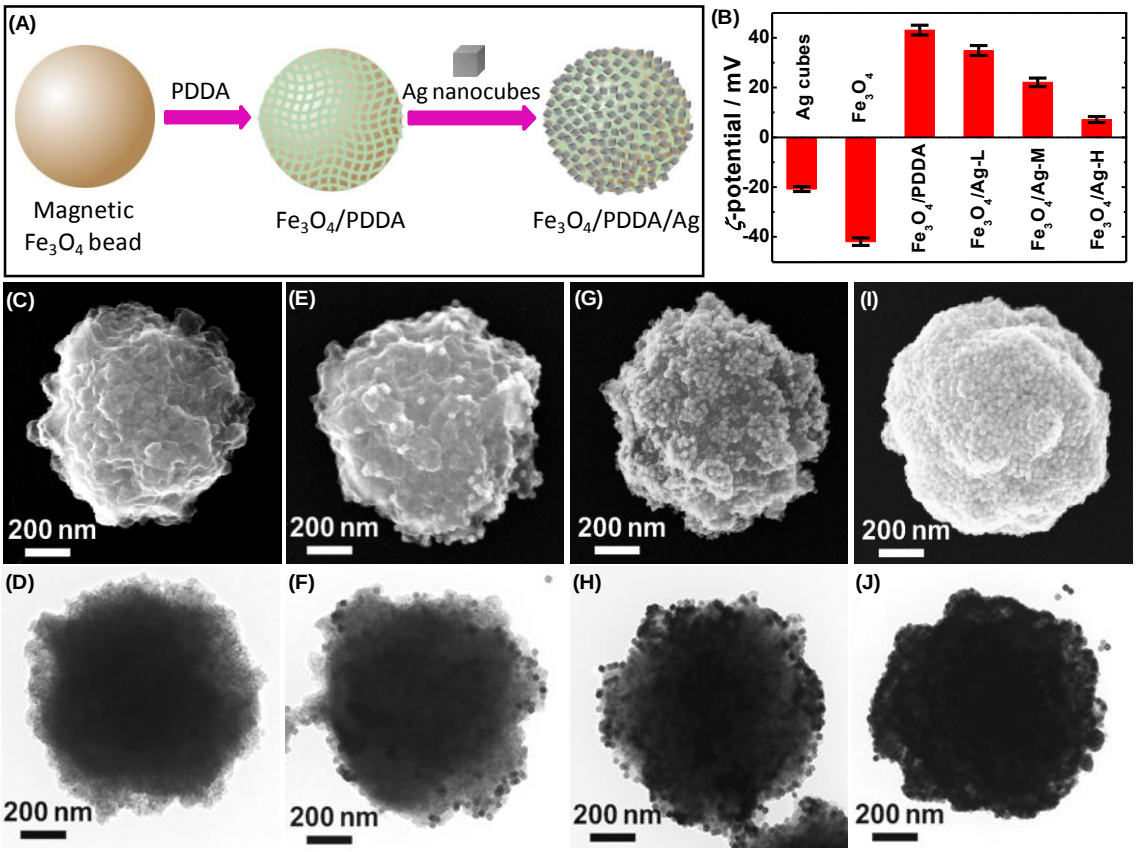

Figure 10.1. (A) Schematic illustration of the fabrication process of Fe_3O_4 bead/PDDA/Ag nanocubes hybrid structures. (B) Evolution of ζ-potential during the layer-by-layer assembly process of Fe_3O_4/PDDA/Ag nanocubes particles. (C), (E), (G), (I) SEM images and (D), (F), (H), (J) TEM images of individual Fe_3O_4 bead, and Fe_3O_4/Ag-L, Fe_3O_4/Ag-M and Fe_3O_4/Ag-H particle. (Ag-L, M, and H represent the Low, Medium, and High coverage of Ag nanocubes on Fe_3O_4 bead)

Figure 10.2B and 10.2E show the SERS spectra of 4-NTP monolayer molecules adsorbed on individual Fe_3O_4@Ag hybrid particle at various reaction times on the excitation of 785 nm laser of (B) 240 μW, and (E) 790 μW, respectively. The Raman bands at 1142, 1390 and 1438 cm^{-1} are assigned to DMAB, and the 1338 cm^{-1} mode is assigned to 4-NTP.[37,47-50] As shown in Figure 10.2C and 10.2F, the ratios between Raman modes at 1438 cm^{-1} (N-N stretching mode of DMAB) and 1078 cm^{-1} (C-S stretching mode of 4-NTP and DMAB) modes were used as being representative of product grow

kinetics to quantify the fraction of DMAB (θ_{DMAB}), as a function of reaction time (t). We collected the time-resolved SERS spectra on 25 individual particles to build the statistical distribution (Figure 10.2D and 10.2G), in which way more reliable and definite conclusion can be draw when comparing the results in different experimental conditions, such as, varying laser power and coverage of Ag nanocubes. It is clearly to found that the reaction kinetics were greatly affected by the laser power, and more interestingly, two-step reaction process were observed when the laser power is as low as 240 μW (Figure 10.2B). When using laser power of 240 μW, no obvious Raman bands from DMAB were observed at the early stage after initiation of the photoreaction, however, the Raman intensity of 4-NTP was kept increasing. The Raman bands from DMAB started to become significantly much stronger as the reaction time reaching about 300 s. In contrast, the reaction was extremely fast when increasing the laser power to 790 μW, that is, strong Raman bands of DMAB were observed at the very beginning of the reaction and no obvious two-step reaction were observed in this case. Our hypotheses on the two-step reaction are as following:

(1) $4-NTP(I) \xrightarrow{t_{ind}} 4-NTP(II)$

(2) $4-NTP(II) \xrightarrow{k} 1/2DMAB$

Where the first step is the photothermally induced chemisorption process, which was experimentally observed as induction time (t_{ind}). The second step involves the photo-reduced of 4-NTP by plasmon-generated hot electrons, giving arise to the formation of DMAB, defined as rate constant k. 4-NTP(I) and 4-NTP(II) refer to the 4-NTP molecule at different adsorption states, such as, varying bind sites and orientations. As shown in

Figure 10.2C and 10.2F, we further performed least-squares curve fitting to the $\theta_{DMAB}(t)$ and $\theta_{4\text{-}NTP}(t)$ trajectories using the following rate equation:

$$\theta_{DMAB} = \theta_{t=\infty} \times (1 - e^{(-k(t-t_{ind}))}) \qquad (1),$$

$$\theta_{4-NTP} = 1 - \theta_{t=\infty} + \theta_{t=\infty} \times e^{(-k(t-t_{ind}))} \qquad (2),$$

Where θ_{DMAB} and $\theta_{4\text{-}NTP}$ are the fraction of reactant 4-NTP and product DMAB, respectively. t_{ind} is the induction time to express the first step reaction, and k is the first-order rate constant to describe the second step reaction. Also $\theta_{t=\infty}$ is the reaction percentage, which is highly dependent on the experimental conditions, such as, laser power, coverage of Ag nanocubes, and coverage of 4-NTP molecules.

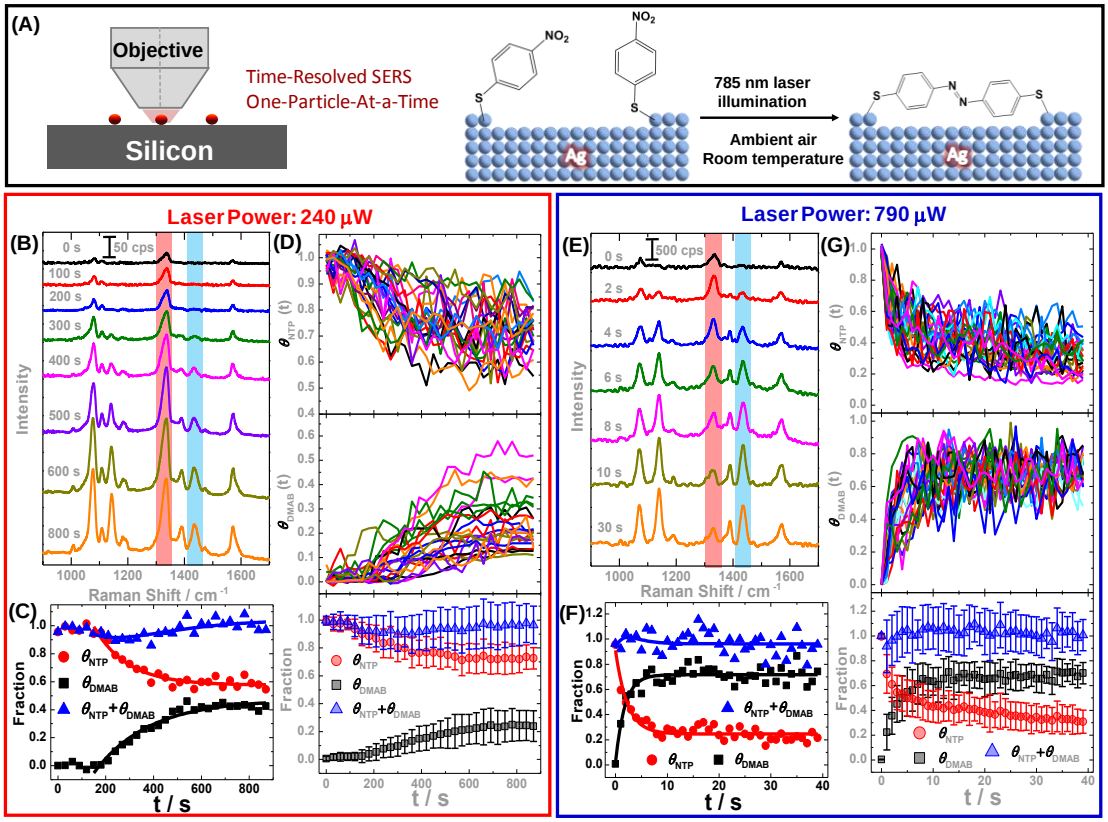

Figure 10.2. Time-resolved SERS measurement of plasmon-mediated photoreaction kinetics. (A) Schematic illustration of the single-particle SERS setup (left panel) and plasmon-driven dimerization of 4-NTP on the surface of Ag nanocubes upon light excitation (right panel). (B,E) SERS spectra of 4-NTP monolayer molecules adsorbed on individual Fe_3O_4@Ag hybrid particle

at various reaction times on the excitation of 785 nm laser of 240 μW (B), and 790 μW (E). (C,F) The corresponding trajectories of θ_{DMAB}, θ_{NTP}, and $\theta_{DMAB}+\theta_{NTP}$ as a function of reaction time under 785 nm laser of 240 μW (C), and 790 μW (F). The results of least-squares fitting are shown as solid curves. (D,G) All individual trajectories of θ_{NTP}, θ_{DMAB} , and the average fractions of θ_{DMAB}, θ_{NTP}, and $\theta_{DMAB}+\theta_{NTP}$ as a function of reaction time under 785 nm laser of 240 μW (D) and 790 μW (G) collected from each individual Fe_3O_4@Ag hybrid particle.

In order to test our hypotheses on the two-step reaction, we moved one step back to work on thiophenol (TP), which has similar molecular structure as 4-NTP except for replacing nitro group with hydrogen group. The reason for choosing TP molecule is that we proposed that surface-adsorbed TP might undergo a similar photothermally induced chemisorption process as 4-NTP, but no subsequent dimerization would be observed. As shown in Figure 10.3A-C, we compared the Raman spectra of TP under varying conditions normal Raman, SERS, SERS after laser illumination. and SERS after thermal heating. None of obvious modification to the spectral line shape of initial SERS spectra were found after the laser illumination and thermal annealing, strongly demonstrating that none of molecular damage were occurred to 4-NTP under our pre-annealing conditions. Significant increase in SERS intensities were clearly observed in both SERS spectra after laser illumination and thermal heating in comparison to SERS spectra, strongly indicating the photothermal effect on TP molecule induced by laser illumination is well mimicked by thermal heating, resulting in similar modification to the SERS spectra, which is line with the previous results from photothermal annealing.[51] More importantly, we also observed downshift to lower energy from two highlighted characteristic Raman bands of TP (1072 cm^{-1}, C-S stretching mode, and 1578 cm^{-1}, C-C stretching mode) in both SERS spectra after laser illumination and thermal heating comparing to SERS spectra. This provides strong evidence on multiple adsorption states of TP on surface of Ag nanoparticles are presented, and would be significantly affected by photothermal and

thermal treatment. While the detailed mechanism might be more complicated than we expected, our experimental results strongly demonstrated that the chemisorption states of molecules on the surface of metallic nanoparticles can be modulated by laser illumination induced photothermal effect, which can be also well mimicked by pre-thermal treatment.

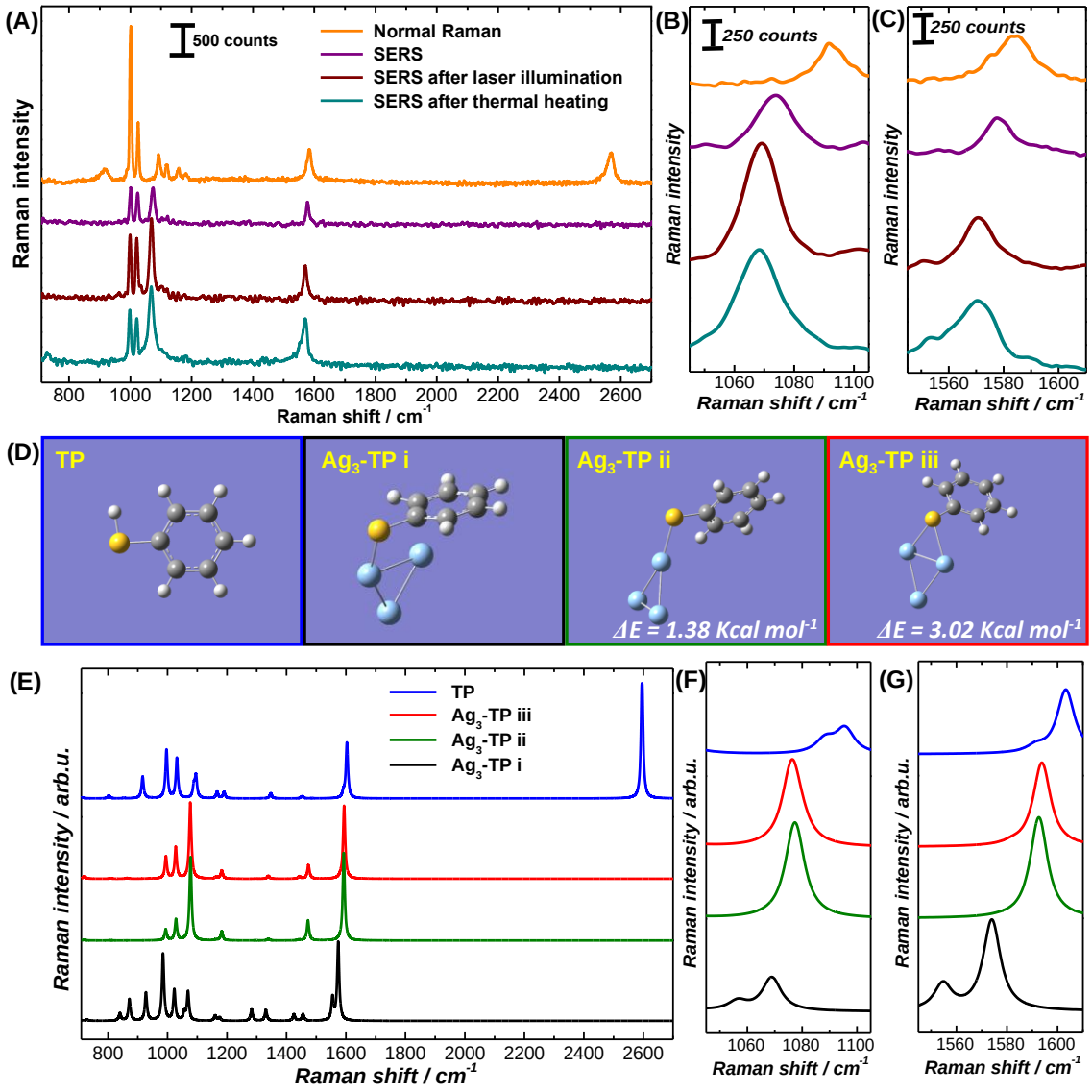

Figure 10.3. Multiple adsorption states of TP on the surface of Ag nanocubes upon thermal and photothermal treatment. (A-C) Normal Raman and SERS spectra of TP under varying conditions were shown for comparison. The 1080 cm^{-1} band (B) and 1575 cm^{-1} band (C) were highlighted for observing the down shift of Raman band. (D) The molecular structure of TP and Ag_3-TP with three different adsorption states in the DFT calculation. (E-G) Simulated normal Raman spectra

of TP and SERS spectra of Ag_3-TP-i, ii, and iii. The 1080 cm^{-1} band (F) and 1575 cm^{-1} band (G) were highlighted for observing the downshift of Raman band, which is in very good agreement with the experimental observation.

We further carried out density functional theory (DFT) simulation to investigate the multiple adsorption states of TP on the surface of Ag nanocubes. Basically, we created a TP molecule, and then formed Ag-S bond between TP and a triangle Ag_3 cluster. After optimization of bother energy and geometry of this cluster, we were able to obtain three adsorption states of Ag_3-TP (marked as i, ii, iii) that have the lowest energy and are the most stable, as shown in Figure 10.3D. More importantly, downshift of Raman band from adsorption state iii to ii, and i were observed from the simulated SERS spectra (Figure 10.3E-G), which is in very good agreement with our experimental observations. The downshift of Raman band from state iii to state i of lowest energy strongly demonstrate that TP undergo adsorption states change to become the most stable adsorption states on the surface of Ag nanocubes upon photothermal and thermal treatment. Our experimental findings and theoretical simulation results on TP provides strong evidence on our hypotheses that there are photothermal-induced chemisorption process of 4-NTP on the surface of Ag nanocubes before initiating the photoreaction.

In contrast to TP, 4-NTP showed up shift of Raman bands (1338 cm^{-1}, O-N-O stretching mode) upon thermal treatment, which might due to the significant difference in charge distribution between TP and 4-NTP (Figure 10.4A). Similar increase in SERS intensities were also observed from 4-NTP after thermal heating, which is in line with previous observations (Figure 10.4B).[51,52] We further carried out the DFT simulation to investigate the multiple adsorption states of 4-NTP on the surface of Ag nanocubes using

the same approach as we did on TP. As shown in Figure 10.3C-D, up shift of Raman bands of 4-NTP-Ag_3 from state iii to i were observed from the corresponding simulated SERS spectra, strongly demonstrating that 4-NTP undergo thermal induced chemisorption process from a more active state to the most stable state upon thermal treatment. To gain more evidence on the photothermal/thermal-induced pre-activation of 4-NTP toward photoreaction, we compared the reaction kinetics and reaction percentage of 4-NTP-coated Fe_3O_4@Ag particles with and without pre-thermal annealing at the laser power of 240 μW. It is interesting to found that the induction time period disappeared after we pre-thermal annealing the samples. Also both reaction kinetics and percentage increased in comparison to the samples without any pre-treatment. Although other surface-adsorbed conditions of molecule, such as, mobility and packing density, might be also affected by thermal treatment, our results clearly demonstrate the pre-activation of 4-NTP toward photoreaction can be modulated by both photothermal effect and thermal annealing.

Furthermore, we systematically investigated the effect of laser power on this photoreaction while keeping other experimental conditions the same. The increase in laser power would give rise to the significant enhancement of local electromagnetic field, expressed as E/E_0, which is due to the correlation between laser power P and local electromagnetic field E is $P \propto \mathcal{E}E^2$. Thus, when laser power is changing, the varying local electromagnetic field enhancement would have significant impact on the photoreaction kinetics via modulating the rate constant k. We performed the time-resolved SERS measurements under excitation at a series of different laser power to build the correlation

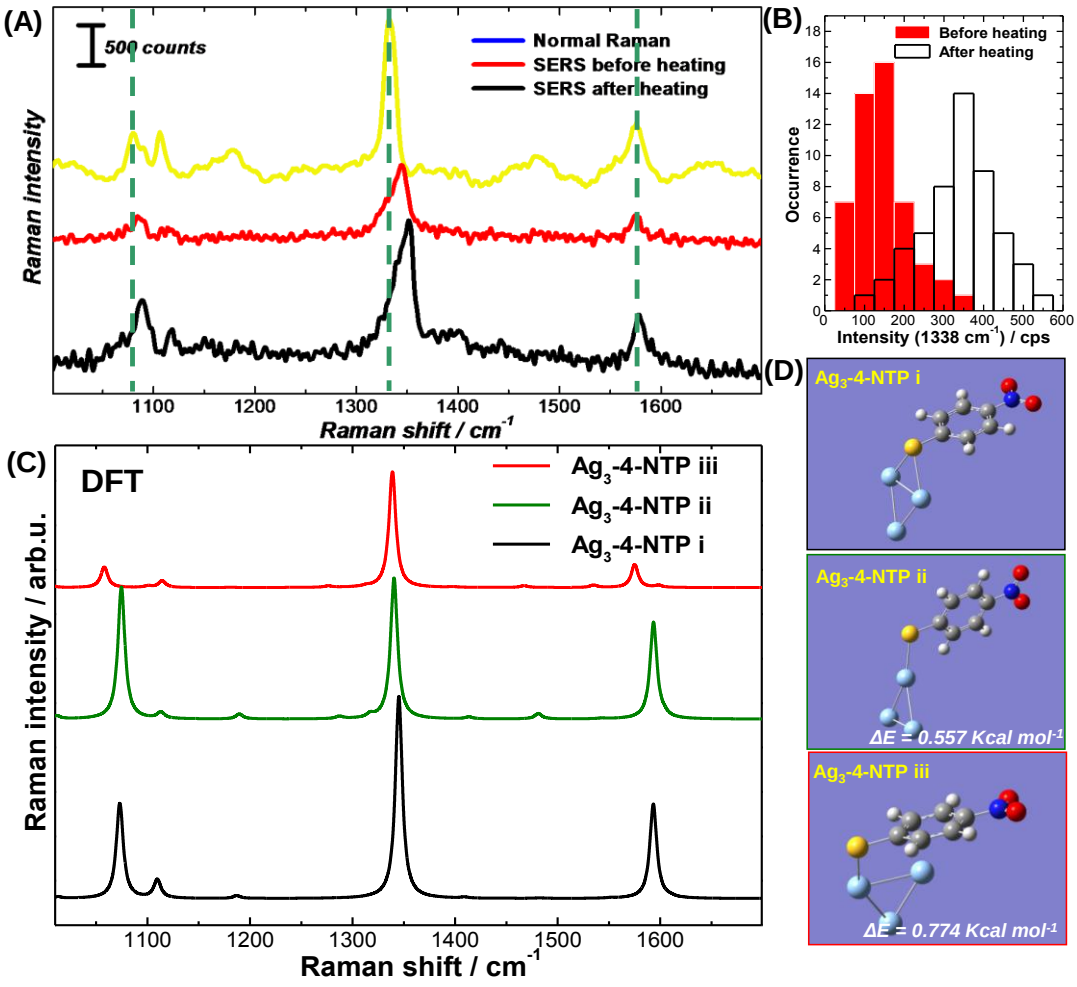

Figure 10.4. Multiple adsorption states of 4-NTP on the surface of Ag nanocubes upon thermal and photothermal treatment. (A) Normal Raman and SERS spectra of 4-NTP under varying conditions were shown for comparison. The 1080 cm^{-1}, 1338 cm^{-1}, and 1575 cm^{-1} band were marked with dashed line for observing the up shift of Raman band. (B) Histograms of Raman intensities of 1338 cm^{-1} (4-NTP) mode obtained from individual Fe_3O_4@Ag nanocubes particle under two different conditions: before heating and after heating. (C) Simulated SERS spectra of Ag_3-4-NTP-i, ii, and iii. The up shift of Raman band can be clearly observed from state iii to state i, which is in very good agreement with the experimental observation. (D) The molecular structure of Ag_3-4-NTP with three different adsorption states in the DFT calculation.

between the excitation laser power and reaction kinetics/percentage. As shown in Figure 10.5A, we plotted the rate constant (k) as a function of the initial Raman peak intensities at 1338 cm^{-1} of 4-NTP (I_{1338}) on the excitation of 785 nm laser with various laser powers

of 0.24, 0.37, 0.62, and 0.79 mW. To address the underlying meaning of the as-plotted figures, we plotted the ensemble-averaged Raman peak intensities at 1338 cm^{-1} of 4-NTP (I_{1338}) and ensemble-averaged rate constant (k) as a function of laser power square, as shown in the inset of Figure 4A. Remarkably, well-fitted linear relationship between I_{1338} and laser power square was observed, when combined with the linear relationship between laser power and $(E/E_0)^2$, further demonstrating that the correlation between I_{1338} and near field enhancement E/E_0 is that, $I_{1338} \propto (E/E_0)^4$. On the other hand, none of detailed information can be gained from the plots of ensemble-averaged rate constant (k) *vs.* laser power square. Therefore, we chose to employ the initial Raman peak intensities of 4-NTP (I_{1338}) to quantify the near field enhancement E/E_0 instead of laser power, when combined with statistical distribution on one-particle-at-a-time, clearly showing the detailed correlation between rate constant (k) and near field enhancement (E/E_0) (Figure 10.5A). We observed very good linear relationship between k and I_{1338} at relatively low laser power, and the super linear deviation start to dominate at relatively high laser power, as shown in Figure 10.5A. As it was previously demonstrated, the Raman peak intensities is proportional to the fourth power of near field enhancement ($(E/E_0)^4$), that is, $I_{1338} \propto (E/E_0)^4$. Therefore, linear correlation between k and I_{1338} from our experimental results strongly demonstrating that the relationship between rate constant (k) and near field enhancement $(E/E0)^4$ is $k \propto (E/E_0)^4$. The as-demonstrated well-fitted linear correlation between k and $(E/E_0)^4$ provide us an unique opportunity to explore the mechanism of plasmonic hot electron injection pathway that involved in this photoreaction. Two main mechanisms on plasmonic hot electron excitation were widely known as we discussed in the introduction part: Landau damping and chemical interface

damping (CID).[27,28,53] A key difference between this two mechanisms is the correlation between rate constant k and near field enhancement E/E_0, which would allow us to experimentally distinguish these two mechanisms though the underlying mechanisms might be much more complicated. $k \infty (E/E_0)^4$ is found to be Landau damping, and $k \infty (E/E_0)^2$ is verified as CID due to their different photon absorption and scattering processes. Therefore, while the mechanism of the hot electron injection process on excited plasmonic nanostructures are still unclear and poorly understood, our experimental results strongly demonstrated that this photoreaction is driven by Landau damping rather than CID. Furthermore, the super linear deviation of k from linear relationship might possibly due to the significant enhanced photothermal effect at relatively high laser power.

As shown in Figure 10.5B-C, the reaction percentage ($\theta_{t=\infty}$) increased at the beginning and then reaches at an equilibrium while the induction time (t_{ind}) significant decreased, and then became zero finally as the laser power gradually increased. The effects of laser power on both reaction percentage and induction time could be attributed to the enhanced photothermal-induced pre-activation of 4-NTP. For the reaction percentage, laser power dependent photothermal effect would induce the local heating near the surrounding of the adsorbed molecular 4-NTP, and further pre-activate 4-NTP toward accepting hot electrons to initiate the photo-reductive dimerization. Very recently, Takeyasu and co-authors reported that a threshold value of laser power was observed for the photoreaction of 4-ATP to be initiated, which is in very good agreement with our experimental findings.[54] On the other hand, the decrease in induction time can be also explained by the enhanced photothermal effect that significantly facilitated the chemisorption process of 4-

NTP as the laser power increased. More interestingly, the photothermal effect can be also well mimicked by thermal treatment, which represents an unique way to optimization of the plasmon-driven photocatalytic process, as well as providing design principle for rational design of high performance plasmonic photocatalyst.

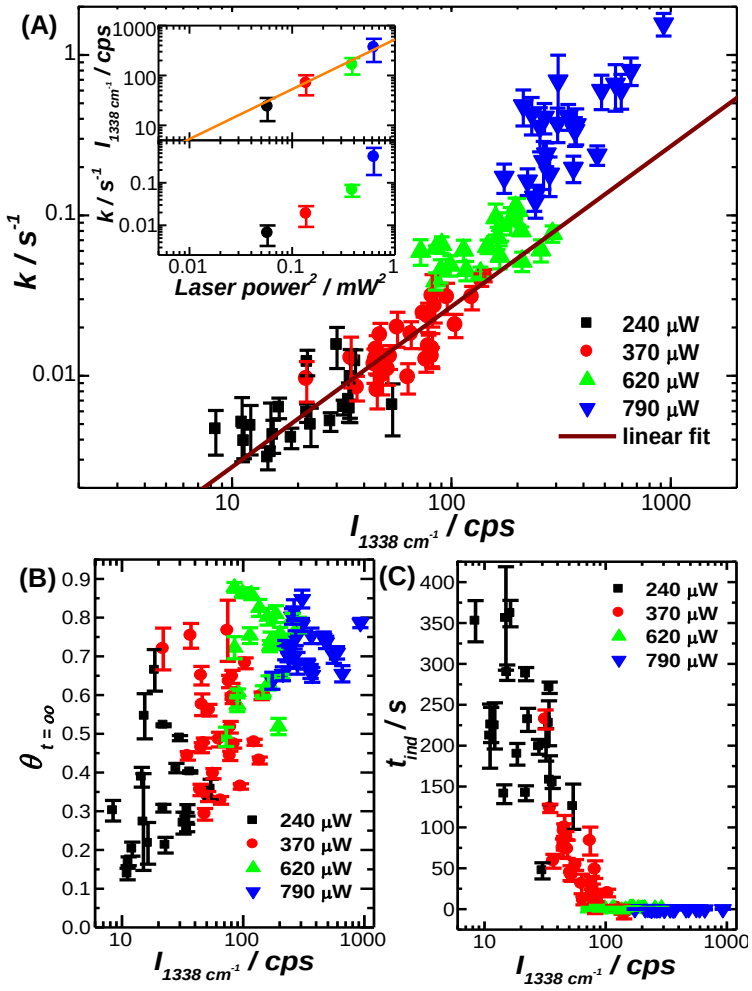

Figure 10.5. Plots of (A) rate constant (k), (B) reaction percentage ($\theta_{t=\infty}$), and (C) induction time (t_{ind}) versus the initial peak intensities at 1338 cm^{-1} (4-NTP) on the excitation of 785 nm laser with various laser power of 240, 370, 620, and 790 μW. The linear fitting result was shown as a solid line in panel A. The inset of panel A shows the initial peak intensities at 1338 cm^{-1} (upper panel) and rate constant k (down panel) as function of laser power square. The tested sample is Fe_3O_4@Ag nanocubes particle with medium coverage. The concentration of incubated 4-NTP solution is 1.0 mM.

Another way to modulate the local electromagnetic field enhancement is the control over the coverage of Ag nanocubes on the Fe_3O_4 bead, which would allow us to study the effects of density of plasmonic hot-spots (local electromagnetic field enhancement) on the photoreaction kinetics and percentage. As shown in Figure 10.6A-C, Fe_3O_4/Ag particles with three different Ag nanocubes coverage (Ag-L, M, and H represent the Low, Medium, and High coverage of Ag nanocubes on Fe_3O_4 bead) were fabricated through simply adjusting the amount of Ag nanocubes that used in the assembly process. Increasing in the coverage of Ag nanocubes on the surface of individual Fe_3O_4 bead would result in increasing the density of hotspots, as well as smaller interparticle gaps with larger local field enhancements.[3] As shown in Figure 10.6C, the SERS intensities were significantly increased as the coverage of Ag nanocubes increased, indicating the enhanced local field enhancement as well as the increase in the amount of 4-NTP molecules. While both rate constant and reaction percentage increased when the coverage of Ag nanocubes changed from low to medium, slight decrease were observed as the Ag nanocubes were further increased to high coverage. The abnormal results, however, can be possibly interpreted by the steric hindrance effect during this dimerization reaction. As the coverage of Ag nanocubes increased, the interparticle gap between each nanocubes would become extremely small, which might not be able to provide enough space for two 4-NTP molecules to change their orientations and then formed a DMAB molecule. Although none of direct evidence were provided to support our hypotheses, we firmly believed this is the possible reason considering the decreasing in reaction kinetics and percentage at high coverage of Ag nanocubes. Moreover, we investigated the effects of the coverage of 4-NTP on the plasmon-mediated photoreaction by systematically

adjusting the 4-NTP concentration in the molecular pre-adsorption step. Our hypotheses is that the formation of DMAB on the surface requires two reduced 4-NTP molecules with appropriate orientations and intermolecular distances to interact with each other to form the dimer structure. It is interestingly to observe that both the rate constant and reaction percentage decreased as the coverage of 4-NTP gradually reduced. In contrast to rate constant, the reaction percentage showed much more dependent on the coverage of 4-NTP, which might due to the large intermolecular distance would make it extremely difficult for molecules to move to a close distance to react.

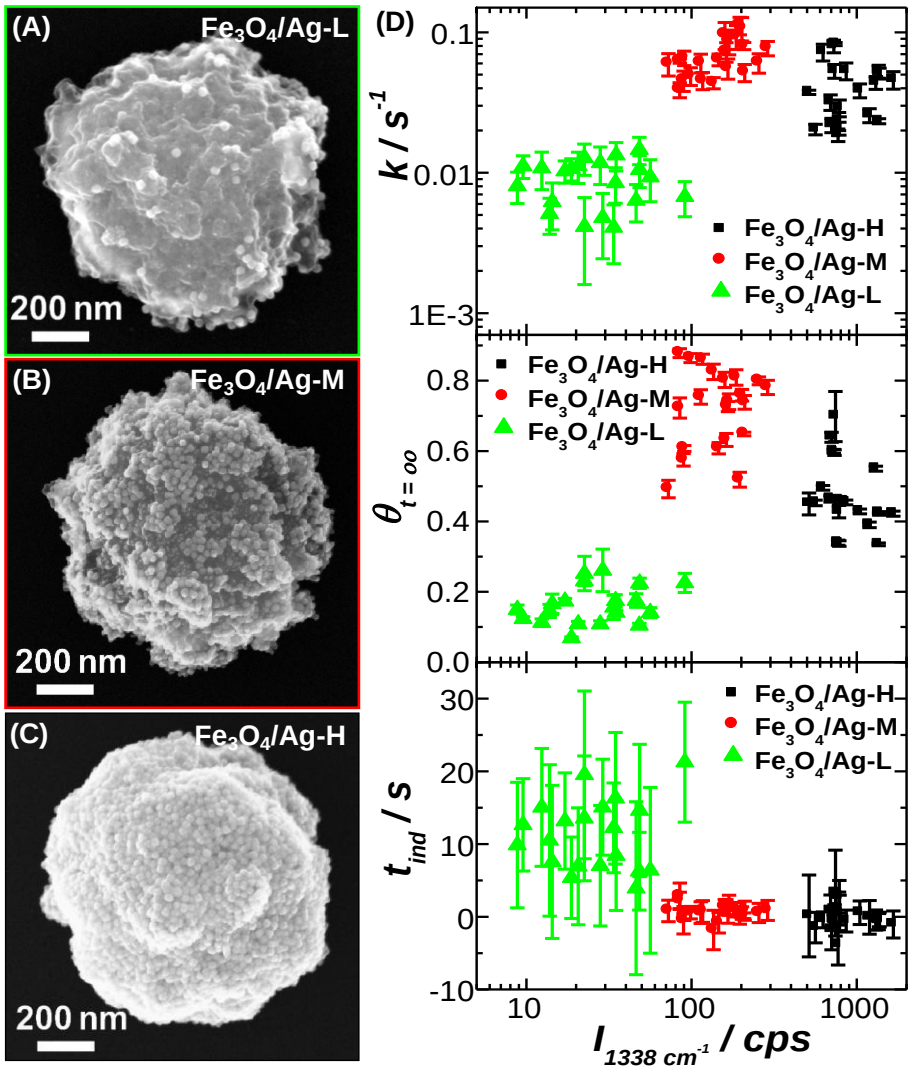

Figure 10.6. Effects of the coverage of Ag nanocubes on the plasmon-mediated photoreaction. (A-C) SEM images of (A) Fe_3O_4/Ag-L, (B) Fe_3O_4/Ag-M, and (C) Fe_3O_4/Ag-H particle. (D) Plots of rate constant (k), reaction percentage ($\theta_{t=\infty}$), and induction time (t_{ind}) versus the initial peak intensities at 1338 cm^{-1} (4-NTP) on the excitation of 785 nm laser with laser power of 620 μW. The concentration of incubated 4-NTP is 1mM. (Ag-L, M, and H represent the Low, Medium, and High coverage of Ag nanocubes on Fe_3O_4 bead)

To further investigate the underlying mechanism of this reductive dimerization of 4-NP in ambient air condition, we carried out a couple of control experiments to test the possible components from air that was involved into this photoreaction. Nitrogen gas was firstly rule out by conducting the photoreaction in pure nitrogen gas flow system, none of DMAB were observed. When quickly switching the surrounding gas from nitrogen to air, the characteristic SERS peaks of DMAB starts to dominate the SERS spectra. Secondly, we demonstrated that water species is not involved in this reaction by immersing the sample in water solution, and only a little amount of DMAB were obtained even when we further increased the laser power. Then, we decided to carried out this experiment under pure oxygen gas though this photoreaction is a reductive dimerization reaction. Surprisingly, we observed the formation of DMAB under pure oxygen gas, and both the reaction percentage and kinetics is comparable to those of ambient air condition. The interesting point is that why we need oxygen in this reductive dimerization reaction. Although no direct evidence can be provide at this point, we do have a hypothesis on the mechanism of oxygen-mediated reductive dimerization. As shown in Figure 10.7A, the excitation of hot electrons would be able to inject into the LUMO of 4-NTP to initiate the photoreaction through a Landau damping pathway. Then, the hot holes remaining on the surface of Ag nanocubes would be consumed by donation of electron from surface physisorbed oxygen, which could greatly facilitate the excitation of hot electrons and

holes to drive this photoreaction. However, at first look at the energy diagram, the huge energetic gap between HOMO of physisorbed oxygen and Fermi level of Ag make the donation of electron from oxygen become impossible. To further explore the possibility, we carried out the DFT simulation on the effect of interaction between oxygen and Ag cluster on the modulation of HOMO of oxygen. As shown in Figure 10.7B, the HOMO of oxygen could be gradually modulated as the interaction between oxygen and Ag cluster enhanced (varying size and orientation of Ag cluster). The HOMO of oxygen became comparable to the Fermi level of Ag when the oxygen is attached onto the big Ag cluster, which well mimicked the surface of Ag nanocubes. This simulation results provide strong evidence on the possibility of donation of electrons from oxygen to consume the hot holes on the surface of Ag nanocubes, which further drive the plasmon-driven photoreaction.

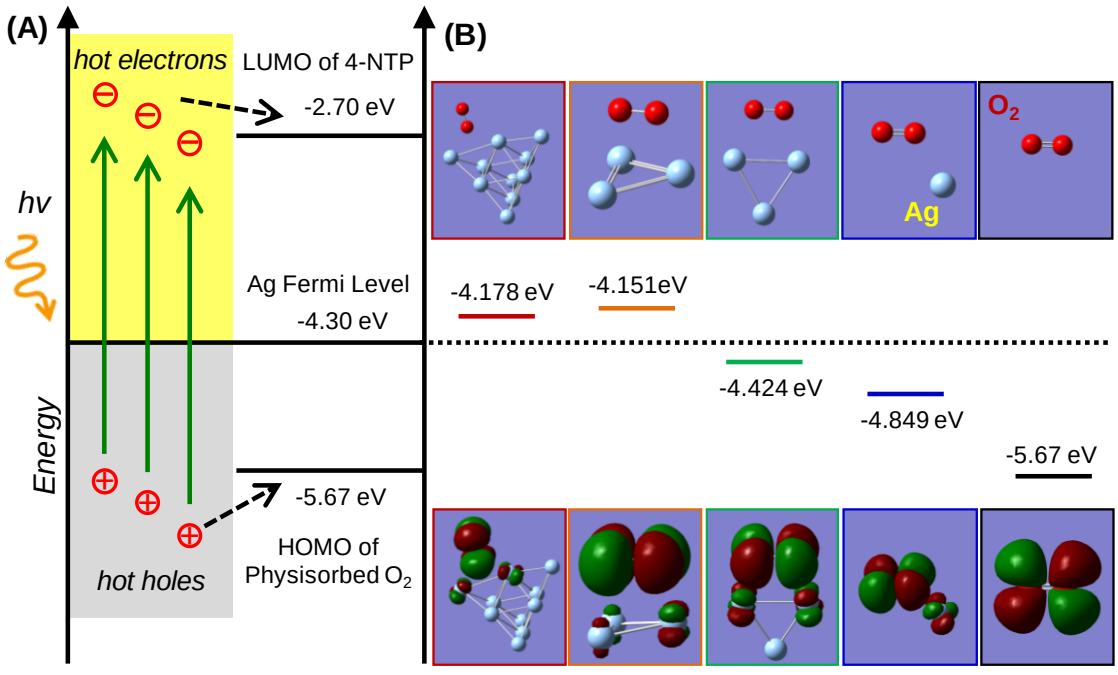

Figure 10.7. (A) Schematic illustration of plasmonic hot carriers driven photoreduction of 4-NTP assisted by O_2 upon light illumination. The hot electrons were injected into the LUMO of 4-NTP,

and the hot holes were accepted by the physisorbed O_2 on the surface of Ag nanocubes. (B) The HOMO energy level of physisorbed O_2 under different chemical environments (varying size and orientation of Ag clusters.) when approaching to the Ag surfaces.

Based on our experimental findings and theoretical results, we proposed the possible underlying mechanism of the plasmonic hot carriers driven reductive dimerization of 4-NTP into DMAB assisted by O_2 upon light illumination, as shown in Figure 10.8. Firstly, the hot electrons/holes were generated on the surface of Ag nanocubes through plasmon decay, and also the 4-NTP undergo photothermal-induced chemisorption process upon laser illumination; Secondly, hot electrons would inject into the LUMO of 4-NTP via Landau damping process to reduce the 4-NTP while the hot holes could be accepted by surface adsorbed oxygen species; Thirdly, transient intermediates of 4-NTP anionic species and oxygen cationic species were presented on the surfaces of Ag nanocubes; Fourthly, two of 4-NTP ionic species would undergo a dimerization process to form DMAB and at the same time produce oxygen anionic species; Finally, the oxygen cationic species and oxygen anionic species would combine to re-produce oxygen species on the surfaces of Ag nanocubes. While the detailed mechanism might be even more complicated, our experimental findings strongly support our above discussion toward detailed mechanism and reaction kinetics model of plasmon-driven reductive dimerization of 4-NTP.

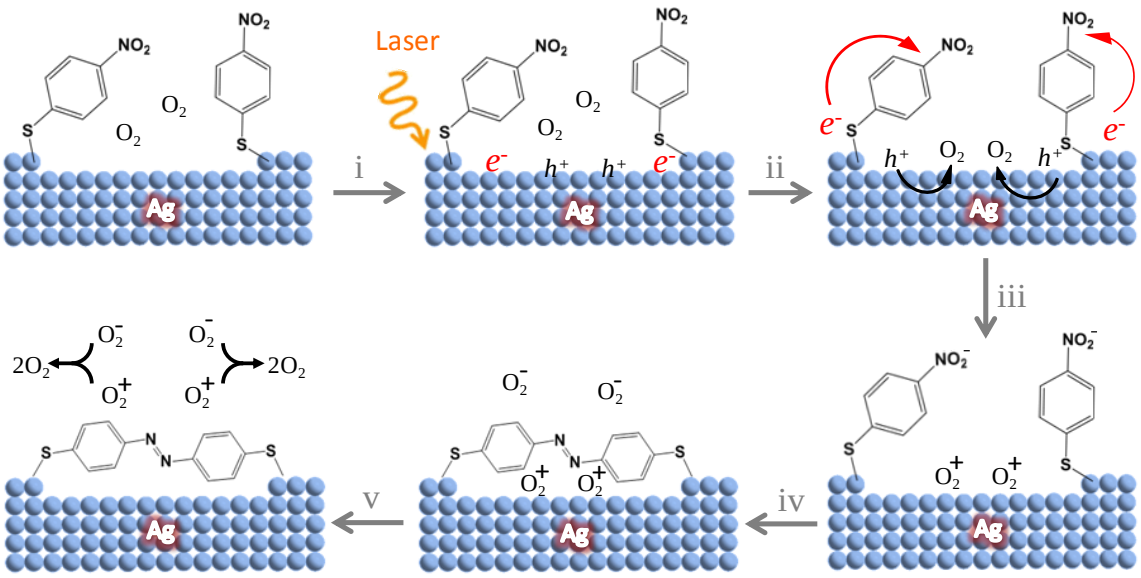

Figure 10.8. Schematic illustration of the proposed mechanism for plasmonic hot carriers driven photoreduction of 4-NTP into DMAB assisted by O_2 upon light illumination.

10.4 Conclusions

In summary, we demonstrated that plasmonic hot carriers driven photo-reductive dimerization of 4-NTP to DMAB assisted by oxygen is a two-step reaction. The first step is the chemisorption process of 4-NTP of the surfaces of Ag nanocubes due to the photothermal effect, which could be also well mimicked by thermal annealing. The second step involves the photo-reduced of 4-NTP by plasmon-generated hot electrons, giving arise to the formation of DMAB. Remarkably, we demonstrated that the reductive dimerization of 4-NTP is driven by hot carriers generated through Landau damping process according to the correlation between reaction rates and local field enhancement. Furthermore, the physisorbed oxygen species on the surface of Ag nanocubes were found to be play a key role in catalyzing the plasmon-driven photocatalytic reactions via consuming the hot holes, which allows us to completely unravel the underlying reaction mechanisms. The knowledge gained through this work would open up an unique

opportunity for wide investigations and applications of plasmonic metallic nanostructures as high-performance catalysts and photocatalysts.

10.5 References

(1) Halas, N. J.; Lal, S.; Chang, W. S.; Link, S.; Nordlander, P. *Chem Rev* **2011**, *111*, 3913-3961.

(2) Xia, Y. N.; Halas, N. J. *Mrs Bull* **2005**, *30*, 338-344.

(3) Rycenga, M.; Cobley, C. M.; Zeng, J.; Li, W. Y.; Moran, C. H.; Zhang, Q.; Qin, D.; Xia, Y. N. *Chem Rev* **2011**, *111*, 3669-3712.

(4) El-Sayed, M. A. *Accounts Chem Res* **2001**, *34*, 257-264.

(5) Nikoobakht, B.; El-Sayed, M. A. *Chem Mater* **2003**, *15*, 1957-1962.

(6) Burda, C.; Chen, X.; Narayanan, R.; El-Sayed, M. A. *Chem Rev* **2005**, *105*, 1025-1102.

(7) Murphy, C. J.; Sau, T. K.; Gole, A. M.; Orendorff, C. J.; Gao, J.; Gou, L.; Hunyadi, S. E.; Li, T. *J Phys Chem B* **2005**, *109*, 13857-13870.

(8) Jin, R. C.; Cao, Y. W.; Mirkin, C. A.; Kelly, K. L.; Schatz, G. C.; Zheng, J. G. *Science* **2001**, *294*, 1901-1903.

(9) Zhang, Q. F.; Han, L. L.; Jing, H.; Blom, D. A.; Lin, Y.; Xing, H. L. L.; Wang, H. *Acs Nano* **2016**, *10*, 2960-2974.

(10) Chen, J. Y.; Wiley, B.; Li, Z. Y.; Campbell, D.; Saeki, F.; Cang, H.; Au, L.; Lee, J.; Li, X. D.; Xia, Y. N. *Adv Mater* **2005**, *17*, 2255-2261.

(11) Willets, K. A.; Van Duyne, R. P. *Annu Rev Phys Chem* **2007**, *58*, 267-297.

(12) Camden, J. P.; Dieringer, J. A.; Zhao, J.; Van Duyne, R. P. *Acc Chem Res* **2008**, *41*, 1653-1661.

(13) Jain, P. K.; Huang, X. H.; El-Sayed, I. H.; El-Sayed, M. A. *Accounts Chem Res* **2008**, *41*, 1578-1586.

(14) Lal, S.; Clare, S. E.; Halas, N. J. *Accounts Chem Res* **2008**, *41*, 1842-1851.

(15) Giljohann, D. A.; Seferos, D. S.; Daniel, W. L.; Massich, M. D.; Patel, P. C.; Mirkin, C. A. *Angew Chem Int Ed Engl* **2010**, *49*, 3280-3294.

(16) Knight, M. W.; Sobhani, H.; Nordlander, P.; Halas, N. J. *Science* **2011**, *332*, 702-704.

(17) Heck, K. N.; Janesko, B. G.; Scuseria, G. E.; Halas, N. J.; Wong, M. S. *J Am Chem Soc* **2008**, *130*, 16592-16600.

(18) Xie, W.; Herrmann, C.; Kompe, K.; Haase, M.; Schlucker, S. *J Am Chem Soc* **2011**, *133*, 19302-19305.

(19) Joseph, V.; Engelbrekt, C.; Zhang, J. D.; Gernert, U.; Ulstrup, J.; Kneipp, J. *Angew Chem Int Edit* **2012**, *51*, 7592-7596.

(20) Huang, J. F.; Zhu, Y. H.; Lin, M.; Wang, Q. X.; Zhao, L.; Yang, Y.; Yao, K. X.; Han, Y. *J Am Chem Soc* **2013**, *135*, 8552-8561.

(21) Xie, W.; Walkenfort, B.; Schlucker, S. *J Am Chem Soc* **2013**, *135*, 1657-1660.

(22) Jing, H.; Zhang, Q. F.; Large, N.; Yu, C. M.; Blom, D. A.; Nordlander, P.; Wang, H. *Nano Lett* **2014**, *14*, 3674-3682.

(23) Zhang, Q. F.; Blom, D. A.; Wang, H. *Chem Mater* **2014**, *26*, 5131-5142.

(24) Zhang, Q. F.; Zhou, Y. D.; Villarreal, E.; Lin, Y.; Zou, S. L.; Wang, H. *Nano Lett* **2015**, *15*, 4161-4169.

(25) Brongersma, M. L.; Halas, N. J.; Nordlander, P. *Nat Nanotechnol* **2015**, *10*, 25-34.

(26) Kale, M. J.; Avanesian, T.; Christopher, P. *Acs Catalysis* **2014**, *4*, 116-128.

(27) Manjavacas, A.; Liu, J. G.; Kulkarni, V.; Nordlander, P. *Acs Nano* **2014**, *8*, 7630-7638.

(28) Wu, K.; Chen, J.; McBride, J. R.; Lian, T. *Science* **2015**, *349*, 632-635.

(29) Christopher, P.; Xin, H. L.; Linic, S. *Nature Chemistry* **2011**, *3*, 467-472.

(30) Linic, S.; Christopher, P.; Xin, H. L.; Marimuthu, A. *Accounts Chem Res* **2013**, *46*, 1890-1899.

(31) Mukherjee, S.; Libisch, F.; Large, N.; Neumann, O.; Brown, L. V.; Cheng, J.; Lassiter, J. B.; Carter, E. A.; Nordlander, P.; Halas, N. J. *Nano Lett* **2013**, *13*, 240-247.

(32) Ueno, K.; Misawa, H. *Journal of Photochemistry and Photobiology C-Photochemistry Reviews* **2013**, *15*, 31-52.

(33) Wang, F.; Li, C. H.; Chen, H. J.; Jiang, R. B.; Sun, L. D.; Li, Q.; Wang, J. F.; Yu, J. C.; Yan, C. H. *J Am Chem Soc* **2013**, *135*, 5588-5601.

(34) Govorov, A. O.; Zhang, H.; Demir, H. V.; Gun'ko, Y. K. *Nano Today* **2014**, *9*, 85-101.

(35) Tsuboi, Y.; Shimizu, R.; Shoji, T.; Kitamura, N. *J Am Chem Soc* **2009**, *131*, 12623-12627.

(36) Deeb, C.; Ecoffet, C.; Bachelot, R.; Plain, J.; Bouhelier, A.; Soppera, O. *J Am Chem Soc* **2011**, *133*, 10535-10542.

(37) Dong, B.; Fang, Y. R.; Chen, X. W.; Xu, H. X.; Sun, M. T. *Langmuir* **2011**, *27*, 10677-10682.

(38) van Schrojenstein Lantman, E. M.; Deckert-Gaudig, T.; Mank, A. J. G.; Deckert, V.; Weckhuysen, B. M. *Nat Nanotechnol* **2012**, *7*, 583-586.

(39) Huang, Y. F.; Zhu, H. P.; Liu, G. K.; Wu, D. Y.; Ren, B.; Tian, Z. Q. *J Am Chem Soc* **2010**, *132*, 9244-9246.

(40) Sun, M. T.; Huang, Y. Z.; Xia, L. X.; Chen, X. W.; Xu, H. X. *J Phys Chem C* **2011**, *115*, 9629-9636.

(41) Linic, S.; Christopher, P.; Ingram, D. B. *Nature Materials* **2011**, *10*, 911-921.

(42) Christopher, P.; Xin, H. L.; Marimuthu, A.; Linic, S. *Nature Materials* **2012**, *11*, 1044-1050.

(43) Huang, H.; Zhang, L.; Lv, Z.; Long, R.; Zhang, C.; Lin, Y.; Wei, K.; Wang, C.; Chen, L.; Li, Z. Y.; Zhang, Q.; Luo, Y.; Xiong, Y. *J Am Chem Soc* **2016**, *138*, 6822-6828.

(44) Mubeen, S.; Lee, J.; Singh, N.; Kramer, S.; Stucky, G. D.; Moskovits, M. *Nat Nanotechnol* **2013**, *8*, 247-251.

(45) Zheng, T. T.; Zhang, Q. F.; Feng, S.; Zhu, J. J.; Wang, Q.; Wang, H. *J Am Chem Soc* **2014**, *136*, 2288-2291.

(46) Wang, H.; Halas, N. J. *Adv Mater* **2008**, *20*, 820-+.

(47) Dai, Z. G.; Xiao, X. H.; Zhang, Y. P.; Ren, F.; Wu, W.; Zhang, S. F.; Zhou, J.; Mei, F.; Jiang, C. Z. *Nanotechnology* **2012**, *23*, 335701.

(48) Zhang, X.; Wang, P. J.; Zhang, Z. L.; Fang, Y. R.; Sun, M. T. *Sci Rep-Uk* **2014**, *4*.

(49) Brooks, J. L.; Frontiera, R. R. *J Phys Chem C* **2016**, *120*, 20869-20876.

(50) Lin, T. W.; Tasi, T. T.; Chang, P. L.; Cheng, H. Y. *Acs Appl Mater Inter* **2016**, *8*, 8315-8322.

(51) Aggarwal, R. L.; Farrar, L. W.; Saikin, S. K. *J Phys Chem C* **2012**, *116*, 16656-16659.

(52) Canpean, V.; Astilean, S. *Spectrochim Acta A* **2012**, *96*, 862-867.

(53) Boerigter, C.; Campana, R.; Morabito, M.; Linic, S. *Nat Commun* **2016**, *7*, 10545.

(54) Takeyasu, N.; Kagawa, R.; Sakata, K.; Kaneta, T. *J Phys Chem C* **2016**, *120*, 12163-12169.

Appendix A

Publications related to the research work described in this dissertation

1) **Qingfeng Zhang**, Yadong Zhou, Guangfang Li, Lichao Sun, Esteban Villarreal, Shengli Zou, and Hui Wang, "Plasmonic Hot Electrons Driven Photocatalytic Reactions: New Insights Gained from Plasmon-Enhanced Spectroscopic Studies", *manuscript in preparation.*

2) **Qingfeng Zhang**, and Hui Wang, "Insights on Plasmon-Driven Oxidative Coupling of Thiophenol-Derivates: Evidence on Steady-State Active Oxygen Species", *manuscript in preparation.*

3) **Qingfeng Zhang**, Hao Jing, Guangfang Li, Ye Lin, Douglas A. Blom, and Hui Wang, "Intertwining Roles of Silver Ions, Surfactants, and Reducing Agents in Gold Nanorod Overgrowth: Pathway Switch between Silver Underpotential Deposition and Gold-Silver Codeposition", *Chem. Mater.*, **2016**, *28*, 2728-2741. (Top 20 Most Read Articles published in this journal over one month period)

4) **Qingfeng Zhang**, Lili Han, Hao Jing, Douglas A. Blom, Ye Lin, Huolin L. Xin, and Hui Wang, "Facet Control of Gold Nanorods", *ACS Nano*, **2016**, *10*, 2960-2974.

5) **Qingfeng Zhang**, Yadong Zhou, Esteban Villarreal, Ye Lin, Shengli Zou, and Hui Wang, "Faceted Gold Nanorods: Nanocuboids, Convex Nanocuboids, and Concave Nanocuboids", *Nano Lett.*, **2015**, *15*, 4161-4169. (Most Read Articles published in this journal over one month period)

6) **Qingfeng Zhang**, and Hui Wang, "Facet-Dependent Catalytic Activities of Au Nanoparticles Enclosed by High-Index Facets", *ACS Catal.*, **2014**, *4*, 4027-4033. (Top 5 Most Read Articles published in this journal over one month period)

7) **Qingfeng Zhang**, Douglas, A. Blom, and Hui Wang, "Nanoporosity-Enhanced Catalysis on Subwavelength Au Nanoparticles: a Plasmon-Enhanced Spectroscopic Study", *Chem. Mater.*, **2014**, *26*, 5131-5142.

8) **Qingfeng Zhang**, Nicolas Large, and Hui Wang, "Gold Nanoparticles with Tipped Surface Structures as Substrates for Single-Particle Surface-Enhanced Raman Spectroscopy: Concave Nanocubes, Nanotrisoctahedra, and Nanostars", *ACS Appl. Mater. Interfaces*, **2014**, *6*, 17255-17267.

9) **Qingfeng Zhang**, Nicolas Large, Peter Nordlander, and Hui Wang, "Porous Au Nanoparticles with Tunable Plasmon Resonances and Intense Field Enhancements for Single-Particle SERS", *J. Phys. Chem. Lett.*, **2014**, *5*, 370-374. (Top 20 Most Read Articles published in this journal over one month period)

Appendix B

Copyright Permission